Thin Films for the Transport of Polarized Ultracold Neutrons for Fundamental Symmetry Study

Russell R. Mammei

Dissertation submitted to the Faculty of the
Virginia Polytechnic Institute and State University
in partial fulfillment of the requirements for the degree of

Doctor of Philosophy
in
Physics

Robert Bruce Vogelaar, Chair
Jean Heremans
Giti Khodaparast
Mark L. Pitt

August 11, 2010
Blacksburg, Virginia

Keywords: Polarized Ultracold Neutrons, Neutron Beta Decay, Standard Model Tests, Polarized Neutron Guides, Diamond-Like Carbon, Pulsed Laser Deposition, Ebeam Evaporation, Electropolishing, Mechanical Polishing, Surface Roughness

Thin Films for the Transport of Polarized Ultracold Neutrons for Fundamental Symmetry Study

Russell R. Mammei

Abstract

The use of ultracold neutrons (UCN) to study fundamental parameters such as the neutron lifetime and decay correlations in polarized neutron beta decay are poised to make significant contributions to our understand of the Standard Model and its extensions. To this end, the UCNA experiment is pursuing a precision measurement (0.2%) of the angular correlation between the neutron spin and the direction of emission of the electron in polarized neutron decay (the A asymmetry). The UCNA experiment makes use of the spallation-driven SD_2 UCN source at the Los Alamos Neutron Science Center (LANSCE). The UCN leave the source and are 100% polarized by passing through a strong magnetic field before their decay is observed by a very sensitive electron spectrometer.

UCN guides facilitate the transfer of UCN from the source to the spectrometer. Common guide materials include stainless steel, copper, aluminum, and quartz. Often a thin film is applied to these components to increase their ability to transport/bottle and preserve the polarization of UCN. In the region of the SD_2 UCN source, ^{58}Ni films are applied, whereas once the UCN are polarized, diamond-like carbon (DLC) films are employed. This dissertation covers the application, process developments, and characterization of these coatings. In addition a study concerning the surface finish resulting from the mechanical polishing and electropolishing of the guides that make up the UCNA beamline is presented.

This work was funded primarily by the National Science Foundation through grants 0099448, 0401526, 0700491, and 1002814.

Acknowledgments

First of all I would like to acknowledge my advisor, Bruce Vogelaar, for his guidance and support during this process. His willingness to allow students to pursue their own interests has really fostered a strong sense of ownership in my work. I would also like to thank Mark Pitt for his guidance and for taking the time out of his busy schedule to teach our QED and Special Topics in Nuclear Physics classes. In addition I would like to thank all the professors at Virginia Tech that have helped me with coating and characterization issues, especially: Jean Heremans, Giti Khodaparast , Hans Robinson, Victoria Soghomonian, Randy Heflin, Kathleen Meehan, Carlos Suchicital, and Gordon Yee.

I would like to thank Albert Young of North Carolina State University (NSCU) for his instruction, guidance, and support during the course of the last six years. I really appreciated his ability to see the importance and opportunities of my work when things looked grim.

Special thanks to Mark Makela at Los Alamos National Lab (LANL) for his guidance and support while I continued his work on the guide coatings for the UCNA experiment.

I would also like to thank all the graduate students that have assisted with the coatings for the UCNA experiment: Grant Palmquist (NCSU), Brittney VornDick (NCSU), Robby Pattie (NSCU), Chris Cottrell (NCSU), Steve Hardy (VT), Matt Joyce (VT), Henning Back (now a research associate with Princeton University), and Brad Williams. In addition several undergrads have also helped with these coatings and should be acknowledged: David Richardson, James Dowd, John Hughes, Elizabeth Bonnel, Devon Triplett, Mike Sperry, Jay Billings, and Brian Skinner.

Thanks to Bryan Dickerson for his creativity and diligence in the design and construction of our target raster system. Without his work our coating processes would not be where they are today.

In addition, I would like thank all the support staff in the physics department at Virginia Tech: Tina Lawrence, Betty Wilkins, Tammy Harris, Lisa Stables, Travis Heath, Roger Link, Scott Allen, John Miller, Ron Stables, Norm Morgan, and Fred Mahone. They were always willing to go the extra mile for what crisis I had at the moment. Special thanks needs to go out to Christa Thomas who always goes out of her way to not only help me but each and

every graduate student in physics at Virginia Tech. You will truly be missed.

I would also like to thank Frank Cromer in the chemistry department, Jerry Hunter of the ICTAS center, and Chris Honig and Clayton McKee of the chemical engineering department at Virginia Tech for their assistance in characterizing my films.

Thanks to the entire UCNA collaboration for their support and guidance during this endeavor, for without your efforts there would be no reason for me to work on UCN guide coatings. I would especially like to thank Andy Saunders, Chris Morris, John Ramsey, and Walt Sondheim at LANL for their insight and support (often monetary) of my work.

Adam Holley, thanks for all your wonderful plots and guidance during my time at LANL. You have a very bright future ahead of you.

Thanks to Steve Irving and his staff at Irving Polishing Inc. for all the work they have done on polishing our beamline components. I really enjoyed working with and staying with Steve during my site visit in 2009.

Thanks to the entire Vogelaar family for opening up their lovely home to me while I was finishing up writing my dissertation.

Thanks to my parents for their encouragement and support in everything that I do in my life.

Finally, I would like to thank my family for their support and advice as I worked to complete this chapter of my life. Special thanks to my wife, Juliette, who put up with me staying late and going in on weekends to supply the coated beamline components. I look forward to what our careers and family life have in store for us.

Contents

List of Figures

List of Tables

Chapter 1

Introduction and Theory

1.1 Introduction

The study of neutron beta decay, where the neutron decays into a proton, electron, and anti-neutrino, has led to significant advances in the understanding of our world and how its constituents interact with each other. It continues to do so today as ever more precise nuclear and free neutron beta-decay experiments are just now testing important aspects of the prevailing theory of particle physics, the Standard Model. Most free neutron beta-decay experiments employ what are called cold neutrons, whose speeds are around 400-1000 m/s ($\sim$1 - 5 meV energies), but one can also use even lower energy neutrons, called ultracold neutrons (UCN). For context, most neutron sources, fission neutrons for example, emit neutrons with with an energy of $\sim$2 MeV. These neutrons are then "cooled" through a variety of elastic collisions. With UCN the neutron is moving at speeds near $\sim$8 m/s and less. UCN have a very unique property that they can reflect off a material surface from any angle of incidence. Thus they can guided many meters from a source of UCN to a decay

trap where the beta decay is observed via a suite of particle detectors. This allows the source of UCN to be heavily shielded, without which the beta decay signals one is trying to observe would be overwhelmed by the signals generated by the source itself. Also UCN can be 100% polarized, that is the neutron has a magnetic momentum which can oriented in a specific direction using magnetic fields, and this polarization can be flipped with close to 100% efficiency. These facts allow UCN experiments to have very different systematic errors than those seen with cold neutrons and the two together provide a robust test of the both the standard model and its theoretical extensions.

The UCNA experiment is doing just this: employing UCN to measure the asymmetry between the neutron polarization direction and the emission direction of the daughter electron in polarized free neutron decay. This parameter is one of many neutron beta decay correlations, and is named A (pronounced "big A"). The experiment utilizes the SD_2 superthermal UCN source at the Los Alamos Neutron Science Center (LANSCE) located at the Los Alamos National Lab (LANL), in Los Alamos, NM, USA. The UCN are generated in the SD_2 source and then allowed to flow through several meters of pipes/tubes, called UCN guides. The pipes thread through two 7 T superconducting solenoid magnets which polarize the UCN before they enter a 1 T superconducting solenoid magnet/electron detector apparatus where the UCN can rattle around inside a series of UCN bottling guides, called the decay-trap guides, until they are lost either through beta decay or other processes. Virginia Tech is responsible for providing these UCN guides. Often the performance of the UCN guides, i.e. how well they transmit UCN, can be improved upon beyond the innate levels of common engineering materials such as stainless steel or copper tubes by applying a coating to the inside of the tubes. To this end the UCNA group at Virginia Tech has developed a UCN guide-coating facility over the past ten years. Here UCN guide substrates are prepared and coated with primarily two thin films: ^{58}Ni and Diamond-like-Carbon (DLC). ^{58}Ni is

exceptionally good are reflecting UCN, in fact it is the material that has defined the energy scale of UCN. ^{58}Ni coatings are primarily used in the SD_2 UCN source region of the system. DLC films are used in the regions where the UCN have been polarized, as DLC is fairly good at reflecting neutrons, but is exceptional at preserving the polarization of the UCN upon reflection. These coatings are applied to a variety of tubing and machined components. The most common substrates are stainless steels, copper alloys, and quartz. The production of these coated guide components is non-trivial and many hurdles have been overcome in developing processes that provide robust long-lived coated UCN guides.

This thesis is devoted to these developments. We will first introduce how UCN interact with the four forces of nature and then develop the theory of neutron beta decay and motivate the measurement of A. Next we will described the UCNA experiment with a focus on the specific requirements of the UCN guides and provide an overview of the current results of the UCNA experiment. Then we will move to a description of the coating facility and the techniques employed to apply the ^{58}Ni and DLC films. Afterward we will describe the thin film and surface analysis tools used to determine the properties of the coatings and the substrates themselves. Next we describe the UCN guide substrate preparation with a focus on the characterization of their surface roughness. Then we discuss the multiple ^{58}Ni UCN source guides and the lessons learned during these coatings. Finally we close with description of the process that was developed to produce an adhered DLC coating on the copper beamline components and detail the various properties of the DLC films as measured by the aforementioned surface characterization techniques.

1.2 UCN Interactions

Most experiments employing free neutrons utilize reactor neutrons or spallation neutrons at

different energies depending on the experiment. The neutrons are often classified into groups depending on their kinetic energy [3]. We will primarily deal with UCN whose kinetic energies are ≤ 350 neV which correspond to wavelengths of ≥ 50 nm. Due to these low energies all four forces: gravity, electro-magnetism, the weak interaction, and the strong force, need to be considered when working with UCN.

1.2.1 Gravity

Due to their low kinetic energy (KE), gravity heavily influences UCN experiments as the UCN will loose or gain 102 neV of KE for every meter increase or decrease in height respectively via the gravitation potential:

$$V_g = m_n g h \tag{1.1}$$

where V_g is the gravitational potential energy, m_n is the mass of the neutron, g is the acceleration from the attraction to the earth, and h is the height change. This effect is very useful as it can be used to accelerate the UCN through material foils used in UCN detectors and velocity spectrometer schemes as described in sections 2.5 and 6.2.

1.2.2 Magnetism

Although UCN cannot be transported with the help of electric fields, they do posses a magnetic dipole momentum (spin $\frac{1}{2}\hbar$) and thus interact with magnetic fields. The interaction in a homogeneous magnetic field follows:

$$V_m = -\boldsymbol{\mu} \cdot \boldsymbol{B}(\boldsymbol{r}) = \pm 60 \frac{neV}{T} \tag{1.2}$$

We see that one spin state sees a potential hill while the other sees a potential well. This barrier can be used to produce a beam composed entirely of one spin state, i.e. 100% polarized. It is also important to mention that an inhomogenious magnetic field will exert a force on the UCN given by

$$\boldsymbol{F_m} = -\boldsymbol{\nabla} V_m = \boldsymbol{\nabla}[\boldsymbol{\mu} \cdot \boldsymbol{B}(\boldsymbol{r})] \tag{1.3}$$

If the neutron's magnetic momentum follows the the magnetic field (the adiabatic case) then

$$\boldsymbol{\nabla}[\boldsymbol{\mu} \cdot \boldsymbol{B}(\boldsymbol{r})] = \pm|\boldsymbol{\mu}|\boldsymbol{\nabla}|\boldsymbol{B}(\boldsymbol{r})| \tag{1.4}$$

For this case to be valid the time dependence of the magnetic field as seen by the neutron must be much less that the Larmor (precession) frequency of the neutron moment in the field:

$$\frac{1}{\tau} = \frac{1}{|\boldsymbol{B}|} \cdot \left| \frac{d\boldsymbol{B}}{dt} \right| \ll \frac{\boldsymbol{\mu} \cdot \boldsymbol{B}}{\hbar} = \omega_L \tag{1.5}$$

Often the time dependence of the applied magnetic fields are tailored so that the adiabatic case applies and this has been done for the magnetic fields used in the UCNA experiment.

1.2.3 Weak Interaction

Free neutrons are not stable and decay through the weak interaction via the process $n \rightarrow p + e^- + \bar{\nu}$. This is the reaction studied by the UCNA experiment, as well as many others, and is described in detail in section 1.7.

1.2.4 Strong Interaction

The neutron does feel the strong force and it is this interaction that gives rise to the total reflection of UCN from a surface. For this treatment we will follow that laid out by Golub et al. [147]. The low energy neutron-nucleus potential follows that of a spherical square well with depth of ∼40 MeV and radius of ∼2 fm. Note this well depth is approximately constant for all nuclei, but with larger radius growing as $\sim R_0 A^{1/3}$ [7]. UCN are so low in energy that their de-Broglie wavelength satisfies

$$kR = \frac{2\pi R}{\lambda_n} \ll 1 \tag{1.6}$$

where k is the wavenumber for the neutron, λ_n is the wavelength of the neutron, and R is the extent of the nucleus's spherical potential. For scattering off this potential the total wavefunction outside the well is

$$\psi = e^{i\boldsymbol{k}\cdot\boldsymbol{r}} + f(\theta)\frac{e^{ikr}}{r} \tag{1.7}$$

where the first term is for the incident beam and the second term is for the scattered wave where $f(\theta)$ is the scattering amplitude which is determined by the boundary conditions at r = R and is a function of the angular momentum state of the incident neutron. In the case for neutrons satisfying equation 1.6, s-wave scattering dominates, as any neutron in a higher angular momentum state will not be in the range of the nuclear potential well and hence not be scattered. Thus we have

$$f(\theta) = constant = -a \tag{1.8}$$

where a is now called the scattering length. Now the wavefunction just outside the well, where R < r < 1/k, follows

$$\psi \approx 1 - \frac{a}{r} = \frac{r-a}{r} \tag{1.9}$$

so that $u = r\Psi$ has the form of a straight line. At $r = a$, $\psi = 0$ and so a appears to be the radius of a hard sphere which would produce the same wavefunction as the actual scattering potential, as perceived from large distances. With the above sign convention, a positive a would imply a repulsion, while a negative a would imply an attraction when observed from far away. One can further apply the boundary condition that $\frac{du}{dr}/u$ is continuous at $r = R$ and find that most nuclei will have positive a.

1.2.5 Fermi Potential

Although perturbation theory can not be used to describe the wavefunction inside the potential well, Fermi realized that it could be used to describe the wavefunction outside the well. To this end, Fermi sought an equivalent potential which could be used to describe the small changes to the wavefunction that is outside the nuclear potential well. Starting with the Schrödinger equation for the neutron-nucleus system we have

$$-\frac{\hbar^2}{2\mu}\nabla^2\psi + [E - V(\boldsymbol{\eta})]\psi = 0 \tag{1.10}$$

where $\boldsymbol{\eta} = \boldsymbol{r} - \boldsymbol{r_n}$ and μ is the reduced mass of the system, not the neutron's magnetic moment. Fermi wanted to find a potential such that

$$-\frac{\hbar^2}{2\mu}\nabla^2\psi + [E - U(\boldsymbol{\eta})]\psi = 0 \tag{1.11}$$

where $U(\boldsymbol{\eta})$ satisfies

$$\begin{aligned} U(\boldsymbol{\eta}) = &\quad -U_0 \quad \boldsymbol{\eta} < \boldsymbol{\rho} \\ = &\quad 0 \quad\quad \boldsymbol{\eta} > \boldsymbol{\rho} \end{aligned} \tag{1.12}$$

where ρ is a distance such that $\rho \ll \lambda_n$, $\rho \gg a$, and $\rho \gg R$. Thus we are looking for a potential U_0 that has a larger range than that of the nucleus and the scattering length, but still shorter than the neutron's wavelength. The wavefunction solution of equation 1.11 will also be a valid solution of equation 1.10 for $r > R$ with the same form as 1.7 where we use the first Born approximation applied to $U(\boldsymbol{\eta})$ to calculate $f(\theta)$ (defined in equation 1.7)

$$f(\theta) = -\frac{\mu}{2\pi\hbar^2} < \boldsymbol{k_f}|U|\boldsymbol{k_i} >= -\frac{\mu}{2\pi\hbar^2}\int d^3\eta U(\boldsymbol{\eta}) e^{i(\boldsymbol{k_i}-\boldsymbol{k_f})\cdot\boldsymbol{\eta}} \tag{1.13}$$

Here we still want s-wave scattering to dominate so that $f(\theta)$ is not dependent on θ. Thus we require that the range of $U(\boldsymbol{\eta})$ to follow a similar criteria as equation 1.6, namely $k\rho \ll 1$. With this assumption we can evaluate $f(\theta)$

$$f(\theta) = -\frac{\mu}{2\pi\hbar^2}\int d^3\eta U(\boldsymbol{\eta}) e^{i(\boldsymbol{k_i}-\boldsymbol{k_f})\cdot\boldsymbol{\eta}} = -\frac{\mu}{2\pi\hbar^2} U_0 \int d^3\eta = -\frac{\mu}{2\pi h^2} U_0 \cdot \frac{4}{3}\pi\rho^3 \tag{1.14}$$

where we have used $e^{i(\boldsymbol{k_i}-\boldsymbol{k_f})\cdot\boldsymbol{\eta}} \approx 1$, for $\eta = [0, \rho]$. We can then rearrange to get

$$U_0 = \frac{-3\hbar^2 a}{2\mu\rho^3} \quad so\ that \quad \int U(\boldsymbol{\eta}) d^3\eta = -U_0 \frac{4}{3}\pi\rho^3 = 2\pi\hbar^2 \frac{a}{\mu} \tag{1.15}$$

So in calculating matrix elements one can use

$$U_F = \frac{2\pi\hbar^2 a}{\mu}\delta^{(3)}(\boldsymbol{\eta}) \tag{1.16}$$

where $\delta^{(3)}$ is the volume Dirac delta function. We note the above has been derived assuming the nucleus could recoil. For UCN scattering from a material surface, the nuclei are considered to be rigidly bound and so the scattering length, a, is replaced with the bound nucleus scattering length

$$b \equiv \frac{m}{\mu} a \tag{1.17}$$

Thus equation 1.16 becomes

$$U_F = \frac{2\pi\hbar^2 b}{m}\delta^{(3)}(\boldsymbol{\eta}) \tag{1.18}$$

Now each nuclei in a solid sample gives rise to its own U_F and the effective interaction is a sum of these potentials:

$$V_{eff} = \frac{2\pi\hbar^2}{m}\sum_i b_i \delta(\boldsymbol{r} - \boldsymbol{r_i}) \tag{1.19}$$

where $\boldsymbol{r_i}$ is the position of the ith nucleus and the sum is over all the nuclei in the sample. Thus the wavefunction of the neutron is a combination of the incident beam and the sum of all the spherical waves scattered by the nuclei in the sample:

$$\psi(\boldsymbol{r}) = e^{i\mathbf{k_0}\cdot\mathbf{r}} - \sum_i b_i \psi_i(\boldsymbol{r_i})\frac{e^{ik_0|\boldsymbol{r}-\boldsymbol{r_i}|}}{|r - r_i|} \tag{1.20}$$

where each $\psi_k(\boldsymbol{r_k})$ is the total wave incident on the kth nucleus. This can be rewritten as

$$\psi(\boldsymbol{r}) = e^{i\mathbf{k_0}\cdot\mathbf{r}} - \int \psi(\boldsymbol{r'})\frac{e^{ik_0|\boldsymbol{r}-\boldsymbol{r'}|}}{|r - r'|}[nb(\boldsymbol{r'})]d^3r' \tag{1.21}$$

where we have made the multiple scattering approximation that $\psi_i(\boldsymbol{r_i}) = \psi(\boldsymbol{r_i})$ and $[nb(\boldsymbol{r'})]d^3r'$ is the sum of the scattering lengths in the volume element d^3r' around $\boldsymbol{r'}$. Operating on both sides of 1.21 with $(\nabla^2 + k_0^2)$ one obtains

$$(\nabla^2 + k_0^2)\psi(\boldsymbol{r}) = 4\pi[bn(\boldsymbol{r})]\psi(\boldsymbol{r}) \tag{1.22}$$

where we have used the identity $(\nabla^2 + k_o^2)\frac{e^{ik_0|\boldsymbol{r}-\boldsymbol{r'}|}}{|r-r'|} = -4\pi\delta^{(3)}(\boldsymbol{r}-\boldsymbol{r'})$ and evaluated the integral using the $\delta^{(3)}$ function. Multiplying by $-\hbar^2/2m$ and rearranging we get

$$-\frac{\hbar^2}{2m}(\nabla^2)\psi(r) + \frac{2\pi\hbar^2}{m}[bn(\boldsymbol{r})]\psi = \frac{\hbar^2}{2m}k_0^2\psi(\boldsymbol{r}) = E\psi(\boldsymbol{r}) \tag{1.23}$$

which is the Schrödinger equation for the neutron moving through a potential

$$V(\boldsymbol{r}) \equiv \frac{2\pi\hbar^2}{m}[bn(\boldsymbol{r})] = \frac{2\pi\hbar^2}{m}Nb \equiv V_F \tag{1.24}$$

This potential, V_F, is called the Fermi Potential where N is the number density of the material and b is, as defined earlier, the bound scattering length of the material. Now V_F is the volume average of the individual scattering lengths of the atoms in the material, which in general are not all the same. The scattering lengths vary from one isotope to another as well as depend upon the spin state of the nucleon and the incident neutron. To account for this, the the scattering length is divided into two parts: a bound coherent scattering length and an incoherent scattering length, which is given by the mean square fluctuations of the scattering lengths in the sample. For example ^{58}Ni has a bound coherent scattering length of 14.4 fm, where as natural nickel's is 10.3 fm. One calculates the Fermi Potential of the material in question using the bound coherent scattering length only. Measured values of both scattering lengths for every element and their isotopes have been tabulated by NIST [125]. Table 1.1 lists the calculated Fermi Potentials for the most common materials used in the UCN guide applications.

Thus we see that the reflection of UCN from surfaces is really a one-dimension potential step (well) quantum mechanics problem, as depicted in figure 1.1. Thus UCN with energy both above and below the Fermi Potential of the material each have a reflection and transmission probability, which are affected by the height of the V_F, which is a function

of the density of the material and its bound coherent scattering length, and its extent, i.e. thickness. Equations for the transmission and reflection probabilities can be found in most quantum mechanics texts books as well as in [147].

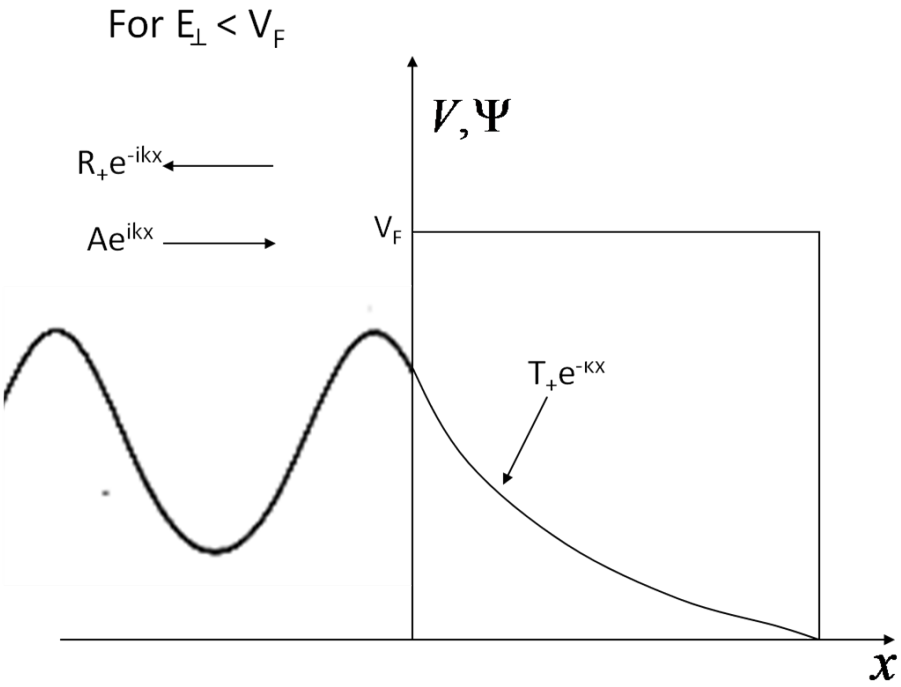

Figure 1.1: Wavefunction of a particle reflected from a step well potential.

1.3 Loss of UCN

In addition to the effective "hard sphere" scattering described by the Fermi Potential, there is a tunneling probability for the neutron to penetrate this barrier. During this time, the UCN can be absorbed by the material or inelastically up-scattered. The former is described by the neutron absorption probability or cross section for the material in question, while the latter is attributed to the transfer of thermal excitations to the neutron, thus giving the neutron a greater energy than the Fermi Potential of the material which greatly decreases the

probability that the UCN will be reflected from subsequent material interactions. The primary absorption processes are (n,γ), (n,α), and (n, p), whose resultant radiation is a source of background in particle detectors that observe the UCN decay. These loss mechanisms can be described by adding an imaginary part to equation 1.24, as these processes are generally irreversible [147]. Here one makes the replacement $U = V_F - iW$ in the Schrödinger equation. By constructing the conservation of probability density equation from the Schrödinger equation, one sees that

$$W = \frac{\hbar}{2} \sum_i N_i \sigma_l^{(i)} v \tag{1.25}$$

where N_i is the density and $\sigma_l^{(i)}$ is the loss cross section, absorption and up-scattering, of the ith isotope. Most $\sigma_l \propto 1/v$ so that W is velocity independent. In practice, when choosing a material one takes the loss probability into account by looking at the wall loss probability per bounce, $\mu(E, \theta)$, which is defined as

$$\mu(E,\theta) = 2f\left(\frac{E\cos^2\theta}{V_F - \cos^2\theta}\right)^{1/2} \quad \text{for} \quad E = [0, V_F) \tag{1.26}$$

where E is the total UCN energy, θ is the UCN angle of approach to the surface, and $f = W/V$. This is connected to the reflection probability through: $|R|^2 \equiv 1 - \mu(E, \theta)$. Table 1.1 includes measured average loss probabilities per bounce for the materials listed.

1.4 Depolarization of UCN

In addition to the above the considerations when selecting a UCN surface, one may also take into account the probability the wall interaction will depolarize the UCN. This is extremely critical in polarized neutron angular correlation experiments, as the correlation is proportional to the degree of the polarization. Thus once the UCN is polarized, one chooses

materials that have a very low depolarization per bounce probability to preserve this polarization. The depolarization occurs through two processes: magnetic field gradients and spin exchange. In the former the neutron's magnetic moment cannot not keep up with the changing field and the adiabatic criteria is violated. The magnetic fields can come from external sources or the magnetic fields produced by the electrons in the material, such as in iron. For this reason, ^{58}Ni coatings cannot be used in much of the UCNA beamline, as the UCN would quickly depolarize from interacting with the magnetic nickel film. A description of this process can be found in [44]. In the latter, unpaired nuclear spins of the elements in the UCN surface can interact with the UCN's magnetic momentum and flip its direction. One looks to the measured depolarization per bounce probability, to which Serebrov has contributed immensely [154] [156], when taking these effects into account. Table 1.1 includes these values for a vareity of common UCN guide/bottle materials. Thus non-magnetic, spin-paired materials should be chosen if one wants to preserve the polarization of the UCN. DLC fits this requirement as it is predominantly made of ^{12}C which is spin paired and non-magnetic.

1.5 Surface Roughness

A third parameter to consider when selecting a material as a UCN surface is the surface roughness of the material. Surface roughness has two effects on UCN scattering: it results in non-specular scattering and increased UCN loss probability. In specular scattering the momentum component parallel to the surface stays constant, while the perpendicular component reverses sign. Non-specular scattering results in a scattered distribution around the specularity scattered direction which spreads out as the surface roughness increases. This tends to promote more surface reflections which can result in UCN being reversed in direction, which is a major concern when attempting to guide UCN. It also increases the loss of

UCN whose energy, E, may have been higher than the V_F of the material but still reflected because $E_\perp = E\cos^2\theta < V_F$. Here the surface roughness changes the angle of approach, θ, which may lead to $E\cos^2\theta > V_F$ greatly increasing the transmission probability through the surface.

Surface roughness can affect the loss probability, $\mu(E,\theta)$, in two ways. If the surface roughness correlation length is large when compared to the UCN wavelength ,λ_n, then the surface looks globally wavy, while locally smooth to the UCN. Thus the losses are primarily due to the increased surface area as compared to the perfectly flat surface. On the other hand if the correlation length is small when compared to λ_n, then the UCN sees the surface roughness as a mixture of voids and material. The voids effectively lower the V_F step seen by the UCN, which alters $\mu(E,\theta)$.

Several authors have taken up the task of modeling the surface roughness, to which Steyerl and Ignatovich have made significant contributions [166] [74]. Most models use similar techniques employed with the reflection of sound and electromagnetic waves, that treat the surface roughness as a perturbation to the flat substrate. This is valid for surface roughnesses up to about 5 nm over several hundred nm, which is reasonable for the highly polished surfaces used in UCN guides. The reader is referred to the above citations as well as [110] and [59] for the implementation of these models.

1.6 Summary

When selecting a material to be a UCN surface one first looks at the Fermi Potential, as this sets the maximum energy a UCN can have and still totally reflect from the surface. As described in chapter 2, the number of UCN $\propto V_F^{3/2}$ and so 2.6 times more UCN will be

initially trapped by ^{58}Ni than stainless steel which is important for most UCN experiments where more statistics are not only welcome but often required. After the Fermi Potential, one usually looks at the loss probability per bounce, and then the specularity/roughness of the surface. For depolarization experiments, one also needs to consider the depolarization probability per bounce. These physics constraints are then coupled to the engineering and cost parameters of the experiment. For example, making a typical 1 m long UCN guide out of ^{58}Ni would cost tens of thousands of dollars which is not feasible for most experiments. For this reason coatings are often applied to more conventional engineering materials, such as stainless steels, copper, quartz, some plastics, etc. Common coatings are ^{58}Ni , Ni, Be, ^{65}Cu, and DLC to name a few. ^{58}Ni and the mixture ^{58}Ni/Mo(10%) are commonly used for UCN as they have a very high Fermi Potential that can bottle/guide more UCN than other materials. For experiments requiring a low depolarization probability per bounce material, Be and ^{65}Cu were commonly used in the 70's-90's as they have a relatively high Fermi Potential and low depolarization per bounce. In the late 90's and into the 00's, DLC became a more attractive replacement for these materials. If properly prepared, DLC has a higher Fermi Potential and lower loss and depolarization probabilities. It is also non-toxic, unlike Be, and costs less than ^{65}Cu. For these reasons several groups around the world, including the UCNA collaboration, have pursued DLC coated guide technologies [88] [59] [13] [11].

1.7 Physics Motivation

The Standard Model of particle physics, also called the quark model, is the primary theory used to describe the strong, weak, and electromagnetic interactions between the constituents of matter: the quarks, leptons, and bosons. In the Standard Model, the neutron is primarily composed of the three quarks, which are the mass eigenstates of the strong force: one up

Table 1.1: Properties of common beamline materials used in the UCNA Experiment. The Fermi Potentials were calculated using equation 1.24 and bulk density values. The spin flip and loss probabilities were taken from [154] [156] and [146].

Material	V_F (neV)	Prob. loss/bounce (10^{-5})	Prob. spin flip/bounce (10^{-6})
^{58}Ni	346	5	5×10^5
316L Stainless Steel	183	<100	∼4000
Cu	170	15	∼1
Quartz	90	59	14
PLD DLC	220-270	<1	∼2
Be	250	7.1	7.2

quark and two down quarks, and is usually denoted (udd). A free neutron is not stable and will decay into a proton, electron, and anti-neutrino, not through the strong interaction but via the weak interaction, and releases 782 keV of energy that is divided between the decay products. Figure 1.2 shows the weak interaction Feynman diagram for neutron beta decay, where one of the d quarks converts into a u quark by emitting a W^- boson. The W^- boson is the mediating particle for the weak interaction, similar to the photon in Quantum Electrodynamics, and quickly decays into an electron and an anti-neutrino. The weak interaction eigenstates are not exactly the same as the mass eigenstates of the strong interaction, but the two are connected via the Cabibbo-Kobayashi-Maskawa (CKM) matrix, where the mass eigenstates are denoted (d, s, b) and the weak eigenstates are denoted (d', s', b'):

$$\begin{pmatrix} d' \\ s' \\ b' \end{pmatrix} = \begin{pmatrix} V_{ud} & V_{us} & V_{ub} \\ V_{cd} & V_{cs} & V_{cb} \\ V_{td} & V_{ts} & V_{tb} \end{pmatrix} \begin{pmatrix} d \\ s \\ b \end{pmatrix} \tag{1.27}$$

The matrix elements, V_{ij}, that connect the two states are determined by experiment, where the relevant matrix element in neutron beta decay is V_{ud}. A major consequence of the Standard Model is that the CKM matrix should be unitary. This implies that $|Vud|^2 +$

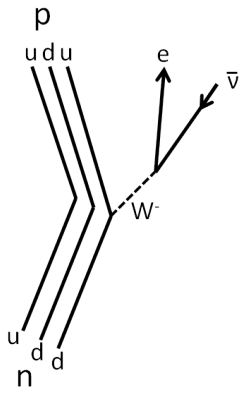

Figure 1.2: Feynman Diagram of neutron beta decay. Here a d valence quark emits a W^- boson and becomes a u quark turning the neutron into the more stable proton. The W^- decays very quickly into an electron and anti-neutrino. The electron and recoil proton, as it is often called, are the detected particles in neutron beta-decay experiments, as the neutrino interacts very weakly with matter and so is difficult to detect.

$|Vus|^2 + |Vub|^2 = 1$. Whether or not the CKM matrix is unitary is discussed in section 1.11, but nevertheless, we can use the mass eigenstates in the description of the transition matrix for a d quark into an u quark with the help of V_{ud} :

$$T_{fi} = \frac{g^2}{8} V_{ud} \cdot \bar{\psi}_u \gamma_\mu (1-\gamma_5)\psi_d \cdot \frac{g^{\mu\nu} - k^\mu k^\nu / m_{w^-}^2}{k^2 - m_{w^-}^2} \cdot \bar{\psi}_e \gamma_\nu (1-\gamma_5)\psi_{\bar{\nu}} \tag{1.28}$$

where g is the weak coupling constant, k is the momentum transfer between quark and lepton, and V_{ud} allows us to use the mass eigenstates, ψ_u and ψ_d. Since $k << m_{w^-}$ in neutron beta decay, equation 1.28 reduces to:

$$T_{fi} = \frac{G_F}{\sqrt{2}} V_{ud} \cdot \bar{\psi}_u \gamma_\mu (1-\gamma_5)\psi_d \cdot \bar{\psi}_e \gamma^\mu (1-\gamma_5)\psi_{\bar{\nu}} \equiv \frac{G_F}{\sqrt{2}} V_{ud} \cdot J_\mu^h J^{l\mu} \tag{1.29}$$

where the propagator term is absorbed into the Fermi decay constant, G_F, J^h_μ is the hadron (neutron-proton) current, and $J^{l\mu}$ is the lepton (electron/anti-neutrino) current described as:

$$\frac{G_F}{\sqrt{2}} = \frac{g^2}{8m^2_{w^-}} \tag{1.30}$$

$$J^{h\mu} = \bar{\psi}_d \gamma^\mu (1-\gamma_5)\psi_u \equiv V^\mu - A^\mu \tag{1.31}$$

$$J^{l\mu} = \bar{\psi}_e \gamma^\mu (1-\gamma_5)\psi_{\bar{\nu}} \equiv v^\mu - a^\mu \tag{1.32}$$

Due to confinement of the quarks in the nucleon, one must evaluate the matrix elements of the whole nucleon instead of just the quarks and so we have grouped the parameterized inner structure of the neutron into vector, V^μ, and axial vector, A^μ, parts. These are defined as follows:

$$V_\mu = i\bar{\psi}_p[g_V(k^2)\gamma_\mu + \frac{g_M(k^2)}{2m_p}\sigma_{\mu\nu}k^\nu + ig_S(k^2)k_\mu]\psi n \tag{1.33}$$

$$A_\mu = i\bar{\psi}_p[g_A(k^2)\gamma_\mu\gamma_5 + \frac{g_T(k^2)}{2m_p}\sigma_{\mu\nu}k^\nu\gamma_5 + ig_P(k^2)k_\mu\gamma_5]\psi n \tag{1.34}$$

where m_p is the mass of the proton, $k_\mu = (p_\mu - p'_\mu)$ is the momentum transfer given to the leptons, p_μ is the incoming momentum of the neutron, p'$_\mu$ is the outgoing momentum of the proton, γ_μ and γ_5 are the Dirac spin matrices, and ψ_p, ψ_n are the wave functions for the proton and neutron respectively. In neutron beta decay the four-momentum transfer $k_\mu \approx 0$ and so the form factors g_V, g_{WM}, g_S, g_A, g_T, and g_p are known as the vector, weak magnetism, induced scalar, axial vector, induced tensor, and induced pseudoscalar coupling constants. g_V, g_{WM}, g_A, and g_P are grouped together as first class, while g_S, and g_T are denoted second class according to their operation under the G-parity operator, $G = Ce^{i\pi I_2}$ where C is charge conjugation that interchanges particles to their antiparticles and the $e^{i\pi I_2}$

is a 180° Isospin rotation about the I_2 axis. First-class currents satisfy the following

$$GV_\mu^I G^{-1} = V_\mu^I \tag{1.35}$$

$$GA_\mu^I G^{-1} = -A_\mu^I \tag{1.36}$$

while second-class currents satisfy

$$GV_\mu^{II} G^{-1} = -V_\mu^{II} \tag{1.37}$$

$$GA_\mu^{II} G^{-1} = A_\mu^{II}. \tag{1.38}$$

According to the Standard Model, second-class currents are not needed to describe neutron beta decay [83] and thus any measured non-null result for these currents would have significant ramifications [40]. In addition, g_P is negligible and so only g_V, g_A, and g_{WM} play a role in neutron beta decay within the Standard Model [2]. Furthermore, taking the Conversation of the Vector Current (CVC) [9] we have: $g_V(0) = 1$ and $g_{WM}(0) = \mu_p - \mu_n$, where μ_p and μ_n are the anomalous magnetic moments of the proton and neutron. g_V and g_A are often expressed as:

$$G_V = V_{ud} g_V(k^2 \to 0) G_F \tag{1.39}$$

$$G_A = V_{ud} g_A(k^2 \to 0) G_F \tag{1.40}$$

$$\lambda \equiv \left|\frac{g_A}{g_V}\right| \cdot e^{i\Phi} \cong \frac{g_A}{g_V} \tag{1.41}$$

Here Φ^2 is the phase angle between g_V and g_A and has been measured to be $180.06° \pm 0.07°$ which is consistent with the standard model [6]. Therefore the Standard Model Lagrangian

without second-class currents can be written as

$$L_{int} = \frac{G_V}{2\sqrt{2}} \cdot \bar{\psi}_p \left(\gamma_\mu (1 + \lambda\gamma_5) + \frac{\mu_p - \mu_n}{2m_p} \sigma_{\mu\nu} k^\nu \right) \psi_n \cdot \bar{\psi}_e \gamma^\mu (1 - \gamma_5) \psi_{\bar{\nu}} \quad (1.42)$$

$$= \frac{G_F}{2\sqrt{2}} V_{ud} (V_\mu + \lambda A_\mu)(v^\mu - a^\mu). \quad (1.43)$$

From this Lagrangian, Jackson et al. [80] calculated the electron distribution function for polarized neutron beta decay, without detecting the spin of the final state particles to be:

$$W dE_e d\Omega_e d\Omega_{\bar{\nu}} \propto p_e E_e (E_0 - E_e)^2 dE_e d\Omega_e d\Omega_{\bar{\nu}} \times \left[1 + a \frac{\vec{p}_e \vec{p}_{\bar{\nu}}}{E_e E_{\bar{\nu}}} + b \frac{m_e}{E_e} + < \vec{\sigma_n} > \cdot \left(A \frac{\vec{p}_e}{E_e} + B \frac{\vec{p}_{\bar{\nu}}}{E_{\bar{\nu}}} + D \frac{\vec{p}_e \times \vec{p}_{\bar{\nu}}}{E_e E_{\bar{\nu}}} \right) \right] \quad (1.44)$$

where $< \vec{\sigma_n} >$ is the spin of the neutron, $\vec{p}_e$ ($\vec{p}_{\bar{\nu}}$) the momentum of the outgoing electron (anti-neutrino), and E_e, $E_{\bar{\nu}}$ is the energy of the outgoing electron and anti-neutrino respectively. The a, A, B, and D are correlation coefficients and b is the so called Fierz interference term. The correlation coefficients can be expressed in terms of lambda as

$$a = \frac{1 - |\lambda|^2}{1 + 3|\lambda|^2} \qquad A = -2\frac{|\lambda|^2 + Re(\lambda)}{1 + 3|\lambda|^2}$$

$$B = 2\frac{|\lambda|^2 - Re(\lambda)}{1 + 3|\lambda|^2} \qquad D = 2\frac{Im(\lambda)}{1 + 3|\lambda|^2} \quad (1.45)$$

Usually time-reversal invariance is assumed, thus the $Im(\lambda) = 0$ and D vanishes which is valid for $\Phi = 180$. One then has three different coefficients to access λ which is an important parameter in nuclear and astrophysical calculations. Assuming $g_V = 1$, one can extract g_A which is a principle goal for precision lattice calculations [25]. It provides information on spin and flavor studies of the nucleon [22] as well as has ties, via the Goldberger-Treiman relation, to studies of the pion [48]. Furthermore, it is used in the calculation of the energy consumption in the sun [4] and in the estimation of the He/H ratio in the early universe [39].

Table 1.2: The current status of the measured neutron beta decay correlation coefficients. Values are taken from the 2008 Particle Data Group (PDG) updated for 2009 and 2010 [6]. *Error includes a scale factor of 2.3 to account for the spread in the four most precise cold neutron measurements which are described in section 1.9.1. We should point out that this row does not include any UCN measurements.

Neutron Correlation Coefficient Status Summary

Coefficient	PDG Value	Error	Percent Error
a $(\vec{p}_e \cdot \vec{p}_{\bar{\nu}})$	-0.103	0.004	3.88%
A $(<\vec{\sigma}_n> \cdot \vec{p}_e)$	-0.1173	0.0013	1.11*%
B $(<\vec{\sigma}_n> \cdot \vec{p}_e)$	0.9807	0.003	0.306%
D $(<\vec{\sigma}_n> \cdot(\vec{p}_e \times \vec{p}_{\bar{\nu}}))$	-.0004	.0006	150%

$$\frac{\Delta|\lambda|}{|\lambda|} \cong 0.27\frac{\Delta a}{a} \cong 0.24\frac{\Delta A}{A} \cong 2.0\frac{\Delta B}{B} \tag{1.46}$$

The current PDG values for these coefficients are presented in table 1.2 and their sensitivity to λ is given by equation 1.46. Hence, a is more sensitive than A, which is more sensitive than B. However the measurement of a is very challenging as it requires a very precise measurement of $\vec{p}_p$ and $\vec{p}_e$ to deduce $\vec{p}_{\bar{\nu}}$. As a result, A has been measured to higher precision than a, thus leading to a more precise value of λ. However with the explosion of neutron sources across the world and the precision now achievable, experiments are in progress to measure the entire neutron correlation alphabet with ever increasing precision [34] [118] [49] [129] [88].

1.8 A Closer Look at A

As previously mentioned, the A parameter is the correlation coefficient between the neutron's spin and the emitted electron momentum. Experimentally, the electron distribution function

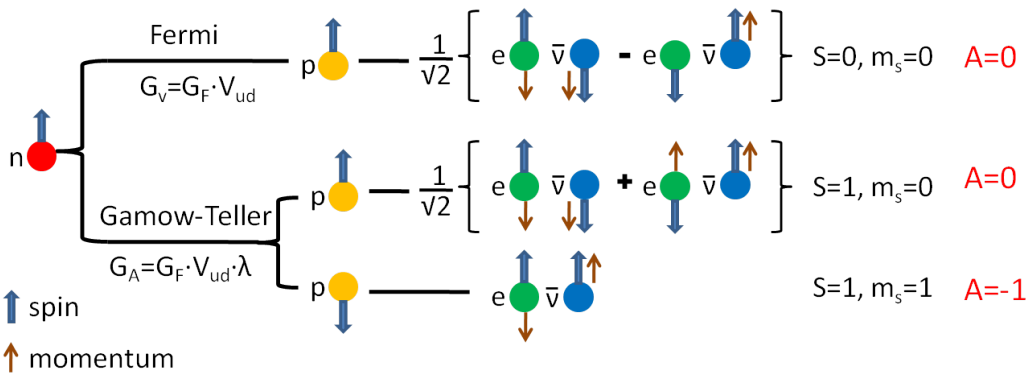

Figure 1.3: The decay of the neutron is a combination of Fermi (vector) and Gamow-Teller (axial vector) decays. Most of the time the system decays into the singlet or $m_s = 0$ triplet states. However a fraction of the time the system decays into the $m_s = 1$ triplet state. The non-null result for A is due to this state.

is given by

$$W(\phi) = 1 + \frac{v}{c} \cdot P \cdot A \cdot \cos\phi \tag{1.47}$$

where v is the electron's velocity, P is the neutron's polarization, A is the beta asymmetry parameter, and ϕ is the angle of emission of the electron. Figure 1.3 shows how the beta asymmetry arises. Thus all measurements of A need to measure the kinetic energy of the electron and the neutron polarization to high precision to make a precision measurement of A. Also, in every experiment to date, the neutron's spin has been flipped which lowers systematic errors related to the polarization and electron energy. Equation 1.47 is valid for A measurements greater than $\sim 1\%$. Below this level, corrections due to g_{WM}, $g_V - g_A$ interference, and the proton recoil, need to be taken into account. Usually the Wilkison form for this correction is applied [172]:

$$A \cong A_0\left[1 + A_{\mu m_n}(A_1 E_0 + A_2 E + A_3/E)\right] \tag{1.48}$$

where E and E_0 is the total electron energy and its end point, respectively, while A_0 is the lowest order term in λ, specifically the A in equation 1.47, and

$$\begin{aligned} A_{\mu m_n} &= \frac{\lambda + g_{WM}(0)}{\lambda(1-\lambda)(1+3\lambda^2)} \cdot \frac{1}{m_n} \\ A_1 &= \lambda^2 + \frac{2}{3}\lambda - \frac{1}{3} \\ A_2 &= -\lambda^3 - 3\lambda^2 - \frac{5}{3}\lambda + \frac{1}{3} \\ A_3 &= 2\lambda^2(1-\lambda). \end{aligned} \tag{1.49}$$

Further radiative corrections of the order 0.1% are also applied as described by [47] and [160]. A experiments are now targeting a precision at the 0.2% level and so the implementation of these corrections is now routine.

1.9 Previous Experiments of A

Prior to the UCNA measurement of A, all previous measurements utilized cold neutron beams to accomplish this task. We briefly review the experiments used by the PDG to produce a value of A in the following few paragraphs, where the respective published values of A are presented in table 1.3.

1.9.1 Perkeo

The Perkeo spectrometer employed the cold neutron beam provided by the Institut Laue-Langevin (ILL), in Grenoble France [15]. Here a collimated beam of cold neutrons were polarized using a super-mirror polarizer and then allowed to flow through a 1.7 m long 2 X

Table 1.3: Summary table of the measured values of A,($< \vec{\sigma}_n > \cdot \vec{p}_e$) neutron beta decay correlation coefficient, of the four cold neutron experiments used in the PDG09 world average and the published UCNA2009 result [136]. The UCNA2009 result is a proof of principle measurement which is highly statistics limited. We should note that H. Abele has also published a review article that quotes a preliminary value of A = -0.11933 ± 0.00034 (∼ 0.3% error) [3]. As it is preliminary, the PDG09 has not used this value in the world average.

Neutron Beta Decay A Correlation Coefficient Summary

Experiment	A Value	Error	Percent Error
Perkeo II*	-0.1189	0.0007	0.6%
ILL TPC	-0.1160	0.0015	1.3%
IAE-PNPI	-0.1135	0.0014	1.2%
Perkeo	-0.1146	0.0019	1.7%
UCNA2009	-0.1138	0.0051	4.4%

2π superconducting solenoid electron spectrometer package. Note this 2 X 2π spectrometer adjusts the $\cos\phi$ distribution described in equation 1.47 to $< \cos\phi >= 0.5$. Most of the neutrons flow right through the magnet where about one in a million of them decay in the fiducial volume of the spectrometer. However due to the high neutron flux, 2×10^8 n/sec, a background subtracted electron rate of about ∼100 Hz per detector was measured. These electrons spiral around the field lines to the ends of the spectrometer, where another set of transverse field magnetic coils directed the electrons onto a set of plastic scintillators located at each end but out of the way of the neutron beam. The experiment was systematically limited due to magnetic mirror corrections arising from the transverse magnetic fields used to guide the electrons out of the beam and onto the detectors, backgrounds associated with the reactor, collimators, and polarizer, and insufficient determination of the neutron polarization across the entire beam cross section.

1.9.2 IAE-PNPI

Often called the Gatchina experiment, since it was carried out at the Gatchina reactor, the Institute for Atomic Energy (IAE) and the Petersburg Nuclear Physics Institute (PNPI) made a measurement of A by tracking the recoil proton in coincidence with the electron emitted in beta decay[38] [180]. Here a super-mirror polarizer was not employed, making the neutron polarization the dominant systematic error in this 1.2% measurement.

1.9.3 ILL-TPC

The ILL Time Projection Chamber (ILL-TPC) experiment sent a beam of polarized cold neutrons through a ^{4}He+CO_2 filled drift chamber operating in delayed coincidence with a plastic scintillator, which together provide tracking and energy information of the beta decay electron. This experiment made a 1.3% measurement of A, where the background subtraction provided the dominant error of 0.8% [153].

1.9.4 Perkeo II

In Perkeo II, the superconducting solenoid and transverse magnetic field end coils were replaced with a split pair superconducting magnet providing a purely transverse magnetic field with respect to the cold-neutron beam. Beta decay electrons are guided by the transverse field onto a set of well shielded scintillators where their energy is measured. The total neutron flux was increased by about a factor of four through the introduction of a ballistic super-mirror cold neutron guide, which compensated for the decrease in fiducial volume from that of the original Perkeo experiment. The typical total measured electron rate was 270 Hz. In addition, the degree of polarization and uniformity across the neutron beam was

increased to 98.9% by the introduction of a crossed super-mirror polarizer system [90]. The Perkeo II collaboration has published two measurements of A providing a combined $\sim$0.6% measurement [1].

1.9.5 Perkeo III

Although a value for A has not been published, the Perkeo III instrument promises to significantly improve on the measurements performed by the Perkeo and Perkeo II systems and should be mentioned. The new instrument is really a combination of the two Perkeo designs that still follows the Perkeo principle of an intense, well-polarized cold-neutron beam and 2 x 2π plastic scintillator spectrometer. The new system employs a 2 m long solenoidal decay region with guide magnetic fields at each end guiding electrons out of the neutron beam, similar to Perkeo. A new pulsed mode cold-neutron beam line with much larger polarized beam cross section is utilized. The system has been shown to measure a 50 kHz beta decay rate and the pulsed mode beam greatly reduces beam related backgrounds. In fact the decay rate was so high that data acquisition issues as well as the rapid radiation damage to the plastic scintillator are making the data analysis difficult. However these challenges are being addressed and Perkeo III collaboration should provide an extremely precise measurement A, as well as other neutron beta decay correlation coefficients in the coming years [117].

1.10 Benefits of UCN for Measuring A

We briefly mentioned that using UCN to measure the beta asymmetry correlation coefficient A provided an attractive alternative to employing polarized cold-neutron beams and their

associated systematics. Cold-neutron beam related backgrounds and polarization issues are the dominant systematics with cold neutron A experiments. The use of UCN addresses these concerns in the following ways. First, UCN can be transported with high efficiency many meters through UCN guides. This allows the experimenter to install adequate shielding around the source of the neutrons, while still being able to pipe them away. Thus many of the backgrounds, i.e. gamma rays that are produced in nuclear reactor or spallation target sources, are reduced to the ambient environment level. Second, UCN can be 100% polarized with magnetic fields at about 7 Telsa. The polarization can then be preserved with suitable UCN guiding materials and magnetic holding fields. With experiments employing the reflection of cold neutrons off super-mirror polarizers, some of the neutrons are captured and produce a gamma-ray flux. This gamma-ray flux requires further shielding of the electron detectors and careful consideration during the electron spectrum analysis. Polarzing a beam of UCN has no such by products.

1.11 Discussion

Beyond the usefulness of λ already mentioned, it is further connected to the neutron's lifetime and V_{ud} via The"Golden Rule" [7]

$$\frac{1}{\tau} = W = \frac{2\pi}{\hbar}|T_{fi}|^2\rho(E) \tag{1.50}$$

where τ is the lifetime of the particular transition, W is the decay probability per unit time, T_{fi} is the transition matrix element, and $\rho(E)$ is the phase space available for the reaction

to proceed. In terms of the neutron beta decay this becomes

$$\frac{1}{\tau_n} = \frac{G_F^2 m_e^5}{2\pi^3}|V_{ud}|^2(1+3\lambda^2)f(1+RC) \tag{1.51}$$

and is sometimes called the "master formula" of neutron beta decay. Here RC are the radiative corrections involved in the beta-decay process. Here we have three unknowns: τ_n, V_{ud}, and λ, where G_F is taken from high precision muon-decay experiments. Thus one can take the value of τ_n and obtain a value for V_{ud} or vice versa after measuring λ. When UCNA was first proposed, obtaining a value of V_{ud} by combining a measurement of λ with the world average value of τ_n was of chief concern, as V_{ud} was a likely candidate for causing the then observed deviation from CKM unitarity. Besides using free neutron decay, V_{ud} can also be obtained by measuring the Ft values in super allowed $0^+ \rightarrow 0^+$ beta-decay transitions through the equation [6]

$$|V_{ud}|^2 = \frac{2984.48(5)sec}{Ft(1+RC)}. \tag{1.52}$$

With Ft values, the F is the the phase space calculation of the decay and t is the half life of the decay. The multiplication of the two is proportional to the inverse square of the matrix element describing the transition [7]. $0^+ \rightarrow 0^+$ is a purely vector transition, Fermi decay, where the initial and final state wave functions overlap perfectly, creating a particularly large decay probability and so these Ft values are close to that of a free neutron. At the time, V_{ud} as measured by $0^+ \rightarrow 0^+$ transitions was in disagreement with the value obtained using the current numbers for λ, from A measurements, and τ_n from free neutron decay. However, the values of A, obtained via cold neutron experiments, were not consistent with each other, while on the other hand most of the measured values of τ_n were consistent with each other and averaged to provide 0.1% error. Thus most of the doubt in the value of V_{ud} obtained from free neutron decay came from measurements of λ and thus A.

Inconsistencies arising from nuclear coulomb and radiative corrections troubled the quoted Ft values of the current $0^+ \to 0^+$ decays. The discrepancy stimulated our more precise measurement of λ and thus V_{ud}, with the help of τ_n, via a new measurement of A using UCN as opposed to the previous cold-neutron beam technique [170]. The spread in the cold neutron measurements of A motivated the use of our different technique with its very different systematics errors/uncertainties. The UCNA proposal was funded and full scale efforts began in the early 2000's to accomplish this task. Meanwhile, a great deal of theoretical work was done to bring the understanding of $0^+ \to 0^+$ decays and their corrections to a new level and as a result they find $V_{ud} = 0.97425 \pm 0.00022$ [168] [56] [27] [115], which is presently the most precise value of V_{ud}, improved by about an order of magnitude. Combining this value of V_{ud} with the current best value of V_{us} obtained from $K \to \pi e \nu$ and $K \to \pi \mu \nu$ decays, one obtains $|Vud|^2 + |Vus|^2 + |Vub|^2 = 0.9999(4)(4)$, where the first error is the uncertainty from $|V_{ud}|$, the second error is the uncertainty from $|V_{us}|$, and $|V_{ub}|^2 \sim 1 \times 10^{-}5$ [6].

Thus the error estimates on V_{ud} as measured by $0^+ \to 0^+$ decays are so tight that a 0.25% measurement of A combined with τ_n would still produce a V_{ud} error a factor of three larger. Therefore the role of free neutron decay in determining the unitarity of the CKM matrix transitioned to becoming a meaningful consistency check for $0^+ \to 0^+$ and even $1/2^+ \to 1/2^+$ decays [159] [128]. We should also mention the PIBETA experiment's efforts to measure V_{ud} . Here the rate of the extremely rare process of $\pi^+ \to \pi^0 e^+ \nu_e$ is measured to $\sim$0.5% and has produced a value of $V_{ud} = 0.9728(30)$ [6], which is in agreement with the $0^+ \to 0^+$ value. Theoretically very clean, the technique needs much higher statistics to be competive to $0^+ \to 0^+$ or free neutron methods.

Nevertheless, as with many things in life, when one door closes another one opens. In 2005, A. Serebrov shocked the neutron community by publishing a UCN material bottle trap τ_n measurement $\sim$7 seconds smaller than the current PDG value, with an error such that the

measurement is 6σ away from the world average [155]. Like some previous τ_n measurements [113], this experiment relied on a material bottle trap to contain the UCN. Serebrov and Fomin then re-analyzed past material bottle lifetime experiments, such as the MamBo and 1993 Mampe neutron lifetime experiments, including quasi-elastic scattering from the walls that was done for the 2005 measurement and this shifted the measured values to be more consistent with Serebrov's 2005 result [158]. So far the PDG has excluded these results in its world average τ_n waiting for future experiments to shed light on the issue. To this end several experiments are currently underway that utilize cold-neutron beam methods and a variety of UCN containment methods such as material bottle traps, magneto traps, and magneto-gravitational traps to measure τ_n [72].

1.12 Conclusion

The study of neutron beta decay is indeed a rich and far reaching field. There are an abundance of neutron beta decay parameters for experiments to measure, of which we have only described a select few: the Ft value of nuclear beta decays along with A and τ_n in free neutron decay. Here Ft values from $0^+ \rightarrow 0^+$ decays provide the most precise value for V_{ud} . Meanwhile A provides the most sensitivity to $\lambda \cong g_A/g_V$ which is connected to V_{ud} via the τ_n. Although there is current discrepancy in the value of the τ_n, experiments are poised to elucidate this issue in the next few years. Be that as it may, the consistency of all these values measured in completely different environments adds weight not only to our understanding of all the different theoretical corrections to these processes, but also to our understanding of the underlying fundamental physics and the Standard Model itself. In fact these experiments are becoming so precise that now they can be used to search for new physics, such as the search for second-class currents to test the conserved vector current

theorem [45], right-handed currents [32], and supersymmetric extensions to the standard model [91]. The next decade will be an exciting one as these theories will be accessed by a multitude of neutron beta-decay experiments.

Chapter 2

The UCNA experiment and Results

The measurement of polarized neutron decay observables, in particular A, using ultra cold neutrons provides two distinct advantages over previous measurements utilizing cold neutrons: UCN are 100% polarizable and can be transported long distances which allows their isolation from the inherent backgrounds, ie gamma rays, that are a by-product of freeing neutrons from their nuclear packages. In the UCNA experiment, these advantages are incorporated by the use of several high-field superconducting magnets to polarize the UCN and many meters of UCN guides which allow the magnets and spectrometer to be kept away from the heavily shielded source.

The UCNA experiment is located in Area B of the Los Alamos Neutron Science Center (LANSCE) at Los Alamos National Lab (LANL) and involves six major equipment items: the solid deuterium (SD_2) source, the prepolarizer magnet (PPM), the adiabatic fast passage spin flipper (AFP), the super conducting solenoid magnet spectrometer (SCS), which includes the β detectors, the cryogenic facilities, and the UCN guides that connect the source through the polarizing magnets and into the spectrometer. A schematic and photograph of

the experiment in area B is shown in Figures 2.1 and 2.2 respectively. Spallation neutrons are produced and then cooled/down scattered to the UCN energy regime in the SD_2 source. These UCN are then guided through a large volume of stacked concrete which provides the necessary biological and experimental shielding. Then the UCN beam is prepolarized by passing through the PPM magnet and makes a 60° bend heading toward the AFP system. These UCN are further polarized and then, as required, have their magnetic moments flipped. The beam is now almost 100% polarized and then is guided into the SCS spectrometer where a set of guides act as a storage bottle for the UCN. If the UCN beta decay while inside the bottle, the emmited electrons spiral around the SCS field lines and interact with the β spectrometers located on either end of the solenoid. The difference over the sum of the number of βs detected in in the two spectrometers, is used to form the experimental A assymetry, where futher details can be found in references [136] and [105].

The UCNA experiment, as with most current nuclear physics experiments, has been active for over a decade. Major equipment items, such as the magnets and spectrometer, began development in the late 1990's. The prototype SD_2 source at LANSCE was extremely successful during this time and was scaled up to the current SD_2 source shown in figure 2.1 [62] [152]. Since then a number of equipment challenges and modifications have occurred and it was not until 2007 when the first A data was taken, which produced a $\sim$5% proof of principle measurement [136]. In 2008, a very large A data set was collected with several system improvements and just released a 1.3% measurement. This result is discussed at the end of the the thesis in chapter 8. More system improvments were made for the 2009 run, but was cut short due to a severe cryogenic line failure inside the source shield stack. However, a signficant amount of polarization data was collected along with a small amount, $\sim$2 M events, of A data. These data is combined with the 2008 data set. Many of these challenges came from problems encountered with the low production and transport of UCN to the SCS

and so the source, especially the source flapper valve, and UCN beamline of the experiment have been modified several times. Because of these changes, I will first describe the major equipment items: SD_2 source, PPM, AFP, and SCS, and the beamline components from the shield wall to the SCS, while discussion of the various SD_2 source flapper valve changes and the shield wall guides are reserved for chapter 6.

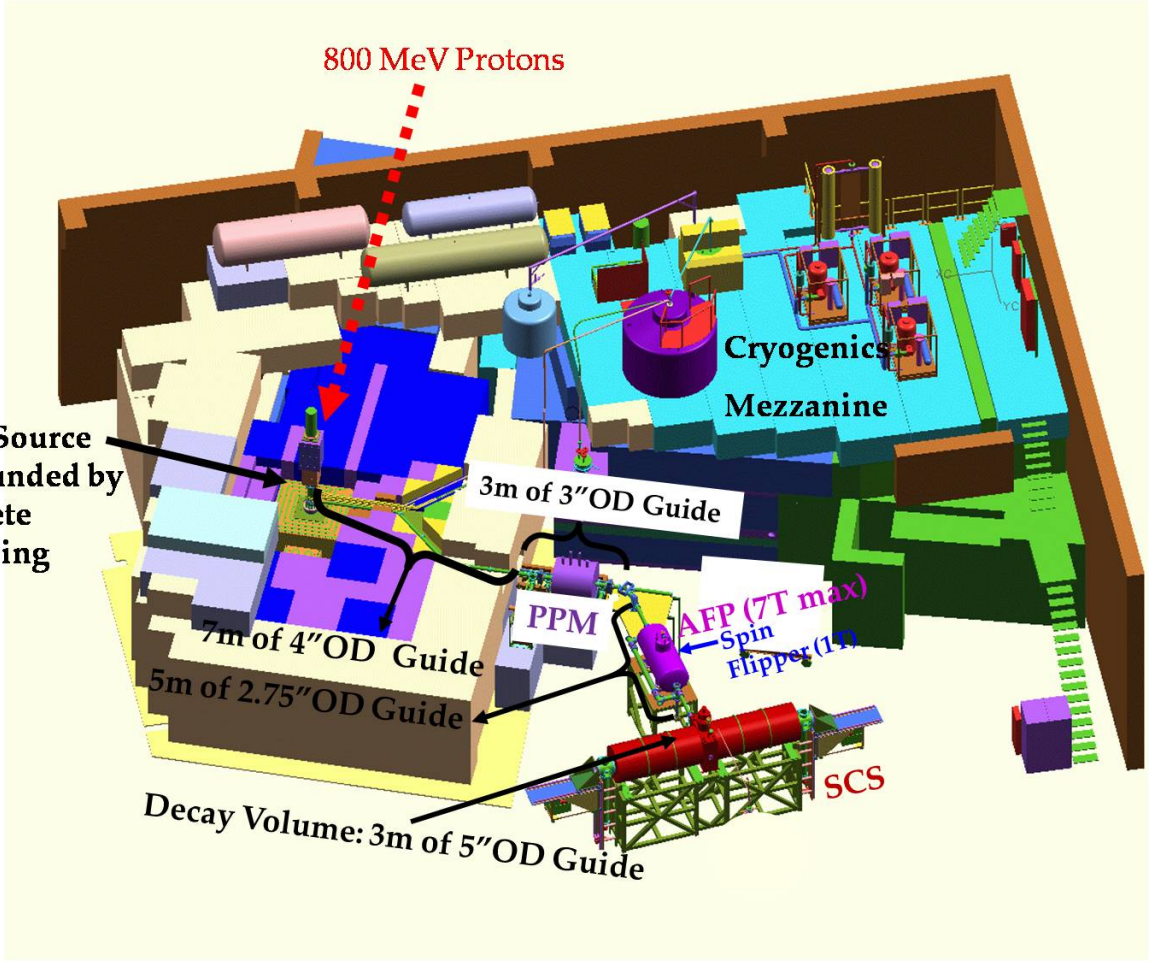

Figure 2.1: Computer aided drawing of the UCNA experimental layout in Area B of the LANSCE facility. LANSCE's 800 MeV proton beam impinges on a tungsten target creating spallation neutrons. Some of these neutrons are moderated down to UCN energies and then piped out to the magnets and spectrometer of the UCNA experiment. Figure used with permission from the UCNA collaboration (2010) [181].

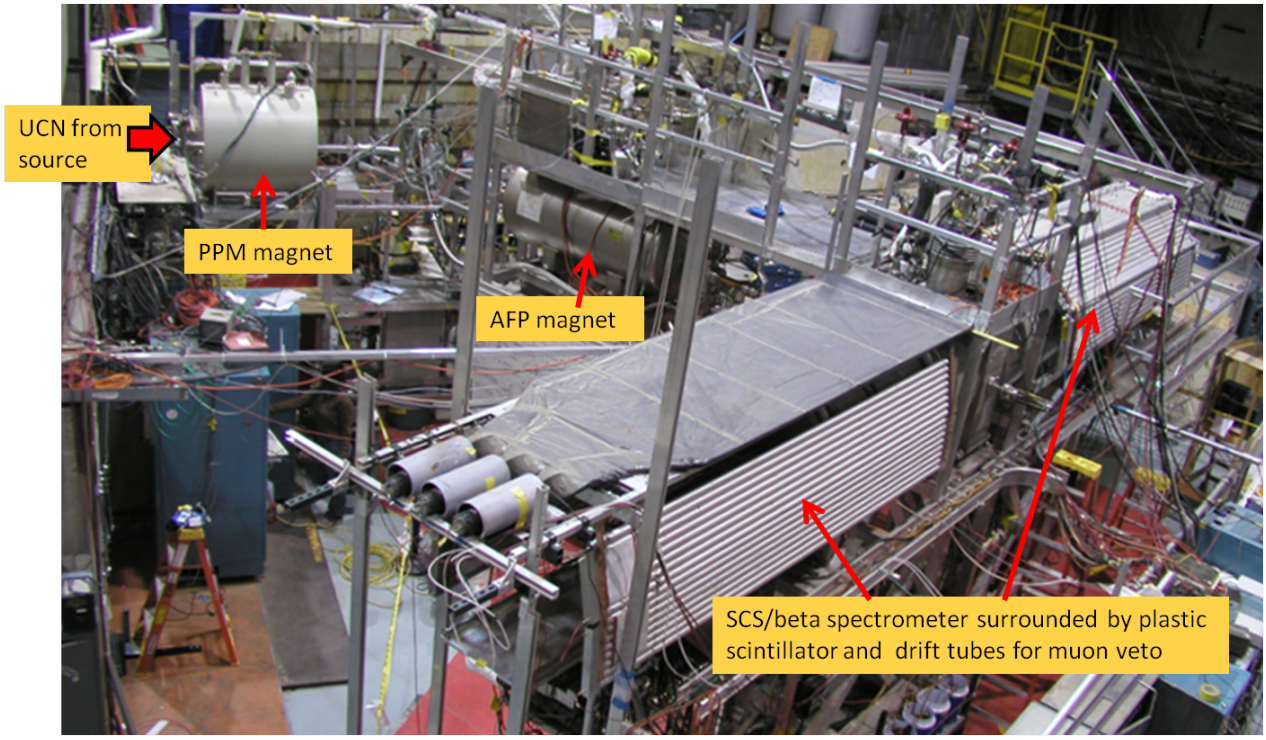

Figure 2.2: Photograph of the UCNA magnets and spectrometer outside of the source shield wall. Figure modified with permission from UCNA collaboration (2010) [181].

2.1 UCN source at LANL

The UCN source at LANL is a super-thermal solid Deuterium source, utilizing spallation neutrons from the LANSCE proton accelerator. Here super-thermal implies that the UCN density in the source, ignoring absorption, grows as $(E_{UCN}/\Delta)e^{\Delta/k_BT}$, where T is the source temperature and Δ is the energy difference between the ground state and the excited state of a two state moderator [147]. Here the up-scattering rate can be made arbitrarily small by decreasing the source temperature. This is in stark contrast to thermal UCN sources where the UCN density grows as $(1/T)^{3/2}$ or $(1/T)^2$ and UCN up-scattering plays a dominant role [147]. Deuterium is one such super-thermal source material, but does exhibit some neutron absorption ($\sigma_{abs} = 4.6\times10^{-4}$) which limits the UCN lifetime in deuterium to at most 200

msec [147]. In practice the observed lifetime is much smaller, $\tau_{SD_2} = 28$ ms, due to thermal up-scattering, nuclear absorption on residual ^{1}H, and exothermic para- to orthodeuterium transitions in the residual para-deuterium in the source [152]. Para-deuterium (nuclear spin = 1 and odd rotational states) is of particular concern as the UCN lifetime in para-deuterium is $\sim$1.5 msec. At room temperature the deuterium is approximately 33% para-deterium and 67% ortho-deuterium (nuclear spin = 0,2 and even rotational states). To lower this concentration the deuterium is passed through an iron-hydroxide-filled cell cooled to a temperature at or slightly below the triple point [102]. This reduces the para fraction to 2-4%, as measured by Raman spectroscopy [120].

A schematic of the spallation target and source is shown in figure 2.3. Approximately 25μC of 800MeV protons are pulsed every 5 secs to impinge on a tungsten target, producing spallation neutrons. These neutrons are moderated and reflected by the surrounding Be and graphite boxes. Some of these neutrons are further cooled in the 30°K polyethylene surrounding the SD_2 volume making cold neutrons and it is these cold neutrons that are down-scattered in the SD_2 crystal to the UCN energy regime. Due to the low lifetime of UCN in SD_2 a valve, nicknamed "the flapper", has been placed directly above the SD_2 volume to seal off the UCN from the SD_2 after production, thereby bottling the UCN in the source guide. The opening and closing of the valve is timed with the incident proton pulse on the tungsten target. It is open when spallation neutrons are coming through the system and closed just after. The entire UCN source volume, including SD_2 volume, flapper, and source guide/bottle have been coated using electron-beam evaporation with ^{58}Ni at Virginia Tech. Mark Makela, then a Virginia Tech graduate student on the UCNA experiment, coated the original UCN source volume in the early 2000's. Since then a series of source inserts have evolved to improve the source production, all of which have been coated at VT and will be discussed in chapter 6.

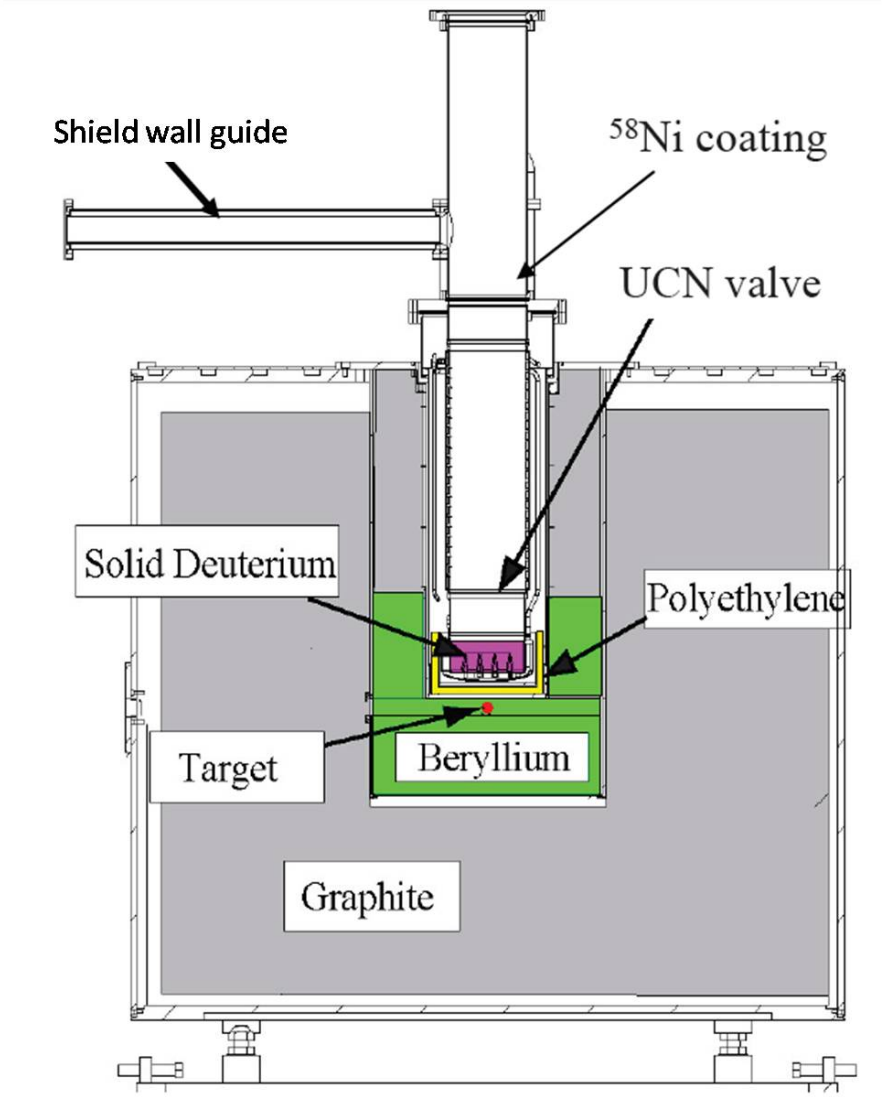

Figure 2.3: LANL SD_2 UCN source. Figure used with permission from UCNA collaboration (2010) [181].

2.2 Prepolarizer Magnet

Once inside the source bottling region, the UCN can leave via an exit guide that travels seven meters, with two 60° bends along the way, before they reach the outside of the concrete shield wall covering the source. The purpose of the bends is to reduce the number of

very cold neutrons (VCN), neutrons with higher kinetic energy than UCN. Neutrons whose momentum perpendicular to the guide surface is larger than the Fermi Potential have a very high probability of being lost in the material. Thus the 60° bends increase the number of these collisions in an attempt to "clean" the UCN beam of VCN. In addition, the bends also reduce the source radiation transmitted to the experimental area. Once outside the shield wall, the UCN are guided through a 6T "off the shelf" superconducting solenoid magnet, called the PPM, from American Magnetics Inc. (AMI). A safety foil, usually aluminum or zirconium, is placed in between two beamline guide sections located in the middle of the PPM. The sole purpose of the foil is to provide a permanent seal in the event that D2 gas fills the source and shield wall guides. This prevents D2 gas from entering the experimental area causing an explosive gas mixture (as little as 4% D_2 in air [165]) while work is being down downstream of the foil. The purpose of the PPM is to boost the kinetic energy, by 360neV, of one spin state of the UCN to increase the probability of transmission through the foil. However, the other spin state sees a 360neV magnetic potential barrier, effectively reducing the number of UCN in the beam line by half.

2.3 Adiabatic Fast Passage Spin Flipper System

To understand how the spin flipper works it is essential to discuss the principle of adiabatic approximation for how the neutron's magnetic moment operates in an external magnetic field. Here, the quantity

$$\kappa = \frac{\omega_B}{\omega_L} \tag{2.1}$$

is utilized, where $\omega_L = -2\mu B/\hbar$ (where μ is the neutron's magnetic moment) is the Larmor precession of the neutron's magnetic moment about the applied magnetic field B and ω_B is the rate at which this field rotates. If $\kappa << 1$, then the change in applied magnetic field is

slow enough that the neutron's spin follows the field direction and adiabatic approximation can be applied. So if the effective magnetic field can be slowly rotated from parallel to transverse to antiparallel, the magnetic moment of the UCN will follow this change and effectively reverse its spin direction in the same manner. This field configuration can be done with static fields and spin flip efficiency greater than 88% was observed for neutron energies ranging from 0.1 to 1000eV[17]. Another method employs the techinque of nuclear magnetic resonance where a rotating RF field is used to provide the required transverse field superimposed on a slowly decreasing holding field. It is this method that the UCNA experiment employs. Equation 2.2 descibes the spin evolution of a neutron under these conditions in the lab frame [103].

$$\frac{d\mathbf{M}}{dt} = \frac{\partial \mathbf{M}}{\partial t} + \omega \times \mathbf{M} = \gamma \mathbf{M} \times \mathbf{H} \tag{2.2}$$

where $\mathbf{M}$ is the magnetization of the nuetron, ω the angular frequency of the applied rotating field, γ is the gyromagnetic ratio of the neutron, and $\mathbf{H}$ is the applied field.

If one boosts to a co-rotating frame with the same angular frequency, ω, then the transverse field appears to be static. The spin precession then follows:

$$\frac{d\mathbf{M}}{dt} = \gamma \mathbf{M} \times \mathbf{H}^{eff} = \gamma \mathbf{M} \times [(H^o - \omega/\gamma)_{\parallel} + H'_{\perp}] \tag{2.3}$$

where ω/γ is a fictitious force resulting from the coordinate rotation, and $H^o_{\parallel}$ and $H'_{\perp}$ are the strengths of the longitudinal and transverse field respectively.

We now see that the fictitious field, ω/γ, slowly subtracts from the decreasing longitudinal field until it cancels it exactly and then flips the direction of the effective longitudinal field. In this way the spin of the neutron changes from aligned to anti-aligned to the longitudinal

holding field.

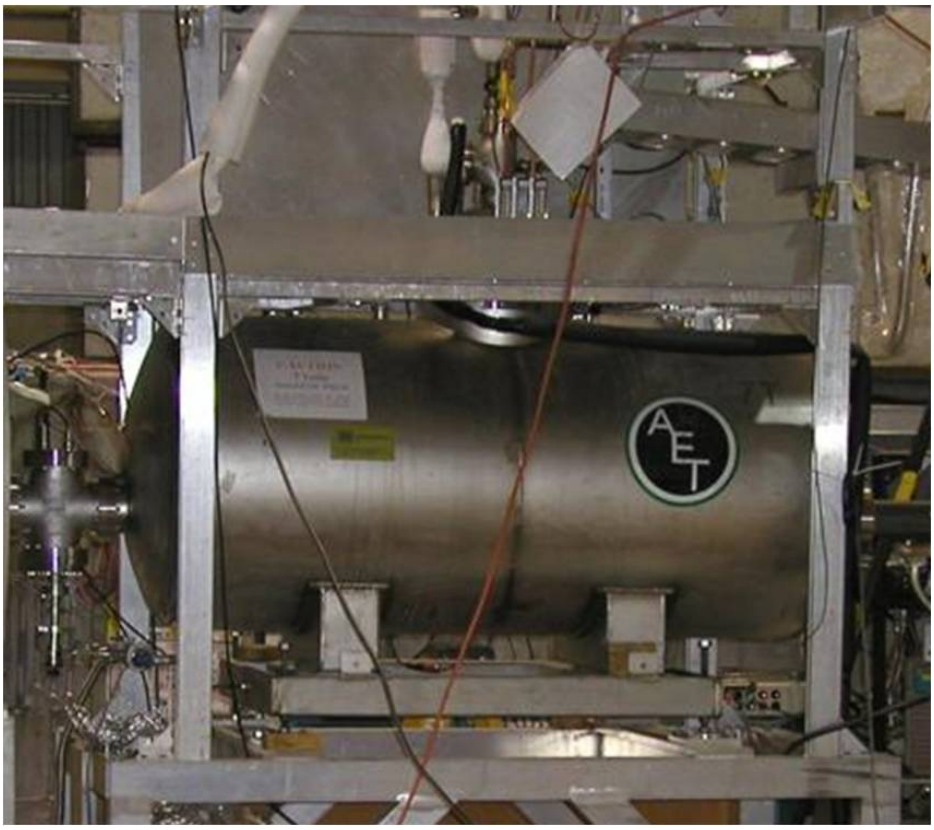

Figure 2.4: Photograph of the custom superconducting solenoid magnet, nicknamed the AFP magnet, made by American Magnetics Inc. Figure used with permission from UCNA collaboration (2010) [181].

In the UCNA experiment, spin flipping is provided by the operation of an RF resonator, which provides the required transverse field, inside a custom superconducting solenoid magnet from American Magnetics Inc, named the AFP magnet. Figure 2.4 shows a photograph of the this magnet whereas a plot of its magnetic field along the length of the beam line can be seen in figure 2.5. The AFP magnet consists of two regions: a high field region, 7T, to polarize the UCN and a holding field region where the field slowly decreases from 2T to 0.5T, with a long slowly decreasing field field centered around 1T. This is where the spin flipper is located. The initial high field further selects the appropriate spin neutrons making

a measured 98.8% polarized beam [66]. The less than 100% polarization is attributed to high velocity oppposite spin UCN that can penetrate the 420neV magnetic potential barrier.

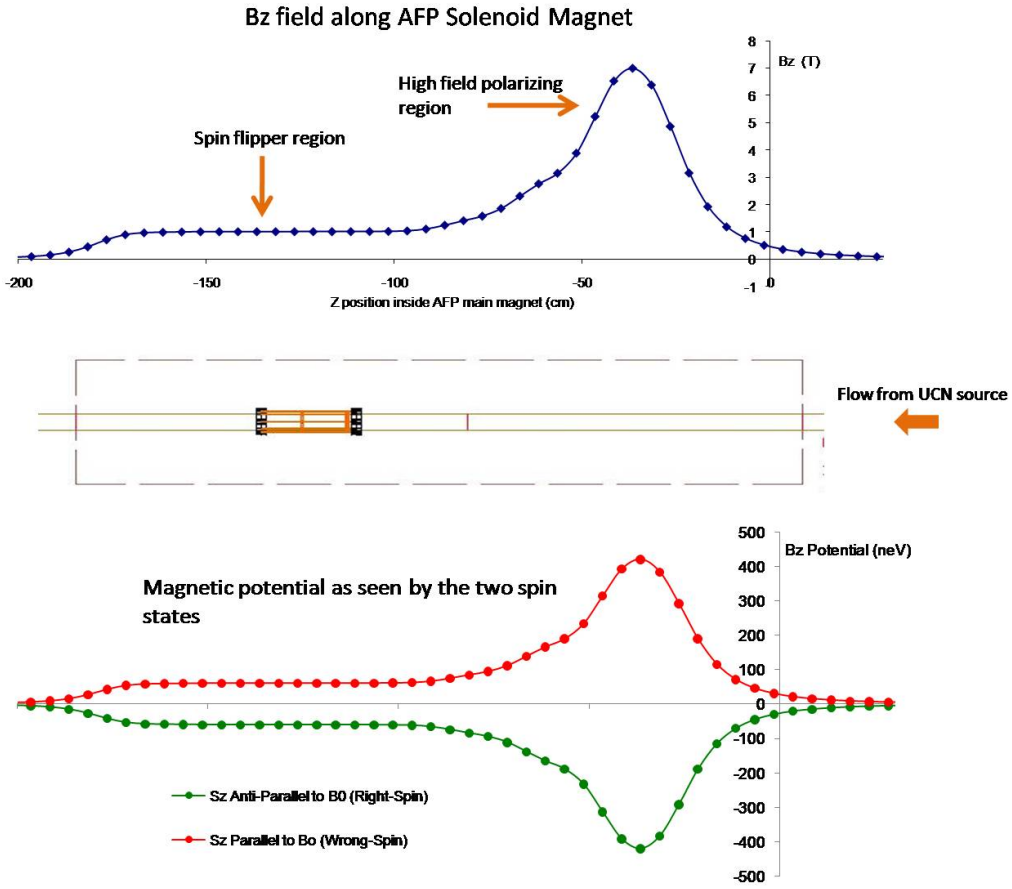

Figure 2.5: Top: Magnetic field along the beam line as a function of position inside the AFP magnet. Middle: cartoon of the AFP system showing the placement of the RF bird cage resonator used to flip the spins of the incoming UCN. A nonconducting DLC coated quartz guide is always placed inside the resonator to allow the RF field to reach the UCN traveling inside it. Bottom: Magnetic potential as seen by the two different UCN spin states. The right spin neutrons see a potential well whereas the wrong spin neutrons see a potential step. Figure modified with permission from Adam Holley (2010) [65].

The spin flip occurs in a 30cm region that straddles the 1T central holding field which has a small constant gradient of 0.1G/cm when shim coils are correctly set [64]. An eight rung bird cage style resonator developed primarily by Adam T. Holley, Chen-Yu Liu, and Albert

Young, shown in Figure 2.6, provides the required ∼5 G transverse field. The resonator is set to operate with a frequency of ∼30Mhz which corresponds to the 1T solenodial field in this region. Details on the technical aspects of the flipper can be found in [103] and [65].

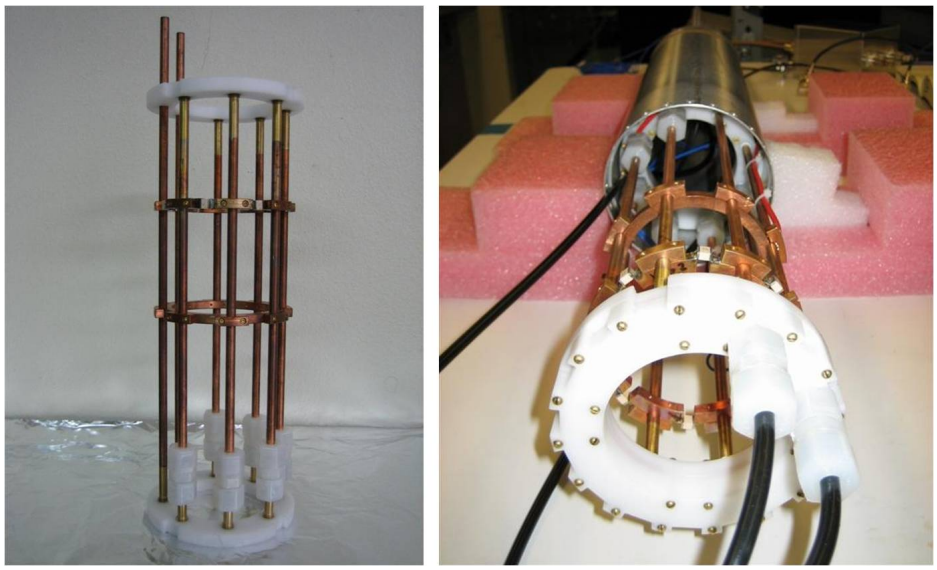

Figure 2.6: Eight rung bird cage style RF resonator. Based on the technique of nuclear magnetic resonance, the resonator provides the necessary transverse field to adiabatically flip the spin of the UCN while sitting inside a relatively constant 1T field. Water cooled copper tubes make up the cage of the resonator, where the water circulates through the white Delrin end caps. On the left, adjustable capacitor and tuning rings are easily seen which provide the necessary flexibility to optimize the flipping efficiency. On the right, the resonator is about to be placed in its housing and is awaiting the insertion of the DLC coated quartz guide. Figure modified with permission from Adam Holley (2010) [65].

2.4 Superconducting Solenoid/ Beta Asymmetry Spectrometer

The Superconducting Solenoid (SCS) magnet is a custom 4.5 m long 1 T superconducting solenoid magnet commissioned from AMI and Meyer Tool and Manufacturing with a very

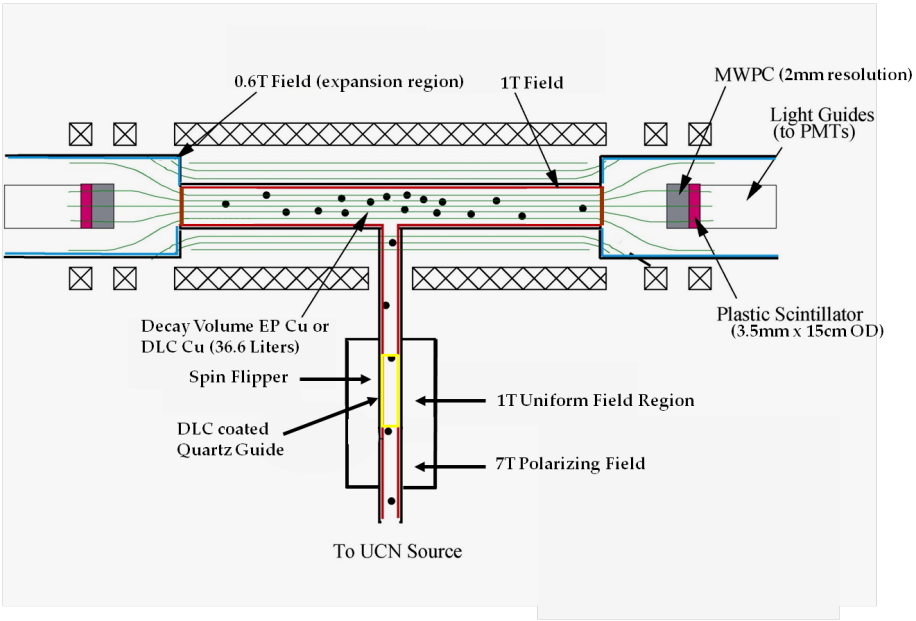

Figure 2.7: Schematic diagram of the UCNA experiment. The UCN are polarized by the spin flipper and then allowed to flow into the decay trap region where their spins align with the magnetic field of the SCS magnet. Once in the trap, the UCN can be lost in a number of ways: up-scattered, absorbed, exit the trap through the inlet, monitor, or trap ends (which has been eliminated with end caps), or beta decay. If they beta decay, the resulting electron, with kinetic energy up to the end point energy of 782 keV, spirals around the field lines towards either detector package, where their position and energy can be recorded. Figure modified with permission from Adam Holley (2010)[66].

uniform field for the central 3m and then a field expansion region on either side to 0.6 T, as shown in figure 2.7 [141]. Depicted in figure 2.8, the two beta detector packages consisting of a Multiwire Proportional Chamber (MWPC) backed by a plastic scintillator are then inserted into the field expansion region. A photograph of the SCS magnet before installation in Area B of LANSCE is shown in figure 2.9. The MWPC provides position reconstruction and thereby defines the fiducial volume for the experiment, as well as provides a handle to control systematic errors associated with missed backscattered events. The plastic scintillator is primarily used to measure the energy of the βs, but can also be used in the fiducial volume definition.

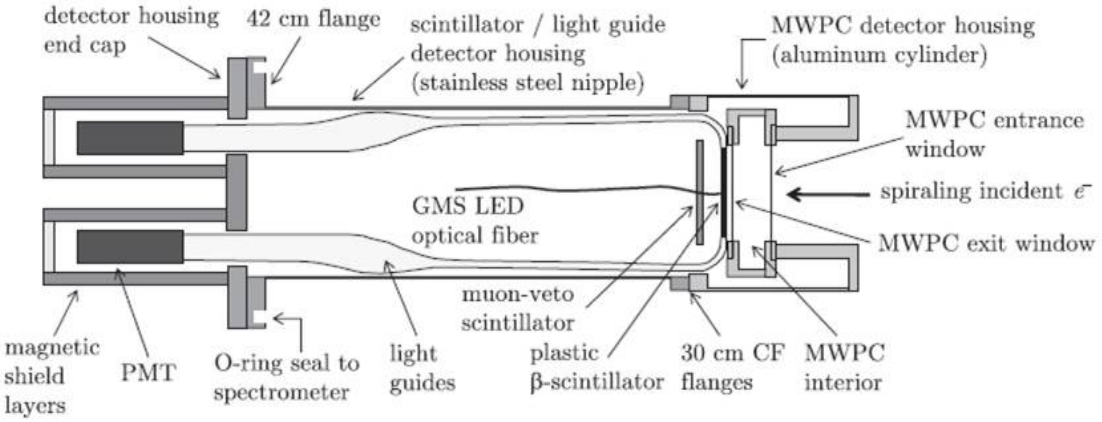

Figure 2.8: Each beta detector package consists of a MWPC backed by a thin scintillator. The MWPC provides position and possible backscattering information, while the scintillator provides an energy measurement of the beta-decay electrons. Light from the beta scintillator is transfered to four magnetic field shielded PMTs. The entire scintillator/light guide/PMT system is housed in a 100 Torr nitrogen environment which is employed to protect the end window of the MWPC. Figure taken with permission from Brad Plaster (2010) [141].

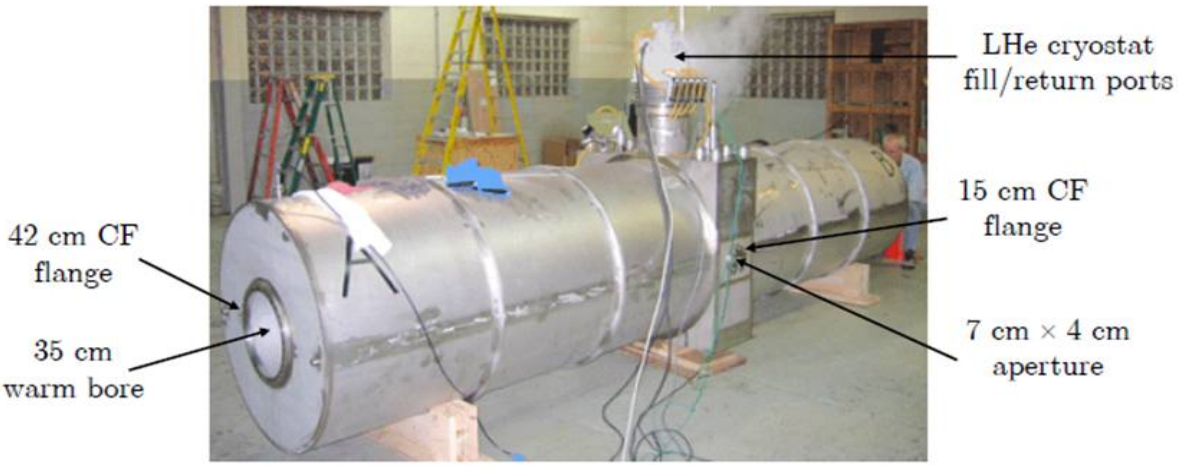

Figure 2.9: Photograph of the front face of the SCS magnet. The UCN enter the magnet from the 7cmX4cm aperture of the magnet. A rectangular hole was chosen to maximize the cross sectional area of the UCN guide feeding the decay trap, while still maintaining the required magnetic field uniformity. Figure used with permission from Brad Plaster (2010) [140].

An introduction of typical MWPCs can be found in [89], however due to the low kinetic energy of the beta-decay electrons, end point energy of 782 keV, the UCNA MWPC's were designed to minimize energy loss and back scattering of the low energy βs [79]. This meant using low Z materials, thin (∼micron) windows, and low ionization gas pressure. With this in mind, the MWPCs were made out of three wire planes, 2 cathodes and 1 anode each with 64, 50-μm thick wires spaced 2.54 mm apart, placed inside an aluminum enclosure with Kevlar wire reinforced mylar windows with thicknesses of 6 μm or 25 μm. Figure 2.10 shows a schematic of the MWPCs, designed and built by Caltech. One hundred Torr of Neopentane was found to provide enough gain while having a a low leak rate through pin holes in the mylar windows.

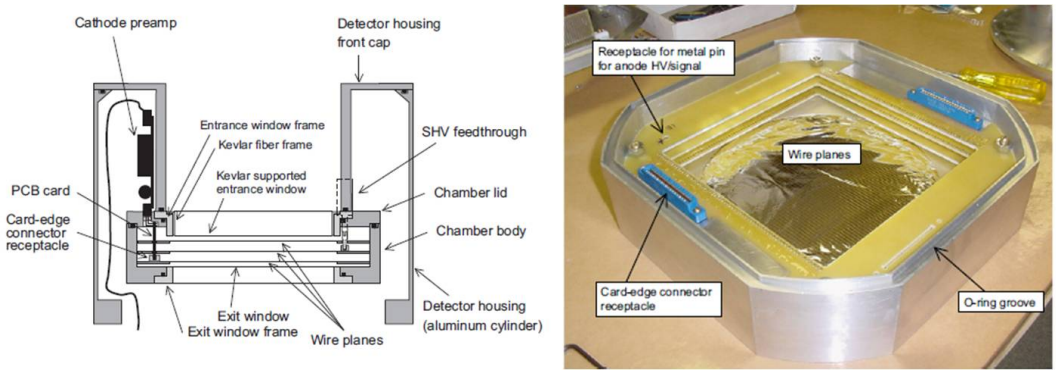

Figure 2.10: Left: schematic diagram of the MWPC system. Right: Photograph of an MWPC without its backing mylar window. Three wire planes, two cathodes and one anode, each with 64, 50 μm thick gold plated wires can be seen in their aluminum housing. Figure used with permission from Elsevier Limited (2010) [79].

Directly, behind the MWPC lies the 0.35 cm thick, 15 cm diameter plastic scintillator with 12 machined UVT light-guides glued to the radius of the disk [141], see figure 2.11. The thickness was optimized to ensure the most energetic beta-decay electron would deposit all of its energy in the scintillator (range of 0.31cm), but not much larger to minimize events created by background gamma rays from the source and neutron capture interactions. Four of the 12 light guides are coupled to a 2 inch PMT located about 1 m away, resulting in 4 PMTs being

employed which allows multi-PMT coincidences. This is useful to suppresses dark noise, cosmic-ray interactions in the lights guides, and gamma-ray interactions in the scintillator. The long distance between the scintillator and PMT is required to ensure the PMTs can be adequately shielded from the SCS magnet field. Figure 2.11 shows a photograph of the light guide/PMT arrangement.

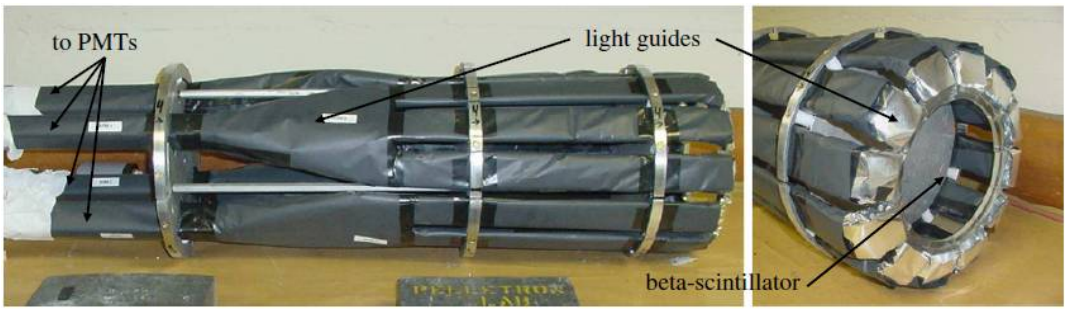

Figure 2.11: Photograph of the scintillator/light guide/PMT assembly. The 0.35 cm thick, 15 cm diameter scintillator disk is connected to 12 ∼meter long light guides along the radius. Four light guides come together at the photocathode of one PMT and four PMTs are used to measure the deposited energy of the beta electrons. Figure used with permission from Brad Plaster (2010) [141].

A series of other detectors have been constructed in order to reject cosmic-ray muons that would otherwise mimic an electron event in the MWPC/β scintillator system. The muon veto system consists of a 2.5 cm thick, 15 cm diameter scintillator disc that sits a few centimeters behind the β scintillator inside the β detector systems, called the "backing veto" and shown in figure 2.8, and then an ensemble of 3 m long, 5 cm diameter, single-wire drift tubes [145] and one large scintillator paddle that surrounds the top and sides of the SCS and β detector carts, called the outer vetos. Figure 2.12 shows a series of photographs of the outer veto configuration. Simulations show that requiring AND coincidences between the MWPC and β scintillator and anti-coincidences with the backing and outer vetos dropped the muon contamination rate to 0.1 Hz [167].

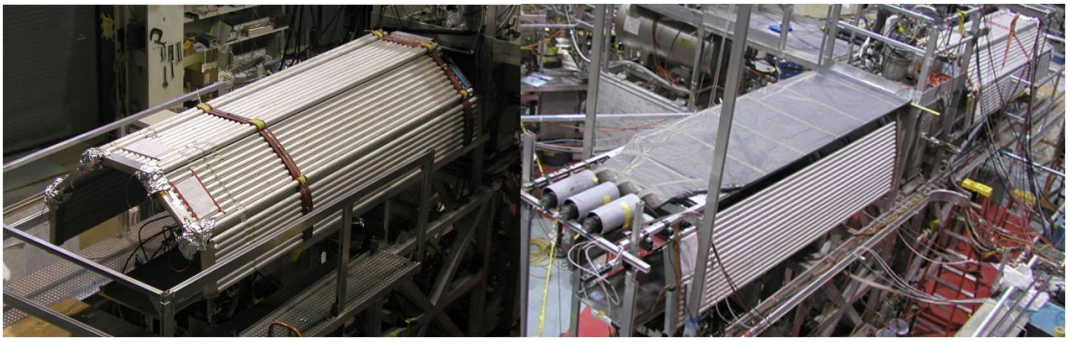

Figure 2.12: Photographs of the outer muon veto system. Left: Ensemble of drift tubes surrounding one of the β detector assemblies. Right: large scintillator paddle covering the top of the SCS with drift tubes rounding the sides. Figure modified with permission from UCNA collaboration (2010) [181].

2.5 UCN detectors

Several ^{3}He proportional gas counters are used to monitor the density of UCN as they travel through the beam line [121]. A CAD drawing and photograph of the detector in use is shown in figure 2.13a. Similar to the MWPCs discussed in section 2.4, the detector consists of several biased wire grids placed inside an active gas volume inside an aluminum enclosure with a very thin entrance window on one end. The active volume is filled with 1 bar of CF_4 and 20mbar of ^{3}He . A neutron that enters the gas volume has a very high probability of being absorbed, lifetime 1.8 x 10^{-3} s at these pressures, by a ^{3}He nucleus producing the reaction ^{3}He(n,p)^{3}H (Q=764 keV) The triton and proton ionize the fluorocarbon gas, producing a signal, which is then read out by the anode plane. Aluminum was chosen for the entrance windows (250 microns thick, alloy 6061T6) because of its handling strength and low neutron absorption cross section. In practice the UCN are accelerated, via gravity, by about a meter before they hit the window, resulting in a measured 50% transmission, see figure 2.13b. Three of these detectors are usually used during beta decay running: one just outside of the source shield wall near the UCN gate vale, one just after the AFP, and

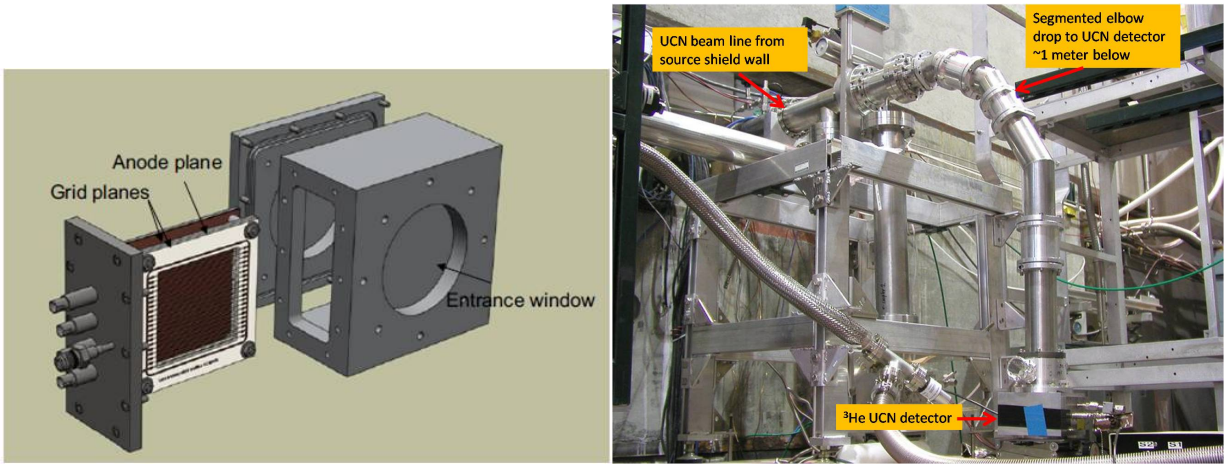

(a) CAD drawing of the UCN detector

(b) photograph of the 1 meter elbow drop guide assembly with UCN detector attached.

Figure 2.13: ^{3}He Schematic drawing and photograph of the ^{3}He UCN detectors used at LANSCE. Figure modified with permission from Chris Morris (2010) [121].

one under the SCS monitoring the density in the decay trap. For all three of these sites, small exit holes are drilled into the horizontal beam guide and another vertical guide, with a ^{3}He detector attached to the other end, mates up to these holes thus allowing the UCN to fall down onto the detector. These detectors are crucial for evaluating source and beamline performance.

2.6 UCNA Beamline

There are two main sections of the UCNA beamline: the region between the shield wall guides and the AFP magnetic and then the region between the AFP magnet to the decay trap guides inside the SCS. We will refer to the latter section as the Polarization Region of the UCNA beamline, although we note that UCN depolarization in between the PPM and AFP magnets is also important as will be discussed at the end of this section. Originally, the beamline was designed entirely out of DLC coated quartz guides, where Haerus HSQ300

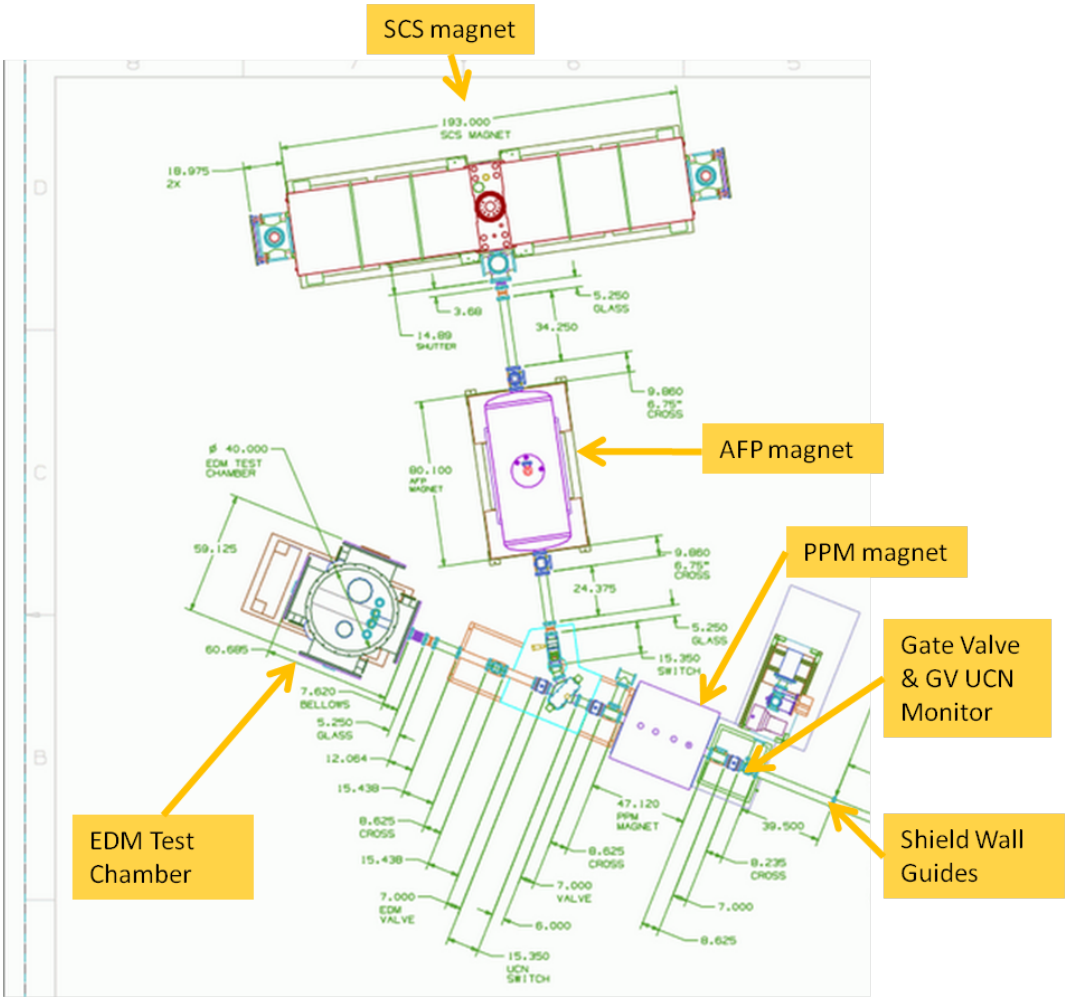

Figure 2.14: CAD drawing of the Area B layout from 2005, where UCN guides connect the four magnets/chambers to each other. Here the UCNA experiment is sharing the UCN beam with a test chamber for an EDM experiment. A switcher guide mechanism is used to switch the flow of UCN between the two experiments. We note the measurements are for the guide jackets that protect the DLC coated quartz tubes and not necessarily the guides themselves. Figure modified with permission from UCNA collaboration (2010) [181].

quartz is employed due to its superior ovality and purity. Figure 2.14 shows a CAD drawing of the beamline layout with this system in 2005. Between the gatevalve (GV) and just before the SCS magnet 70 mm OD by 2.2 mm wall DLC coated quartz guides were employed. After this a square DLC coated quartz guide, ∼1.5 inch on a side by ∼1.5 mm wall, was used to pass through the rectangular bore of the SCS, shown in figure 2.16, and mate against the

center guide of the decay trap guides. A series of transition plates on a rail system was used to make the junction between round to square guide. In addition the other end of the square guide was laser cut to match the radius of curvature of the decay trap guides. The decay trap guides, totaling 3 meters, are located on a rail system inside the SCS, as shown in figure 2.15, and were made of 101 mm OD by 3 mm wall DLC coated quartz. A hole was laser cut into the center decay trap guide to accept the square guide, as well as another smaller hole, diameter $\sim$0.125 inches, to feed a UCN monitor located directly underneath the SCS magnet. Two 50 cm long decay trap guides butted up against the center decay trap guide. Two more 50 cm long roughened decay trap guides butted up against these to complete the 3 meter long decay trap section. These end guides were roughened to increase the diffuse scattering in hopes of increasing the time the UCN spend inside the trap, which would increase the observed beta-decay rate. The roughened decay trap guides, shown in 2.17, were roughened along their ID by using a diamond scribe in a lathe.

The standard guide length was one meter and was housed in a stainless steel vacuum guide jacket, as shown in figure 2.18, if not already housed in a vacuum system, such as the decay trap guides inside the SCS vacuum. The quartz tube was held in the guide jacket with copper couplers/supports. Figure 2.19, shows one such coupler. In this way various length guide sections are used to connect the the UCN from the shield wall to the square guide. In all, there were about 16, 70 mm OD DLC coated quartz guides, of various lengths, that needed to be coupled together from the shield wall to the square guide. These guides were produced in 2004. Each of these connections had three gaps: two from the guide to the copper coupler junction and one from the coupler-to-coupler junction. Unfortunately, there was really no concern to the flatness of the quartz tubes and depending on how the tubes were cut, rotated or pushed through the diamond saw, and fire polished the flatness level could be $>$ 0.010 inches. Simulations showed that these gaps were a significant loss

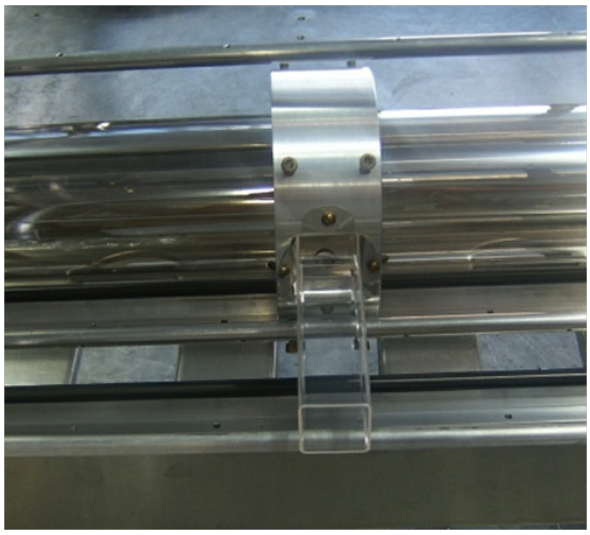

(a) Practice square quartz guide mating to the center decay trap guide.

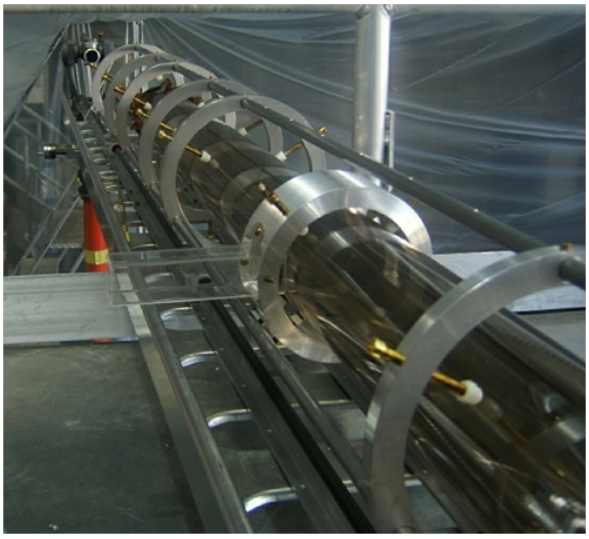

(b) The three decay trap guides in their rail system.

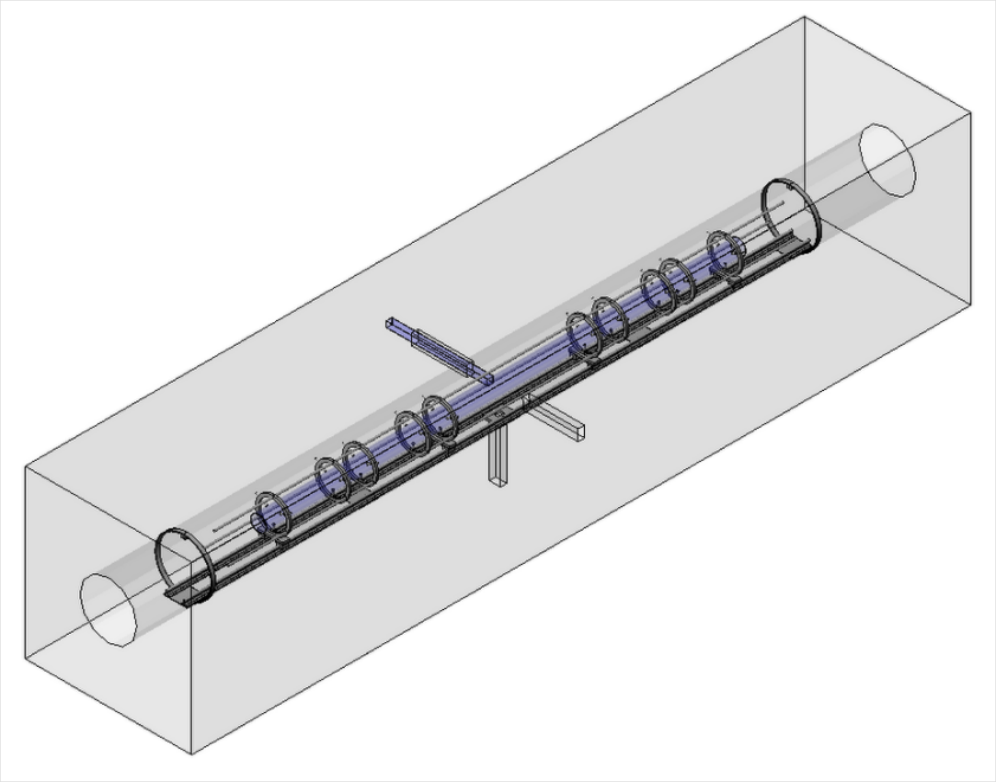

(c) CAD drawing of the quartz decay trap inside the bore of the SCS magnet.

Figure 2.15: UCNA decay trap system fitted with quartz guides. Figure modified with permission from UCNA collaboration (2010) [181].

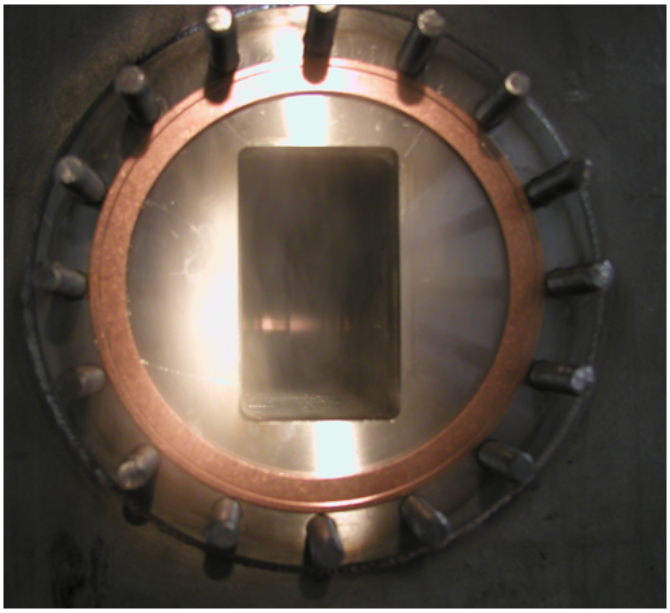

Figure 2.16: Rectangular bore of the SCS magnet through which a square or rectangular UCN guide passes to mate up to the central decay trap guide. Figure used with permission from UCNA collaboration (2010) [181].

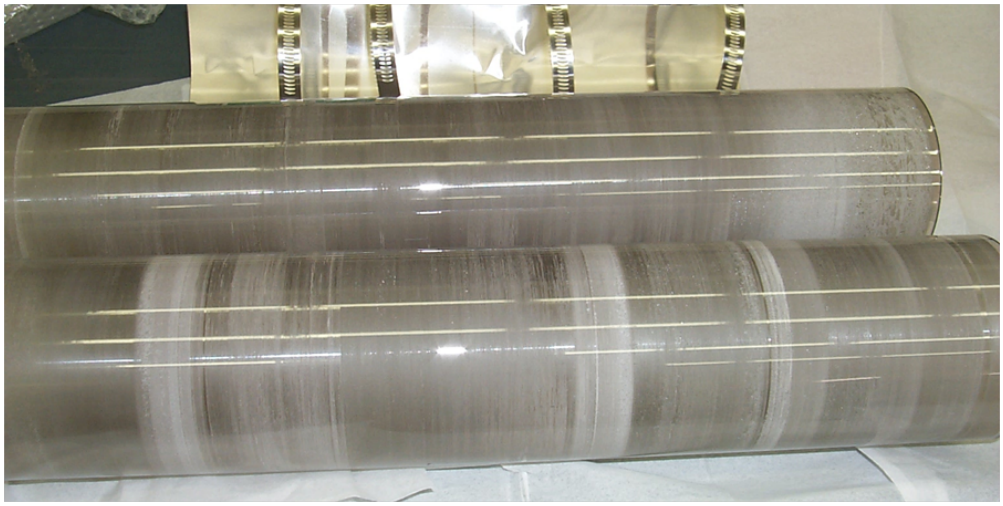

Figure 2.17: DLC coated diffuse decay trap quartz guides. The ID of the tubes were roughened on a lathe fitted with a diamond scribe. The dull brown/gray color is indicative of the coating being too thin, ∼50-70nm thick.

point for UCN in the UCNA beamline and recommended gaps on the size of 0.002 inches per junction. To address this issue the quartz tube grinder system, described in chapter 7, was constructed.

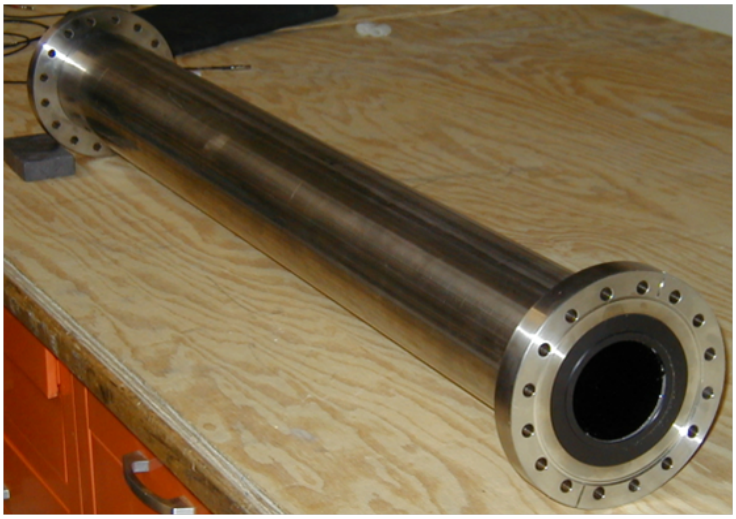

Figure 2.18: Stainless steel vacuum guide jacket used to provide the vacuum for the DLC quartz UCNA beamline. In the picture an acetal coupler is used to hold the guide. These were later replaced with copper versions. Figure used with permission from Mark Makela (2010) [111].

Meanwhile, it was determined that most of our DLC quartz guides did not have a thick enough coating, see chapter 7. Due to time constraints in making a thicker set, the collaboration decided to modify the beamline to employ uncoated, polished stainless steel and copper UCN guides, except for the RF spin flipper region of the experiment where a nonconductive guide is required. With the metal tubes, the guide jackets were not used as the tube material provides the vacuum wall of the beamline. In addition, it is fairly easy to obtain the required flatness level on the ends of the metal tubes on a standard professional lathe. To connect guides together, an aluminum coupler is clamped, with an O-ring, to both ends of a guide and then two guide sections are butted up against each other. Another O-ring seal between the two couplers provides the vacuum seal. This provided a much smaller gap beamline.

Figure 2.19: Example copper coupler used to hold the quartz guides. This particular coupler has two extra wide slots to accommodate water and electrical lines used by the RF spin flipper.

First, 3 inch OD RATH True10 stainless steel tubes were connected at the GV and run through the PPM, with the PPM safety foil in-between two guide sections. The down stream PPM guide mated to an 18 inch center-line-radius elbow 60° elbow, as shown in figure 2.20. The elbow then mates to a guide switching apparatus, called the "switcher". The switcher is designed to either allow UCN through from the shield wall to the AFP magnet or allow UCN from the AFP magnet side of the beamline to fall to a UCN detector. The latter is used to measure the depolarized fraction of UCN in the Polarization Region of the experiment. The switcher was fitted with 2.75 inch OD stainless steel electropolished tubes. Figure 2.21 shows the inside of the a switcher with DLC coated quartz guides. Here the "slide" guides ride on a pneumatically actuated rail that is operated hundreds of times over the course of a year. The placement of the guides is critical, as over time the guides/rail move to the point where they will not move freely past each other; shattering in the case of quartz guides and denting in the case of metallic guides. This is one location where metallic guides really make sense.

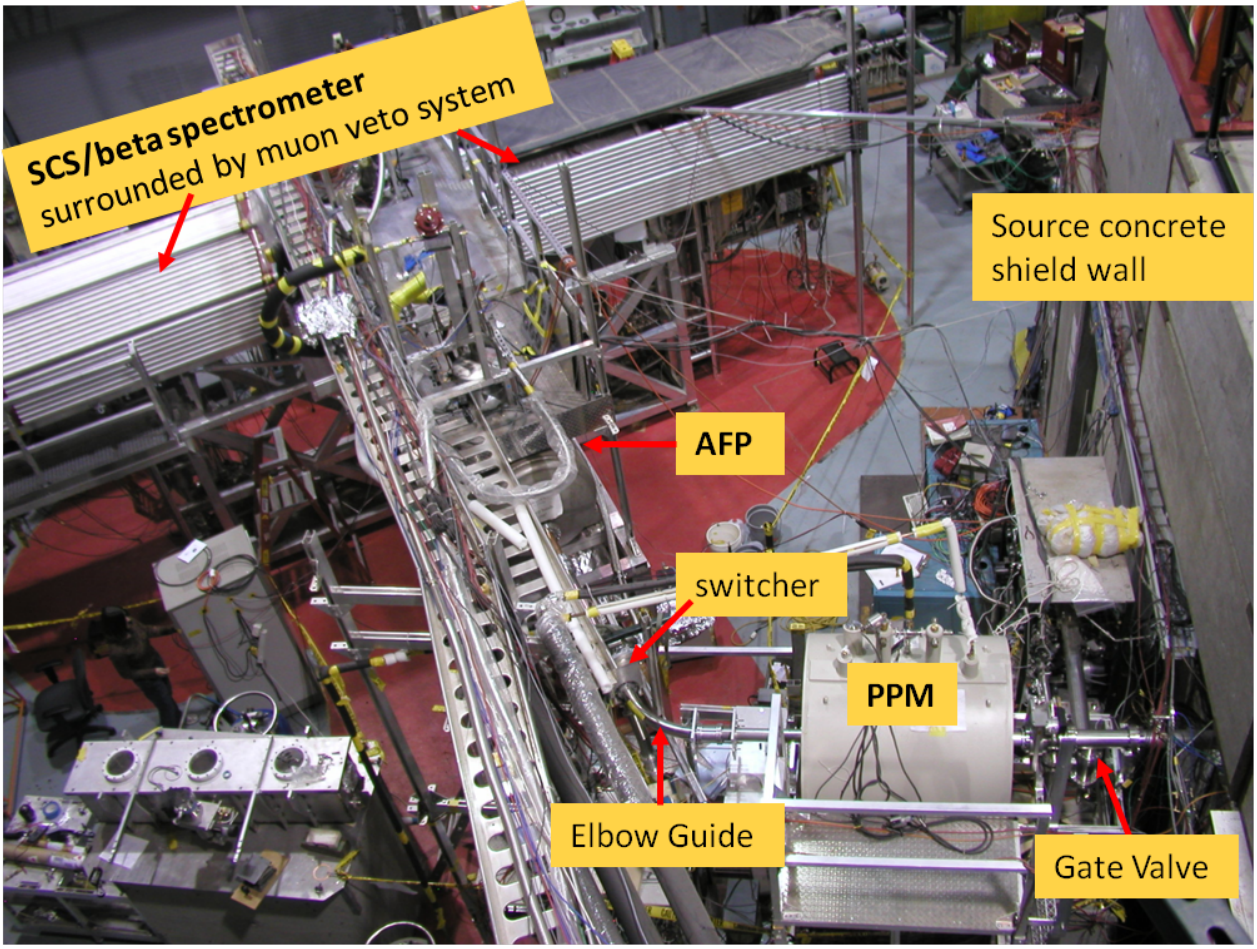

Figure 2.20: Birds-eye view of the UCNA experiment showcasing the the guide sections from the shield wall to the 60° elbow. In 2010, the stainless steel guides between the PPM and the switcher were replaced with electropolished copper guides to reduce the amount of UCN trapping between the two magnets. Figure modified with permission from UCNA collaboration (2010) [181].

After the switcher, 2.75 inch OD by 0.065 inch wall guides are used up to the SCS. Just after the switcher, as can be seen in figure 2.22, another electropolished stainless steel guide, ∼24 inches long, makes the connection to a one meter long electropolished copper guide that enters into the AFP magnet. Now we are in the holding field of the AFP magnet, where the RF spin flipper is located. Here a DLC coated quartz guide, guide g31, is employed as required. Next another meter long copper guide is connected to the quartz guide, but has a

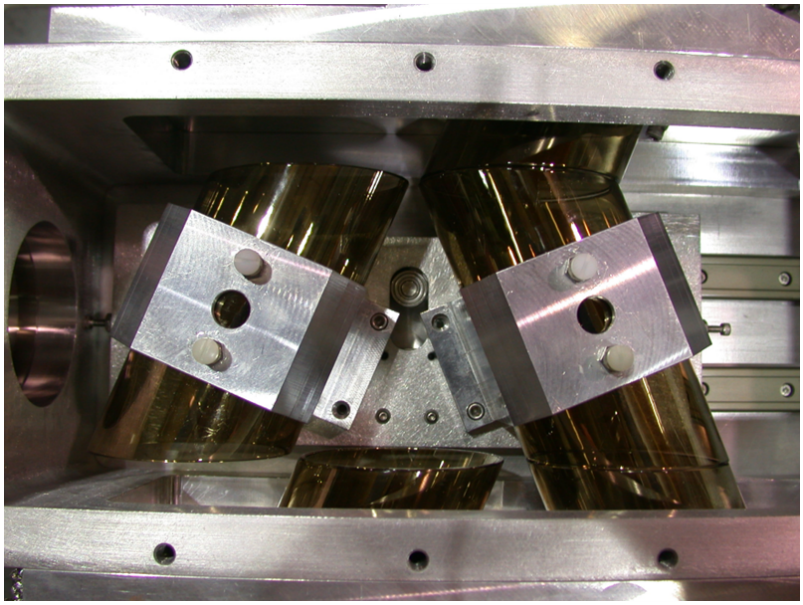

Figure 2.21: DLC coated quartz switcher guides. Five guides are used to make up the switcher: three in/out guides with one side cut at a 67.5° angle and the other side cut 90° with respect to the length of the guide and two slide guides where both sides are cut at a 67.5° angle. When operated, the guides either allow the UCN to travel straight through or bends the UCN by 45° . The gold color of the DLC coated quartz guides is indicative of a $>$ 100 nm thick coating. Figure used with permission from UCNA collaboration (2010) [181].

0.125 inch diameter hole through one side at its midpoint. This guide is called the "Fe foil guide", where the hole allows UCN to fall to a UCN detector with an iron foil just before the detector. The Fe foil is extremely helpful in tuning the RF flipper. Next another $\sim$34 inch long copper tube meets up to a round-to-rectangular transition plate. Unfortunately, the transition plate rail system has never been fully realized, and a thin copper plate with a rectangular hole is used instead. A rectangular guide, shown in figure 2.23, is used instead of a square guide, in an effort to reduce the number of bounces UCN have make before entering the central decay trap guide. Like the square quartz guide, one end of the rectangular guide is machined with a radius so that it will mate with the center decay trap guide. The decay trap guides are made of three, one meter long 5.125 inch OD 0.125 inch wall copper tubes, that are clamped together as shown in figure 2.24. Here the clamps help minimize the gaps

in the trap. The center guide has a rectangular hole and a 0.125 inch diameter hole cut through one side separated by 90° . Again the 0.125 inch diameter hole allows UCN to fall to another UCN detector and helps monitor the density of UCN in the trap. The decay trap guides were mechanically polished up to the finish left by a color compound loaded sisal wheel, instead of up to the finish left by a color compound loaded cotton buff like all the other copper tubes. This was done to increase the amount of diffuse scattering in hopes randomizing the UCN distribution in the trap. To help bottle the UCN, thin beryllium coated Mylar windows were placed on the two ends as shown in figure 2.25.

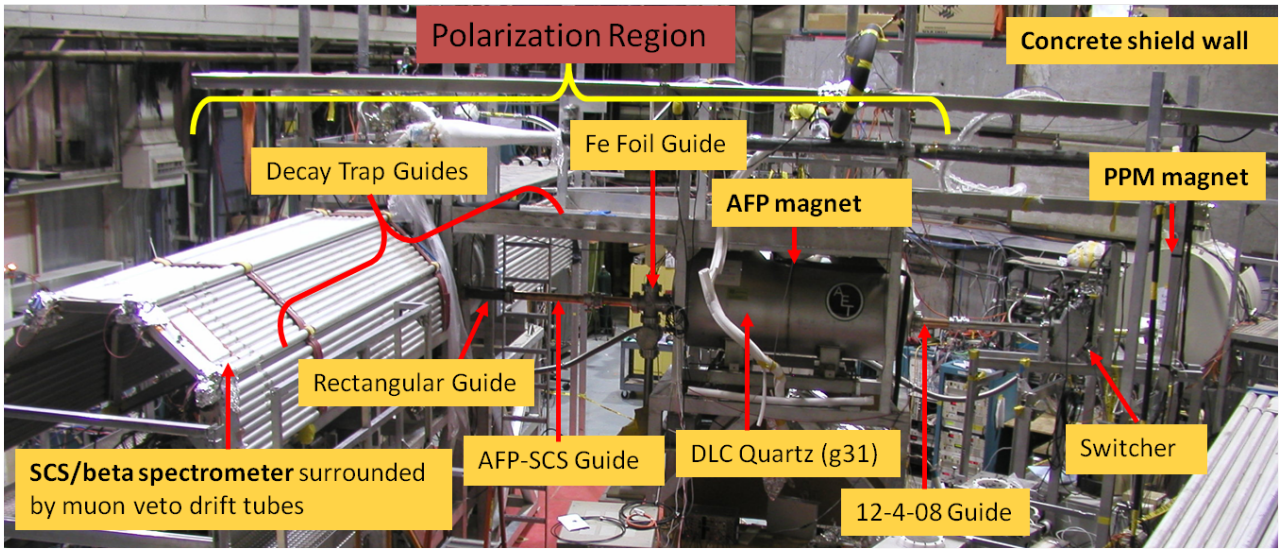

Figure 2.22: Side view of the UCNA experiment showcasing the Polarization Region of the experiment as of December 2008. The Polarization Region guides are labeled according to their DLC coated copper guide names as detailed in chapter 7. Figure modified with permission from UCNA collaboration (2010) [181].

This was the beamline configuration used for the 2007 and 2008 UCNA data sets. In 2009, the Polarization Region of the experiment, everywhere were copper guides were used, was fitted with DLC coated copper guides coated with the DLC Copper process described in chapter 7. In addition to these guides, the ∼24 inch long stainless steel guide between the switcher and the AFP magnet was replaced with a mechanical only polished copper tube,

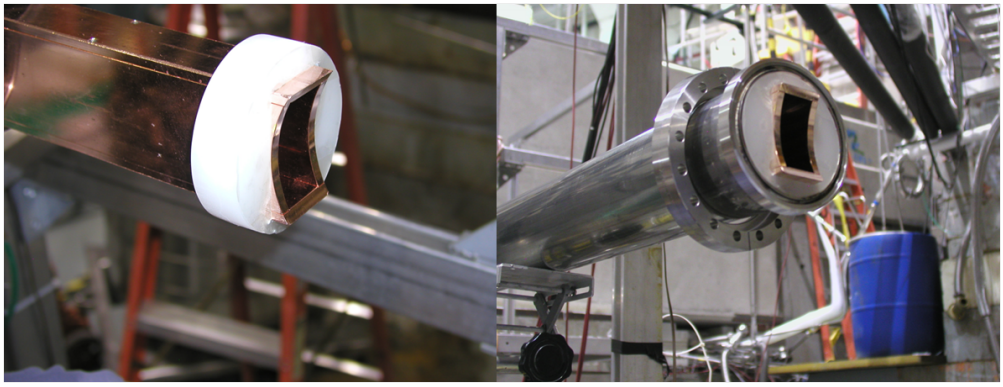

Figure 2.23: Rectangular guide used in the 2008 data set. The guide is made out of four plates bolted together. This same guide was then coated with DLC for the 2009 and 2010 UCNA beta-decay runs. Figure used with permission from UCNA collaboration (2010) [181].

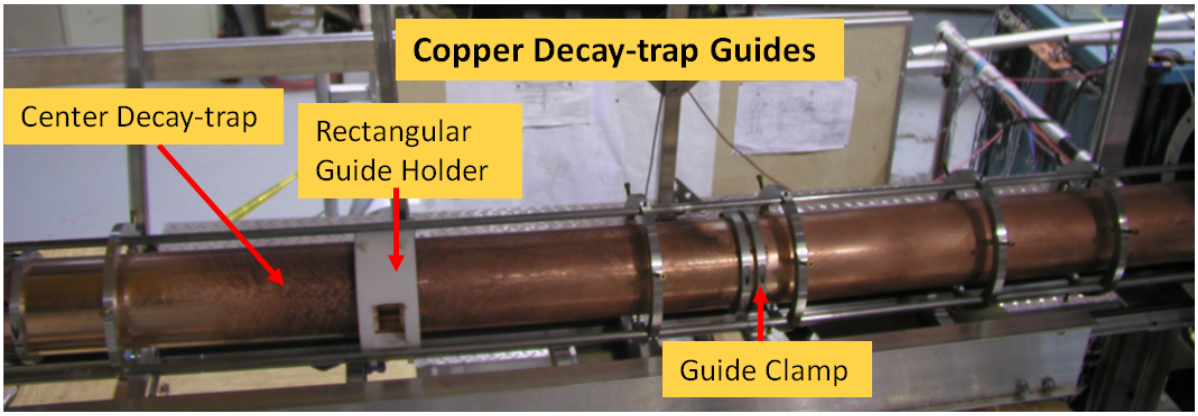

Figure 2.24: Copper decay-decay guides inside their rail holding system. Clamps were added at each junction to reduce the size of the gaps. Figure modified with permission from UCNA collaboration (2010) [181].

as an electropolished version was unavailable at the time.

It was soon discovered that depolarization from the stainless steel guides in-between the PPM and AFP magnets reduced the UCN flux through the AFP magnet by about about 50%. The UCN after the PPM are polarized, but become depolarized after making a number of bounces in the stainless steel guides on their way to the AFP. The AFP magnetic field has the same sign as the PPM and so about half of the UCN see a potential hill and become

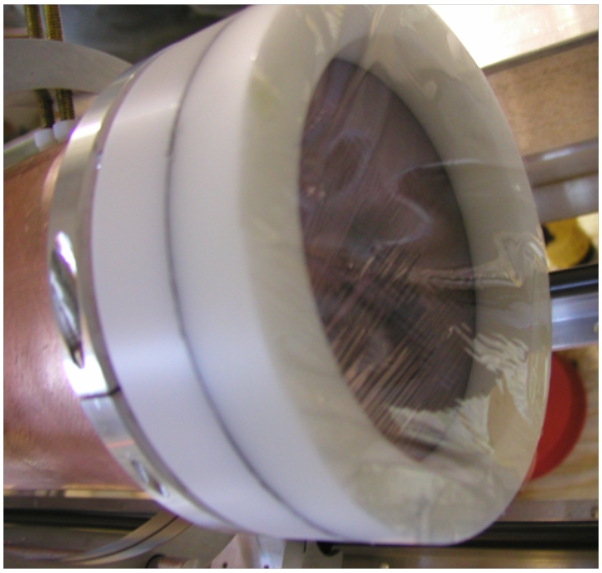

Figure 2.25: Beryllium coated Mylar end caps placed on each end of the decay trap section to help bottle the UCN. The Cellophane covering the foil holder is there to protect the window and is removed during the final decay-trap guide installation. Figure used with permission from UCNA collaboration (2010) [181].

trapped, and eventually lost, in-between the PPM and AFP. The collaboration knew about this, as it is one of the reasons DLC coated quartz guides were employed in this region, however at the time equivalent copper (and other non-depolarizing guides for that matter) were not easily available. For 2010, the Virginia Tech UCNA group has furnished the 3 inch and 2.75 inch OD copper guides to alleviate this problem. Now almost all the guides of the UCNA beamline from just before the PPM on, have been furnished by Virginia Tech (the rectangular guide and transition plate were provided by LANL). Here electropolished copper guides are placed from just before the PPM to just before the AFP, and then DLC coated copper guides take over from the AFP to the decay-trap guides in the SCS, where (of course) a DLC coated quartz guide, g31, is placed in the RF spin flipper region. For reference, Table 2.1 lists the guide lengths that make of the 2010 UCNA beamline.

Table 2.1: 2010 UCNA Beamline Guide Lengths

Guide Location	Guide Name	OD (in)	Length (in)
GV-PPM	Upstream PPM	3	44.00
PPM-elbow	Downstream PPM	3	26.00
Elbow	60° Elbow	3	18 in CLR
Switcher	3 in/out and 2 slide guides	2.75	6.03 and 5.47
Switcher-AFP	Switch-AFP	2.75	26.94
Upstream AFP	12-4-08	2.75	39.37
RF Spin Flipper	g31	2.75	39.37
Downstream AFP	Fe Foil	2.75	39.37
AFP-SCS	AFP-SCS	2.75	33.34
Rectangular	Rectangular Guide	2.31 by 1.58	28.00
Decay-trap	g60,g63, center decay trap	5.13	39.37

Chapter 3

UCN Guide/Components Coating Facility at Virginia Tech

3.1 Introduction to Deposition Methods

The use of thin film coatings has grown tremendously over the last few decades. The semiconductor and optical coatings industries have spurred the primary developments in thin film technology. However, now the automotive, manufacturing, and consumer products industries are fueling development with an increased interest in wear-resistant coatings [93]. In all cases the thin film provides a functionality that is lacking in the underlying substrate. In the case of UCN transport, thin films allow one to build components out of more common materials such as stainless steel, copper, plastics, etc, and then have the surfaced appropriately coated for particular UCN applications. For example, almost all the UCN surfaces in the SD_2 LANSCE source are made from stainless steels and coated with ^{58}Ni because of ^{58}Ni's much higher Fermi Potential . To this end, thin film coatings are usually ascribed to

two different kinds of deposition processes: physical vapor deposition (PVD) and chemical vapor deposition (CVD). All the coatings made for the UCNA experiment at Virginia Tech utilize PVD processes. This chapter will briefly discuss these two deposition genres and then will focus on the particular techniques used at Virginia Tech to apply the coatings for the UCNA experiment.

3.1.1 Chemical Vapor Deposition

CVD films are made by reacting two or more precursors, usually in gas form, together in vacuum to produce a third, and often many more, species that can deposit on substrate, as depicted in figure 3.1. An advantage of CVD processes is that the deposition is relatively uniform and conforms to a wide variety of shapes and sizes, similar to an electroplating process. Sometimes the chemical reaction rate between the species is enough to form the desired film, but more often the reaction is assisted in some way. Common methods for this include: heating the substrate, applying an RF/DC bias to the substrate or chamber as in Plasma Enhanced Chemical Vapor Deposition (PECVD), bombarding the substrate with ions (usually argon, oxygen, hydrogen, etc.). An assortment of assisted techniques are used to produce a variety of coatings [28]. In fact, diamond-like carbon (DLC) is commonly produced by a CVD method. Here hydrogenated carbon precursors, usually Methane or Acetylene and hydrogen gases [50], are used to form the carbon film. This method was first explored by the UCNA collaboration, in the late 1990's/early 2000's, and a sample was produced by the SURMET corporation [110]. The major draw back with CVD deposited DLC is it's high hydrogen concentration, usually 30-50%, which signifcantly lowers the Fermi Potential , due to hydrogen's negative coherent scattering length, despite relativley high densities [137][19]. In the past CVD-DLC films used to be quite rough on the UCN scale, but current assisted CVD techniques, such as those mentioned above, produce films on the

order of ∼1 nm (RMS) roughness [104]. If deuterated precursors are used then the Fermi Potential can be signficantly increased: from ∼160 neV to 220 neV[171][85]. More detailed information concerning CVD deposition can be found in [139][135].

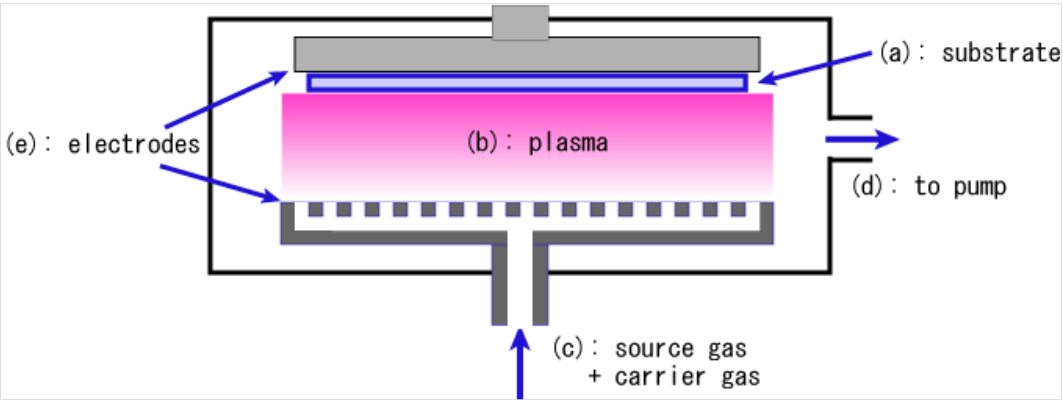

Figure 3.1: Diagram of a typical plasma enhanced CVD deposition chamber.

3.1.2 Physical Vapor Deposition

PVD involves a physical process, not a chemical process as in CVD, to produce a vapor of an evaporant material (usually starting in solid form) which can then interact with a substrate. Common forms of PVD systems include resistive and electron-beam (ebeam) thermal evaporators, sputtering systems, and pulsed laser deposition systems and are usually operated in vacuum to high vacuum pressures, although some plasma-spray coatings are applied in atmosphere. Resistive thermal evaporators involve the use of high currents to resistively heat a "boat" or crucible that holds the source material. The source material indirectly heats up past its melting/sublimation point and its vapor pressure increases. Most depositions occur when the vapor pressure is around 10^{-2} Torr. This type of evaporation is common for non-refractory metals or ceramics with melting points below 1500° C. One downside to resistive heating is that it is a "hot" process, as a lot of heat is radiatively

lost from the boat itself heating the chamber and substrate. As these items heat up their outgassing rates increase which could contaminate the substrate/film being deposited. An alternative to resistive thermal evaporation is ebeam thermal evaporation. Here an electron beam is used to directly heat the source material, instead of relying on thermal contact with a boat/crucible. Ebeam evaporation is the primary method used to apply the ^{58}Ni films required for all the UCN source components and is discussed in section 3.4

Sputtered deposition (SD), often just called sputtering, relies on the impact/momentum transfer of accelerated ions to release source atoms from the bulk source target. Bombarding ions are generated by striking a plasma near the target material, via a RF or DC discharge. These ions are accelerated toward the target and can knock off source atoms that leave in the form of ions/neutrals/clusters, and electrons depending on their angle of incidence and energy. Often a magnetic field is applied to trap these secondary electrons near the target which are then used to sustain the bombarding ion plasma. The knocked off source atoms, with energies on the order of several eV, leave the surface with a $\cos\theta$ distribution and can interact with the substrate. Argon is the most common bombarding ion, because of its inertness and relatively inexpensive cost, however sputtering with krypton, xenon, and mercury are used as well. The larger mass of these atoms allows more energy transfer to higher mass source atoms, thus increasing the sputtering efficiency/yield. One advantage of sputtering over thermal methods is that alloy films with a particular stoichiometry can be produced, if one takes into account the different sputtering efficiencies for the different elements. In fact, ^{58}Ni/Mo(10%) UCN guides have been made through magnetron sputtering by Serebrov [157] [142]. One should note that a different film structure develops from sputtering versus thermal methods, due to the different energies of the "evaporating" atoms.

Pulsed laser deposition (PLD), also called pulsed laser evaporation, pulsed laser ablation, laser sputtering, etc., has become a viable alternative to other PVD and CVD methods over

the past 20 years. This technique makes use of a laser beam to generate an energetic plasma of target material, which then expands outward in a plume toward a substrate. The plasma under these conditions is very energetic, having kinetic energies from tens to hundreds of eV, so that the plume composites may drive into the substrate initiating subplantation growth. However, different materials can be added to interact with the ablation plume to promote chemical, as well as physical, processes to occur on the substrate. For example titanium nitride thin films can be made by ablating a titanium target in a nitrogen atmosphere. Here the plume collides with the gas molecules producing a variety of species (ions, excited molecules, etc) which can participate in chemical reactions on the substrate [108]. PLD is an excellent method for producing high quality DLC films, as the carbon ions in the plume have the required energy, ∼100 eV, to form the diamond bonds. Chapter 7 is devoted to this process. In addition, PLD can also be used to make alloy films, as the laser energy density on the target is so high that a small volume of target material is completely vaporized thus preserving the stoichiometry, and there is some interest in using this method to produce ^{58}Ni/Mo(10%) films as an alternative to ebeam evaporated ^{58}Ni films.

We should emphasize the difference in energy of the depositing atoms for the various thin film producing methods. Here thermal evaporation, sputter deposition, and PLD produce vapor plumes with ∼0.2 eV, ∼5 eV, and ∼100 eV of kinetic energy, respectively, without any addition treatments such as target biasing or collisions with chamber gas molecules. The film structure and configuration, as well as the adhesion of the film, are quite dependent upon these energies. For example, thermal evaporation of carbon will produce graphite bonded films, where as PLD of carbon can form diamond and graphite bonded films. Also with PLD and SD, 2^{nd} order sputtering can become an issue as the plume atoms knock off substrate atoms and even previously adhered target atoms, which can be used to ultimately produce a well adhered film, as all the weakly bonded atoms are knocked off. Each technique has its

own niche as well as enhancements/modifications and so one really needs to have a broad knowledge of the deposition techniques available in order to make the desired film/structure. References [119] and [37] provide a good start in developing this knowledge.

3.2 Coating Thickness

Before discussing the particular systems used to apply the thin film coatings for the UCNA beamline, we briefly discuss the amount of coating required. As noted in figure 1.1, there is a transmission probability associated with each UCN-wall interaction. The transmitted UCN wavefunction follows an exponential form, $T_+e^{-\kappa x}$, where $\kappa = \sqrt{\frac{2m}{\hbar^2}(V_F - E_\perp)}$ and $E_\perp$ is the energy of the neutron perpendicular to the V_F surface. The penetration length $1/\kappa$ varies from $(\lambda_n/2\pi)$ for E = 0 to infinity for E = V. Thus the penetration length is dependent upon the V_F of the surface, where for Fermi Potentials larger than 200 neV the minimum penetration length is less than 10 nm. It was generally accepted that ten times this should be adequate, leading to the thickness goal of 100 nm. However, motivated by the poor SD_2 source and guide performance, further calculations were done taking into account the many bounces the UCN undergo as they make their way through the beamline. Figure 3.2 shows one such calculation from Mark Makela. Here he assumed the ucn needed a 107 bounces to traverse the shield wall guides to the PPM, and that every bounce was a head on collision (although not physical it provides a worst case scenario). Here we see that the number of transmitted UCN asymptotically approach a certain value that is dependent on the V_F of the coating. At a 100 nm we are still at the "knee" of the curve, while at about 150 nm the knee has leveled out. Motivated by calculations such as these we moved are target thickness to 150 nm or more.

One challenge with increasing the thickness of the thin films, is that the internal stress

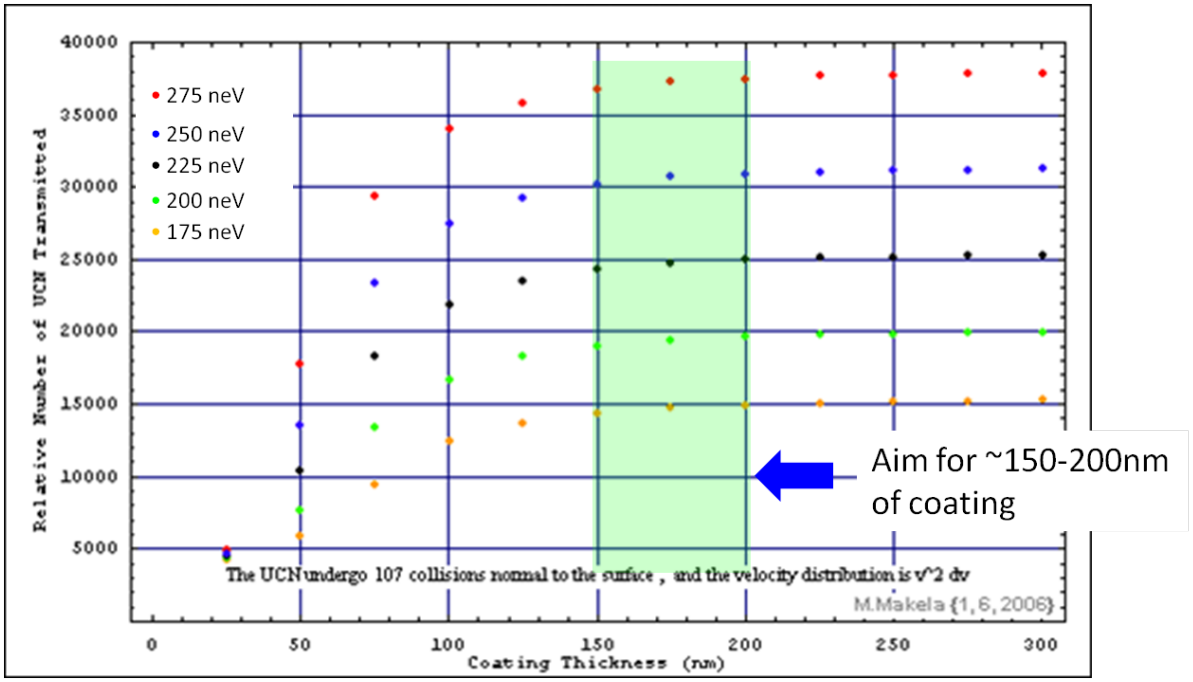

Figure 3.2: Transmitted UCN versus coating thickness for several different Fermi Potentials. The standard UCN distribution, v^2dv up to the critical velocity associated with each Fermi Potential, was employed. Figure modified with permission from Mark Makela [111].

of the films usually increases as well. There are generally three classes of thin film stress: epitaxial, thermal, and intrinsic/growth stress, where thermal and intrinsic growth stresses are the most important in our films. Thin films will delaminate or peel away from their substrate due to these stresses. In chapter 6, we will show a number of ^{58}Ni films that delaminated, usually, from the thermal stress of bringing the component and film to LN_2 temperatures. Figure 3.3, shows the result of a particular high stress DLC film grown on a glass slide. DLC is known to have high internal compressive stress, which generally increases as the density of the film increases [94] [148]. Usually micron size mountains will develop, the so-called snakes of DLC delamination [110], that tend to propagate and grow. If the bond between the film and substrate is particularly weak, theses mountains will grow into the large scale semi-free standing DLC film shown in the upper right of figure 3.3. Thus

when we moved to applying at ∼150 nm or more of coating on all our UCN components, we ran into several stress related delamination issues, especially with our DLC coated copper components. This motivated the development of our new ^{58}Ni ebeam source coating and DLC Copper process discussed in chapters 6 and 7.

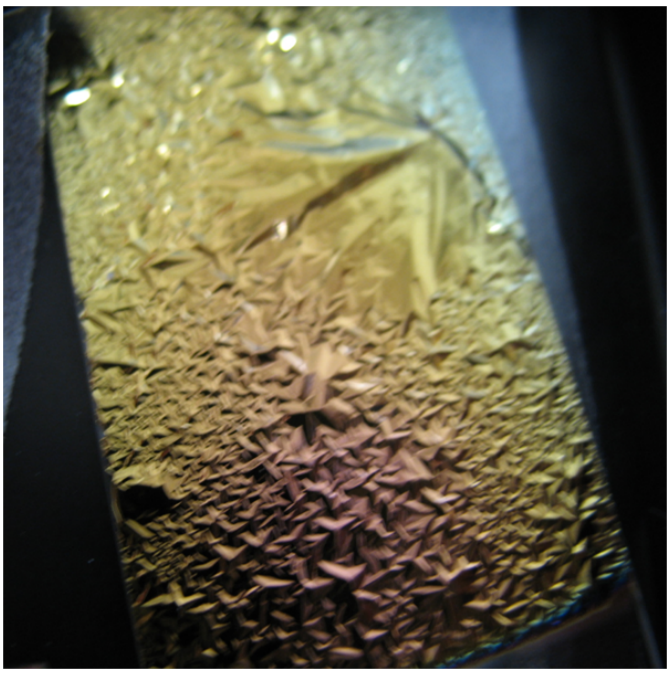

Figure 3.3: Delaminated DLC film from its glass slide substrate.

3.3 Tube Coating Chamber

To put into context the following discussion concerning the ebeam and PLD tube coating systems, which are primarily used to apply thin films on the ID of UCN guides for the UCNA experiment, it is useful to describe the tube coating vacuum chamber that both systems utilize. As shown in figure 3.4, the tube coating chamber is a 3 m long,16 inch diameter stainless steel cylindrical chamber with several additional 2.75 inch and 8 inch Conflat ports. The deposition source is located at the ∼center of the chamber and the UCN

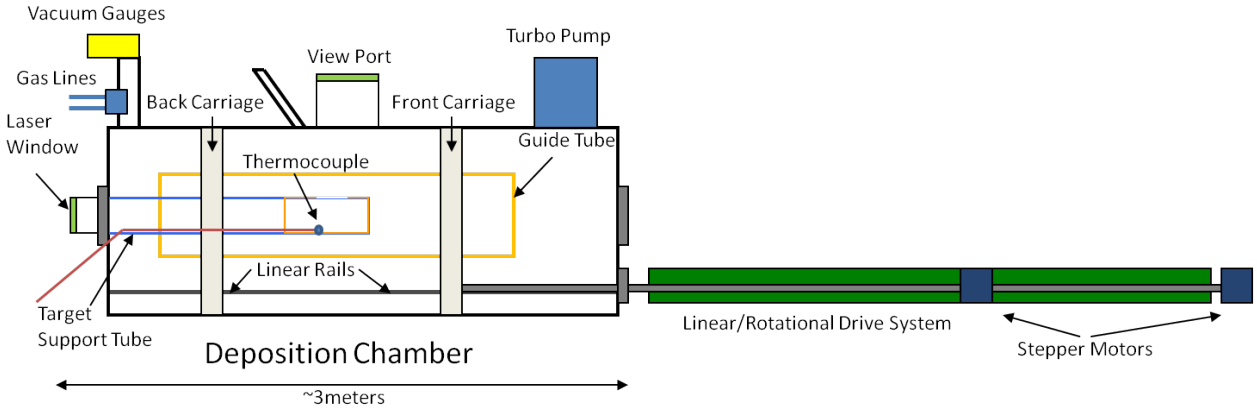

(a) Diagram of Tube Coating Chamber

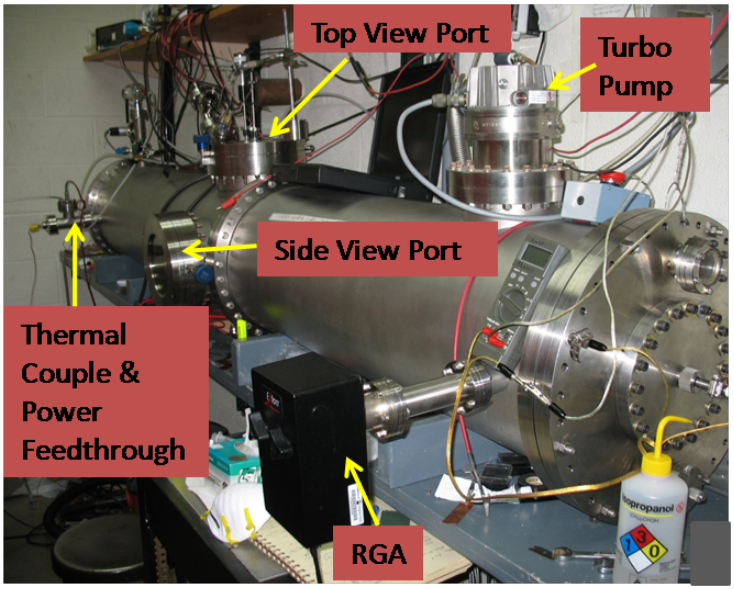

(b) Photograph of the Tube Coating Chamber

Figure 3.4: Diagram of the baseline tube coating chamber at Virginia Tech. Further modifications are made depending on which type of deposition process is used: ebeam or PLD

guide tube is pushed/pulled and rotated over the source, via a two point carriage system. Here a front carriage and a back carriage, shown in figure 3.5, are connected via aluminum rods. Each carriage has two linear bearings that glide along a rail system inside the chamber. A set of custom diameter mounting plates is bolted to the inner ring of each carriage and

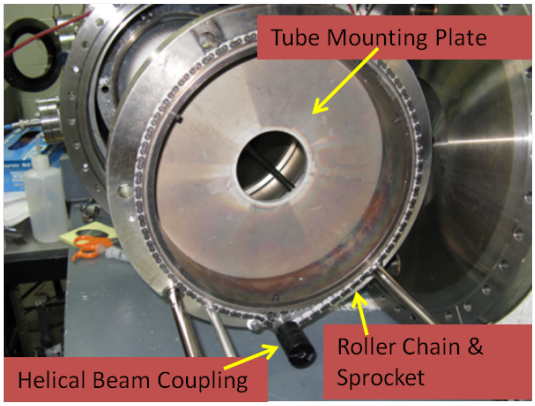

(a) Front Carriage

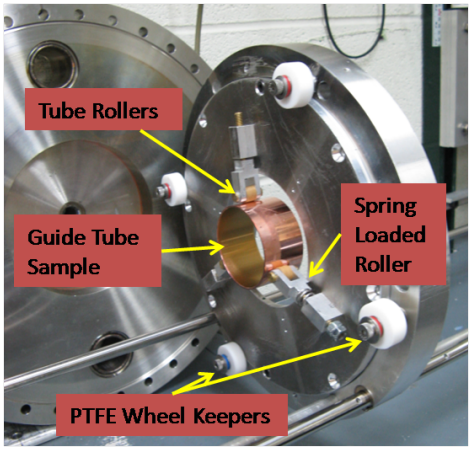

(b) Back Carriage

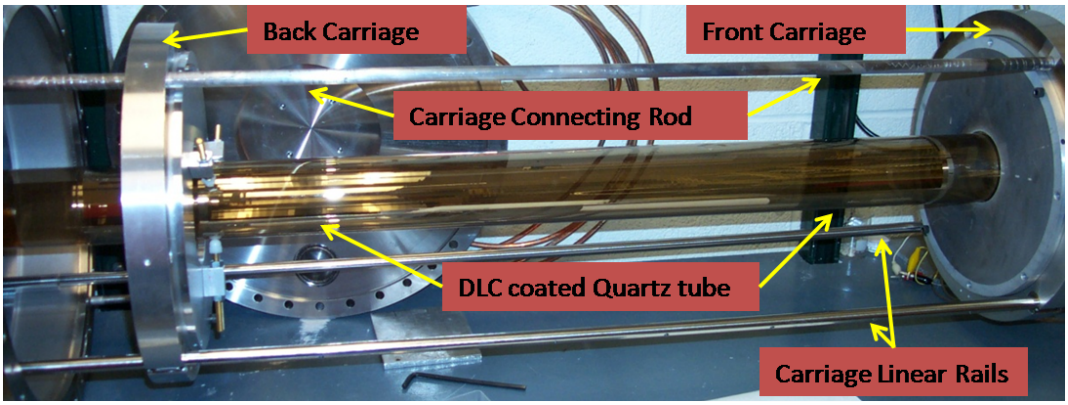

(c) Whole Carriage

Figure 3.5: Photographs of the guide/tube carriage system. Both carriages rotate via a 12 inch diameter thin section roller bearing (hidden). Custom mounting plates are made for each guide diameter. (a) The Front Carriage: Torque from the 1/4 inch diameter drive rod is coupled through a helical rod coupling to rotate a sprocket chain (ANSI 25) driven rotation system. An acetal/SS link chain is used to prevent galling. (b) Back Carriage: A spring loaded roller system has been added to provide another degree of freedom for the rotation of the guide tube in addition to the thin roller bearing. PTFE wheels act as bearing keepers to prevent the bearing from walking out during use. (c) Whole Carriage: The two carriages are connected via aluminum rods. As pictured the back carriage has an older style of guide holder where nylon acorn nuts provide the surfaces that allow the tube to rotate. These were later replaced with the rollers shown in figure 3.5b.

the guide tubes are threaded through the these holes. At the front carriage the tube is fixed via three set screws and a hose clamped coupler, while the back carriage has a set of rollers

that tubes up to 6 inch in diameter rotate along. For larger diameter tubes, the rollers are not used and set screws are used to fix the tube to the mounting plate. With this carriage system, tubes with diameters of ∼2.75 inch to ∼9 inch and up to ∼40 inch in length can be coated. Mounting plates have also been made to hold flat guide substrates, as shown in figure 3.6 and the system is now configurable to coat the outside of rods as shown in section 6.5.

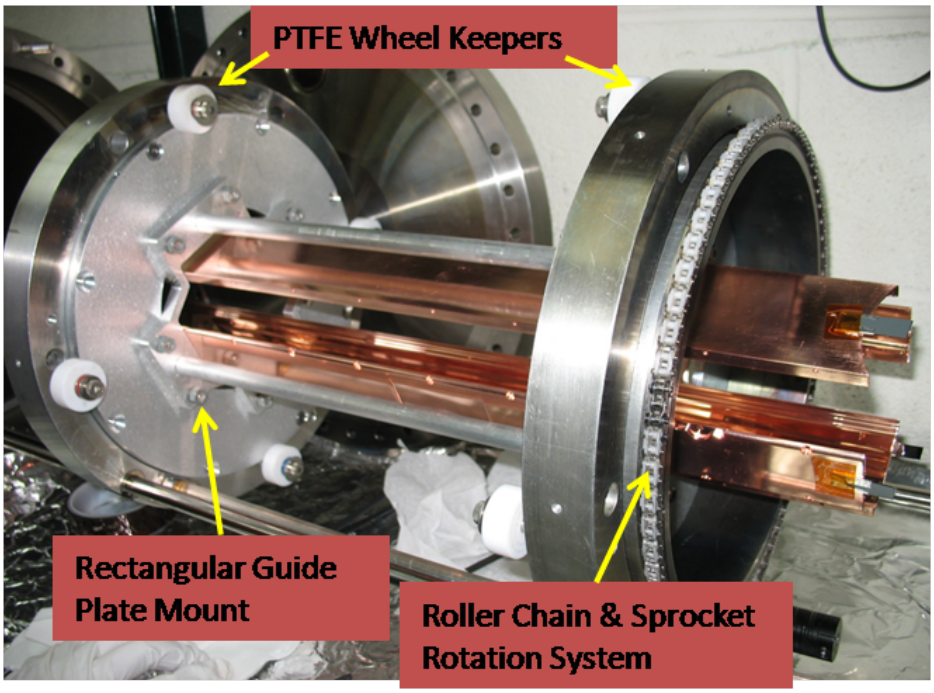

Figure 3.6: Photograph showing the carriage system with the copper plates that make up the rectangular guide in the UCNA beamline.

The standard guide tube drive and rotation settings are 2.6 cm/min and 12 rpm and are provided by a custom stepper motor drive/rotation system outside the vacuum chamber, as shown in figures 3.4 and 3.7. This system rotates and pushes/pulls a precision 1/4 inch diameter stainless steel rod, called the drive rod, through a Conflat to Quick Connect tube flange that provides the vacuum seal. The other end of the rod is connected to the carriage/chain

drive system via a helical rod coupling. Fomblin Y-VAC3® grease is used to reduce the drag from the Quick Connect Viton O-ring as well as improve the vacuum seal during the drive rod motion. The sprocket/chain rotation and stepper motor drive/rotation systems have greatly increased our confidence in these systems. In fact during depositions where heating is not used, the drive/rotation system has never failed, in contrast to the previous internal O-ring rotation and external DC motor drive/rotation systems which routinely failed.

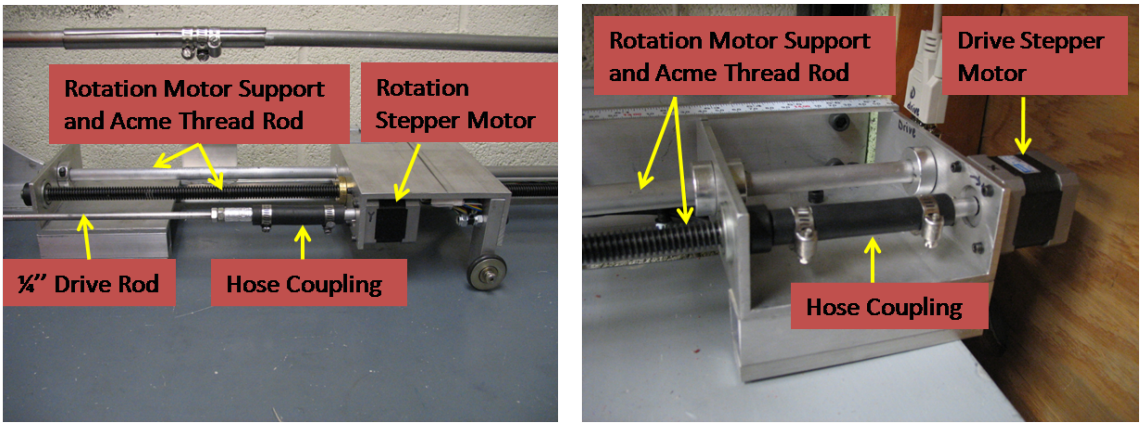

(a) (b)

Figure 3.7: Photographs of the drive/rotation stepper motor system. The high torque NEMA 23Y motors are controlled via a SSXYMicro77 controller. Semi-ridged neoprene hose material couples the shafts together via hose clamps and pins. (a) Rotation motor coupled to the 1/4 inch drive rod. The motor itself is mounted to a section of aluminum U-channel that is supported by an aluminum and acme thread rod. (b) Drive motor coupled to the Acme threaded rod which moves the rotation motor mount.

The system is brought to vacuum via a Varian Turbo V301 Navigator turbo pump (280 L/sec for N_2) backed by a Varian TriScroll 300 dry roughing pump. The Bayard/Alpert ionization and Convectron pressure gauges are located on the opposite end of the chamber as the turbo pump and provide a measure of the highest pressure in the chamber. Depositions usually begin after ∼12 hours of pumping (overnight) at which time the ion gauge reads 2×10^{-6} Torr, and after 3 days of pumping base pressures in the range of 5×10^{-7} Torr are common. In addition, the pressure at the deposition point in the chamber has been

measured, via the installation of an residual gas analyzer (RGA) on the 45° angle port near the center of the chamber, to be about an order of magnitude lower than that indicated by the ion gauge at the other end of the chamber.

3.4 Ebeam Evaporation Systems Used at Virginia Tech

Ebeam evaporation, in contrast to resistive heating, is a much "cooler" thermal process. Here electrons are generated through thermionic emission, usually collimated, and accelerated through an anode held at several kV. These electrons carrying several keV of energy then bombard the source material which is located in a pocket, called a crucible, machined into a water cooled copper hearth. Usually, the source material is placed in a crucible liner which is then placed in the pocket of the copper hearth. A discussion of crucible liners can be found in section 3.5.2. The source material is heated by slowly increasing the current of electrons emitted by the filament, called the filament current (usually measured in mA). In this way refractory source materials and ceramics can be evaporated. Typically, the electron beam is bent 180° and focused into the center of the source material as shown in figure 3.8. Most systems incorporate several pockets which can be linearly translated or rotated so that the focus of the beam hits the center of the source material in each pocket. In addition these systems often include an electromagnet system that rasters the electron beam focus, which prevents a hole from being drilled through the source material. One should note that magnetic source materials maybe be difficult to heat until the Currie temperature is reached, as the magnetic field from the material itself disperses the focus of the beam. For these cases, one should constantly adjust the position of the focus, with minimal raster during the initial ramp of the filament current until the beam becomes stable (i.e. the Currie temperature is reached). In the case of nickel, once the material starts to glow a dull reddish color, the

Currie temperature, 360° C, has been passed. Three ebeam systems were used to provide the ^{58}Ni coatings for UCN source components and will be described in greater detail below.

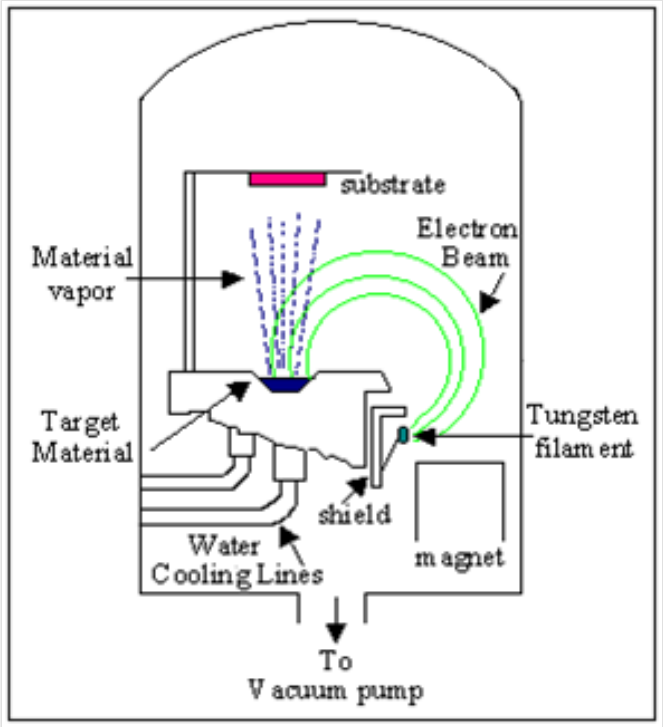

Figure 3.8: Diagram of a typical ebeam evaporation chamber.

3.4.1 Electrical and Computer Engineering Ebeam

The Electrical and Computer Engineering's (ECE) ebeam was used in 2004 and early 2005 to apply ^{58}Ni films on a series of source components (source insert scenario three described in section 6.4.2) when our single-pocket tube coating ebeam, described below, was not working. Shown in figure 3.9, the system is a 24 inch diameter stainless steel bell-jar style refurbished Thermionics coating system that employs a five pocket linear style 3kW (2 cc crucible size) water cooled ebeam system with oscillating raster magnets. Samples are held ∼10 inch away

from the source material via a stationary ring-stand style mount designed to hold several 2 inch diameter Si wafers at a time. Just next to the sample holder is a water cooled crystal deposition rate monitor, which is discussed in section 3.5.1. The chamber is brought to high vacuum ($\sim 2x10^{-6}$ Torr) by a CTI-8 cryopump (1500 L/sec for air) which is backed by a 26 cfm oil-sealed rotary-vane roughing pump. With this chamber, mounting of the components was facilitated via stainless steel wire, office style binding clips, and alligator clips.

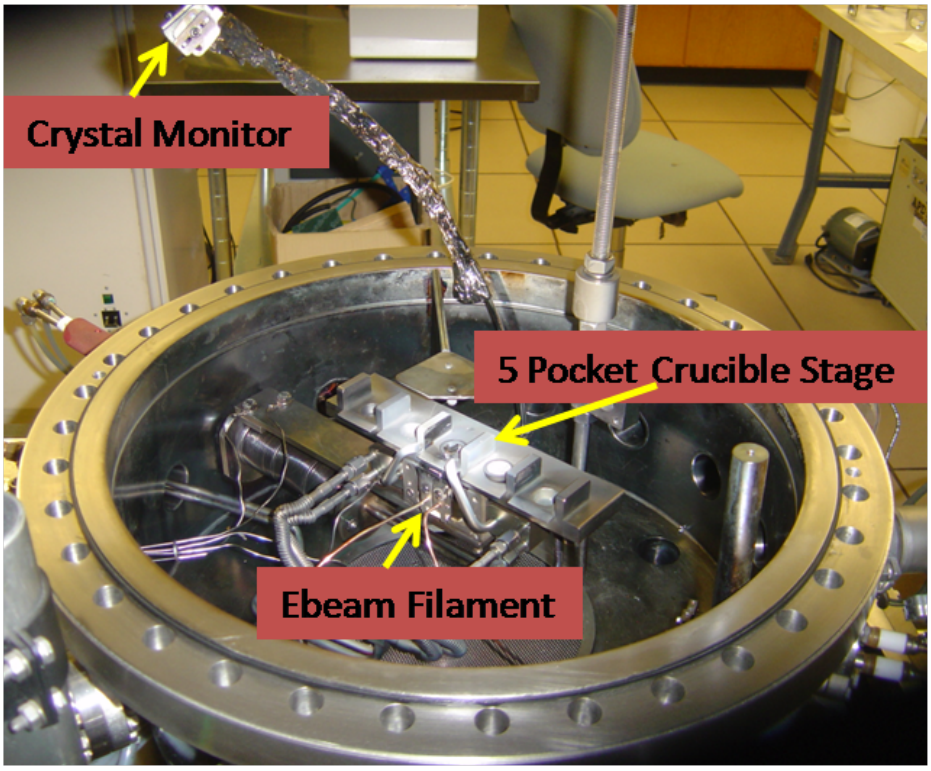

Figure 3.9: Photograph of the ECE ebeam deposition chamber

3.4.2 Physics Department's VE-100 Coater System

The Physics Department obtained a 24 inch diameter stainless steel bell-jar style Thermionics VE-100 Coater system in in the Fall of 2005 and this has been used since to apply the ^{58}Ni

coating to the source insert components (2007 and 2009 source inserts described in section 6. The system boasts a four pocket (2 cc crucible size) rotary style 3 kW (4.2 kV accelerating potential) water-cooled ebeam system with oscillating raster magnets and a 1 inch diameter puck-style water cooled magnetron sputtering system. Samples are held ∼12 inch away from the ebeam source material via a rotating 6 inch diameter plate that can be translated over the ebeam or sputtering target. A water cooled crystal deposition rate monitor is positioned next to the sample holder and one 500 W quartz lamp heater illuminates the sample holder, see figure 3.10. The system is brought to high vacuum ($\sim 1\times10^{-6}$ Torr) by a 520 L/sec turbomolecular pump backed by a 10.6 cfm oil sealed rotary vane roughing pump. A custom mounting plate and clamps have been made to accommodate the variety of shapes and sizes of components to be coated and is shown in figure 3.16. The rotation feature of the sample holder provides a more uniform coating across the 6 inch diameter disks than without rotation, and the use of the quartz heat lamps has become an essential step in providing a well adhered ^{58}Ni coating.

3.4.3 Tube Coating Ebeam

A custom-length ebeam system was purchased in order to apply ^{58}Ni to the ID of tubes in the tube coating chamber. Although this deposition in principle could be done with PLD, the correct laser focus and energy parameters would need to be found, not to mention the difficulty in obtaining ^{58}Ni in a plate form so PLD could be used. Ebeam evaporation on the other hand is a proven evaporation technology and can accommodate wide range of ^{58}Ni forms (plate/pellets/pieces). In addition the ebeam can be used in conjunction with the PLD system to make multilayer coatings, most notably DLC capped ^{58}Ni coated UCN guides. One design constraint is that the ebeam system needed to fit inside of the standard UCNA guide ID of ∼65 mm (OD ∼70 mm). Combined with cost limitations, a single pocket

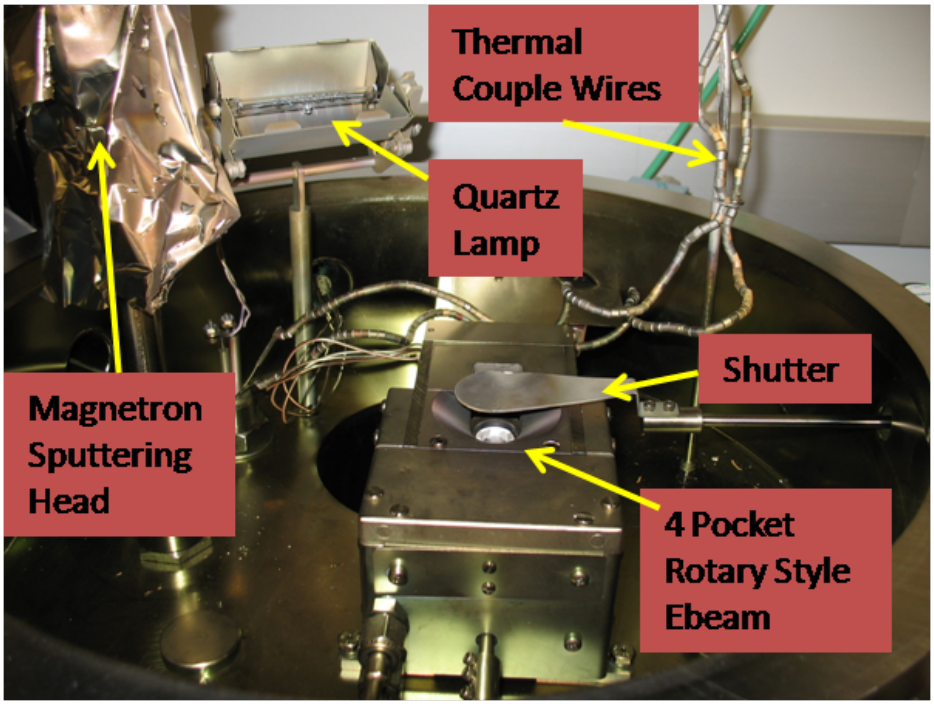

Figure 3.10: Photograph of the Physics Department's VE-100 Coater System

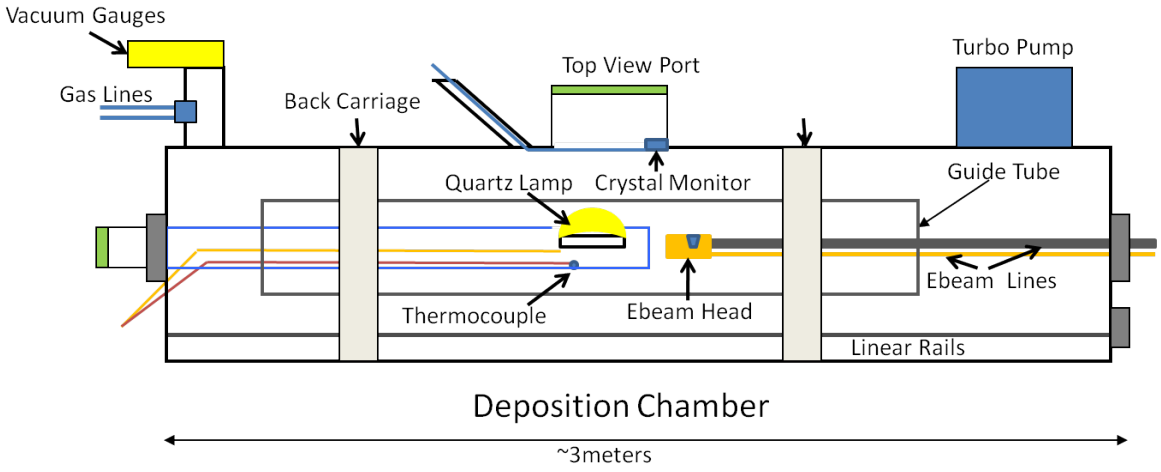

Figure 3.11: Diagram of the tube coating chamber setup for ebeam evaporation.

(2 cc) water cooled 3 kW (4-5 kV accelerating potential) system was chosen from MDC Vacuum Products Inc. The design takes MDC's standard single pocket ebeam deposition gun and increases the length of the support rod and electrical/water cooling lines(see figure

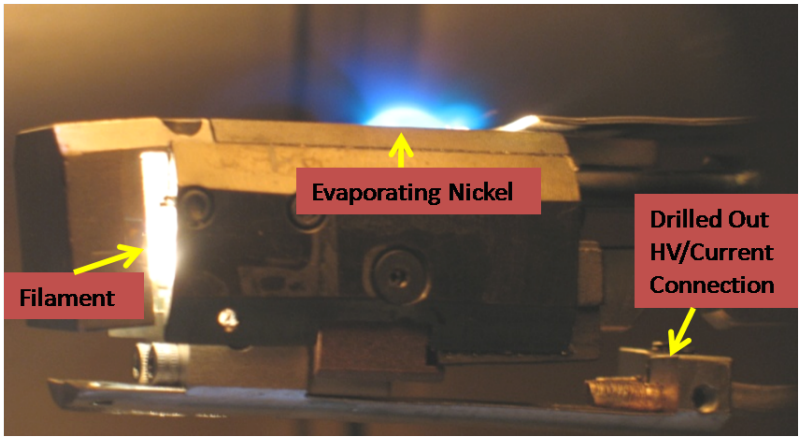

Figure 3.12: Photograph of the ebeam head, during use, of the tube coating chamber ebeam. The faint blue arc is the magnetically guided electron beam emitted by the filament. Here the vapor density of the evaporating nickel is so high that one can see the photoemission of the nickel atoms via electron recombination or excitation. Also shown is the HV lines that are now allowed to expand through the drilled out HV ebeam head connections.

3.13a). The water lines are clamped to the support frame. The electrical lines were threaded through washer-like aluminum oxide insulators. These insulators were supported in stainless steel tubes which were then fastened to the support rod. The system was designed so that the the entire assembly would fit through a 1.5 inch diameter hole (the standard hole in a 2.75 inch Conflat flange) and thus have room for small thermal expansion changes in ebeam head position while in a 65 mm ID tube.

Unfortunately, the expansion of the copper lines, due to heating, seemed to not be properly taken into account. The high voltage/current lines constantly pushed the head of the ebeam vertical (as much as 1 inch) making it impossible for the UCN guide to thread over the source material, as well as pushed against the grounded stainless steel aluminum oxide washer holders, causing a short. This was fixed by the following modifications: completely making our own electrical line insulating holder scheme (as shown in figure 3.14), drilling out the positive stops on the ebeam head HV leads, which allowed the lines to semi-freely expand instead of pushing the ebeam head up, and using a thick O-ring on the flange to adjust the

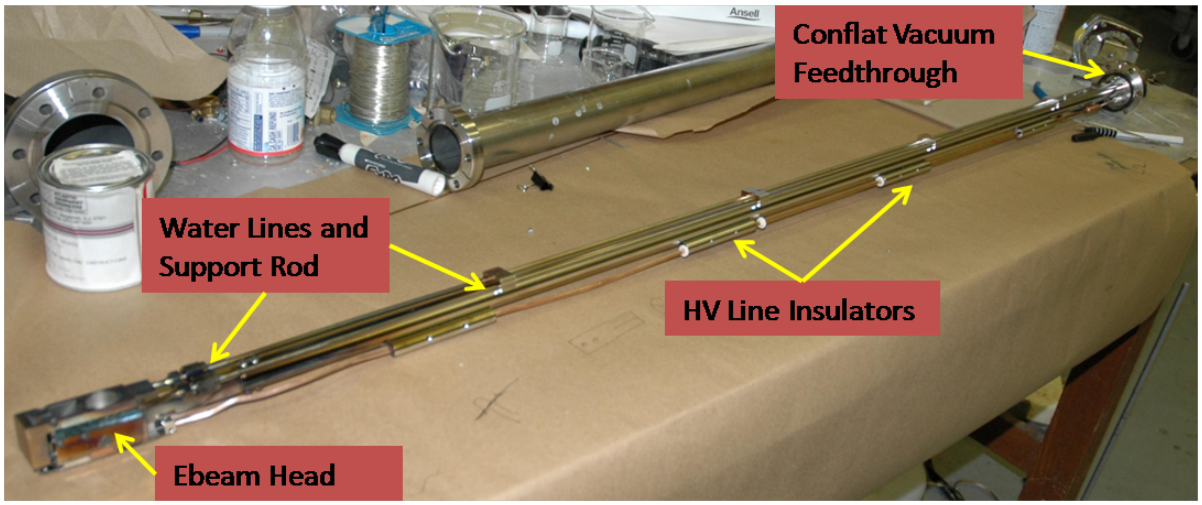

(a) Original tube coating ebeam

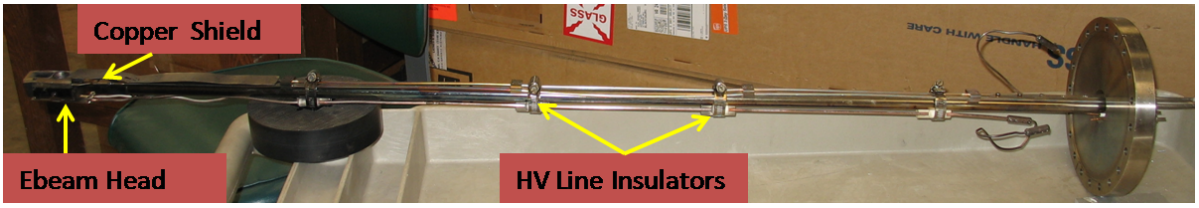

(b) Modified tube coating ebeam to address HV arcing and differential heating issues. The copper shield prevents stray electrons from bombarding the water lines and support rod

Figure 3.13: Photographs of the tube coating ebeam before and after modifications.

position of the head slightly lower than vertical while at room temperature, so that once in use the ebeam head would be relatively horizontal. Beyond this, the HV insulators require cleaning, via sandblasting, to remove the conducting film that built up over time causing arcs to ground. In addition, due to the length of the depositions (several hours) it is unrealistic to expect someone to constantly monitor the power supply and several times the deposition effectively stopped without the operator knowing, thus causing non-uniform thicknesses over coated components as well as extra time. Thus an audible alarm that sounds when the HV has been cut off (i.e. arc to ground detected) has been wired into the HV power supply to alert the user to stop the drive system. Eventually this could be wired directly to the control module to stop the stepper motors, but now with the alarm this is caught very quickly (over

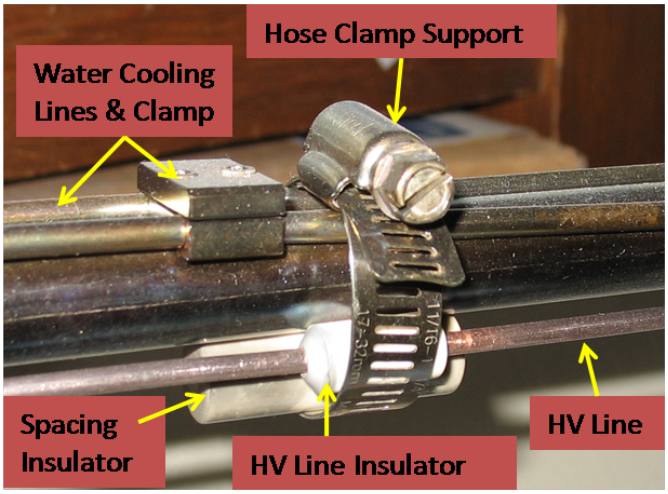

Figure 3.14: Photograph of the modified HV insulation scheme to address the constant arcing issue seen with the original design. Here a hose clamp holds the two HV lines threaded through two ceramic insulators spaced apart by another ceramic insulator.

seconds) and the HV supply only needs to be restarted, without ramping the current, and the deposition continued.

3.5 Quartz Lamp

Ever since the adhesion difficulties encountered with applying ^{58}Ni on the 2007 source components, see chapter 6, a quartz lamp has been used before, during, and after every ebeam deposition. Figure 3.15 shows a photograph of the lamp unit that is held by the target support rod, which is shown in figure 3.11. The quartz tungsten halogen (QTH) lamp emits wavelengths from the ultraviolet (UV) to the near-infrared (NIR) ($\sim$240 nm to $\sim$2700 nm) with the majority of the light in the high visible to NIR range [132]. The lamp heats up the surface, increasing the surface energy, which increases the desorption rate of contaminates, mostly water molecules, on the surface as well as in crevices and pores of the component. In addition, although approximately three orders of magnitude less intense, the UV emis-

sion nonetheless breaks carbon to carbon bonds in long carbonaceous materials, like that of human saliva vapor acquired from breathing near the component) as well has O-H bonds in water molecules [86] [29]. These bonds require ∼4-5 eV to break which is equivalent to ∼250-300 nm. These two processes help to volatilize the contamination on the surface of the components which then has a chance to be pumped out of the vacuum chamber. It is also important to note that the lamp needs to stay on during the deposition as the monolayer formation, of say water, forms very quickly. At 10^{-6} Torr, the monolayer formation is on the order of a second. Only when the pressure (partial pressure) is on the order of 10^{-9} Torr is the deposition time on the same scale of the monolayer formation time (about an hour) [131].

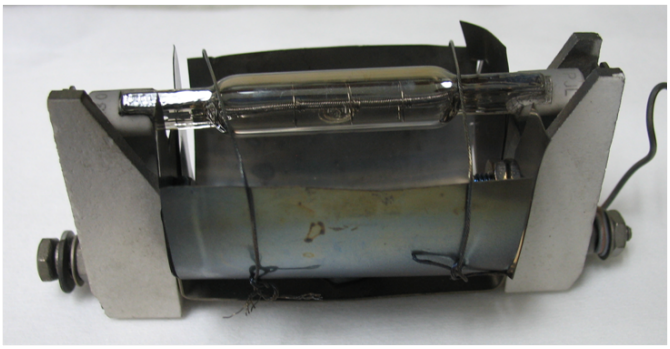

Figure 3.15: Photograph of the quartz lamp installed during ebeam depositions in the Tube Coating Chamber. The IR spectrum from the lamp helps the desorb water molecules from the substrate surface which can be pumped away, while the UV region helps break up and desorb organic material which adhered to the substrate during installation in the coating chamber.

3.5.1 Crystal Deposition Rate Monitor

Crystal deposition rate monitors, sometimes called crystal microbalances, measure the deposition rate (usually in Å/sec) and accumulated thickness (usually in kÅ) and are extremely useful for determining the correct deposition settings, i.e. the filament current in ebeam evap-

oration. First developed in the late 1950's and into the 70's, the method involves detecting the frequency change of a quartz piezoelectric crystal driven at a resonant frequency, usually 6 MHz, as the thickness of the material changes from the accumulation of the deposited thin film. This was first described by the Sauerbrey Equation [151] 3.1.

$$\Delta f = -\frac{2f_o^2}{\sqrt{\rho_q \mu_q}} \frac{\Delta m}{A} \tag{3.1}$$

Where f_o is the resonant frequency (Hz), Δf is the frequency change (Hz), Δm is the mass change (g), A is the piezoelectrically active crystal area (cm^2), ρ_q is the density of quartz ($\rho_q = 2.648 g/cm^3$), and μ_q is the shear modulus for AT-cut crystal quartz (AT corresponds to cut angle, 35.25° with respect to the normal, of the crystals edges)($\mu_q = 2.947 \times 10^{11} g/cm \cdot s^2$) from which the thickness of the deposited film can be obtained from $thickness = \Delta m/A \cdot \rho_{film}$.

The change in frequency is directly related to the additional mass of the film depositing on the crystal and is good for frequency changes of less than 2%, as the deposited film is treated as a small increase in the quartz thickness itself. To take the deposited film's properties into account, most crystal monitors employ a Z-matched equation, equation 3.2, which takes into account the acoustic impedance of the film [107].

$$\frac{\Delta m}{A} = \frac{N_q \rho_q}{\pi Z f_c} \tan^{-1}\left(Z \tan\left[\pi \frac{f_o - f_c}{f_o}\right]\right) \quad where \quad Z = \sqrt{\frac{\rho_q \mu_q}{\rho_f \mu_f}} \tag{3.2}$$

Here f_c is the frequency of the coated crystal (Hz), N_q is the frequency constant for AT-cut quartz crystal (1.668×10^{13} Hz·Å), ρ_f is the density of the film, and μ_f is the shear modulus of the film. This is often called the Z ratio, or Z factor, in programing crystal monitors for different films and extends the reliability of the thickness measurements made by the crystal to frequency changes up to 40% of f_o. Thus crystal monitors require at least two inputs, the

density of the film and the Z ratio of the film, both usually assumed to be close to the bulk values (which is not applicable to all films, as in the case of PLD DLC films since the density of the film changes depending on deposition parameters). Sometimes the crystal cannot be mounted in the same relation to the evaporation source as the components. Thus a "tooling" factor is used which to first order is just a geometric $\frac{1}{r^2}$ correction to the differences in the distances from the evaporation source to the crystal and item to be coated. Sometimes this tooling factor includes the $\cos\theta \cdot \cos\phi$ contribution to the solid angle correction, where θ is measured from normal to the evaporating source and ϕ is measured from the normal of the substrate to the straight line connecting the source and substrate, but often this is neglected. This is the case for the two bell-jar style ebeams used as the monitor is placed very close to the substrate holder, see figure 3.16. However, the tooling factor must be taken into account when using the ebeam in the tube coating chamber. In order for the tube carriage to move freely over the evaporating source the crystal monitor is positioned as shown in figure 3.11. For example, the 2009 source insert tube is 3.75 inches away from the source material while the crystal monitor 7 inches away, which leads to a $(7/3)^2 = 348\%$ tooling factor. Due to their robustness and relitvely low cost, crystal rate monitors have become a standard item in modern deposition systems. Other methods exist, such as in-situ ellipsometry, but these are usually reserved for special purpose research and development chambers.

3.5.2 Crucible Liner Choices

Most ebeam source material is placed in a crucible liner instead of of the actual crucible pocket in the copper hearth. This allows the source materials to be easily interchanged between different evaporant materials and helps ensure the purity of the source material itself. Common crucible liner materials are: graphite, aluminum oxide, tungsten, copper, and molybdenum, and the selection depends on the evaporant source material. One should

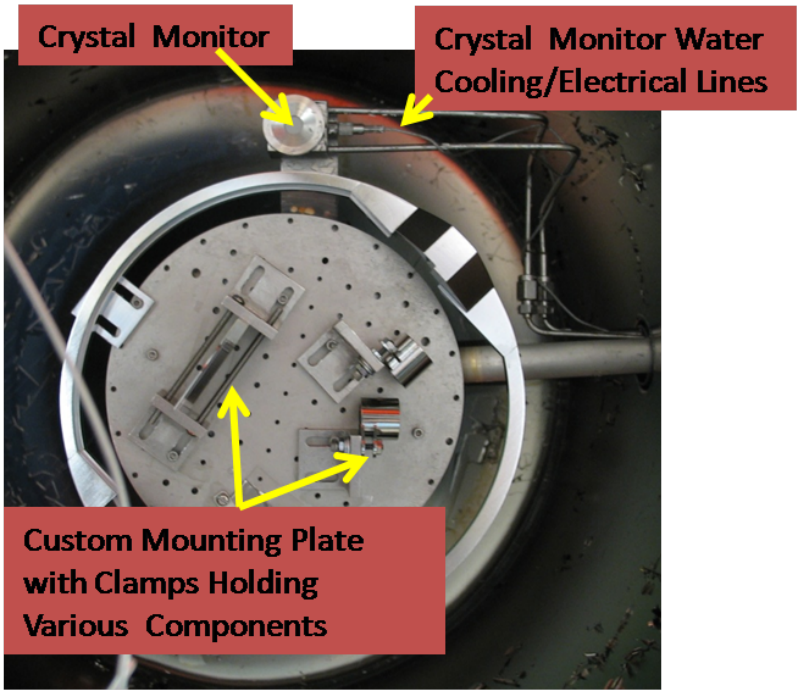

Figure 3.16: Photograph of the substrate holder and crystal rate monitor used in the physics department's bell-jar style ebeam. The monitor is positioned at approximately the same height as the substrate holder.

chose liners that have a much lower vapor pressure at the evaporation temperature than the evaporant as well as those that do not readily alloy with evaporant. In preparation of thin film depositions, one usually "conditions" the new source material/crucible combination by doing a short ebeam deposition without the substrate present. This allows the source material and liner to outgas/clean without contaminating the substrate as well as allows the user to find the approximate filament current settings for the desired deposition rate. For the SD_2 UCN source components we are most concerned with the evaporation of ^{58}Ni , due to its high Fermi Potential , for which graphite crucibles are recommended by ebeam crucible manufacturers.

However, due to our very long coating times, on the order of several hours, the carbon permeates, through convection, the entire nickel source and as the concentration of carbon

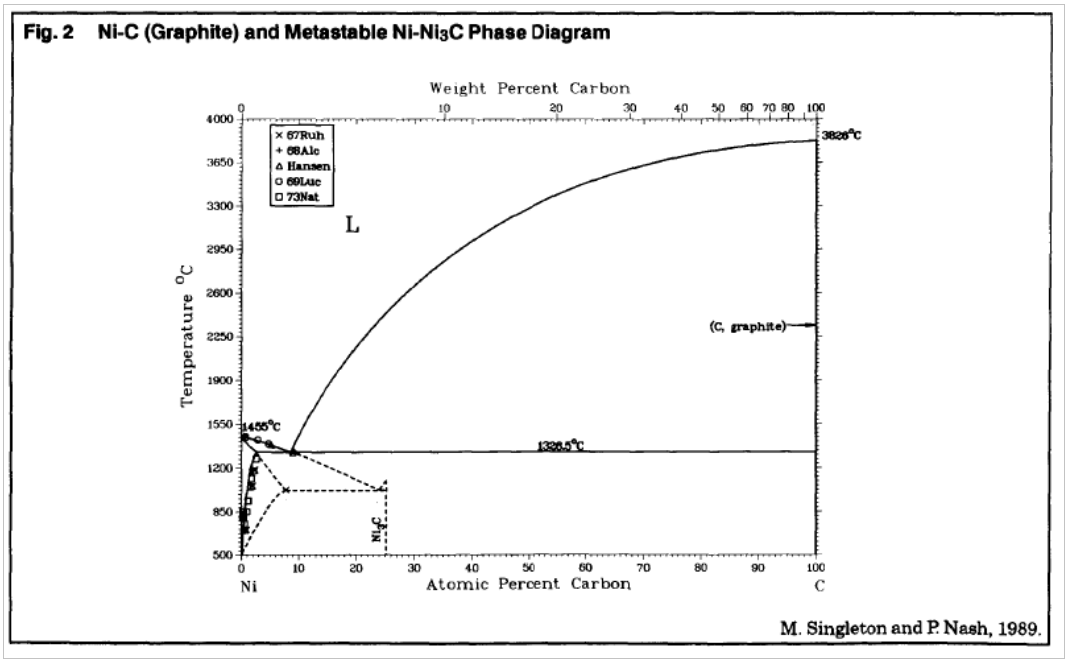

Figure 3.17: Binary phase diagram for the Carbon-Nickel System. Used with permission from Springer (2010) [163].

increases, it takes more and more heat to convert the nickel into the liquid phase (see figure 3.17). With our unrastered tube coating ebeam, a depression in the evaporant source develops, as usual, but over time less and less nickel flows into the depression. Eventually a hole in the ^{58}Ni and sometimes through the bottom of the graphite crucible develops, see figure 3.18a. In practice this hole can be filled by heating the nickel/carbon mixture around the hole with a rastered ebeam, but this only prolongs the life of the crucible in the unrastered ebeam for a short time. One can add more ^{58}Ni material into the hole, but this quickly mixes with the carbon and is really only useful for short deposition times. Since the ^{58}Ni material is very expensive and can be difficult to obtain, one is loathe to make a fresh ^{58}Ni /graphite crucible and so an alternative crucible liner that does not alloy with the nickel and reclamation process was sought.

(a) (b)

Figure 3.18: Comparison of the nickel melts in graphite and alumina crucibles after several ebeam deposition runs. (a) Hole drilled through the ^{58}Ni and graphite crucible. Notice the more crystalline structure indicating Ni_3C carbide formation. (b) ^{58}Ni in an alumina crucible after several depositions. The nickel does not alloy with the alumina, however the alumina crucible does eventually crack from thermal stresses during the deposition process.

3.5.3 Aluminum Oxide Liners and the Reclamation of ^{58}Ni

Aluminum oxide (alumina) is the next liner of choice as it does not easily alloy with nickel and has a couple of orders of magnitude lower vapor pressure than nickel during nickel's evaporation. During the conditioning phase, the nickel will not "wet" to the alumina surface, but will ball up to minimize surface tension. However during long depositions, the alumina surface gets hot enough that this surface tension is overcome and the material "wets" to the surface. Once this happens the alumina will most likely crack due to the stresses arising from the different coefficients of thermal expansion of nickel and alumina. One mediates this by very slowly ramping the ebeam filament current, and thereby temperature, up and down slowly (usually $\sim$5 mA for every 2 minutes), but eventually the crucible will crack, as shown in figure 3.18b. However, since the nickel does not alloy with the alumina, one can easily mechanically separate the two. This is done by squeezing the crucible in a machine shop vice, padded by a cleanroom wipe. The wipe helps prevent vice materials from embedding

into any part of the nickel that may get put back into a new crucible.

This removes the majority of the alumina from the nickel, but thin layers of alumina on the nickel surface may still remain. To completely clean the nickel of the left over alumina, one can use further mechanical techniques (turning on a lathe or sanding), but both these methods could leave embedded material that could end up in the evaporated film. A chemical etching approach was tested where the nickel/alumina was submerged in a Potassium Hydroxide (KOH) ($\sim$30% by weight in H_2O at $\sim$20° C) solution contained in a high density polyethylene container. This solution was chosen based upon etch rates published in [173], where the alumina should react readily with the base, but not at all with the nickel. After submersion for 24hours, no effect on the alumina or nickel was observed. Several other attempts were done at higher solution temperatures up to 100° C, but again the alumina remained attached to the nickel. The etch rates quoted in [173] were concerned with etching thin films of alumina and nickel, and so may not be applicable to bulk versions. In light of this, the sample was submerged in a Hydrofluoric Acid (HF) ($\sim$49% by volume in H_2O at $\sim$20° C) solution for $\sim$24hours, and here the alumina and nickel were both etched as expected. All the alumina was gone and the about $\sim$1/3 of the nickel (by weight) had gone into solution.

Although the alumina was completely removed, at least to the eye, the loss of nickel is unacceptable and the further studies varying the concentration and submersion time (and maybe solution agitation), should be done before the method becomes standard procedure. In practice, the mechanical separation is good enough that the material can be put into a new alumina crucible and reconditioned with the ebeam. Here the previously adhered alumina pieces will not dissolve in the nickel, but rise to the surface of the liquid metal and eventually migrate to the cooler edges of the new crucible. Once this happens the nickel in the center is ready to be deposited. Following this procedure no alumina or aluminum above

has been observed, at least at the ∼1% level, in the ^{58}Ni thin films as measured by Auger Electron and X-ray Photoelectron Spectroscopy on ^{58}Ni coated Si witness strips.

3.5.4 Conditioning Powdered ^{58}Ni for Ebeam Evaporation

Usually ebeam source material (evaporant) is purchased in pellet form, usually 1/8 inch diameter by 1/8 inch long cylinders and is easily obtained. One prefers these cylinders as they have a very low surface area (oxide) to volume ratio and easily fit inside the crucible liners. One wants to minimize the amount of oxide in the source material, as these oxides can cause "spitting" as the oxygen is released during the dissociation of the oxide during the deposition/conditioning process. ^{58}Ni on the other hand is purchased from isotope suppliers and comes in plate, pellet (∼mm^3), and powder forms depending on what the isotope supplier has in stock. Due to the low demand and high cost for the material, most suppliers do not keep a full stock of each form. In addition, depending on market conditions, suppliers resist commissioning new isotope separation runs, and so the end user is stuck with what the supplier has in stock. Fortunately, we have been able to obtain either pellet or plate form ^{58}Ni most of the time. However in 2006 only several grams of powder form were available, which motivated a series of tests to determine how to condition the powder for use in an ebeam evaporator. The difficulty with powder, and especially nickel powder, is that the powder tends to fly out of the crucible during conditioning with the ebeam. Firstly, the powder is attracted to the permanent field shaping magnets used in an ebeam and second the powder charges up, being coated in a semiconducting oxide, and electrostatic forces push the particles apart. Thus some other method of conditioning is recommended (usually required) when dealing with powder source material.

In light of this, we attempted to melt natural nickel powders of various mesh sizes using a

(a) (b) (c)

Figure 3.19: Attempting to melt the ^{58}Ni powder with a thermal evaporator: (a) Nickel powder inside a graphite crucible sitting in a tungsten wire heater in a thermal evaporator. (b) The sintered nickel powder ingot after heating in the thermal evaporator. (c) The hole drilled through the sintered pellet with non-rastered tube coating ebeam.

thermal evaporator. Figure 3.19a shows some 500 mesh nickel powder in a graphite crucible in a tungsten wire evaporation source holder in a thermal evaporator system located a the Triangle Universities Nuclear Laboratory. A tungsten wire holder and a crucible evaporation source heater were used to heat of the nickel powder. All these tests ended up sintering the powder, shown in figure 3.19b, as the oxide present on the surface of the nickel grains prevented evaporation. Attempting to melt the sintered powder with the non-rastered tube coating ebeam resulted in drilling a hole through the material (in a similar fashion as done with the Ni_3C material), as shown in 3.19c. However, the grain structure of the material around the hole looks more like solid nickel than the sintered nickel pellets. This material was then installed in the physics department's rastered ebeam system where a successful melt was obtained. As shown in figure 3.20, successful melts were also made from a sintered only crucible as well as with a fresh nickel powder crucible with the rastered ebeam. For every conditioning process, the filament was ramped up very slowly as significant spitting occurred from charge build up and oxygen release from the NiO dissociation. For each setting the spitting was allowed to die down before increasing the filament current again. The ramp rate averaged out to be $\sim$5 mA/2 minutes on the way to a $\sim$150 mA filament current. The three

different preconditioned crucibles had about the same amount of spitting which resulted in about ∼50% mass loss. A 50% loss rate is really unacceptable, given that the material is ∼$500-$1000/gram, and so this method is really only useful as a last resort. This was the case during some of the 2006 source insert coatings. After this initial crisis, the rest of the powder was smelted into ^{58}Ni ingot at Los Alamos National Lab.

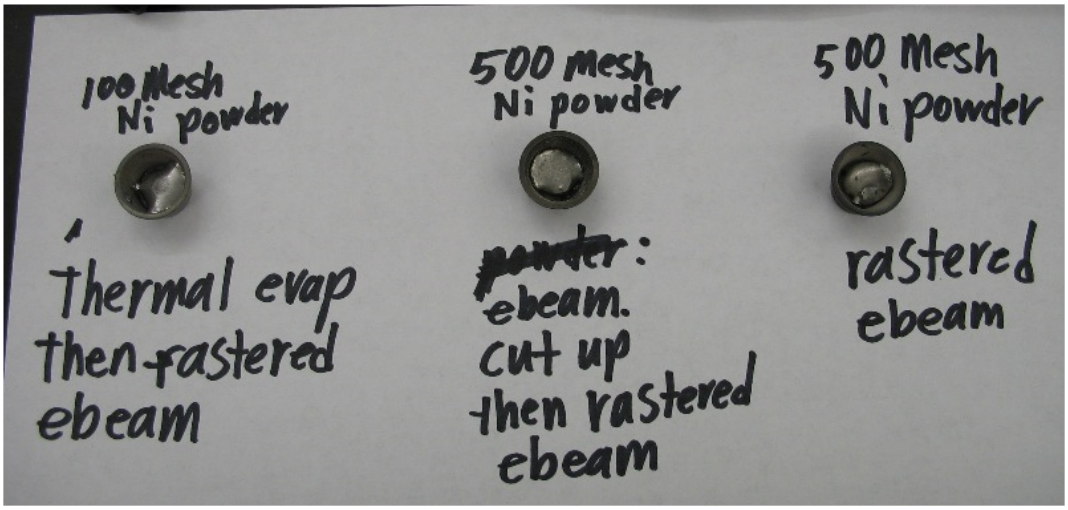

Figure 3.20: Natural nickel ebeam crucible melts resulting from rastered ebeam heating of nickel powders of various mesh sizes and preconditioning

3.6 Pulsed Laser Ablation

The laser ablation process can be conceptualized as a sequence of three coupled steps: laser-target interaction, laser-plume interaction, and ablation plume expansion [10]. The laser-target interaction locally heats the surface of the target to the point of evaporation, generating the initial plasma plume consisting of electrons, target ions and atoms in a variety of cluster sizes (see figure 3.21). The energy of the plasma plume can be further increased by absorption of laser energy via the inverse bremsstrahlung process, depending on the pulse

length and energy density of the laser in question, and from more material being ablated off the target surface. Finally, as the laser pulse ceases, the plasma plume expands outward. During this expansion many different types of processes occur from momentum transfer and ionization, to recombination and radiative de-excitation. Each of these interactions affects the plume species and their kinetic energy.

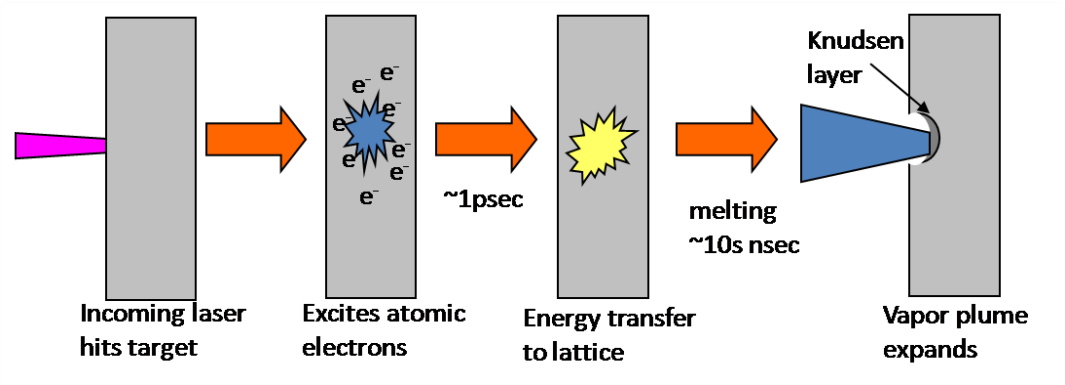

Figure 3.21: Diagram depicting the plasma plume formation for laser pulse lengths on the nanosecond time scale. As the surface layer reaches its evaporation temperature, a so-called Knudsen layer develops between the vaporized material and the target where the density of particles is so high that each particle has undergone 2-3 collisions. It is this layer that couples the heat energy from the plasma plume to the target bulk [174][179].

3.6.1 Plume Formation

When light interacts with materials it primarily couples to the electrons of the material. The electrons then transmit this energy to the atomic lattice of the material and the material begins to heat up. If the laser energy is beyond the threshold for vaporization of the material, then a plasma is initiated. The transmission of energy from the electrons to the lattice occurs on the order of a few picoseconds (see figure 3.21). For pulse lengths above a few picoseconds, heat diffusion and optical absorption play a significant role in how energy is distributed inside the material, leading to subsurface heating and the ejection of large clusters of target

material [174]. For pulse lengths below a few picoseconds, as in the femtosecond laser pulses put out by Ti:sapphire lasers, heat diffusion is insignificant[179] and more of the laser energy goes into plasma creation. This can be further increased if the optical absorption depth approaches the ablation depth, which for most materials implies UV wavelengths. However, as the pulse length decreases, the laser energy per shot decreases and so the threshold for vaporization may not be met. Thus one needs to optimize the laser wavelength, laser pulse length, and pulse energy for the type of plasma plume one wants to form.

For the case of nanosecond long pulse length lasers, as used in the PLD setup for UCN guide coating at Virginia Tech (25 nanosecond/248 nm wavelength), the plasma plume begins to form while the laser energy is still hitting the target. As the plume grows it becomes ionized, primarily from electron-neutral collisions in the Knudsen layer. These electrons then absorb some of the laser energy via inverse bremsstrahlung, thus increasing the mean electron speed in the plume. This increases the frequency of electron-neutral ionization resulting in more light absorption and so the process continues until the laser pulse ends. In this way very energetic plumes, with constituent kinetic energies on the order of 10-100s of eV, can be produced [174].

In the beginning of the plume expansion the density of the electrons, ions, and neutrals is high enough so that the propagation is not collisionless. These ions and neutrals often include clusters of atoms. The ions and electrons are generally moving very fast (high temperatures) from the energy absorbed through the inverse bremsstrahlung process and coulomb repulsion/attraction. If the inverse bremsstrahlung process is efficient, the ionization fraction is high at the start of the plume. The neutrals gain kinetic energy from interactions with these ions and electrons via momentum transfer, ion-electron recombination, and electron transfer between ions and neutrals. These interactions occur as the plume expands outward until the mean free paths of the particles become large enough that the plume can be considered

a collisionless system (in the absence of background gases). At this time the neutrals will have a kinetic energy on the same order as the ions. If however the ion density is not very high at the start of the plume, then the neutral's kinetic energy can be much lower once the plume becomes collisionless. To increase the kinetic energy of the plasma plume one could try to increase the absorption by inverse bremsstrahlung. This may be achieved by ablating at large angles with respect to the target normal; thereby increasing the effective length the light has in the Knudsen layer before reaching the solid target [134]. Indeed our group, motivated by this effect, moved from a 45° angle (with respect to the laser beam) graphite target to a 30° angle target where the DLC coating appeared more diamond like.

Keeping track of every particle and its interaction with the rest of the plasma species is a daunting task which requires large computational power. To address this problem models have been developed that treat the plasma with dynamical gas equations [162][182][179]. In the early 1990's isothermal and adiabatic solutions to these equations were used to describe the expansion of the plasma. Over time the adiabatic solution has become the accepted theory as it correctly accounts for significant temperature gradients inside the plume. Most of these models require sophisticated numerical computations, although in 1993 Anisimov et al. published an analytical solution [8]. One of the interesting features predicted by these models is the how plume spatially expands with forward peaking per equation 3.3

$$n(r,\theta) = \frac{C}{r^2} cos^m \theta \tag{3.3}$$

where C is a constant, r is the distance away from the target, and m is the plume peaking parameter. The value of m can range from two to tens of units depending on the laser and target conditions [8]. An interesting feature of the adiabatic expansion model is how m increases with increasing laser spot size and energy on the target. During the beginning phase of the plume formation the constituents undergo many collisions and these collisions

tend to cancel momentum trajectories parallel with the target while enhancing trajectories normal to the target [57].

3.7 PLD System at Virginia Tech

Every PLD system consists of four key components: a laser, focusing optics, a target, and a substrate. Usually the target and substrate are kept in a vacuum chamber at pressures around several Torr to the ultra high vacuum range depending upon the desired film. The laser and optics (usually) are kept outside the chamber and the beam is allowed to enter through a laser window. A schematic of the PLD system used at Virginia Tech to apply thin films to UCN guides is shown in figure 3.22. In addition to these components some type of target or laser rastering/movement system is employed so that target pitting is minimized.

3.7.1 Excimer Laser

A Lambda Physik, LPX305i excimer laser [24], 50 L non-Nova lasing tube running at 248 nm wavelength with a 25 nanosecond pulse length and located in the Physics Department, provides the laser light energy for the PLD guide coating system at Virginia Tech and is shared with the Material Science and Engineering department through the MicrON initiative. A photograph of the inside of the laser is shown in figure 3.23. A mixture of UHP grade of Kr, F(4%)/He(balance), and Ne (buffer) gases are recirculated through the lasing tube where an electrical discharge pumps the lasing process. Here the excited dimer KrF^*, lifetime $\sim$2.5 ns, decays, via stimulated emission at 248 nm to a repulsive ground state KrF, lifetime $\sim$0.1 ps [110]. The laser tube can also produce light at 193 nm (ArF), 308 nm (XeCl), and 350 nm (XeF) with the appropriate gas mixtures, although the maximum light energy is different

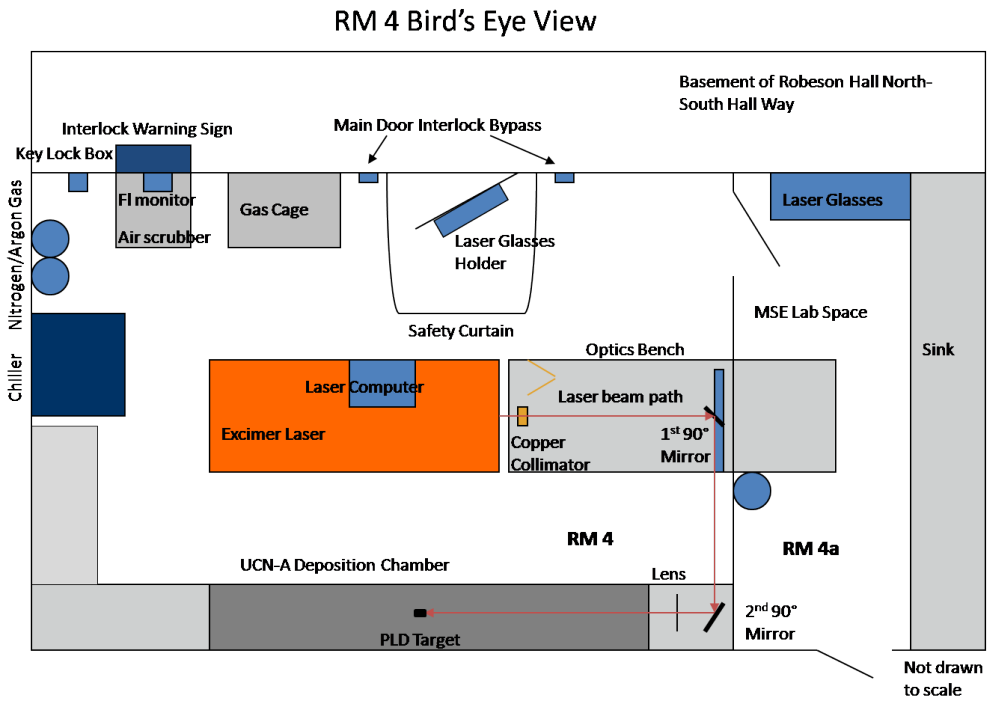

Figure 3.22: Diagram of the laser, optics, deposition chamber housed in RM 4A of Robeson Hall at Virginia Tech.

for each wavlength. For 248 nm, the maxiumum energy is 1.2 J/pulse at 10 Hz and comes in an rectanglular shape, $\sim$ 10 mm by 25 mm. However, the laser has been equiped with "unstable" resonator optics on the ends of the laser tube in an effort to reduce the beam divergence, which without these optics is 1 by 3 mrad, for users whose laser target path length is relatively long. This reduces the maxiumum output of the laser to $\sim$1 J/pulse at 10 Hz. Becuase the fluorine is so reactive with the electrodes and other laser tube materials, the lifetime of the gas is $\sim$2 weeks without use. The lifetime during constant use is dependent upon the laser energy employed, but typically requires refilling about every 12 hours during runs at $\sim$450 mJ/pulse after the copper laser beam collimator, which is discussed in the next section.

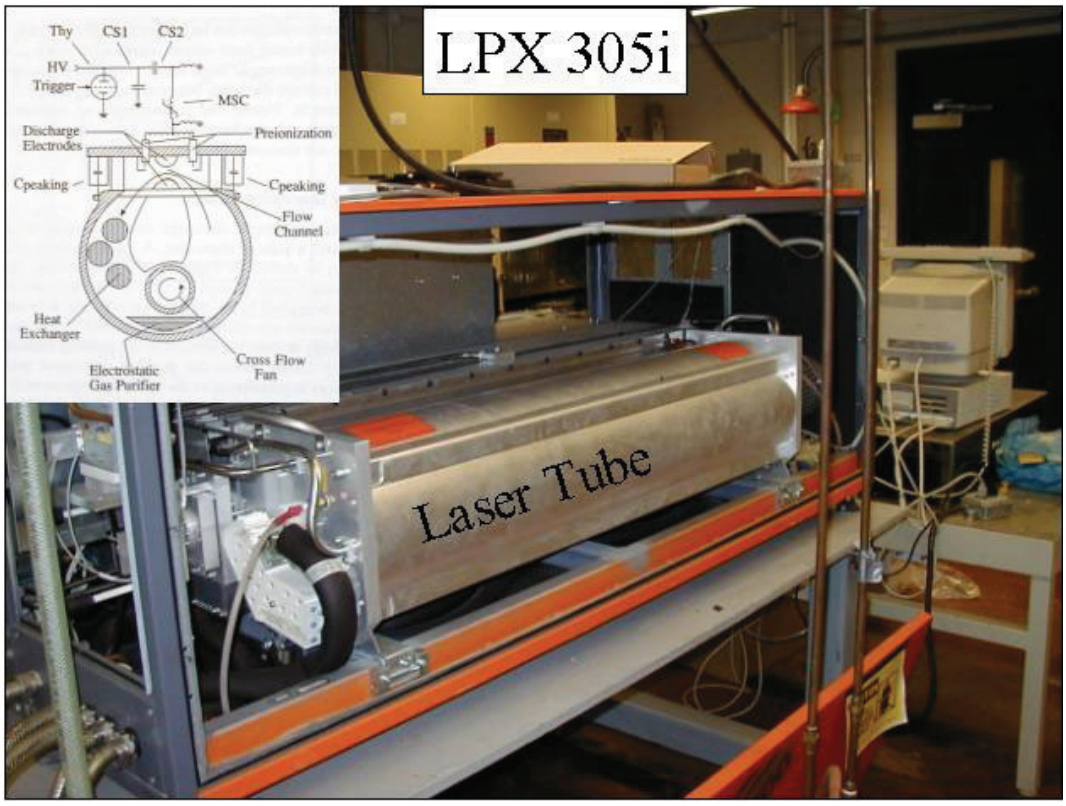

Figure 3.23: Photograph of the LPX 305i laser employed in the UCN guide coating facility at Virginia Tech. The upper left diagram shows the inside of the laser tube. Here Kr,F, and Ne gas is recirculated across the flow channel between two discharge electrodes which once ignited provide the energy required to begin the stimulated 248 nm light emission process of the excited KrF^* molecule. Figure taken with permission from Mark Makela (2010) [110].

3.7.2 Optics

A copper collimator, shown in figure 3.24a with cross section ∼10 mm by ∼25 mm, is located just outside the output end of the laser. This blocks the beam halo around the nominal rectangular 248nm beam and is aligned using flash paper and/or by maximizing the energy after the collimator as measured by a hand held laser power meter (Ophir Nova meter). A lot of energy is lost during this collimation process. Before the collimator the energy is ∼1 J/pulse at 10 Hz and after is ∼600 mJ/pulse at 10 Hz. After the collimator

the beam makes two $\sim 90^{\circ}$ bends before traveling through a 248nm anti-reflection coated fused silica plano convex lens (focal length = 1398 mm from CVI Melles Griot [51]). Various vendors have been used for the mirrors, but Acton Optics [77] mirrors have provided the lowest reflection losses on the order of $\sim$2%, even though every vendor claims less than 1% reflection losses. Once through the lens, the beam is directed through another anti-reflection coated laser vacuum window. Often just the air side is anti-reflection coated as the vacuum side becomes coated with evaporation source material, but both sides can be anti-reflection coated at a slightly higher price which helps the trasmission during the first few hours of after installation. Usually the window needs to be replaced after $\sim$20hours of DLC coating and after a ^{58}Ni tube coating session when one wants to change over to a DLC session (as the ^{58}Ni readily absorbs the 248 nm beam). The converging lens was chosen such that the miniumm beam waist occurs at approximately the center of the deposition chamber. Typical per pulse energy losses (at maxiumum laser energy) through the optics system are approximately: 1J to 600 mJ through the collimator, 600 mJ to 590 mJ from the first mirror, 590 mJ to 525 mJ from the 2nd mirror, 525 mJ to 520 mJ through the lens, 525 mJ to $\sim$ 380mJ through the laser window, where the beam energy fluates on the order of 15 mJ/pulse. These measurements are made by taking laser energy readings before and after each optical element with the laser power meter. One should not subject the power meter to the focused excimer beam as it will burn a hole in the meter head. Thus to make this measurement the converging lens is removed and the meter head positioned at the center of the chamber ($\sim$target location).

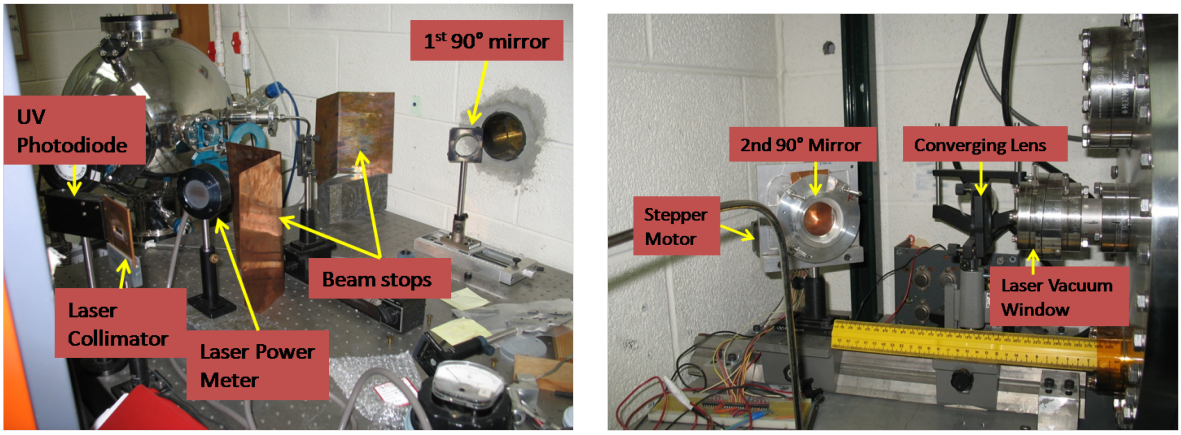

(a) Optics Bench 1.

(b) Optics Bench 2.

Figure 3.24: Photographs of the Optics Bench used during PLD Coating. The ruler shown in figure 3.24b is used to define the lens position.

3.7.3 Tube Coating Deposition Chamber Setups

Figure 3.26 show the chamber setup for PLD. PLD targets can be positioned three different ways, depicted if figure 3.26: 1. Static target placed inside the target support tube. 2. Static target mounted off the load end of the chamber. 3. Movable target via the target rastering system. Methods 1. and 2. raster the laser beam by adjusting the 2nd bend mirror attached to a stepper motor controlled movable mount, see figure 3.24b. Method 2. was developed to enable coating tubes with an ID smaller than 2.5 inches, where the 2 inch OD target support tube is taken out of the chamber and a 0.5 inch one mounted on the load side of the chamber after the guide to be coated is loaded into the chamber, as shown in figure 3.26b. This was specifically designed for the 1.5 inch X 1.5 inch square quartz guide required to penetrate through the SCS and mate with the decay trap guides. Method 3. uses a set of pincers to hold the target which is then controlled by a target raster system. It was developed to better control which parts of the ablation plume hit the substrate. Nominally, a collimator is placed above the target which helps define the energy and cluster size of the plume that hits the

substrate, as the center of the plume contains the highest energy and smallest cluster sizes [174]. This topic is discussed further in chapter 7. When one rasters the laser spot on the target, the solid angle accepted through the collimator changes, where at the edges of the raster pattern the lower energy part of the plume is allowed to hit the substrate, as depicted in figure 3.25. This is not ideal for DLC where the density of the film is highly dependent on the kinetic energy of the plume.

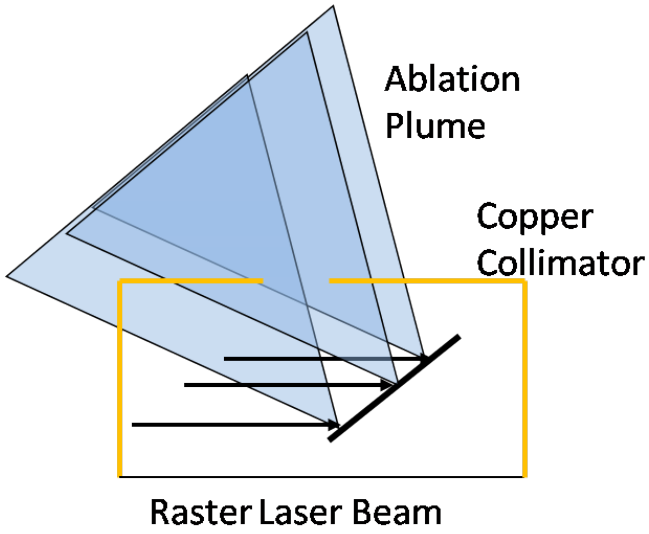

Figure 3.25: Cartoon showing the approximate portions of the plume that make it through the copper collimator as the laser spot is rastered along the target. Thus different plume constituents with different kinematics are allowed to deposit on the substrate. In the case of PLD DLC, this tends to reduce the density of the film resulting in a lower Fermi Potential . If one rasters the target instead of the laser spot, then the solid angle accepted by the collimator stays constant.

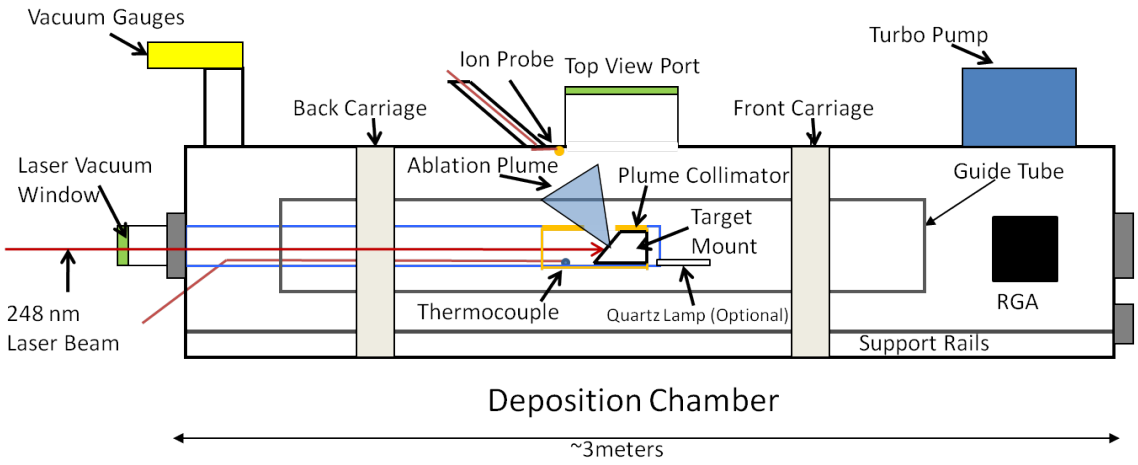

(a) PLD Method 1.

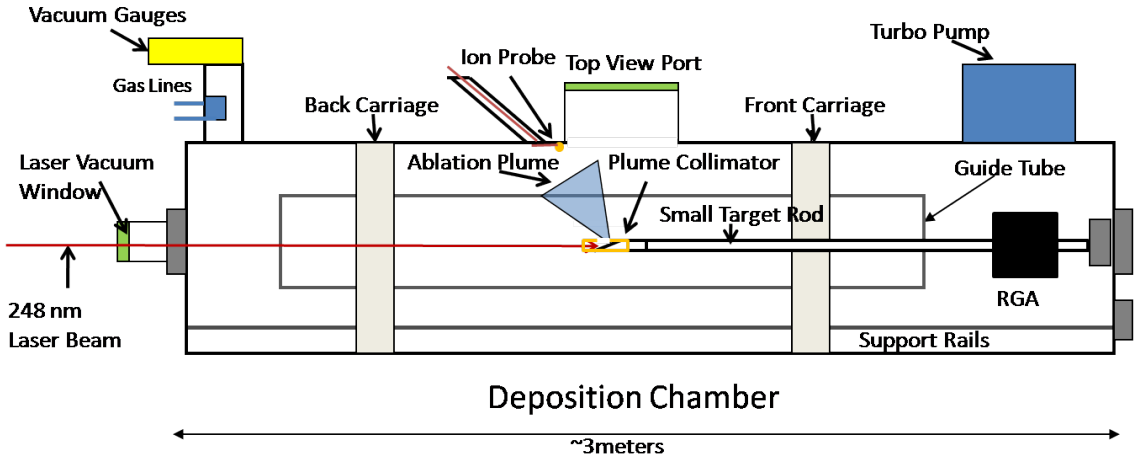

(b) PLD Method 2.

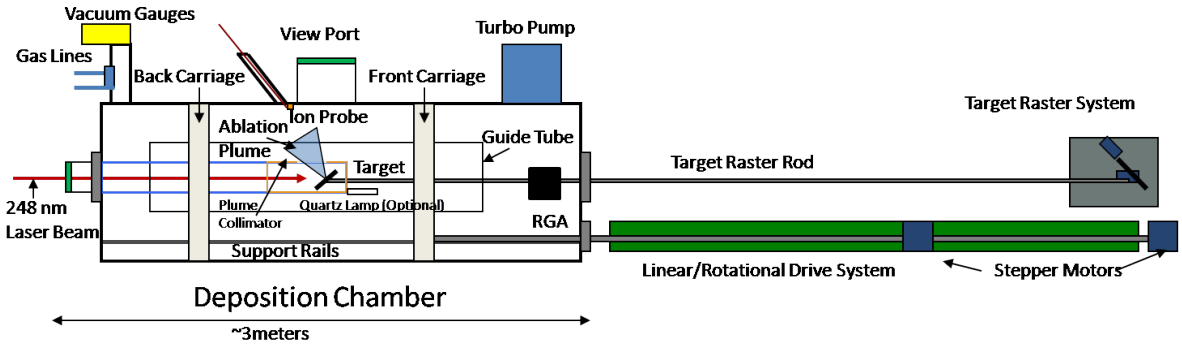

(c) PLD Method 3.

Figure 3.26: PLD methods

If one rasters the target instead, the laser spot and collimator geometry is constant and the accepted sold angle of the plume stays the same. In fact, rastering the target is standard practice for most research and development PLD systems/chambers, but rastering the target in the tube coating chamber is an extraordinary engineering challenge. Here the target is held via a set of spring pincers connected to a tube which is connected to the end of a solid rod. The rod then passes a Quick Connect Viton O-ring seal. Another tube clamps to the air-side of the rod and is connected to the stepper motor driven target raster system shown in figure 3.27. The target is moved in and out and side to side using the O-ring as the see-saw pivot point. The side-to-side motion is provided by a stepper motor controlled rack and pinion system. The end of the target tube is mounted to a miniature linear motion ball bearing slide where the movable section is connected to the rack. This whole side-to-side ensemble is mounted onto the movable carriage of a stepper motor controlled threaded-rod linear slide. This is then mounted to a pivot plate where the angle with respect to the horizontal can be adjusted so that as the carriage moves along the linear slide the target moves up and out, or down and into, the chamber all while still being able to move side to side. The stepper motors are controlled via a BiStep2A controller from Peter Norberg Consulting [130] and an in-house Perl script. Method 3. was designed and installed in the summer of 2006 and has been used ever since for tube IDs 2.6 inches and larger where as UCN guides below this diameter still use method 2.

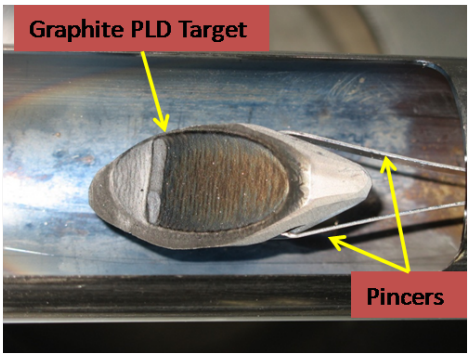

(a) PLD Target with Pincers

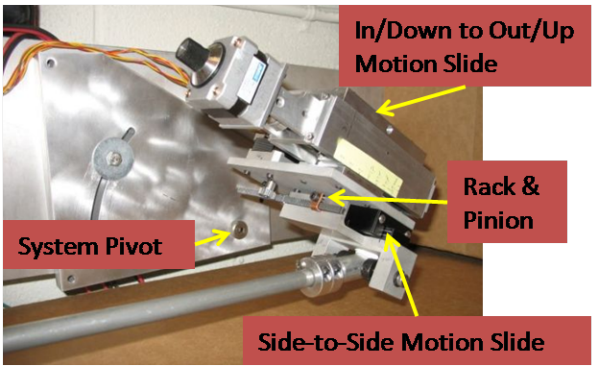

(b) Target Raster Drive System

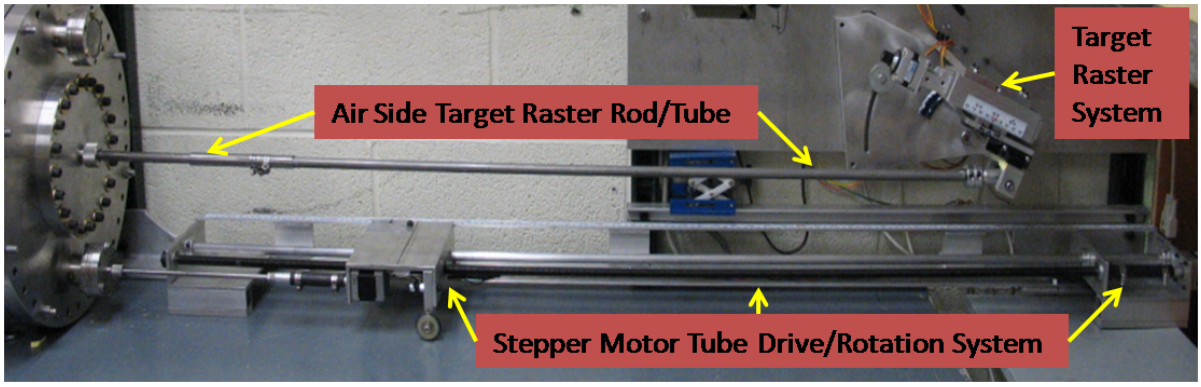

(c) Target Raster Rod

Figure 3.27: PLD Method 3. Target Raster System

Small Disc Components

One down-side with utilizing the target raster system (method 3.) is that the component to be coated needs to be installed before the target installation and alignment. Thus the target needs to be taken out each time a new UCN beamline component is installed for coating. Some of these components are small enough that they can be introduced into the chamber via the top view port, see figure 3.28. This allows quick turn around of components as the target does not need to be realigned after each one. To facilitate this, the view port has been modified with several 7 mm diameter ACE thread Viton O-ring sealed ports. A 1/4

inch diameter rod is pushed through these ports with the item to coated mounted on one end and a DC drive motor/helical rod coupling on the other. The glass ports are situated such that the beamline component intersects the ablation plume and is rotated in order to produce a more uniform coating, shown in figure 3.29. In fact, depending on the size of the component, particular portions of the ablation plume can be selected which can produce different film structures. This was done for some for the copper decay-trap plug and Round to Rectangular Transition plate and will be discussed in chapter 7.

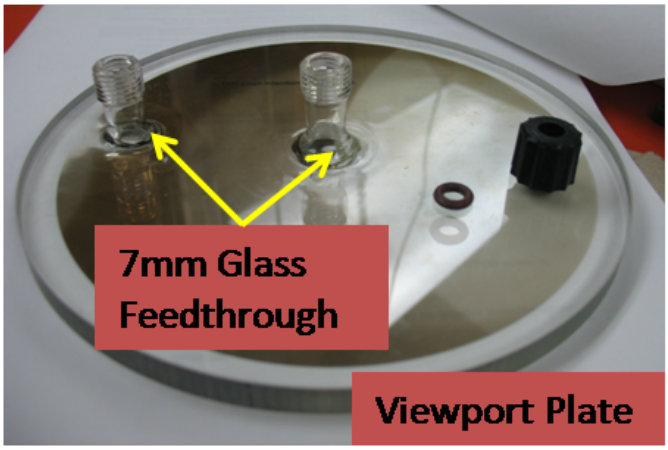

Figure 3.28: Photograph of the view port borosilicate plate (3/8 inch thick) with 7 mm Viton O-ring sealed glass feedthroughs from which components can be manipulated while in vacuum.

3.7.4 Target

Several target designs have been used from 2004-2010. Rastering method 1. and 2. originally used elliptical targets, 1.25 inch diameter x 0.25 inches thick and 0.5 inch diameter x 0.25 inches thick respectively, situated at a 45° angle with respect to laser beam/horizontal in an aluminum mount held via a set screw. These targets require professional machining, which causes concern that contaminants from cutting tools/fluids/handling could end up being

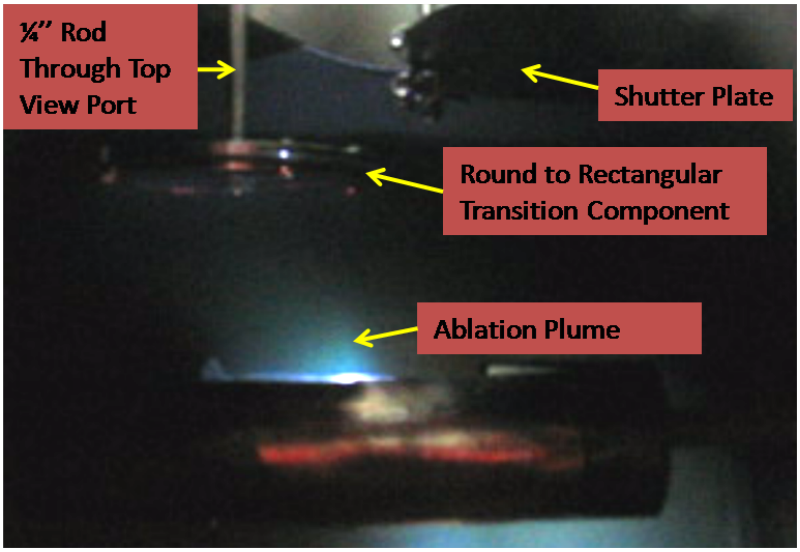

Figure 3.29: Photograph of the deposition process for coating the Round to Rectangular Transition plate that connects the round guides to the rectangular guide that feeds the decay trap held inside the SCS. The shutter plate is used to block the component from being coated during laser cleaning of the target.

deposited with the target material, despite target cleaning efforts. To address this concern as well as shorten the target production time, mounts requiring rectangular shaped targets were made which allow one to make targets without sophisticated cutting tools. Here 45° aluminum mounts as well as 30° copper mounts were made. The target mount material was changed from aluminum to copper for three reasons: if there was a laser beam excursion off the target we would rather have the higher Fermi Potential of copper than that of aluminum, see table 1.1, copper absorbs more of the 248nm light than aluminum (63% versus 8% [110]) thus reducing stray 248nm light from hitting other parts of the SS chamber which could release ferromagnetic elements into the chamber atmosphere which could end up ahereing to a UCN guide, and finally copper has a higher heat capacity which would help keep the target cooler than an aluminum version. Figure 3.30a shows the target mounts for Method 1. and 2. Method 3. utilizes an octagonal shaped target with groove slots milled into the thickness to accommodate holding via a set of pincers. A picture of the final product is shown in

figure 3.30b. The original pincers were made out of spring steel. While these worked well at holding the target, they introduced a highly ferromagnetic material close to the ablation region. These were later replaced with brass versions, which removed the ferromagnetic materials but also reduced the holding effectiveness of the pincer. Beryllium copper versions are currently being pursued which should solve this issue.

After the target have been machined they are wiped clean with Ethanol, ultrasonic cleaned in DI water for about 5 mins, rinsed with DI, and allowed to dry overnight. After being used for a PLD coating session, the target can be resurfaced in the following way: sand the the front surface flat using 600 grit SiC sandpaper, coarser grits can be used but it is easy to over sand wasting the target material, rinse the target in DI water, ultrasonic clean the target in DI water for 5 mins, the water will be become dark gray with carbon particulate, replace the DI water, and ultrasonic clean the target in the fresh water for another 5 mins. The ultrasonic cleaning action removes the most of the carbon particulate embedded during the sanding process, leaving a surface that looks the same as a fresh unused target. With the 0.25 inch thick targets, this process can be used up two two times when coating meter long guides before having to be replaced.

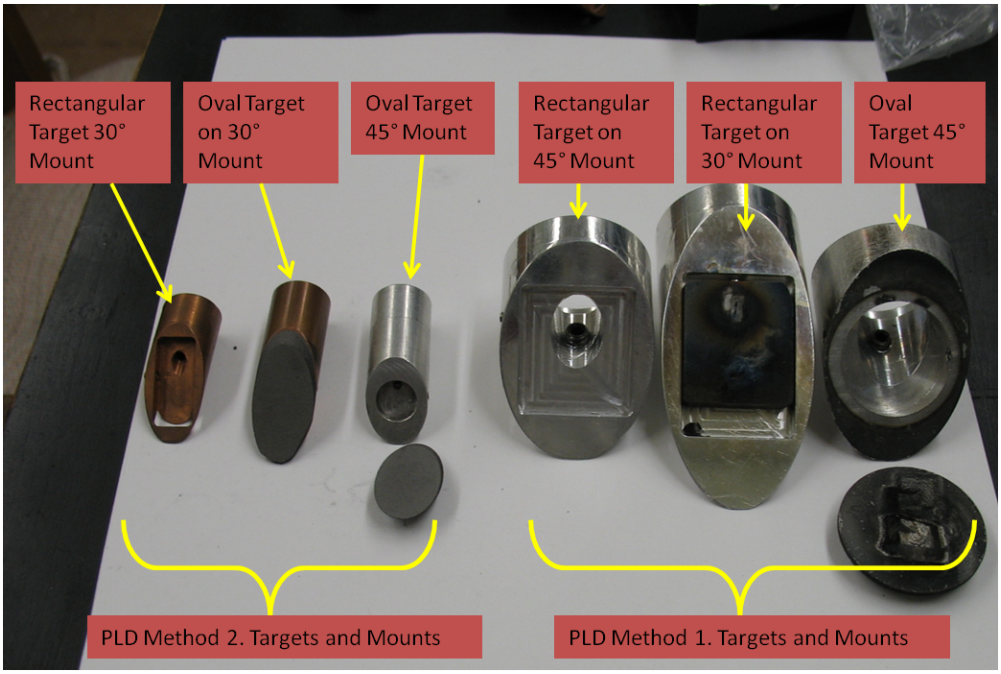

(a) PLD Method 1. and 2. Target Mounts

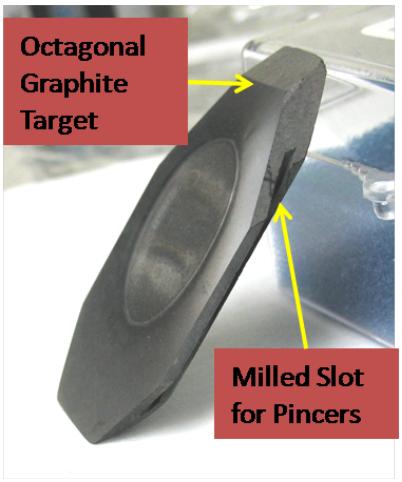

(b) PLD Method 3. Target

Figure 3.30: Target Mounts for the three different PLD setups.

3.7.5 TOF Ion Probe

The TOF ion probe, often called a Langmuir probe, is a simple device that is used to monitor the PLD process [134] [57] [116]. Often the probe is used to measure the plasma potential, electron temperature, electron density, and ion density of the steady state plasmas [99], but we use it to measure the C^+ kinetic energy in our carbon ablation plumes as done in [144]. The standard tip style used is a 4 mm diameter copper disc. This disc is located 85° with respect to the target plane, see figure 3.26, and Kapton taped to the top of the chamber. Kapton coated vacuum wire is soldered to the disc and run out to an MHV feedthrough. Figure 3.31 shows the circuit employed, which is monitored with an oscilloscope. Applying a negative bias to the disc allows one to monitor the ion current of the plume, most notably the ion kinetic energy of the dominant ion species. This can be done by using the laser pulse itself, measured via a UV photodiode, as the start time. The time corresponding to the peak of the positive voltage signal, as seen on an oscilloscope, is used as the stop time, see figure 3.32. Then a velocity is formed using the measured distance and the measured δT between the laser pulse and the time of the ion peak. One can include the estimated time for the light to travel to the target, but this is ∼13 ns and negligible as the plume time scale is on the order of microseconds. Then, assuming a certain mass species, on can calculate the kinetic energy. Usually a bias of -3 V is used during normal monitoring. The probe offers a powerful in situ diagnostic to monitor the ablation plume over the course of a deposition. For example, numerous authors have found that the highest density DLC is formed when the carbon ion energy is ∼100 eV [148]. Thus it is extremely important to adjust the the laser energy to obtain this ion kinetic energy and keep it there during the entire coating run. However the laser vacuum window gets coated during this time which absorbs some of the laser energy, thus reducing the amount of laser energy hitting the target which reduces the carbon ion kinetic energy of the plume. By routinely measuring the carbon ion energy

during a coating run, the laser energy can be increased to compensate for this effect. At the very least, the probe provides a baseline from which plasma conditions can be compared to coating structure/properties that is reproducible.

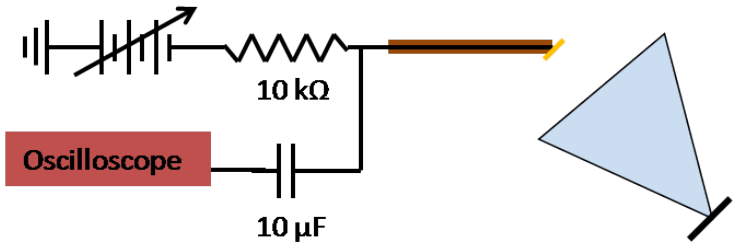

Figure 3.31: Ion probe circuit diagram.

3.7.6 Auxiliary Chamber Components

Residual Gas Analyzer

Sometimes an Extorr 200amu (with electron multiplier) Residual Gas Analyzer (RGA) is mounted off an unused 2.75 inch port, to monitor the gas species in the chamber. Here thermionic electrons are accelerated across a small gap inside the RGA head. Chamber gas atoms in their path have a probability of being "cracked"/ionized, which is a function of gas species and their pressure/density. The process is identical to how a Bayard-Alpert (B/A) hot filament ion gauge works. These ions are then attracted to a quadrapole mass filter that guides a particular mass group of ions toward a Faraday cup/or toward an electron multiplier that converts one ion into an avalanche of electrons thereby increasing the signal generated by that single ion [41]. With the electron multiplier partial pressures on the order of 10^{-14} Torr can be resolved. Although usually located far away from the ablation plume itself, a peak at the evaporants mass can be seen, which is expected as not all of the evaporant

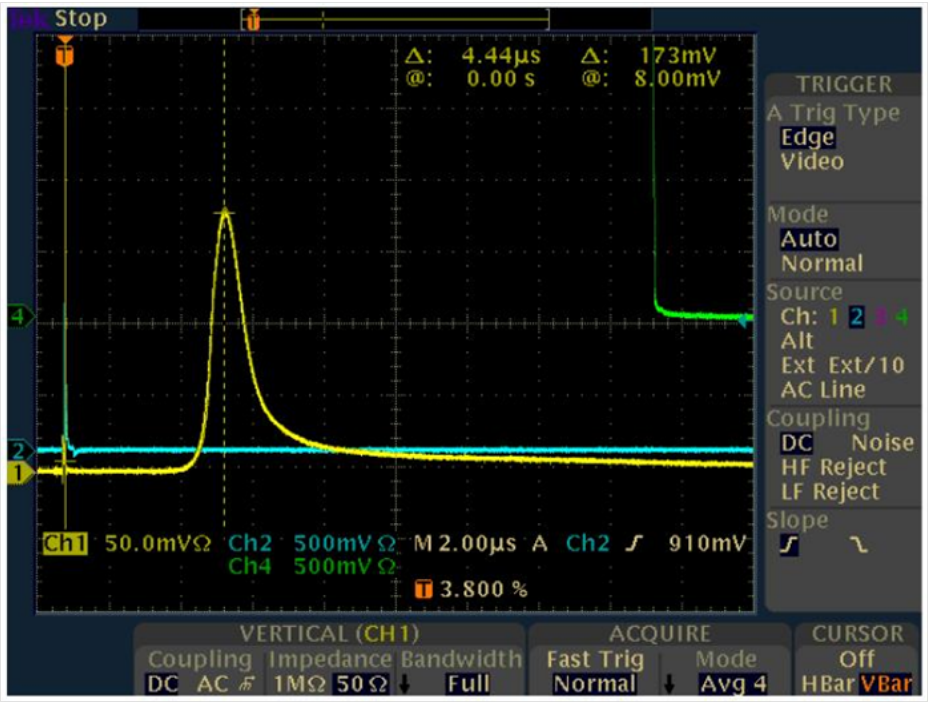

Figure 3.32: View of the Oscilloscope measuring the ion current during a PLD DLC deposition. Channel 1. (yellow) is the signal measured from the probe (biased at -3 V). Channel 2. (blue) is the signal from the UV Photodiode which is physically located next to the laser beam collimator, see figure 3.24a. Channel 4 (green) is the TTL pulse put out by the laser. A ΔT is formed between the photodiode signal and the peak of the ion probe signal. Combined with the measured PLD target to probe distance one can calculate the velocity of the ions hitting the probe. Notice there is a small peak in channel one overlapping the photodiode signal. This signal arises from target reflected 248 nm light releasing some electrons from the ion probe via the photoelectric effect. This can be used as an alternative start time instead of the UV Photodiode.

species adheres to the substrate or chamber/chamber components. The is useful in tracking the evolution of gas species during a coating run. For example one can look for Fomblin grease break down and/or air leakage into the chamber from the operation of the drive rod.

Quartz Lamp

The quartz lamp used during ebeam evaporation cannot be used during a PLD run as it will be in the way of the laser beam, target, or target raster support tube. Although high density DLC is made when the substrate is close to room temperature, see chapter 7, the quartz lamp can be used to clean the substrate before deposition (one just needs to wait for the tube to cool down) and should be very useful for helping PLD metal films adhere to the tube substrate. To provide this option, a miniature quartz lamp was built so that it could be mounted underneath the target raster tube and still not obstruct the path of a 2.6 inch ID guide tube, as shown in figure 3.33.

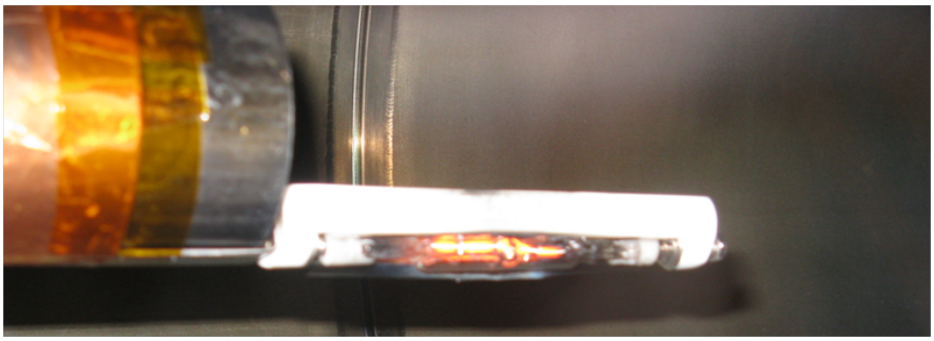

Figure 3.33: Photograph of the low profile quartz lamp for use with 2.6 inch ID tubes and larger.

Thermocouples

Two type K thermocouples are mounted inside the chamber. One thermocouple, named the Internal Thermocouple (ITC), runs along the inside of the target support tube and is situated to measure the temperature either inside the target support tube or positioned to measure the temperature just outside of the target support tube via a small hole. This provides a lower bound to the temperature of the target or the temperature of the guide

itself as the guide threads over it. The other thermocouple is located at the bottom of the chamber where the wires are held by Kapton tape to the walls of the chamber in order to prevent getting caught as the carriage translates back and forth.

Crystal Monitor

The crystal monitor has not been used to date to monitor PLD depositions in the tube coating chamber. In principle the monitor could be used to monitor our PLD depositions, however density and Z factor calibrations would need to be done for each film, as these factors could be very different than their standard values for PLD films. This is especially true for DLC films. In addition, significant modification to the tube coating chamber and/or ebeam water lines would be required to position the crystal face in view of the ablation plume without obstructing the motion of the carriage system.

3.8 Summary

Virginia Tech is responsible for providing the thin film coated beamline components for the LANL SD_2 UCN source and UCNA beamline. This includes coating the surface of a variety of machined components as well as the inner diameter of UCN guide tubes. To accomplish this task, ebeam evaporation and PLD techniques are employed and a custom tube coating vacuum chamber with a specialized carriage system that can linearly translate and rotate UCN guide substrates over a deposition source has been developed. This system has been upgraded to employ an in-vacuum sprocket/chain rotation system and an air-side stepper motor drive/rotation system, which has greatly improved the reliability of the system. Here PVD processes, ebeam evaporation and PLD are employed.

Ebeam evaporation is the method used to apply the required ^{58}Ni thin films on all the UCN source components. This has primarily been accomplished through the use of our custom-length tube coating ebeam and the physics department's VE-100 bell-jar style ebeam system. Here thermionic electrons are emitted from a tungsten filament, collimated, accelerated, and focused to bombard, and thereby heat up, an evaporant source material. While the VE-100 coater system has been mostly a "turn key" tool, the custom-length tube coating ebeam required significant modifications in order to consistently operate smoothly. The use of a quartz heat lamp and crystal rate monitor have been found to be essential for producing a well adhered ^{58}Ni coating on the UCN source components and are now both installed and operated during every ebeam deposition (section 6.5 discusses the evolution of these discoveries in detail). In addition, during the long coating sessions required by the UCN source components, graphite crucible material began to alloy with the ^{58}Ni source material allowing the ebeam to drill holes through the crucible. This effectively stopped the use of the crucible, as well prevented the relatively easy reclamation of the very expensive nickel, and motivated a new choice of crucible material, Al_2O_3, which allowed the ^{58}Ni to be reclaimed after several coating runs. Also, a method to prepare nickel ebeam crucibles from powder source materials was established, in the event that ingot, plate, or pellet form ^{58}Ni are not available.

PLD is the method used to apply the DLC thin films on the UCNA beamline components, most notably the components in the depolarization region of the experiment. Here a 248 nm, 25 ns pulse length laser beam is focused onto a graphite target vaporizing a very small part of the target material. A very energetic plasma plume composed of ions, electrons, neutrals, and clusters ablate off the target surface and interacts with the desired substrate. The highest energy and smallest cluster species tend to be closer to the center of the plume (i.e. normal to the target surface) and so the plume often is collimated to accept or reject the different

species. To prevent drilling a hole through the target, the laser or the target is rastered and both methods have been developed. Rastering the laser beam, although technically easier, allows different portions of the plume to pass through the collimator, while rastering the target prevents this, as the laser spot/collimator geometry is constant. PLD methods 1. and 2. utilize a motorized mirror to move the laser spot, while PLD method 3. employs a motorized target system. An ion probe has been installed to monitor the collimated plume during depositions and has become an invaluable tool for improving the reproducibility of the films on the many UCN guides.

Chapter 4

Surface Analysis Equipment

4.1 Surface Characterization

After a coating has been applied it is critical to perform quality-control checks to ensure the film has all the features it needs for its intended application. For example every UCN guide coating needs to be 150 nm or more thick and a very low level of foreign elements, especially ferromagnetic materials, on the surface as well as throughout the film. In addition, the surface topology of the film affects how UCN transport along the guide and so this needs to be characterized. In the case of our DLC films an estimate on the diamond likeness is useful in estimating the Fermi Potential of the coating, which is very influential to the ultimate beta-decay rate seen in the experiment. Unfortunately, surface testing of each beamline component is often not an option as the size of the component is too large or the test is destructive to the coating. Thus 1 cm by 2 cm long witness strips are included in every coating session which can later be analyzed by several surface science techniques. Often these witness strips are cut from undoped $< 100 >$ silicon wafers, but occasionally they are

made from electropolished copper and stainless steel plates. With this in mind, this chapter is devoted to introducing the reader to the techniques used to analyze these witness strips which provides valuable information as to the composition and quality of the film on the actual UCN beamline component.

4.2 Stylus Profilometry

Physical thickness measurements are made by measuring the step height between a coated and uncoated region of a witness strip. A portion of each witness strip is tightly wrapped in aluminum foil and positioned during the coating session so that a 1 cm^2 area is coated along with some of the aluminum foil. After the coating the foil is removed, providing a thickness step that can be measured by a stylus profilometer. A Dektak 3® stylus profilometer by Veeco Instruments has been used up until early 2010, when the physics department purchased its own Dektak 150+® stylus profilometer. Both systems utilize a diamond tipped stylus, 2.5 micron radius, to float along the surface of the sample to be scanned. The stage is manually leveled by scanning the uncoated section of the silicon witness strip and then correcting for the tilt as much as possible before scanning over the silicon/coating step height; the rest of the tilt is leveled out in software. Silicon witness strips are almost always used for this measurement as the copper or stainless steel versions have too much curvature to provide a reliable level from which to measure the step height. Figure 4.1 shows an example scan taken from the Dektak 3 tool. Three regions of the step height are scanned and averaged together, which can be accomplished in about 15 min. These measurements have become a valuable tool in determining when to stop a deposition. Once the expected thickness has been reached, the chamber is vented, usually with Argon, and a witness strip pulled for a thickness measurement on the profilometer, before completely taking the component out.

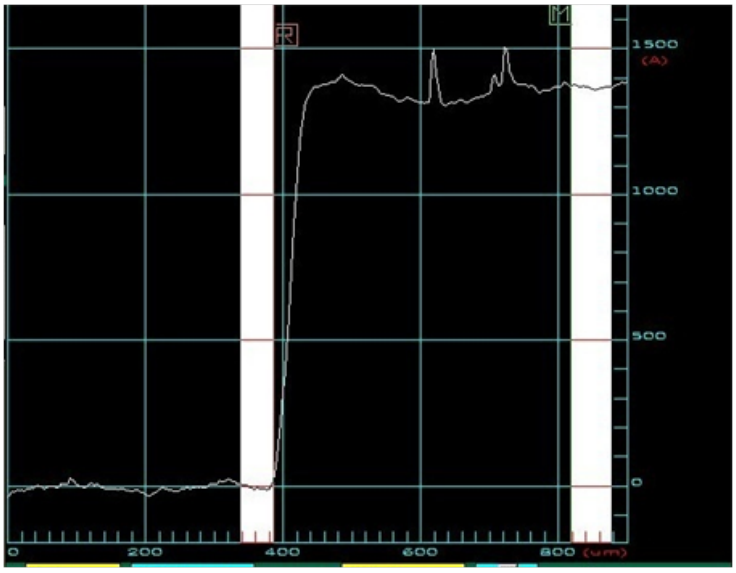

Figure 4.1: Example Dektak 3 profilometer trace measuring the step height of one of our DLC coated witness strips. The "R" (reference) and "M" (measurement) bands correspond to what regions of the scan the software uses to calculate the average surface height.

Figure 4.2: Example Perthometer M4P trace measuring the surface roughness of one of our copper guides before electropolishing.

In the industrial polishing business the surface roughness is usually measured by an industrial profilometer. Similar to the Dektak profilometer this is a portable, lower resolution version that can be laid inside the ID of our UCN guide tubes where a stylus is then scanned along the surface. The polishing company we nominally employ, Irving Polishing [143], uses a 5 micron radius diamond tipped Perthometer M4P® stylus profilometer. Figure 4.2 shows an example scan from the Perthometer M4P. The stylus force is 0.8 mN, the vertical resolution

is 2 μinch (50 nm), and the usual scan length is 0.2 inches (where 0.03 inches of this length is cut off at the beginning and end of the measurement leaving ~0.15 inches as the actual measurement length). Equation 4.1 and figure 4.3 describe the common roughness metrics used.

$$R_a = \frac{1}{l_m}\int_0^{l_m} |y|dx, \qquad R_{rms} = \sqrt{\frac{1}{l_m}\int_0^{l_m} y^2 dx}, \qquad R_{max} = \max_i[R_{zi}], i = 1...5 \tag{4.1}$$

The arithmetic average R_a is the most common metric, but R_{rms} can also be used, and we have started to track the R_{max} parameter as well. The calculation of R_a and R_{rms} can also be done by the Dektak® type profilometers. Unfortunately, the scan length resolutions for the two profilometers are not ideal for measuring the roughness on the UCN scale. The micron size tips are too large and the fine features that a UCN would interact with do not show up in these scans. For this reason, high resolution AFM scans are performed to provide this level of detail. Nevertheless, the industry profilometer is useful as each UCN guide tube can be measured easily. This is used to track the changes in surface roughness during the different polishing steps, primarily between the mechanical polishing and electropolishing steps, and provides a quantitative number that the polishers can strive toward.

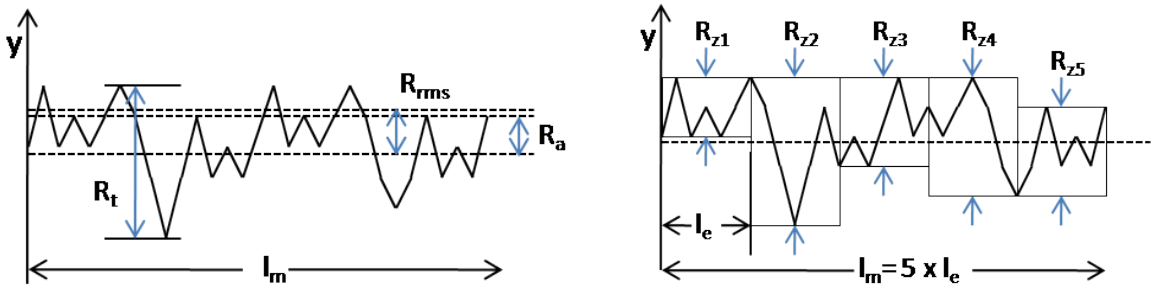

(a) Diagram showing the R_a and R_{rms} of a fictitious scan.

(b) Diagram showing how R_{max} is calculated.

Figure 4.3: A sample profilometer trace used to illustrate how the R_a, R_{rms}, and R_{max} values are derived.

4.3 Variable Angle Spectroscopic Ellipsometry

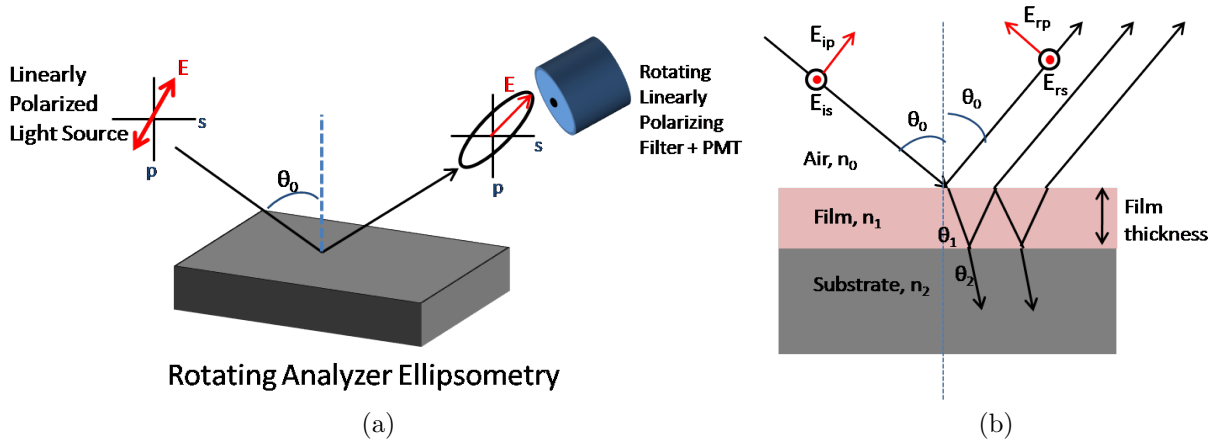

Figure 4.4: Schematic views of a Rotating Analyzer Ellipsometer (RAE). (a) Monochromatic light is linearly polarized and directed at the sample to be studied. The reflected light is then passed through a rotating linearly polarizing filter and then detected by a photodiode. An average of the ratio r_p/r_s is made for each wavelength/angle combination. Optical models are then fit to this data to extract the optical constants and thickness of the film. (b) Multiple reflections occur at the air/film and film/substrate interfaces resulting in destructive and constructive interference of the total reflected light as the incident light's wavelength is varied. It is this interference that allows the ellipsometer to measure the thickness of various thin film layers.

Ellipsometry is a common tool to used to obtain the optical constants and thickness of thin films. We currently employ a J. A. Woollam Variable Angle Spectroscopic Ellipsometer (VASE), located in the Electrical and Computer Engineering department at Virginia Tech, that has a 15-90° angular range and a 250-1100 nm detectable wavelength range. Here a Xe-lamp double-chamber monochromator selects wavelengths from 190-1700 nm. The light is then linearly polarized and directed at the sample which is held at a particular angle of incidence. In general the light reflected from the sample is elliptically polarized which then enters a rotating linear polarizer before being measured by a silicon photodiode, which is sensitive from 250-1100 nm, as shown in figure 4.4a. Usually the analyzer is rotated many times (about 30) for each wavelength/angle combination and the data averaged to produce

an intensity as a function of rotating analyzer angle which can be parameterized using Jones matrix analysis of the optical elements, including the sample, into a measurement of the ellipsometric parameters, ψ and δ [176]. These parameters are related to the complex Fresnel reflection coefficients, $\tilde{r_p}$ and $\tilde{r_s}$, of the sample for p-polarized (in the plane of incidence) and s-polarized (perpendicular to the plane of incidence) light, respectively, through the relation:

$$\tan(\psi) \cdot e^{i\delta} = \rho = \frac{\tilde{r_p}}{\tilde{r_s}} \tag{4.2}$$

All rotating analyzer ellipsometers are more sensitive when the light entering the detector is circularly polarized, which corresponds to $\Delta = 90°$. Here the light intensity allowed to pass through the analyzer to the detector is constant, thus producing a constant voltage pulse which is much higher than the noise floor at all times. If the light is linearly polarized as it enters the analyzer, then the voltage signal output from the photodiode oscillates, dipping into the noise region of the detector. In addition, Δ can mathematically range from 0° to 360° , but for an RAE it is mapped onto a 0-180° range, as the RAE cannot determine the handedness, left or right, of the reflected light. This provides ambiguity when Δ is measured to be 0° or 180° . Thus when choosing which incident angles to use, one should strive to obtain Δ measurements around 90° . Usually three incident angles are chosen such that the Δ measurements are slightly below, around, and slightly above 90° .

Once data has been collected, an optical model describing the dispersion/absorption is then built and fitted to the ψ and δ data using the Levenberg-Marquardt non-linear regression algorithm [177] to minimize the Mean Standard Error which is given by equation 4.3.

$$MSE = \frac{1}{2N-M}\sum_{i=1}^{N}\left[\left(\frac{\psi_i^{mod}-\psi_i^{exp}}{\sigma_{\psi,i}^{exp}}\right)^2+\left(\frac{\Delta_i^{mod}-\Delta_i^{exp}}{\sigma_{\Delta,i}^{exp}}\right)^2\right] = \frac{1}{2N-M}\chi^2 \tag{4.3}$$

Here N is the number of (ψ, Δ) pairs, M is the number of variable parameters in the model, and the σ are the standard deviations on the experimental data points. Many models exist, such as strict tabulated optical constants, Cauchy Dispersion, and Effective Media Approximation not to mention the anthology of absorbing oscillators, and developing an appropriate model is one of the biggest challenges with ellipsometry. Prior knowledge of the film or films, such as the chemical makeup, is crucial to determining which model to start with and usually several revisions will be required before an acceptable model of the film/film stack is derived. However, once this is done, fitting the model to new data is easy and very useful in tracking changes from sample to sample of the same film. Often a step height profilometer measurement is made on the sample to use as a constraining value during the fitting procedure. The particular models used in our analysis is described in chapter 7.

4.4 X-ray Photoelectron Spectroscopy

X-ray Photoelectron Spectroscopy (XPS or ESCA), is a non-destructive tool for determining the elemental composition, except for hydrogen and helium, and chemical state of a sample at the near surface of the sample (about the top 10 nm or so) via the photoelectric effect. Here aluminum K-alpha X-rays (1486 eV) and magnesium K-alpha X-rays (1253 eV) are directed at the sample located in an UHV environment, see figure 4.5. These x-rays penetrate several microns into the surface and are absorbed by the core electrons of these atoms. If the photon energy, $h\nu$, is larger than the binding energy, BE, of the electron, then it will escape the atom with kinetic energy E_k becoming a photoelectron, following equation 4.4.

$$h\nu = EB + E_k + \phi \qquad \Longrightarrow \qquad EB = h\nu - E_k - \phi \tag{4.4}$$

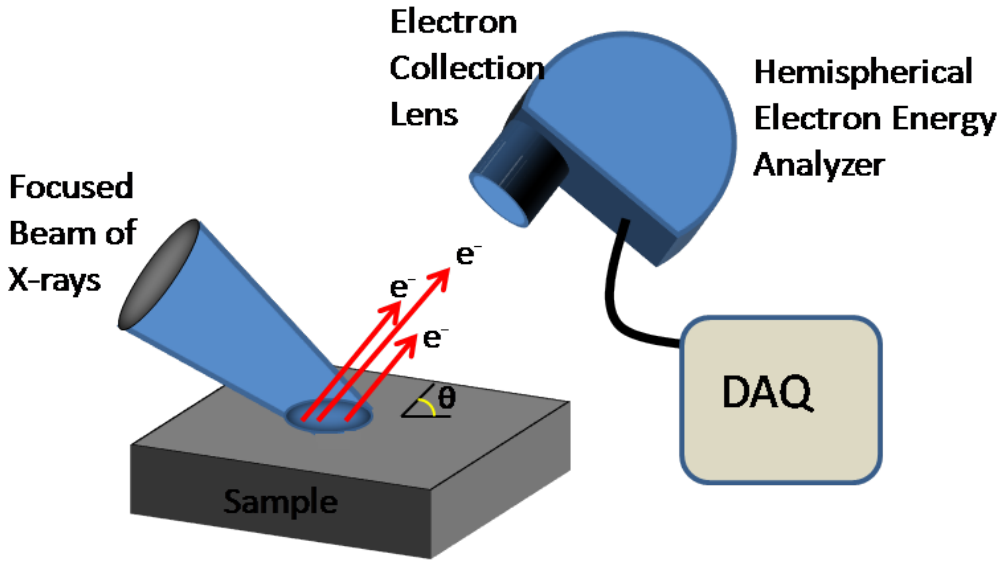

Figure 4.5: Diagram of a XPS system. Known energy X-rays induce photoelectrons to leave the near surface of the sample. These electrons have a particular kinetic energy corresponding to the binding energy of the electron in the parent atom. These binding energies are not only unique to the element but also shift slightly depending on the atom's environment and are used to provide elemental as well as chemical identification of the sample.

Here ϕ is the work function induced by the analyzer, not the material. The energies of these electrons are usually measured with a hemispherical electron energy analyzer that measures the number of electrons leaving the sample as a function of kinetic energy with a resolution of about 0.5 eV. In this way a very sensitive measurement of the BE is made via equation 4.4. Now the BE of the core (non-valence) electron of the element is unique and can be used as an identifier of that element. Furthermore, the BE of that core electron can shift slightly depending on the chemical environment of the element and in this way chemical structure can be deduced. This fact has been used determine the concentration of diamond bonded carbon atoms to graphite bonded carbon atoms in our DLC films, as there is about a 1 eV shift in the BE between these two states. In addition to just identifying the elements and their chemical state at the surface of the sample, the concentration, in atom percent, of each

element can be derived using equation 4.5.

$$C_i = \frac{I_i/S_i}{\sum_i I_i/S_i} \tag{4.5}$$

where I_i is the peak intensity for element i and S_i is the sensitivity factor for that peak which corrects for the photo-ionization cross sections of each element as well as detector inefficiencies. Here XPS can be used to detect compositions on the order of about 1 atom percent. In addition, sputtering systems, usually Ar^+ ions, can be incorporated into XPS machines to provide depth profiling of the sample. Usually an XPS scan is taken, then the sample sputtered for some time, and the process repeated in order to obtain an elemental composition profile of the film as a function of depth. The sputtering depth is usually calibrated to an oxide, such as tantalum oxide, but it is best to measure the sputtered trench depth, with a profilometer for example, in order to calibrate the sputtering time to a depth for the particular sample. The down side with this method is that oxides tend to form during the XPS scan phase of the process, leading to unreliable oxygen concentrations. For this reason, we have used XPS to examine the surface of the film without sputtering with the Perkin-Elmer 5400 XPS/ESCA, located in the chemistry department at Virginia Tech.

4.5 Auger Electron Spectroscopy

Analogous to XPS, Auger electron Spectroscopy (AES) measures the kinetic energy, E_k, of an auger electron leaving an atom of the surface. Here 3 keV electrons bombard a sample's surface and can eject a core electron, in state E_{core}, of one of the atoms leaving a hole behind. This hole can be filled by a higher shell electron, in state E_1, releasing energy in the transition, equal to the energy difference between states E_{core} and E_1. This energy can be

transferred to another higher shell electron, in state E_2, which will be ejected from the atom if the transition energy gained is greater than the binding energy of the electron. Thus the emitted electron has kinetic energy:

$$E_k = E_{core} - E_1 - E_2 \qquad \Longrightarrow \qquad E_2 = E_{core} - E_1 - E_k \tag{4.6}$$

This transition is often labeled in an ABC format, where A is the shell of the core electron,

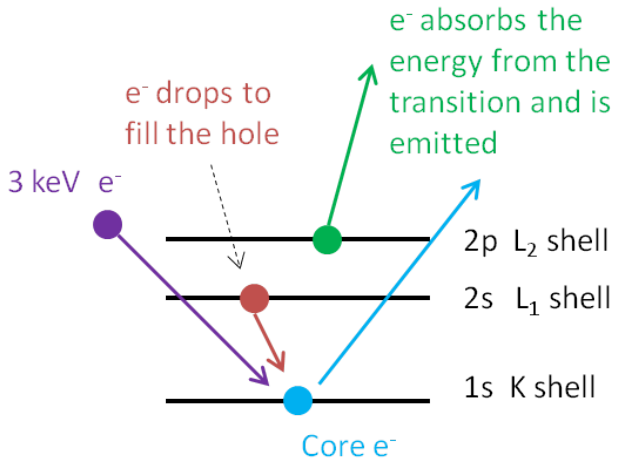

Figure 4.6: Diagram of the Auger electron emission process. In the diagram a 3 keV electron knocks out a core level electron in the K shell (s-orbital) leaving a hole. An L_1 shell (2s electron) drops down to fill the hole losing energy. This energy can be emitted in the form of radiation or be transferred to an electron in a higher shell, the L_2 shell (2p orbital) in this case. The energy gained by this electron is usually much higher than its binding energy and so the electron is emitted. This electron is termed an Auger electron after Pierre Auger who properly identified the electron emission process.

B is the shell of the electron that fills the hole, and C is the initial shell of the emitted electron. KLL, LMM, and MNN are the most common transitions employed in AES. The binding energy, E_2, is unique to each element and can be used to identify the elements in the sample as well as their concentrations at the sample's surface, in a similar way to XPS concentration analysis. As with XPS, the emitted electrons can multiple scatter with atoms

above it smearing out the initial kinetic energy. Thus only electrons from atoms near the first few nanometers of the surface, about 10 nm, are detected with accurate kinetic energies. Often AES is paired with the sputtering of the samples surface to create a depth profile, in a similar way as with XPS, except the sputtering can occur at the same time as the AES profile is taken, significantly reducing the oxide formation of the sample. Again the sputtered trench depth should be measured independently to calibrate the sputtering time to the depth of particular sample. Nevertheless, elemental composition depth profiles can be made with minimal oxygen contamination from oxide growth during profiling. A Perkin-Elmer 610 Auger Electron Spectrometer, located in the chemistry department, is used to perform Auger depth profiles of our ^{58}Ni and DLC coatings in order to look for foreign elements, especially ferromagnetic materials as a function of depth.

4.6 Secondary Ion Mass Spectroscopy

Secondary Ion Mass Spectroscopy (SIMS) is a widely used trace element analysis tool where a samples surface is sputtered in a UHV environment with high-energy ions, usually oxygen or cesium, releasing photons, electrons, ions, and neutral sample atoms into the vacuum. The sputtered ions, called secondary ions, are channeled and then separated by a mass filter where they are counted. Relative sensitivity factors are then used to correct the ion yields for sputtering yields and ionization efficiencies of the sample. With these in hand, SIMS is able to measure trace elements on the order of parts per billion depending on the sample and trace element in question. We employed Virginia Tech's Cameca IMS 7f GEO Magnetic Sector Secondary Ion Mass Spectrometer, located in Virginia Tech's CRC ICTAS facility, to search for hydrogen contamination as a function of film depth for our DLC and ^{58}Ni coatings on silicon substrates. Hydrogen is a major concern for UCN surfaces because of its

negative scattering length and relatively high neutron absorption cross section. Our coatings should have very low hydrogen concentrations, but they needed to be measured. For this measurement Cs^+ ions were used to sputter the samples while the spectrometer was set to look for H^- anions. Due to the low expected concentrations, the detector settings were forced to always look for H^- anions instead of scanning over a larger mass range. This data is presented in section 7.11

4.7 Atomic Force Microscopy

The number of applications of Atomic Force Microscopy (AFM), also known as Scanning Force Microscopy (SFM), have exploded in the past few years as it is an invaluable tool for studying all sorts of properties at the nanoscale. In our case we use the AFM to look at the surface roughness of our guide substrates as well as our ^{58}Ni and DLC films. The primary components of every AFM are a: cantilever/tip, laser and photodiode detector, and very precise piezoelectric movement elements. Here a cantilever with a specific spring constant and a very sharp tip, on the order of about 20 nm in radius, is mounted in a piezoelectric mount, see figure 4.7. A laser is focused on the back of the tip and the reflected light measured by a photodiode. As the tip moves the photodiode signal varies which is used to piezoelectrically control the height of the cantilever, which provides a height measurement of the sample's surface at that particular (X,Y) location. This is called running the AFM in Contact Mode. Alternatively, the cantilever can be driven at a particular frequency, usually 0.5 to 5 MHz, and positioned to lightly tap the surface and the photodiode measures the amplitude and phase lag of the oscillating tip. As the tip is scanned over the sample, the amplitude and phase lag vary, due to a variety of tip-surface interactions, which are then used to adjust the tips physical height and driving frequency. This provides height information as

well as phase information of the surface and is called running the AFM in Tapping Mode.

Tapping Mode scans were performed with a Cypher® Scanning Probe Microscope, from Asylum Research, with the assistance of Clayton McKee and Chris Honig from Dr. Ducker's group in the Chemical Engineering department at Virginia Tech. Scans were performed to investigate the roughness of the copper guide substrates as they underwent different polishing processes. These results are presented in chapter 5. Scans were also performed on witness strips from our ^{58}Ni ebeam source coating runs and DLC guide coating sessions. These results are presented in chapters 6 and 7.

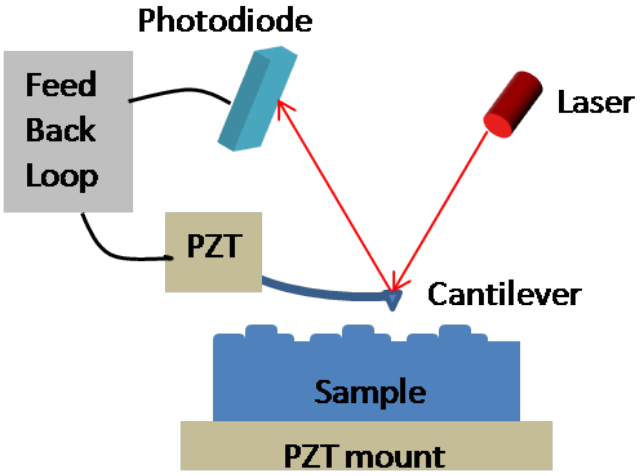

Figure 4.7: Schematic diagram of the essential components of an AFM. An sharply tipped cantilever, sometimes oscillating as in Tapping Mode and sometimes held at a constant deflection as in Contact Mode, is scanned across a samples surface. A laser spot is focused onto the back of the tip of the cantilever which is reflected into a photodiode. As the tip moves up and down the signal in the photodiode changes which is fed to a computer which then adjusts the height of the cantilever mount. The height changes are recorded as well as other parameters for each (X,Y) position of a scan. Usually square scans of about 30 micron X 30 microns to 1 micron X 1 micron are performed on our samples.

4.8 Scanning Electron Microscope

On occasion we used the Leo (Zeiss) 1550 Scanning Electron Microscope (SEM) located in Virginia Tech's CRC ICTAS building to look at a cross section of the our ^{58}Ni and DLC coatings. Cross sections were produced by snapping the coated silicon wafer witness strip and positioning the sample so that an edge on view of the break line could be obtained. An electron beam is scanned along the samples edge where multiple interactions occur, such as secondary electron and x-ray emission. In our case, secondary electrons are detected with an in-lens detector. The sample is scanned and an image produced according to the secondary electrons emitted, which is a function of the emitting element, chemical state of that element, and the topography. A low magnification scan is produced to search for a suitable region where the coating did not delaminate from the silicon surface during the breaking process. Once this is found a high resolution scan of that region is performed. In this way the thickness of the films with a resolution on the order of a few nanometers can be obtained. In addition, the Leo (Zeiss 1550) tool has an X-ray energy dispersive spectrometer that can detect the X-rays emitted from the sample which provides information about which elements are in the film and substrate.

Chapter 5

Component Preparation and Cleaning

5.1 Introduction

The beamline of the UCNA experiment has utilized a variety of tube substrates over the last 5 years. DLC coated quartz guides were selected to make up most of the beamline components, but due to poor quality control on the thickness of the DLC film, suitable alternatives were employed: mostly stainless steel and copper materials. Stainless steel was the primary UCN guide substrate material for most of the SD_2 source inserts, SD_2 source shield wall region(see 6.3), and up to the depolarization region of the experiment. 150 nm thick DLC coated guides were planned for the depolarization region of the beamline, but copper tubes were purchased and polished to as part of a contingency plan for the guides in this region, just in case enough DLC quartz coated guides could not be successfully produced within the time constraints of the experiment. This came to bear in 2007 where a few DLC coated quartz guides were prepared for the AFP spin flipper region and the rest of the depolarization region was made up of highly polished uncoated copper tubes. This configuration was used until 2009, when

most of the bare copper was replaced with DLC coated copper versions. This chapter is devoted to the polishing and cleaning procedures employed for these beamline components, where the characterization of the surface roughness, especially of the copper substrates, is emphasized.

5.2 Quartz Tube Preparation

Quartz and glass tubes have been previously used in other UCN experiments because of their very low surface roughness [35]. Quartz is preferred over other glasses because it has a very low concentration of impurities that could cause depolarization and it is readily obtained in tube form. Also, quartz is transparent to the 30MHz RF signal used by the AFP spin flipper. For these reasons, Mark Makela pioneered the use of quartz tubes as the substrate material for our PLD DLC films. A lot of effort went into developing and characterizing the quartz tube preparation process, details of which can be found in Mark Makela's Thesis [110]. The following summarizes the process:

1. The quartz tube is cut to length on a diamond saw, rinsed with water, and then the ends are fire polished using a hydrogen flame.

2. The tube is chemically etched for 10mins in the following acid solution: 5% (50% electronic grade) HF + 1% HNO_3 (Conc.) + 3% HCl (Conc.) + 91% H_2O located in a PVC pipe acid station.

3. The tube is then dipped into 3 other DI water filled PVC pipes for 10mins each with a DI water rinse in between.

4. A lens paper lined Kimwipe® "Q-tip" style bob attached to a nylon rod is pushed through the quartz tube to dry the inside surface. The outside is dried by hand with Kimwipes® . Sometimes two swipes are needed.

5. The tube is then loaded into a home made vacuum oven where it bakes for 24 h at 200° C to remove leftover hydrocarbons and then 24 h at 400° C to remove water from the quartz. After the baking process pressures in the mid 10^{-7} Torr are obtained.

Here the HF removes about a micron of the tubing surface, and the nitric and hydrochloric acids attack metal impurities that might be in the material. The acid etch procedure has been shown to lower the average surface roughness to less than 0.5 nm [110]. Once the chamber is cooled off, which takes about 6 h, the tube is immediately loaded into the coating chamber. We have followed this process in our quartz-tube preparation procedure with the addition of a custom quartz tube facing tool and a solvent cleaning procedure before dipping the tubes in the acid solution. A glass saw has been fitted with a diamond grinding wheel and mounted to precisely grind the faces of the quartz tubes. Once aligned, the faces can be ground flat to $\pm$ 0.002 inches, as any flatter often resulted in cracking the quartz tube during the alignment process. This is to ensure that UCN lost through gaps between guide sections are minimized. The tube is rinsed with water and then very lightly fire-polished with a hydrogen flame. The fire polishing seals the microcracks on the ends of the tube which strengthens the ends from chipping during handling. It also increases the adhesion of the DLC coating on the face and inside edge of the tube. The DLC almost always delaminates from non-fire polished edges. Great care goes into the fire polishing and our glass shop specialist, Tom Wertalik, is able to minimize the material flow so that face flatness becomes $\pm$ 0.003 inches. Then the tubes are ultrasonic cleaned, at 40 kHz, in Acetone (5 min), Methanol (5 min), and DI water (5 min), as shown in figure 5.1b. Only half of the tube can be cleaned at one time, and so one half of the tube goes through the cleaning process, is rinsed with copious amount of DI

water, flipped, and then the other half goes through the process.

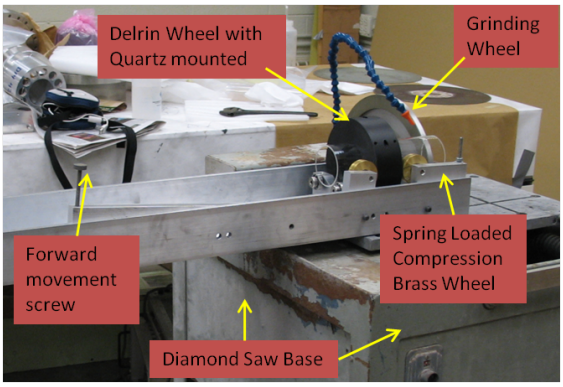

(a) Quartz Tube Grinder

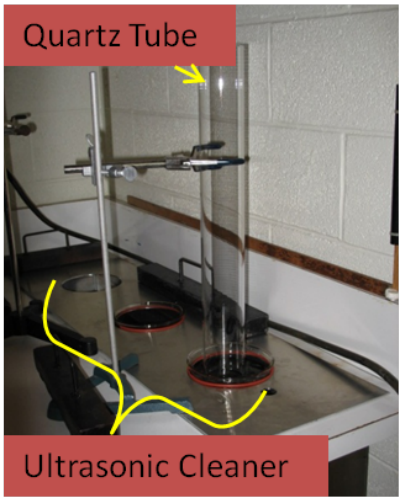

(b) Ultrasonic Cleaning Station

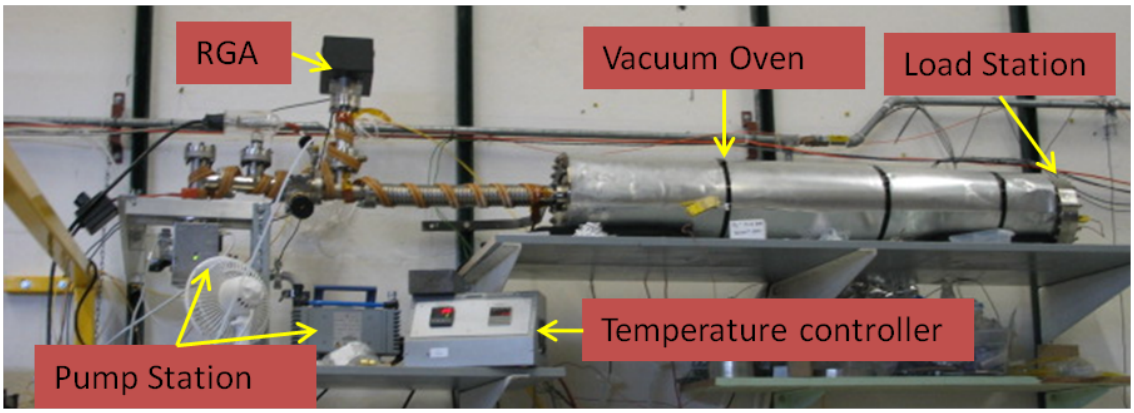

(c) Vacuum Oven

Figure 5.1: Photographs of the Guide Tube Cleaning Stations. (a) Quartz Grinder used to polish the tubes flat. The tubes are aligned to a very flat faced acetal wheel using set screws. The tube is rotated and the deviations measured by dial test indicator. The set screws are adjusted until the deviations are $\pm$ 0.002 inches. Then the quartz tube is slowly pushed up against the water cooled grinding wheel using the forward movement screw. (b) An 6 x 20 x 20 inch ultrasonic cleaning station is located in RM 1 of the Virginia Tech Physics department. The solvents are poured into 10 cm or 13 cm diameter test tubes and held above the bottom of the ultrasonic cleaner using an aluminum plate. (c) The UCN guide/component vacuum baking oven. The oven is made by wrapping high temperature heat tapes ($\sim$2500 W total) around an electropolished 5.75 inch ID nipple with 8 inch CF flanges on the ends. This is then wrapped with insulation and an aluminum sheet. The vacuum is provided by a 60 L/sec turbo pump backed by a dry diaphragm pump. The parts to be baked are loaded onto a stainless steel tray. A type K thermocouple protrudes into the oven from the load end and is used by a programmable temperature controller to measure the temperature inside the oven.

Then the tubes go through the same acid etch and baking procedures as described above. Two 70 mm OD tubes can be installed in the oven at the same time. At one time we thought that we could clean a series of tubes and then bag them in class 100 cleanroom polyethylene bagging material (CleanTuff® 6mil thick material [26]) filled with an argon atmosphere. However, we encountered DLC adhesions problems on these "clean" quartz tubes after they sat for many months which we attributed to moisture and oxygen seeping through the polyethylene. Thus we now use the vacuum oven itself to protect clean tubes until they are ready to be installed. We have since found oxygen and moisture barrier bagging material (S-600 metalized polyethylene tubing material [106]), but we only use them to bag the final products.

5.3 Metal Substrate Preparation

The primary metal alloys used for the beamline components are: 304 and 316L stainless steels and 101, 110, and 122 copper alloys. All of the tubes are equivalent to 1/2 hard, US alloy 122 (phosphorus de-oxidized) tubing material. This equivalence is because most of the 2.75 inch OD copper tubes are actually from England and produced according to Great Britain's BSEN12449 CW024A regulations, which are approximately equivalent to US alloy 122 general engineering standards. All the metal substrates go through a mechanical polish and then an electropolishing procedure. The goal of the polishing is two-fold: to reduce the surface roughness and two provide a clean, low contaminant surface. Certain diameters, nominally 3 and 4 inch OD, of mechanically polished and then electropolished stainless steel tubes can be purchased commercially, such as RATH's True 10 [46] or Trent's 10MAX® 316L stainless steel tubing [169]. This tubing is very uniform from lot to lot and usually purchased in 20 ft lengths. UCN guides are made with this material by rough cutting them

and then facing the ends to length on a lathe, producing a tube face flatness that is less than $\pm$ 0.003 inches. Care is taken to reduce the amount of cut material from sliding around the inside of the tube and scratching the polished surface by pulling the material out of the ID of the tube frequently or setting up a compressed air system to blow the material out of the tube during the cutting process. For other diameters not commercially sold pre-polished the material is cut, faced to length, and then polished. Likewise, custom components are machined and then polished.

5.3.1 Mechanical Polishing

Before 2005, the mechanical polishing of most short tubing material was performed in-house at Virginia Tech. Hand sanding was done with various grits of silicon carbide (SiC) sand paper (220 up to 1200), and then a pneumatic die grinder was used with medium density cotton buffs loaded with either cut or color polishing compounds. It is very important during the hand-sanding procedure to ultrasonic clean the components between grit changes. If this is not done, pits from loosely trapped grit/material will become visible during the final ultrasonic cleaning process. The parts were polished for several hours to a fine mirror finish. Then the components were sent out for electropolishing. In 2005, we were introduced to a mechanical polishing company,Irving Polishing [143], that worked closely with the electropolishing company we usually use, Able Electropolishing [75]. Since then we have developed a good relationship with Steve Irving, the president of Irving Polishing, and his crew. They have provided almost all of the mechanical polishing of our stainless steel and copper components. In the industrial polishing business the quality control and surface roughness are usually measured by a trained eye and an industrial profilometer, which is described in section 4.2. This portable profilometer can be laid inside the ID of our UCN guide tubes where a diamond tipped stylus then scans the surface.

Our stainless steel machined components are usually specified to have 32 μinch R_a 's when leaving the machine shop. If possible, the flat surfaces are then sanded on a SiC belt sander, with higher and higher grits, before being polished with a medium density sisal wheel with cut/color compounds and then with a cotton buff with cut and color compounds on high RPM constant torque buffing machines which produces a high luster mirror-like finish. Stainless tubes, such as the machined 2009 source insert, are polished with large, high rpm air tools as shown in figure 5.2. Unfortunately it is difficult to obtain cross cutting strokes by polishing the tubes in this fashion, which results in notable polishing lines perpendicular to the length of the tube. This is the limiting factor for obtaining very smooth UCN guide tubes, especially on our copper substrates. When polishing components where the polishing direction can be changed frequently, such as with the many SD_2 source insert components, close to mirror finishes with only very light polishing lines are observed, which then electropolishing often removes.

The mechanical polishing of our copper beamline components has mirrored that of our stainless steel components. Specifically, the tubes are polished in the following sequence with a high-rpm rotary tool: silicon carbide 180, 240, 300, 400, 500 grit paper, then a medium density sisal wheel with white cut/color compound, and finally a cotton buff with a white color compound. The copper plates that make up the rectangular guide have been polished in a similar method but starting with a 300 grit paper instead of 180. It is very easy to obtain a mirror finish on the copper plates, however the fine circumferential polishing lines remain on the ID of the copper tubes, providing only a close-to-mirror finish.

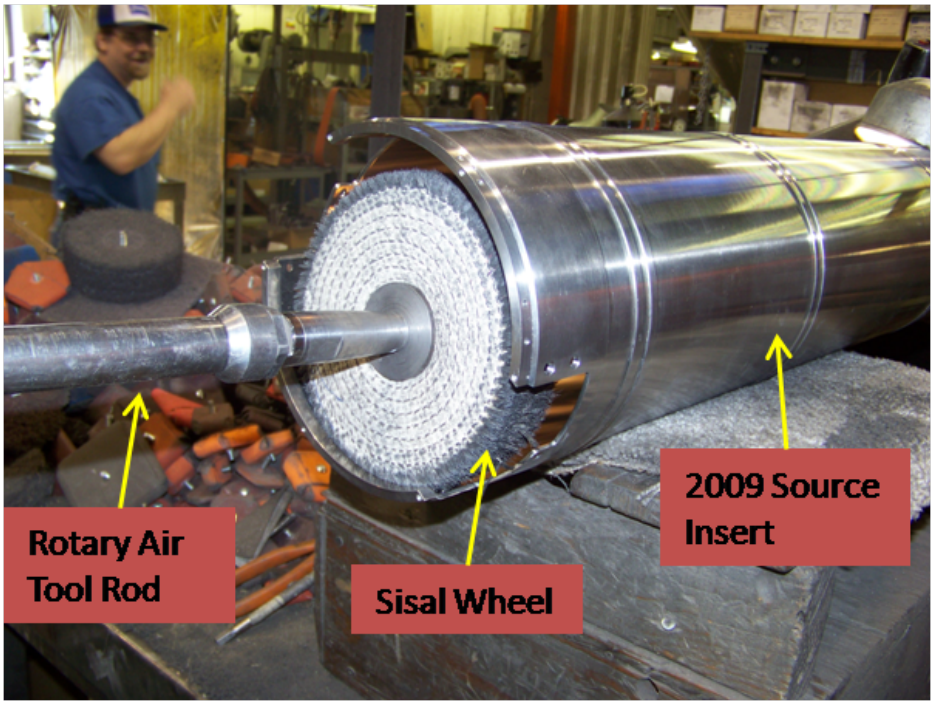

Figure 5.2: Photograph of the mechanical polish process for the 2009 source insert tube taken during a site visit. Here a sisal wheel pneumatically rotates while the rod is pushed in and out of the tube. Figure used with permission from Steve Irving (2010) [143].

5.3.2 Electropolishing

After the components have been mechanically polished, they are normally sent to be electropolished. Able Electropolishing is one of the largest electropolishing companies in the U.S. and have been the only company able provide a reasonable finish on our copper components. During the electropolishing process the component is thoroughly degreased and connected to the anode of a DC power supply while submersed in a temperature controlled electrolytic acid solution. Cathodes are strategically placed in the solution and a current is allowed to flow between the part and the cathode causing an oxidation/reduction reaction. Two polishing processes are generally thought to occur: anodic leveling and anodic brightening [101] [100]. Anodic leveling arises from a difference in dissolution rates between peaks and valleys on the surface, resulting from the difference in the concentration of electric field

lines at the two locations, and smooths the surface on the micron scale. Anodic brightening affects features below the micron scale where the effects of the metals microstructure, are suppressed and the polishing proceeds through diffusion controlled random atom removal [92]. How these two processes are controlled depends on the desired effect. For UCN applications anodic brightening is more important as the UCN sample surface features on the hundreds of nanometers scale.

A typical rule-of-thumb with electropolishing is that it cuts the R_a of the surface in half, but this rule begins to break down for R_a values above 32 μinches and below about 10 μinches. Above 32 μinches the R_a is decreased by more than half and below 10 μinches it is decreased by less than half. Furthermore, when the R_a is nearly 1 or 2 μinches , electropolishing tends to increase the R_a by 1 or 2 μinches , as measured by an industrial profilometer. Here the process needs to be tailored for anodic brightening which is much more difficult to control than anodic leveling. In addition to surface smoothing, electropolishing is used to clean and passivate the surface of the component. Commercially, the electropolishing process removes 0.0001-0.002 inches from the component depending on the solution, material, and its geometry. Thus most surface contamination is stripped, and in the case of stainless steel a chromium-oxide rich surface is left that inhibits corrosion [97]. In the case of copper, the surface is also stripped and a passivated thin copper-oxide surface is left, as the copper components have a bright almost pink color after electropolishing indicating a thin oxide layer. Thus the electropolishing process is not only a polishing and deburing process, but a cleaning one as well, which is a major reason for why we use electropolishing.

5.4 Copper Plate Finishing Results

The difficulty with polishing copper was acutely realized during the polishing process of the 2009 rectangular guide plates. These plates were polished in the usual manner and before electropolishing had a mirror finish. After electropolishing the surface was frosted to the eye indicating higher surface roughness. From discussions with the electropolisher, it was decided to make a practice copper plate with different mechanical finishes and then have it electropolished, as shown in figure 5.3. Instead of specifying finishes in terms of R_a , we decided to specify the finishes according to the last polishing step used, as this is easily reproducible. For each finish, two separate spots were scanned with an industrial profilometer before and after electropolishing and averaged together. Table 5.1 shows the results of these measurements. Here the 50% rule with electropolishing breaks down somewhere between an R_a of 14 and 6 μinches . In fact, as the finish gets closer and closer to mirror-like, the electropolishing seems to double the surface roughness as measured by an industrial profilometer. Not surprizingly, this is also the case for tube samples with the same polishing method/finish as shown in table 5.3. Also, it appears that one can stop at a 600 grit finish and then electropolish instead of buffing to a mirror finish before electropolishing.

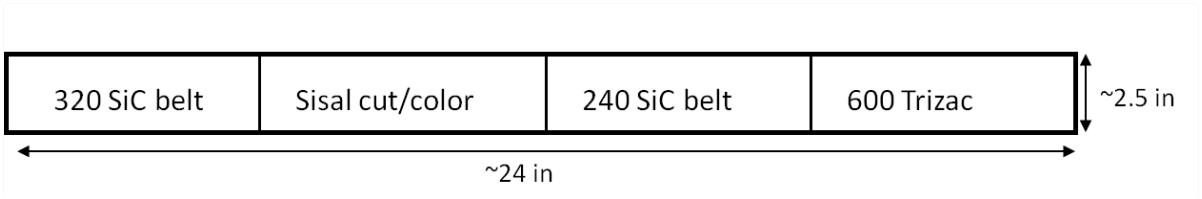

Figure 5.3: Diagram of the 1/4 inch thick copper practice plate used to measure the surface roughness of different mechanical finishes before and after electropolishing.

Although the standard in the industrial polishing industry, the perthometer is really measuring the surface roughness on a completely different scale than sampled by UCN. To get an idea of what what a UCN "sees", AFM measurements were performed on cutouts of

Table 5.1: Summary of the mechanical polishing and electropolishing of the practice copper plate. *The "All Cotton Buff" numbers, which are an average of 13 different plates, are provided for comparison. All measurements were made with a Mahr M4P Perthometer.

Plate Polishing Summary

	Mechanical Polish		Electropolished	
Finish	R_a (μin)	R_{max} (μin)	R_a (μin)	R_{max} (μin)
240 grit	25	252	11	74
320 grit	14	153	7	53
600 grit	6	78	5	37
Sisal Wheel	3	32	5	58
All Cotton Buff*	2	16	4	33

the practice plate. During the AFM sample preparation, care was taken to not scratch the surface to be measured. This was accomplished by cutting out 1 cm x 1 cm AlphaWipe® squares. They were taped onto the sample using masking tape. The masking tape hung generously over the wipe onto the sample plate. The sample was cut out with a hacksaw cutting through the tape, while making sure the tape between the blade and the soft wipe remained adhered to the metal surface. In this way, 2 cm x 2 cm samples were made, with the inner 1 cm^2 area being protected. The samples were prepared for the AFM measurements by first ultrasonic cleaning them in Acetone (5 min), Methanol (5 min), a 2% Citranox® solution (20 min), Ethanol (5 min), and then finally blow-drying them with UHP N_2. Figures 5.4 and 5.5 provide examples of these scans where the somewhat deep holes seem to appear in most samples after they have been ultrasonic cleaned in Citranox® . Table 5.2 summarizes the results of these plate sample scans. The 30 micron scans follow the general trend established by the profilometer scans, however at finer and finer scales this trend breaks down. This is not unexpected since the profilometer's tip is 10 microns in diameter (compared to the 40 nm diameter tip of the AFM cantilever) and so is not able to see features below this limit. Nevertheless a cotton buffed then electropolished mirror plate appears smoother than just a mechanically polished plate, contrary to what your eye may lead you to believe.

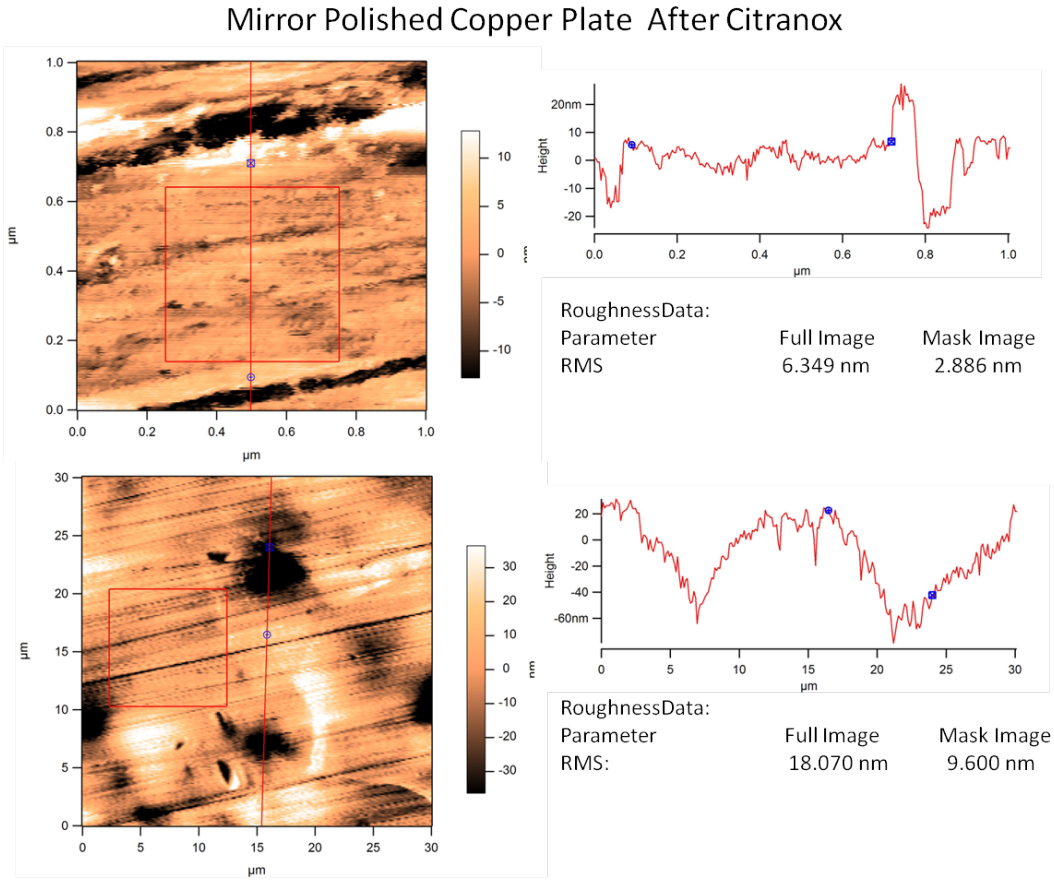

Figure 5.4: Surface roughness scans of a cotton buffed copper plate sample. Here one can see the polishing lines left from the buff. All measurements were made with an Asylum Research Cypher AFM in Tapping Mode.

Table 5.2: Summary of the AFM surface roughness scans of electropolished copper plate samples at different scan sizes. Representative areas were visually selected via a microscope and the average roughness was calculated for the entire scan size box. *The 600 grit sample was ultrasonic cleaned in the organic solvents, but not Citranox® . All measurements were made using an Asylum Research Cypher AFM in Tapping Mode.

Electropolished Plate Samples AFM R_a

Finish	30 μm Scan	10 μm Scan	1 μm Scan
*600 grit	20 nm	6 nm	2 nm
Sisal	29 nm	5 nm	1 nm
Cotton Buff	7 nm	3 nm	1 nm

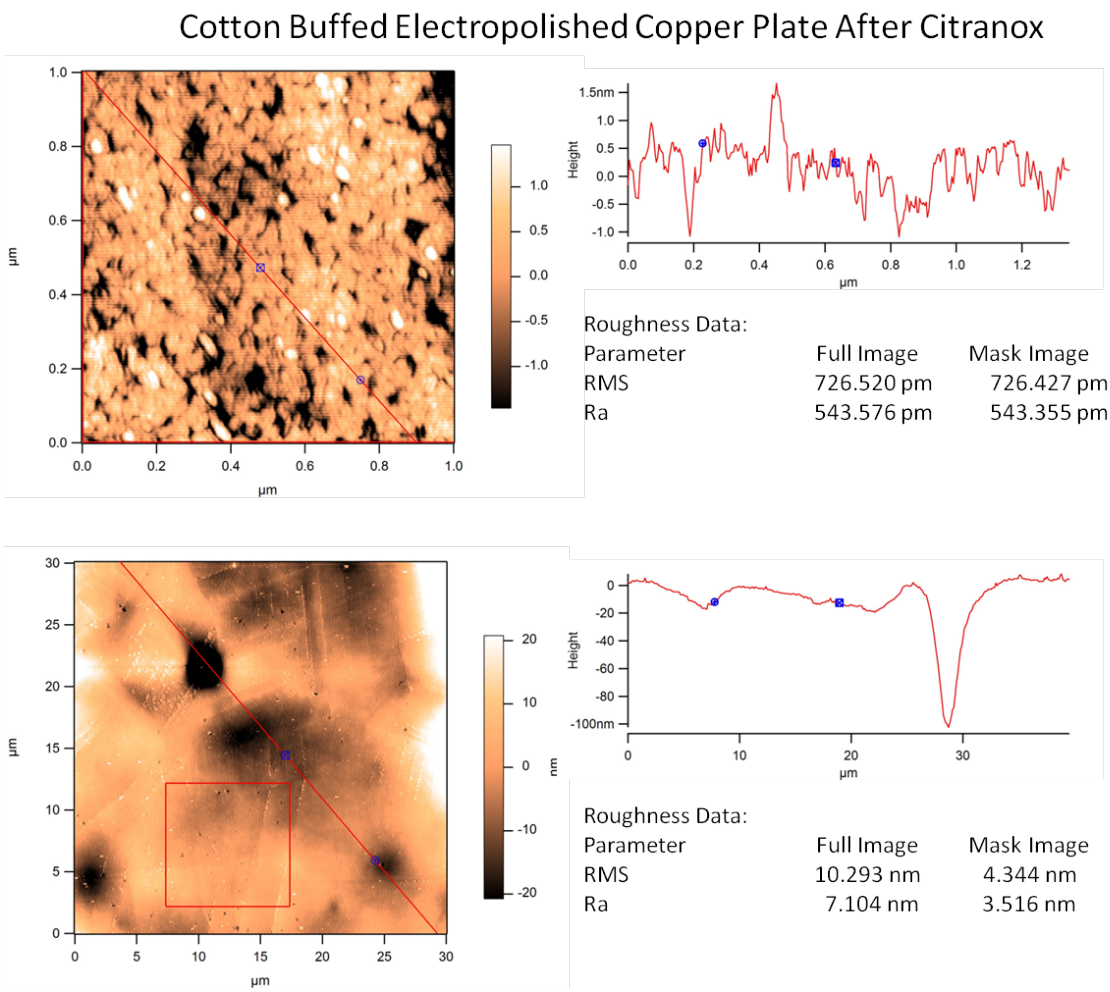

Figure 5.5: Surface roughness scans of a cotton buffed then electropolished copper plate sample. Here one can make out the grain sizes of the copper surface from the 1 micron scan. All measurements were made with on an Asylum Research Cypher AFM in Tapping Mode.

5.5 Copper and Stainless Steel Tube Roughness

Profilometer scans have also been performed on many of the copper tubes used in the UCNA experiment both before and after electropolishing. All the UCN guide tubes have been polished with the recipe described in section 5.3.1. The UCNA decay-trap tubes followed this same procedure but did not include the cotton buff finish, in efforts to create a slightly rougher surface on the tube which would provide more diffuse reflections and result in a better

Table 5.3: Summary of the mechanical polishing and electropolishing of the UCNA beamline guide substrates. The copper sisal entries are an average of measurements performed on the 5.125 inch OD decay trap guides. The Cotton Buff entries are an average of measurements performed on 3 inch and 2.75 copper tubes. Entries missing are due to measurements not taken during during the polishing process. All measurements were made with a Mahr M4P Perthometer.

Tube Polishing Summary

	Mechanical Polish		Electropolished	
Finish	R_a (μin)	R_{max} (μin)	R_a (μin)	R_{max} (μin)
Copper Sisal	N/A	N/A	4	N/A
Copper Cotton Buff	2	18	4	31
SS 2009 Source Insert	N/A	N/A	4	28

bottling guide. These results are provided in table 5.3. Again it seems that electropolishing roughens the surface on a large scale by a factor of two or so. As with the plate samples, tube sample cutouts were taken from 2.75 inch OD test tubes and prepared in a similar fashion to the plate versions for AFM surface roughness measurements. Figures 5.7 and 5.6 show AFM scans for a mechanically polished tube and an electropolished tube. The results are also condensed into table 5.4, which also includes scans for a Trent 10MAX® electropolished stainless steel tube sample, which is similar to the tubes that make up the shield wall guides in the SD_2 UCN source. Here it is clear that electropolishing the mechanically-polished copper tubes improves the surface roughness on the UCN scale and there is not much difference, at least on the 30 micron or less scale, between the electropolished copper and the purchased electropolished stainless steel version.

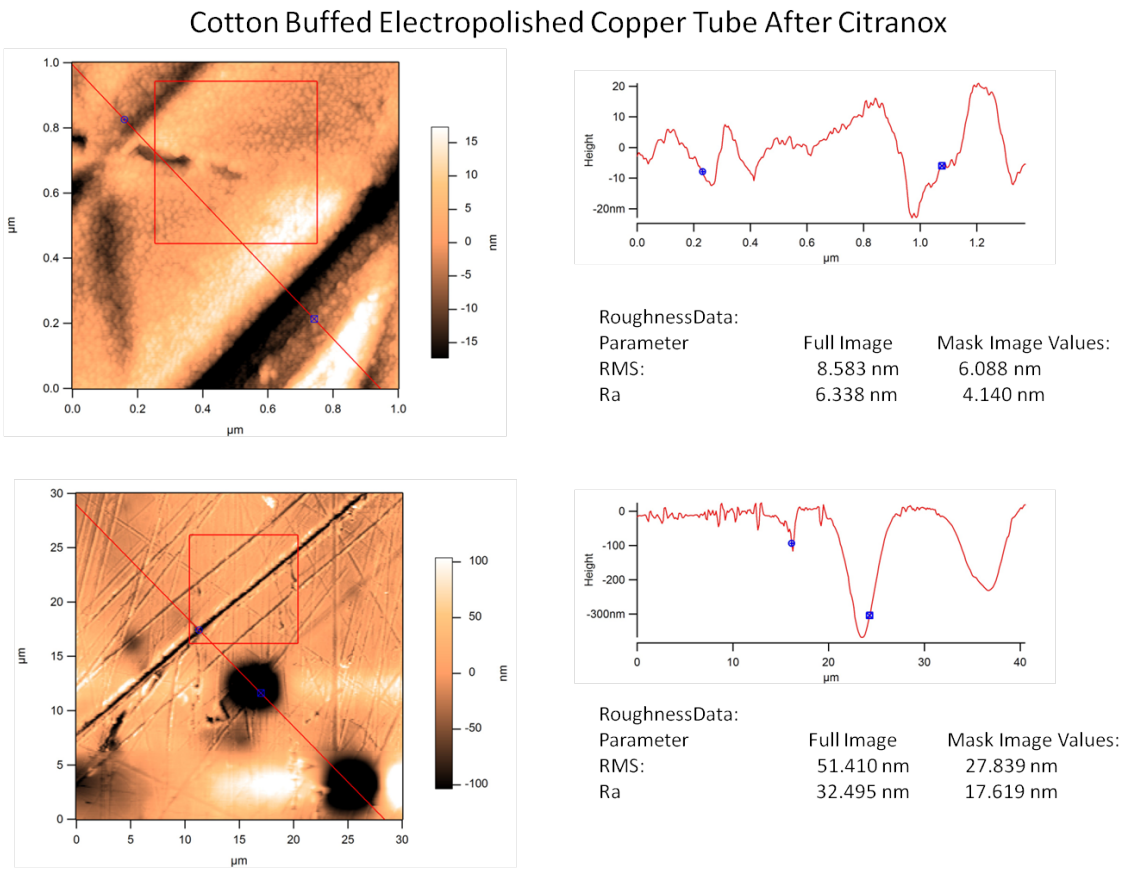

Figure 5.6: Surface roughness scans of a cotton-buffed then electropolished copper tube sample. All measurements were made using an Asylum Research Cypher AFM in Tapping Mode.

Table 5.4: Summary of the AFM surface roughness scans of copper tube samples at different scan sizes. Representative areas were visually selected via a microscope and the average roughness was calculated for the entire scan size box. *The 600 grit sample was ultrasonic cleaned in the organic solvents, but not Citranox® . All measurements were made using an Asylum Research Cypher AFM in Tapping Mode.

Tube Samples AFM R_a

Finish	30 μm Scan	10 μm Scan	1 μm Scan
Mechanically Polished Copper	53 nm	40 nm	23 nm
Electropolished Copper	32 nm	11 nm	6 nm
SS Trentweld 10MAX®	41 nm	11 nm	3 nm

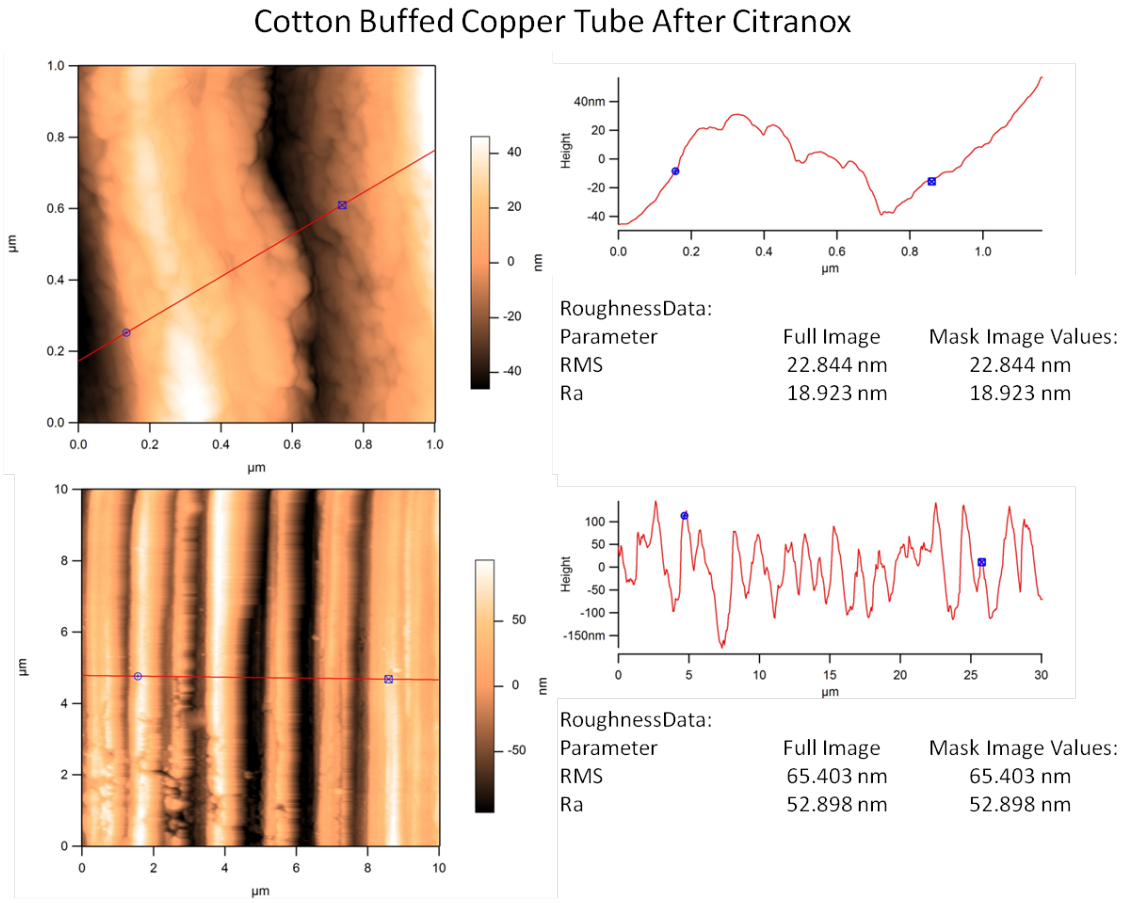

Figure 5.7: Surface roughness scans of a cotton-buffed copper tube sample. All measurements were made using an Asylum Research Cypher AFM in Tapping Mode.

5.6 Polishing Discussion

From looking at tables 5.1, 5.2, 5.3, and 5.4 we see electropolishing both increases the long-scale roughness, as measured by a profilometer, and decreases the short-scale microroughness, as measured by an AFM. Although both scales are important for UCN transmission through guides, more weight is given to the microroughness, as this is the scale that determines the amount of non-specular scattering. Thus electropolishing is a beneficial step, based upon our tube AFM measurements, as it lowers the microroughness as well as cleans the surface. Therefore polishing the copper surface with various stages of grit/compound up to a color compound loaded cotton buff and then electropolishing does produce a smoother surface. We note that profilometer measurements made on the electropolished 600 grit plate sample, indicate that one does not have to polish up to the cotton buff step, however AFM measurements of this sample show that indeed the roughness is much larger on the micron scale than that of an electropolished cotton buffed plate sample. Nevertheless, it would be ideal to reduce this long scale roughness, as well as obtain even smoother microroughness levels to achieve those measured on our quartz tubes.

We seem to be limited by the mechanical polishing process itself and the softness/quality of the copper substrate, especially when it comes to polishing our UCN guide tubes. Here it is very difficult to cross ones polishing lines, resulting in some deep groves that never get smoothed out. This may be improved by automating the mechanical polishing wheel to turn at a certain rate while moving in and out along the length of the tube for a long time. Another option would be to turn the polishing wheel/buff 90° , like that of a right angle die grinder, so that the buff cuts along the length of the tube. This would ultimately leave polishing lines along the length of the tube which should be better for UCN transport. Further options include a slurry, maybe even a nonlinear slurry, polishing method like that

used in chemical mechanical planarization (CMP) of copper in the microelectronic and optics industries [36] [55]. Slurry methods have had mixed results on machined components such as complicated valve bodies, but may work well for tube sections [78]. Also, although the electropolishing process seems to produce reasonable surfaces, it is quite expensive at $450 for a meter long tube. An in-house electropolishing station may prove more cost effective and provide smoother surfaces in the long run. In addition, copper etchants, such as phosphoric acid, may provide a viable alternative to electropolishing [70].

5.7 Cleaning the Copper Substrates

Early in the development of ≈150nm thick DLC films on copper, it was suspected that the native oxide layer on the copper surface was adversely affecting the adhesion of the DLC. To address this, Citranox® , produced by Alaconox, has been used to reduce the oxide layer, as well as clean and passivate the surface. The ultrasonic cleaning process that had been developed for the quartz tubes was modified in the following way to accommodate this step for the copper tubes: ultrasonic clean in Acetone (5 min), Methanol (5 min), 2% Citranox® solution in filtered water (20 min), 200 proof Ethanol (5 min), and concluding with a 200 Proof Ethanol rinse. Here the Ethanol was used instead of DI water, because the DI water will readily reoxidze the surface. XPS analysis of the Ethanol rinsed samples showed that there is not any extra carbon contamination over that seen from a filtered water ultrasonic cleaned and rinsed surface and that the Ethanol rinsed sample had less of an oxide layer. In addition Ethanol alows for more efficient drying of the components so one only needs to blow dry the ID of the copper tubes with dry N_2 instead of drying the inside with a soft wiper tipped rod.

5.8 Conclusion

A significant amount of resources goes into preparing each guide component for use in the UCNA beamline. For the quartz substrates the same "polishing" procedure developed by Mark Makela is still used, with the addition of a solvent cleaning process prior to the etching procedure. Also, a programmable vacuum-oven temperature controller helps ensure that the components are baked for the correct amount of time. All the metal components are mechanically polished and then electropolished, where the resulting surface roughness after both processes has been quantified via an industrial profilometer and AFM surface scans. Although it may not be optically visible, AFM studies show that electropolishing after mechanically polishing provides a smoother surface at the sub-micron scale. Several profilometer and AFM measurements were performed that provide benchmarks for future UCN guide roughness studies and provide valuable roughness parameters for UCN Monte Carlo simulations. It is also apparent that the mechanical and electropolishing procedures currently employed produce at least an order of magnitude rougher surface than that of quartz substrates. Although not unexpected, if one desires quartz-like surface roughness a different polishing technique will need to be investigated.

Chapter 6

Coatings for the LANL SD_2 UCN Source

6.1 Introduction

The exploration of a UCN source at LANSCE began almost 14 years ago, with a UCN rotor which used Doppler-shifted Bragg scattering of 400 m/s neutrons to obtain neutrons in the UCN energy regime [33]. Next followed a pulsed spallation SD_2 source which thermalized spallation neutrons into cold neutron (CN) energies where they then downscattered via phonon emission in a solid or liquid into the UCN energy regime[147][16][170]. Over the next few years, the promise of very high UCN densities from a pulsed SD_2 source became a reality when in 2000 the world's largest UCN density, $\sim$98 UCN/cm^3 was measured at the LANSCE prototype SD_2 source [87]. Previously the largest density of UCN achieved was 41 UCN/cm^3 at the ILL. Riding the wave of this success, a much larger SD_2 source was planned and built to supply UCN for the UCNA experiment and future UCN experiments

in Area B at LANSCE. By 2004 the source pictured in figure 2.3 was built and ready to deliver UCN to the UCNA experiment. However, several challenges were encountered with the new, larger SD_2 source and several modifications were made over the last 5 years where each modification required coating with ^{58}Ni at Virginia Tech. This chapter summarizes the history of these changes with an emphasis on the challenges encountered during the coating of the individual components and the lessons learned from these developments.

6.2 2004/2005 UCN Source Diagnostics

The original production source, based upon the prototype source developed at LANSCE, delivered far fewer UCN to the SCS decay trap, by about a factor of 200, than expected. Several factors can cause this drop such as: large gaps between guide components where UCN can leak out, areas of highly absorbing media in the beam line, and areas with low Fermi Potential materials to name a few. One way to get a better handle on which factors dominate, is to measure the UCN energy spectrum. One way is to do this is to build a chopper-style UCN velocity spectrometer [43]. An other way is to use gravitational or magnetic fields to effectively block lower-energy UCN from reaching a UCN detector A third method is to fill a section of guide with various amounts of 1/v absorbing gas such ^{3}He . These three methods were performed and their data incorporated into a Monte Carlo simulation of each method assuming the spectral density of UCN follows $\rho(v) \propto v^2 dv$, for $v < v_guide$ where v is the velocity of the UCN and v_{guide} is the velocity cut-off for total internal reflection in the guide [123][150][69]. Although there are some discrepancies between the models, it is generally accepted that the velocity spectrum arising from a transport system with a 80-100 neV Fermi Potential matched the data much better than that expected from a 270neV Fermi Potential (the ideal Fermi Potential of the DLC coating) cut-off transport system.

Taking this result and incorporating it into a Monte Carlo model of the UCN source and shield-wall guides, the major loses of UCN came from the source itself and the first two DLC-coated quartz shield-wall guides connecting to the source [123]. The model showed the main losses in the source were caused by the source valve/shutter obstructing part of the UCN flow, less than adequate neutron-flux moderation down to CN energies, exposed bare stainless steel components, and possibly contaminated or thin ^{58}Ni coating on the vertical guide, often called the source bottle, connecting the SD2 crystal to the shield wall guides $\sim$1 m away. The coating on the shield-wall guides were assumed to be of low density and/or low thickness in addition to having substantial gaps between sections. From visual inspection the DLC coating looked a bit thin on quartz tubes, but little documentation was kept and witness strips had not become a part of the standard coating practice when these guides were made and so one could only speculate. As a result, coating quality control, especially thickness, became a major, if not the most important, concern during my time at Virginia Tech. Thus a source overhaul was planned that included replacing the source shield-wall guides, attempting to add more polyethylene moderator, and making a ^{58}Ni coated source bottling guide and new flapper/shutter mechanism, which together was called a "source insert".

6.3 LANL SD_2 Source Shield Wall Guides

The diamond-like carbon coating on the quartz shield wall guides was known to be thinner than the usual 100 nm (recall we increased the thickness of our coatings in 2006 before the shield wall guides were coated, see section 3.2), as well have a lower than desired Fermi Potential. However due to time constraints associated with testing the SD_2 source, the collaboration agreed to install these guides with the intention of always replacing them at

a later date. However the expected time involved in making and installing a thicker/high quality set did not fit into the experimental schedule. So alternative commercial guides were modeled. RATH True 10, 316L stainless steel (SS) tubes have consistently shown to have decent transmissions >95%, similar to DLC quartz, and a calculated Fermi Potential of ∼185 neV. These tubes are mechanically polished, electropolished, cleaned, and cleanroom packaged, all in house, and are certified to have an average roughness (RA) no greater than 10 microinches (254 nm) [46]. They are designed to be used in the pharmaceutical and food processing industries where product transfer tubes need to be smooth, to reduce the risk of chemical build up in pits/defects, and contaminant free. Due to their availability and high tube-to-tube uniformity, the shield wall guides were changed to 4 inch OD, RATH True 10, 316L stainless steel tubes. The larger OD was selected in order to reduce the number of bounces as compared to the 2.75 in OD tubes which lessens the impact of stainless steel's loss/bounce probability.

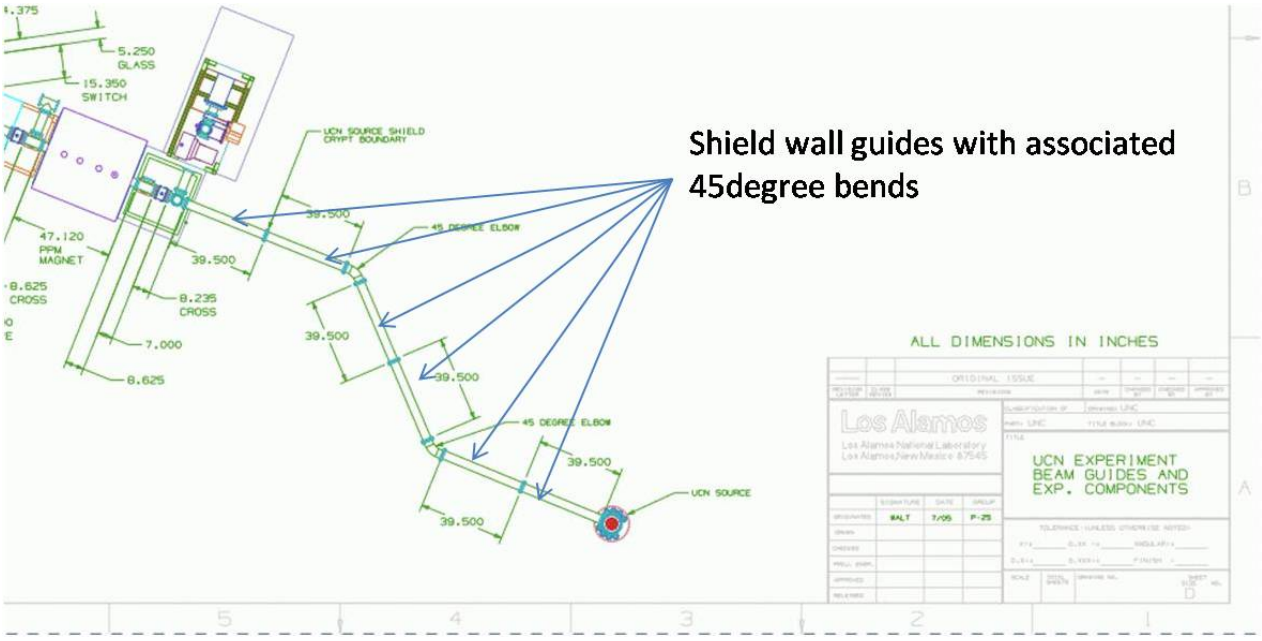

Figure 6.1: CAD drawing of the UCN source shield-wall guides. Modified with permission from UCNA collaboration (2010) [181].

In addition to the material change, the shield-wall guides were welded together and/or welded to Conflat (CF) Flanges to produce a lower-gap system than previous coupling schemes while providing a vacuum seal. A CAD drawing of the source beam line configuration is provided in Figure 6.1. Straight sections were made by welding two, 1 m long tubes together and then welding CF flanges to the ends. In addition, two 1/8 inch diameter holes were also drilled into the sides of each guide section, where two 1/8 inch outer diameter tubes were welded into the holes to provide ports for UCN monitors. The 45° bends were made by employing 45° elbows each with a 6 inch center line radius and welding CF flanges to the ends. Elbows were used instead of straight/angled cut sections, to provide the UCN a gradual bend. Thus three 2 m-long straight sections and two 45° elbows were used to pipe the UCN through the shield-wall. Unfortunately, the TIG welds left an unknown surface that extended out about 1/2 inch from each weld as the various metals in the alloy precipitated out and oxidized with the residual air [109]. These rings are suspected to be a loss point for UCN. Chemical analysis, such as XPS and/or SIMS could be performed on sample welds produced by repeating the welding process to investigate these surfaces. Examination of the actual surface resulting from the welds is not possible, but similar examples could provide insight into these surfaces.

These shield-wall guides have been in place since 2006 and the resulting spectrum, shown in figure 6.2, was obtained in 2007 (note this also includes the installation of a source insert discussed in section 6.4.3 below). Replacing these guides with a higher Fermi Potential material would obviously increase the flux outside the shield-wall. Possible alternatives include ^{58}Ni coated stainless steel, nickel coated stainless steel, or diamond-like carbon coated stainless steel or quartz. The nickel coatings might withstand the previously used TIG welding process; however the diamond-like carbon coating will almost certainly delaminate due to thermal expansion mismatch with the stainless steel substrate during the welding

process.

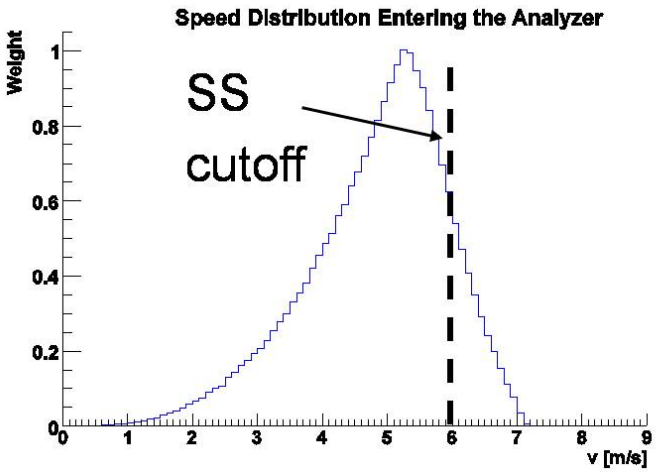

Figure 6.2: The 2007 UCN velocity distribution generated by employing an solenoid magnetic field to axially analyze the UCN energy distribution, in conjunction with a Monte Carlo simulation after replacing the shield-wall guides with SS versions and the installation of a new source insert in 2006. The distribution is in fair agreement with that expected from a SS Fermi Potential transport system. Figure used with permission from Adam Holley (2010) [65].

6.4 LANL SD_2 Source Inserts

Ultimately, four separate source inserts have been made by various groups, but all have been coated at Virginia Tech. Modeling of various source designs occurred in 2004 when the first signs of something being wrong with the source surfaced. Based upon these models a new source insert was installed in 2005, 2006, 2007, and 2009. In this section I will briefly outline the different designs modeled, then delve into the aspects of each insert with emphasis on the challenges encountered and lessons learned during the coating process.

6.4.1 Source Insert Simulations

Three different source inserts were modeled, pictured in figure 6.3. Scenario 1 was essentially a refurbishment of the original source, which involved coating the flapper rods and other uncoated stainless steel with ^{58}Ni, improving the specularity (smoothness) of the reflector plate, and cleaning the ID surface of the ^{58}Ni coating source tube itself. Scenario 2 employed a 7" ID stainless steel DLC coated tube insert with a flapper that obstructed the insert by $\sim$40% during filling, but had the support rods on the outside of the insert and only the flapper actuator rods in the UCN volume. Scenario 3, involved using a 4" ID quartz tube coated with DLC and constructed into an elbow which would direct the UCN from the source to the exit guide. In this case a shutter type flapper could be used to provide a completly unobtructed view from the SD_2 to the source bottle. Initial simulations showed an continuous/equilibrium output for the three scenarios of: 16, 26, 63 over the 2004 source design [61]. In addition scenario 3 had the option of attaching a polyethylene slab underneath the shutter to improve CN production, which seemed to increase the UCN output by another factor of 1.25.

At the time, scenario 3 was the obvious choice and so the University of Washington and LANL invested a significant amount of resources to produce a working source bottle/guide design, shutter actuation mechanism, and cold polyethylene insert. These efforts led to a reduction of the source tube ID to 2.95" from 4" and the realization that residual gaps could be somewhat large and difficult to control. The reduced diameter was chosen so that a shutter/flapper could be made to completely open and close the source-insert tube and also facilitates the mating to the 2.75" OD exit UCN guide in the shield-wall. To eliminate gaps at the elbow joints, a sodium silicate (water glass) solution, 1.0 ml of sodium silicate: 0.7ml of DI water: 0.12 g of potassium hydroxide was tested to act as a glue [63]. This left the

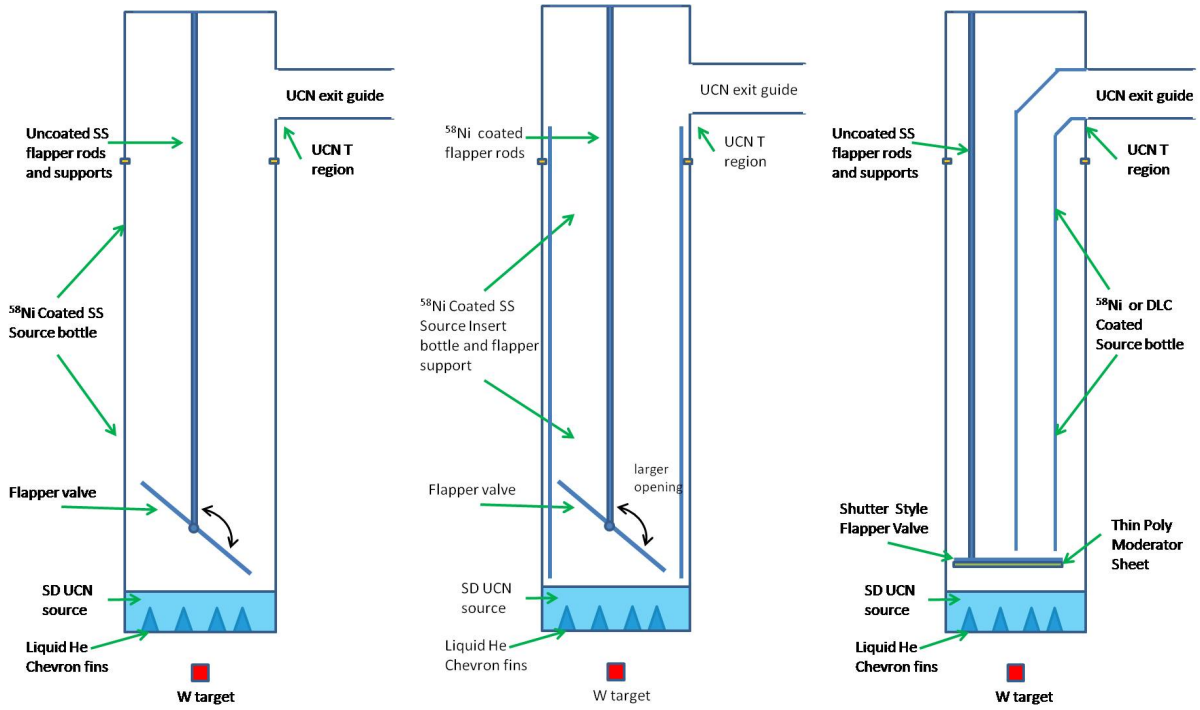

(a) Scenario 1 (b) Scenario 2 (c) Scenario 3

Figure 6.3: Diagrams of the different source insert options:
a. Vacuum-clean source bottle, and ^{58}Ni coat all the bare SS in the UCN volume.
b. Install a fresh ^{58}Ni coated stainless steel insert and improved flapper opening angle.
c. Have smaller UCN guide pipe UCN to exit guide directly and install shutter-style flapper with extra poly moderator underneath.

gaps at the ucn exit guide and shutter. Further modeling showed that if the gaps were too large (3 mm at the ucn exit guide and 6 mm at the shutter) then scenario 2 and 3 become equivalent in terms of UCN output. Nevertheless, the achievable gaps were thought to be smaller than these and the production of the scenario 3 source insert continued.

6.4.2 2005 Source Insert/Scenario 3

DLC quartz versions of the guides were made, but were not used because some of the coatings showed signs of delamination and RATH True 10 3" OD 316L stainless steel versions were made. The shutter involved an aluminum plate attached to a counter-weight made from a specially forged PbBi alloy in addition to some stainless steel bolts used for mounting the pieces together. The special alloy was used to reduce the overall neutron activation of the insert. These parts were mechanically polished, cleaned, and coated at Virginia Tech. Standard cut and color compounds along with medium density cotton buffs in a pneumatic die grinder were used to polish the components to as close to a mirror finish as possible. They were then sonic cleaned in lab soap (Alconox/water solution), acetone, methanol, De-Ionized (DI) water and then rinsed with more DI water, following the standard recipe. The pieces were then blow-dried with Ultra High Purity (UHP) N_2 and then baked in a vacuum oven at 200 C for 24 hours. They were then bagged in polyethylene bags with Ar ready to be transfered to the ebeam coating chamber.

In preparation for learning how to operate the ebeam, sample strips of Al were prepared with the same polishing and cleaning processes. The sample pieces were then mounted in a Bell Jar style ebeam evaporator, with a crystal rate monitor attached, see section 3.5.1 for details on crystal rate monitors, provided by the Electrical and Computer Engineering (ECE) department at Virginia Tech. The following coatings were tested on two substrates

each: ∼15 nm of Cr, then ∼100 nm of Ni and just ∼100 nm of Ni, where all the materials were deposited at a rate of ∼10 Å/sec and were held in 2cc graphite ebeam crucible liners. The Cr layer acts as an adhesion, "sticky", layer that helps bind the nickel to the aluminum substrate. The Cr/Ni sample passed several tape tests while the Ni-only layer failed them. The tape tests were performed with Scotch 9425 (regular office tape) and Kapton (acrylic adhesive) tapes. The other two samples were baked in an Ar environment at 200C for ∼12 hours, to see if this light annealing procedure would improve the adhesion of the thin films. Both annealed samples passed tape tests and several liquid nitrogen (LN_2) cold tests. Here the coated component is submerged in LN_2 , where it quickly reaches ∼77° K. Once in equilibrium, the component is then taken out and allowed to warm up in air. After reaching room temperature if the coatings is still adhered, the coating is said to have passes the LN_2 test. As a result of these test samples it was decided to coat the flapper assembly with ∼15 nm of Cr and then ∼100 nm of ^{58}Ni and then bake them in an Ar atmosphere over night at 200C for good measure. The counter-weight and flapper, creatively mounted together in the coating chamber, required 6 depositions: one each for the top and bottom, and then 4 sides rotated by 90°. The tops and bottoms of the mounting hardware were coated alongside during one of these depositions.

In addition to the source guides and flapper assembly, Los Alamos commissioned a HDPE source cover cylinder and several rings and disks that could lay between the chevrons (SD2 cooling fins) of the original source design, see figure 6.4. The addition of this poly was expected to increase the CN production directly near the SD_2 and therefore increase the number of CNs downscattered into the UCN regime. The poly was flash coated/encapsulated with several microns of 304 stainless steel and then Nickel by Deep-Coat Metalizing, Inc. [76] in order to reduce the outgassing and aid in the adhesion of the ^{58}Ni coating. One has to consider the relatively low melting point of polyethylene, ∼130° C, and take care not to

(a) (b) (c)

Figure 6.4: Detailed figures of the Scenario 3 source insert metalized poly moderator:
a. CAD drawing of poly source insert cover and cylinder
b. Photograph of the poly source insert cylinder, before coating, and the SD_2 source chevron.
c. Photograph of the poly cylinder mounted for coating along with an extra disk and ring.
Figure modified with permission from UCNA collaboration [181].

heat the poly past this point during the deposition. In addition, coating of the ID of the cylinder required the use of the tube coating chamber where a custom ∼30 inch long single-pocket ebeam from MDC is employed and described in 3.4.3. To apply a Cr/^{58}Ni coating via the ebeam, using this chamber, one needs to break vacuum and swap out the evaporant materials. It is really best to not break vacuum if at all possible, and so adhesion tests were performed on the metalized coating with only nickel instead of Cr/Ni.

To find acceptable settings associated with the ECE chamber, one of the metalized disks and rings were ultrasonic cleaned with Acetone, Methanol, and DI water and mounted ∼12 inches from the ebeam source and coated with nickel. The first test, with deposition rates near 10 Å/min, completely melted the small disc and but left ring intact (its larger mass was able to absorb more heat before melting). However, the coating on the ring passed several tape tests and so it was decided that the metalized HDPE parts could just be coated with ^{58}Ni and didn't necessarily require a Cr/^{58}Ni . With this in mind a second ring and disk were coated at a deposition rate of ≈3 Å/sec and both pieces survived and passed tape tests.

In addition, drive, rotation, and filament current settings were found for some test poly discs held at about the same radius as the ID of metalized poly cylinder. With the settings for both chambers known, production work began to produce coatings on all the possible UCN exposed surfaces. The top and bottom of the cylinder, ring, and disk were coated in the bell-jar style ebeam. The cylinder was held to a mounting plate, with thin stainless steel wire such that the face being coated was still ∼12 inches from the ebeam source, while the ring/disk were held with alligator clips again ∼12 inches from the ebeam source. Care was taken to reduce the shadowing as much as possible from the mounting hardware, but nevertheless some surface area, although small, did not receive the recommended 100nm ^{58}Ni . The cylinder, along with the third set of ring/disk were loaded into the tube coating chamber as shown in figure 6.4c and coated with ^{58}Ni using the settings found during the HDPE disk test.

6.4.3 2006 Source Insert / Scenario 2

Due to the less than satisfactory performance of the Scenario 3 source insert, a Scenario 2 source insert was developed which focused on: a ^{58}Ni coated source bottle liner and a new flapper. Scenario 2 builds upon the lessons learned through the original source and it was felt that with proper engineering, the butterfly style flapper could be made to open up to ∼90° , thereby minimizing the number of UCN blocked from a straight path into the source bottling region. The liner was made by rolling a sheet of #8 mirror finish mechanically polished stainless steel into the form of a tube, which was then tack welded in several places, instead of along the entire seam. This was done to prevent the contamination/roughening of the mirrored surface along the seam. In preparation for coating the source insert, several samples of the same material were coated with Cr/^{58}Ni and just ^{58}Ni . Both samples passed tape tests and LN_2 cold tests and so it was decided to coat the insert without a Cr layer and

thus not have to break vacuum in order to swap out the Cr crucible for the ^{58}Ni crucible.

In order to clean the ∼7 inch diameter, ∼25 inch insert, a dedicated heated recirculating cleaning station was made from an 8 inch PVC pipe, heat tapes, an immersion heater, and 3.1 gal/min Teflon lined recirculating pump. The SS source tube was cleaned in a recirculating 2% Liquidnox® in DI water solution warmed to ∼50° C for ∼6 hours, rinsed with copious amounts of the DI water, then taken into a cleanroom where it was aggressively wiped down with Alpha wipes soaked in Acetone and Methanol. It was then rinsed again in copious amounts of DI water, then blow dried with UHP N_2. The tube was loaded into the tube coating chamber and the coating process began with the same parameters as was used with the poly cylinder. Unfortunately, the coating process was not smooth at all and the chamber was vented several times for the following reasons: high voltage lines shorting to ground, purposely vented to pull witness strips in order to measure thickness accumulation, and most problematically that the electron beam kept drilling a hole through the nickel and graphite crucible. The high-voltage arcing issue has been discussed in section 3.4.3. It was incorrect to assume that the same deposition parameters (electron beam current/deposition rate) used for the metal encapsulated poly cylinder would be valid for this coating session. There were too many variables - such as the electron beam spot size and position change as a function of accelerating high voltage, and repeated heat and cool cycles, and that fresh ^{58}Ni material evaporates much more readily from new loadings than from previously evaporated nickel/graphite crucibles. When the expected thickness was reached after 8 passes, assuming ∼22 nm/pass, the chamber was vented with argon and witness strips measured for thickness. These strips showed a profilometer measured thickness of ∼20 nm, not the expected 180 nm. At this point the value of having some sort of deposition rate monitor was acutely realized. Most evaporation systems employ a crystal micro-balance monitor, discussed in more detail in section 3.5.1, to provide this data. A crystal monitor was identified and modified such

that it could be mounted inside the coating chamber while not obstructing the linear path of the source insert tube (see figure 3.11) and was used to measure the deposition rate before and after each pass. Ever since, the installation of the cyrstal monitor has been an essential part of setting up the tube coating chamber for ebeam evaporations.

The problem of the hole developing in the ^{58}Ni/graphite crucible is that the deposition rate of evaporant decreases as the hole develops, as well as the possibility of evaporating carbon atoms which then deposit onto the insert (in fact this is one reason graphite was used, because it has a very low neutron absorption cross section). To address this a preemptive approach is taken by most commercial ebeam systems where a rastered electro-magnet is used to sweep the electron beam focus around the material in the crucible. In our single pocket, non-rastered ebeam this can be prevented by increasing the electron beam current which tends to melt more of the material in the crucible which then falls into the well of evaporating ^{58}Ni. This occurs because the electron beam has a halo around it. However, due to our extended coating times, the nickel and graphite crucible begin to react to form a nickel carbide compound that our electron beam halo cannot get hot enough to melt and have flow into the hole. Thus, increasing the electron beam current just increases the size of the hole. In addition, almost every time the hole develops during a coating pass when the ebeam head is obstructed from view. Thus the lowest observed deposition rate is used to estimate the thickness/pass which causes more ^{58}Ni to be deposited on some areas of the of source insert than others. To address this issue, once a hole is discovered, the chamber is vented and the crucible taken out to be remelted using a rastered ebeam evaporator. This can prolong the life a few more hours, but as the graphite concentration increases, it becomes harder and harder to get the nickel to flow and cover the hole in the crucible, even with rastering. Thus a new crucible with fresh ^{58}Ni has to be conditioned (melted) and was used for the last $\sim$80 nm of the coating. In the end, witness strips experiencing the entire

coating process showed ∼400 nm of ^{58}Ni coating. Interestingly enough, the effect of each vacuum break could be seen in the growth of the coating. This can be seen in figure 6.5, which shows a SEM micrograph of the cross sectional view of one of these witness strips. Here distinct layers can be seen, where each line corresponds to a vacuum break and then subsequent new ^{58}Ni nucleation and growth. The sample was made by breaking the witness strip in half and looking edge-on with the microscope. Despite eventually getting enough ^{58}Ni onto the surface, something had to done to address the fairly short usable lifetime of the ^{58}Ni loaded graphite crucibles. To this end, an aluminum oxide crucible along with a procedure to recover the ^{58}Ni was developed and is described in section 3.5.2.

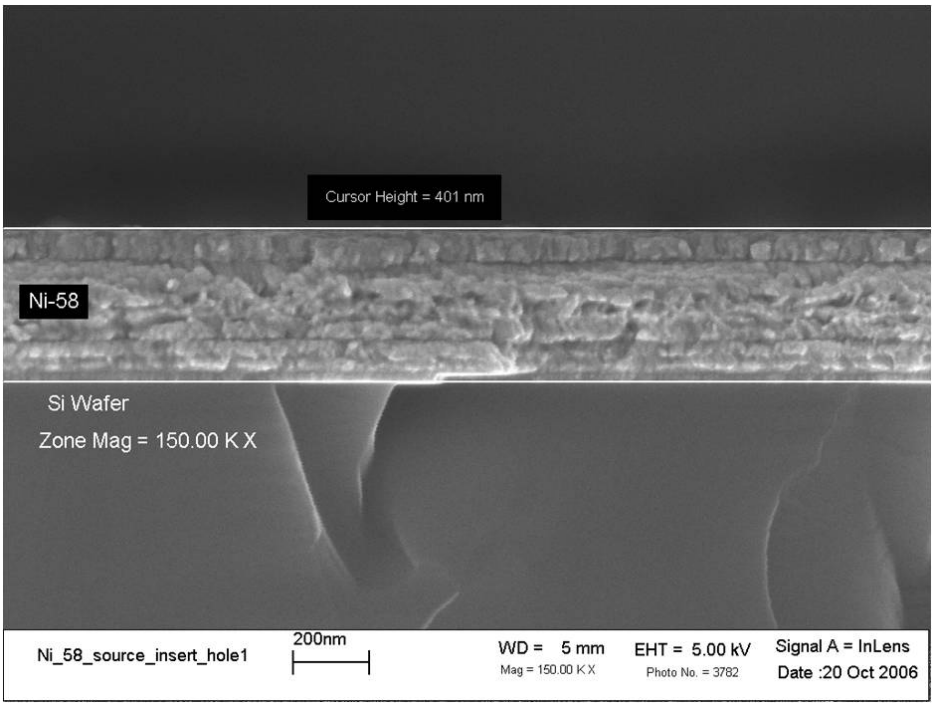

Figure 6.5: SEM micrograph of the cross section of a ^{58}Ni coated Si witness strip from coating the 2006 source insert. Several lines can be seen throughout the cross section, corresponding to a venting incident.

In addition to the source insert liner, a new flapper with associated hardware was coated. By this time, the physics department at Virginia Tech had purchased its own bell-jar style

thin-film deposition system (see figure 3.4.2) and so this was used instead of the ECE at VT's system. One major benefit of this system, is that the substrate holder can rotate during the deposition which increases the uniformity of the applied coating. Figure 6.6 shows a partially constructed flapper and an example of how the flapper parts/hardware were coated. The components were cleaned with the standard procedure and then had ∼15 nm of Cr and ∼180 nm of ^{58}Ni applied, where some components required 6 depositions to coat all the sides.

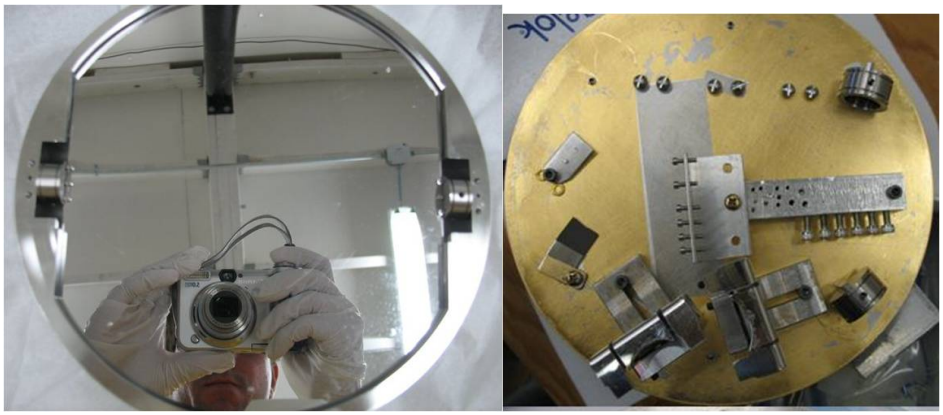

(a) Flapper before coating. (b) Flapper hardware before coating.

Figure 6.6: Photographs of the 2006 flapper.

6.4.4 2007 Addition of Permanent Poly Moderator

In early 2007 Mark Makela made several neutron moderation measurements, in a mock SD_2 source geometry as shown in the upper right of figure 6.7 where ^{3}He detectors were located where the SD_2 would normally be and was surrounded with 1/2" thick poly bricks. A ^{252}Cf source was used as a neutron source, to simulate the tungsten target, and the rate in the a ^{3}He detectors was measured as a function of poly "top layer" thickness. These measurements also matched reasonably well to a simulation of the original source with added poly directly underneath the SD_2 source [178]. All this verified the motivation for encasing SD_2 in the polyethylene. Given that the amount of poly that actually made it into the bottom of the

original source was ∼0.13 cm and ∼0.5 cm along the walls of the SD_2 [112], another attempt at adding more poly around the SD_2 source was made. The reasonably successful butterfly flapper/insert design prevented the "full trap design", but more poly could be added around the SD_2 source (in a space designed to be a vacuum thermal break) as well as directly underneath the SD_2 source. About 5 cm of poly was added underneath the SD_2 source, close to the maximum amount without greatly impacting the rest of the source operation.

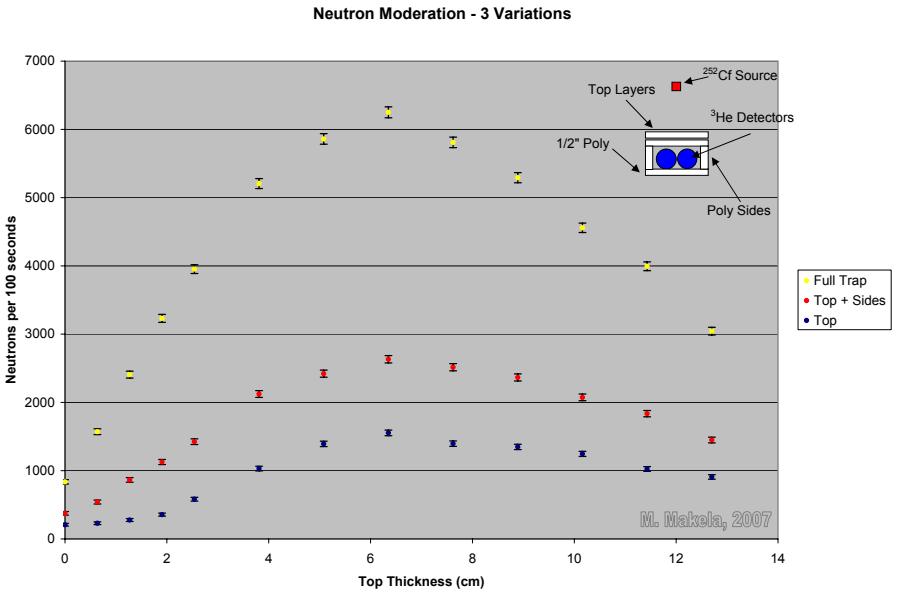

Figure 6.7: Cold neutron measurements with various poly moderator thickness in a mock SD_2 source geometry. Based upon these measurements as well as supporting simulations ∼5 cm of poly was added in between the W target and the SD_2 source. Figure used with permission from Mark Makela (2010) [112].

6.5 2007 Source Insert

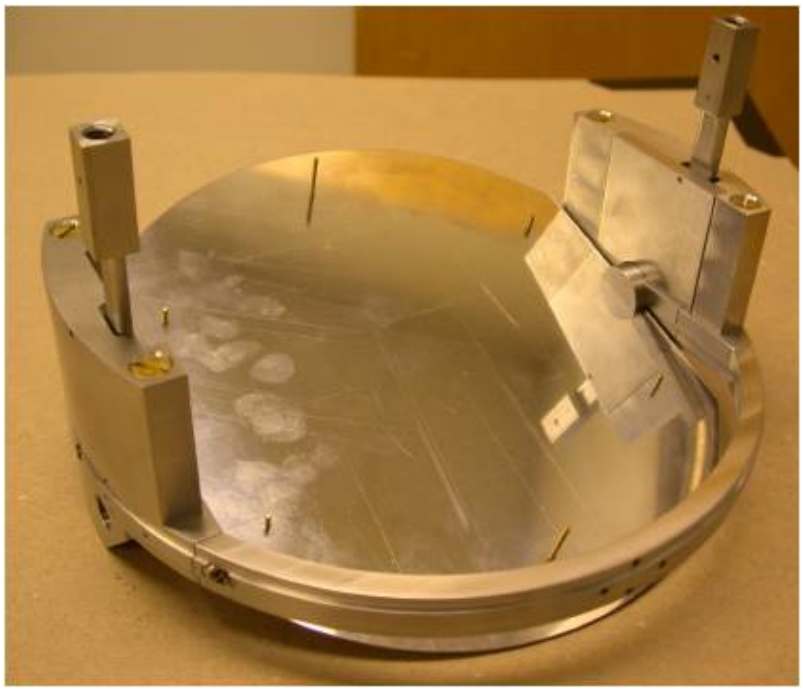

Figure 6.8: The 2007 assembled lower flapper system before cleaning and coating. Figure used with permission from UCNA collaboration (2010) [181].

The 2006 source insert had several gaps/crevices where UCN could enter and eventually become lost, and so a flapper system based on the 2006 design, but with a focus on reducing these gaps was created. The bottling region was again made by rolling a sheet of #8, mirror finish, polished stainless steel sheet into the form of a tube, and held by several tack welds along the seam. The flapper system required many more 304 and 316L SS components to be coated, including the OD of two flapper actuator rods. A picture of the assembled flapper before coating is provided in figure 6.8. These components were machined at LANL and then electropolished by a different company than we normally use. To aid in the holding of the components along with the numerous screws/bolts requiring coating and custom holder was made and is shown in figure 6.10. Here "L" brackets out of aluminum were made such that

they could lightly clamp the coated components which also required ∼6 depositions. The same cleaning procedure and coating plan as was used with the other flapper components from previous inserts was used (∼15 nm Cr and then ∼180 nm ^{58}Ni). After coating many of the parts, they were cold tested with LN_2 and upon their return to room temperature each one of them had some sign of delamination. In fact the coating on some of the components started to peel during the deposition, as shown in Figure 6.9.

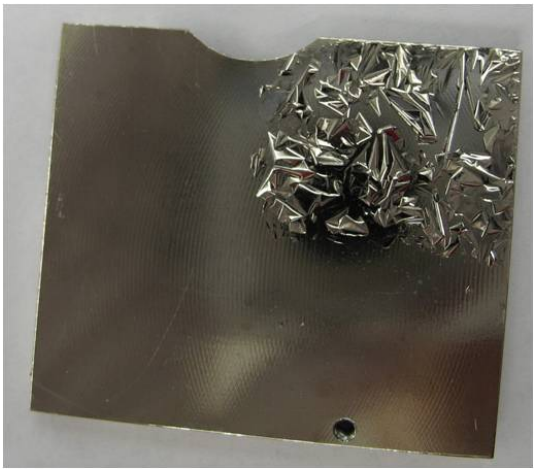

Figure 6.9: Photograph of the delamination of a 2007 flapper component after a LN_2 cold test.

Some more small machined components were prepared with the same cleaning and coating recipe, except the samples were glow-discharge cleaned for ∼20 min with the following parameters: UHP Argon flowing through a slightly open vacuum valve such that pressure inside the chamber stayed close to 100 mTorr and a transformer operating at 956 V/31 mA at 60 Hz. This transformer was readily available and provided the desired low power of ∼30 W which was chosen in order to prevent the sputtering of the substrate itself. Despite these efforts, the coating on the machined components still delaminated to some degree during LN_2 cold tests. Several reasons were postulated as to why the coatings delaminated: contamination during handling/mounting, inadequate cleaning procedure not removing something

left over during the electropolishing process, increased film stress due to the thicker films resulting from the multiple layers, etc. Nevertheless, these parts were shipped out to Irving Polishing to have the coating polished off and re-electropolished at Able Electropolishing. Meanwhile, we began coating a series of SS samples with different solvent cleaning steps (variations of soap, acetone, alcohols, and DI water), with and without Ar glow discharge before deposition, with and without a Cr interlayer, and different sample materials (# 8 mechanically polished 304 and 316 SS plates, flapper material (electropolished #8 mechanically polished 304 SS plate), and Trent Electropolished 316L SS tube). The samples were then tape tested and the following conclusions drawn: the coating adhered better to electropolished samples than non-electropolished ones, a Cr layer seems to aid in the adhesion of the ^{58}Ni, and sonic cleaning with DI water in addition to rinsing with DI water is important.

Thus, motivated by the fact the entire UCNA experiment was being held up by the coating of these components and armed with the above information it was decided to coat the flapper with the most successful cleaning/coating recipe for the flapper material. The flapper plates were assembled and the screws (holding the two plates together) were "riveted" by deforming the end of the screw with a center punch and a hammer. By this time class 100 cleanroom grade gloves and wipes were used to hold the flapper during the mounting process in hopes of reducing the contamination to the flapper surface. The source bottle side of the flapper plate was coated first then flipped and the SD_2 side was coated with no additional liquid/solvent cleaning in-between coatings. After coating the flapper it was LN_2 cold-tested and passed with no signs of delamination. With this success, we continued coating all the repolished/re-electropolished components and screws in the same manner with the addition of a vacuum bake at 200° C for ∼24 hours just before mounting the components into the chamber. All but two components passed the LN_2 cold tests. Although not fully robust, the development of the cleaning and coating process was moving in the the right direction and

it appeared that baking the components was a helpful addition to the process.

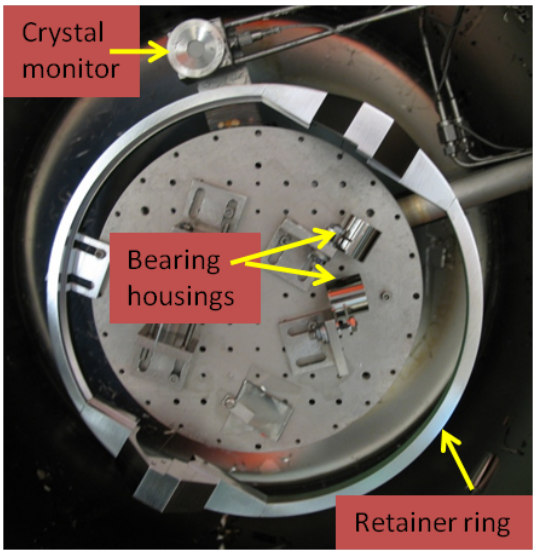

Figure 6.10: Photograph of the mounting scheme used to coat the 2007 flapper retainer ring and source cylinder faces. The ring and cylinder was held with thin gauge SS wire through screw holes in the part and mounting plate so as to not obstruct the evaporant flux. The bearing housings that previously failed the LN_2 cold test were repolished, recleaned, and recoated during these depositions.

The ∼7 inch diameter flapper retainer ring and short length source cylinder would not fit in our ∼6 inch diameter vacuum oven and so we could not bake these components the way we vacuum baked the small machined components. To address this it was realized that we could use the quartz lamps already set up in the bell-jar style deposition chamber. The ring and cylinder were mounted, one at a time as shown in figure 6.10, in order to coat the faces of the cylinders and allowed to bake between 100-125° C (as measured by the internal thermocouple situated next to the components in view of the lamp radiation) for ∼14hours and then coated with the same recipe, but this time with the Quartz lamps on during the depositions. In addition the lamps were left on for 3 hours after the deposition, where the temperature was kept at ∼100° C to provide a light annealing effect. Once the temperature inside the deposition chamber reached ∼25° C, the chamber was vented and the component

either flipper to coat the other side or quickly bagged in class 100 cleanroom polyethylene bagging material with argon. Once the faces of both items were coated the ID's of these components were coated in the tube-coating chamber with the single pocket custom-length ebeam installed. The ring and cylinder were connected to each other via hose clamps and SS shim stock, effectively making one slightly longer tube, and attached to the front carriage. In addition a a glow-discharge igniting electrode was installed as well as the water-cooled crystal monitor to obtain deposition rate information. The components were glow discharged cleaned at an Ar pressure of ∼300 mTorr and electrode setting of 956 V/31 mA/60 Hz for ∼30mins, before depositing the ^{58}Ni. This Ar pressure was chosen to maximize the discharge brightness, as viewed by the eye, on the rings. The rings were coated with ∼125 nm of ^{58}Ni, as measured on a witness strip, and then another ∼75 nm was applied. A Cr interlayer was not used in hopes of eliminating any vacuum breaks during the coating process. The retainer ring passed the LN_2 cold test, but the cylinder did not as a ∼3 cm^2 area had delaminated. After some discussion, we decided to aggressively wipe off what coating would come off, resonic clean, and then coat the the component again. The delaminated region had increased into the faces of the cylinder from these processes and so both faces were recoated in the bell-jar style ebeam. The ID would be coated along with the source insert. Despite this failure, it suggested that either baking the components, via the quartz lamp, before and during the deposition and/or applying a Cr interlayer were crucial steps in the coating process.

2007 Source Bottle

The ∼30 inch long source-insert bottle was cleaned in the same manner as the 2006 version. However, we decided to install a quartz lamp and Type-K thermocouple to bake out the cylinder before, during, and after the deposition as shown in figure 3.11. The flapper cylinder, a newly machined flapper retaining ring (the previously coated one had some design issues

and a new one was made), and source insert were coupled together again with hose clamps and shim stock. The tube was rotated at ∼12rpm and driven in and out at ∼1 in/min over the quartz lamp and glow discharge igniting electrode, while flowing argon and pumping to maintain a pressure of ∼300 mTorr of pressure as measured by the convectron gauge. The internal temperature measured by the thermal couple quickly rose to $> 150^\circ$ C. The tube was baked out like this for 2 hours and then the ^{58}Ni deposition started at deposition rate of ∼4 Å/sec, as measured by the crystal monitor.

Over the course of coating these pieces, several temperature related failures occurred, often in the middle of a pass, which required venting with argon to fix. Differential heating of tube mounts caused extra friction on rotational bearing surface requiring more torque from the rotation motor that could be transfered through the Viton O-ring. As a result the O-ring often slipped and even came out of its groove. To combat this, the set screws holding the back carriage/bearing system together were completely loosened and retaining washers, first made out of Delrin then Teflon (the change due to Teflons's higher melting point) were added to hold the bearing in place, but still allow the bearing to rotate relatively freely, see figure 6.11. In addition, the internal temperature was closely monitored so that the temperature stayed around 125° C. Unfortunately, it took several bake/deposit/Ar vent iterations to home in on these settings before one could guarantee the thickness of ^{58}Ni was greater than 180 nm. In the end, 16 linear passes were taken over the evaporating ^{58}Ni material, since a pass was re-done if a failure occurred during the middle of a pass and it became evident that a more temperature-tolerant-in vacuum rotation system was required. Step height measurements of the witness strips attached to these components showed the last eight continuous passes (vacuum-break free) applied ∼250 nm of ^{58}Ni, while the entire coating process, including all 16 passes, provided ∼560 nm of ^{58}Ni.

The ∼30 inch long source-insert tube was too big to LN_2 cold-test at Virginia Tech,

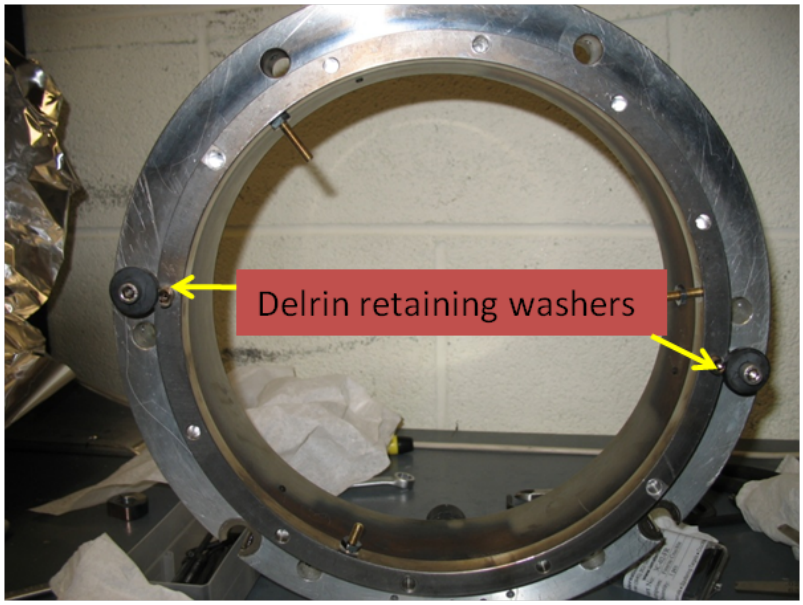

Figure 6.11: Photograph of the Delrin retaining washers mounted to the back carriage in order hold the bearing in place, but allow it to rotate more freely. PTFE versions were soon added to both carriages in order to allow the entire carriage system to rotate more freely.

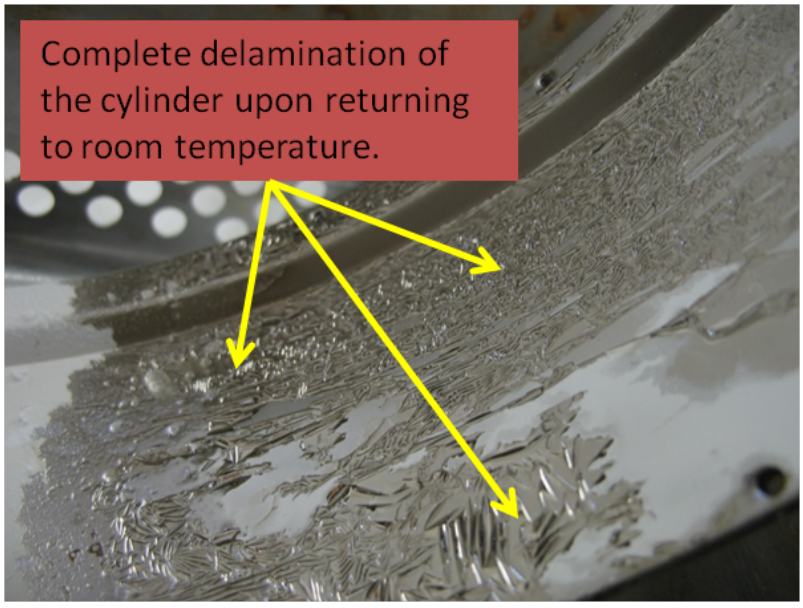

Figure 6.12: Complete delamination of the ^{58}Ni film on the source insert cylinder after several coating/vacuum break sessions.

however the flapper retainer ring and cylinder were tested in LN_2 . The new ring passed the cold test, but the cylinder completely failed the cold test again. Figure 6.12, shows the delamination of the coating upon the return to room temperature. It is unknown whether the delamination occurred because of high film stress (since some places had $\sim$1 μ of ^{58}Ni), a thick oxide layer, or other contamination that developed during the exposure to air/water/solvents and was not removed by the quartz lamp. It was decided to try to remove all the coating and start again. The entire coating came off with repeated LN_2 dunks and then the part was ultrasonic cleaned in a slightly acidic (pH of 3) 2% Citranox® in water solution, the usual solvents, and then given a generous DI water rinse. The part was recoated with ^{58}Ni, where the quartz lamp was employed for all the depositions, and passed two LN_2 cold tests. Albeit disheartening at the time, and important lesson was learned from this ordeal: once a coating delaminates the entire surface needs to be free of previous coating before re-cleaning and trying again.

1/4" diameter Rod Coating

The coating of the two, $\sim$25 inch long, 1/4 inch diameter actuator rods presented a whole new challenge for our coating process since the OD (rather than ID) needed to be coated. One possible answer to this challenge involved the two rods moving linearly over ebeam, while not rotating. After enough coating had been applied to a side, the chamber could be vented and rods rotated and the coating process repeated. However, a method that would rotate the rods while they moved over the ebeam was preferred, since it didn't require breaking vacuum. A chain/sprocket driven system was designed and built as shown in figure 6.13. This method, if it worked, could also provide the rotation system for coating the ID of components. The rods were cleaned and coated in a similar method as the long source insert, again employing the quartz lamp. New actuator rod ends, this time made out of

nickel, were also coated in this fashion. The coating process was now quite robust as both rods were able to withstand aggressive rubbing with an AlphaWiper® (required to unscrew the rods from the mounting system) and in the case of the small actuator rod ends passed several LN_2 cold tests.

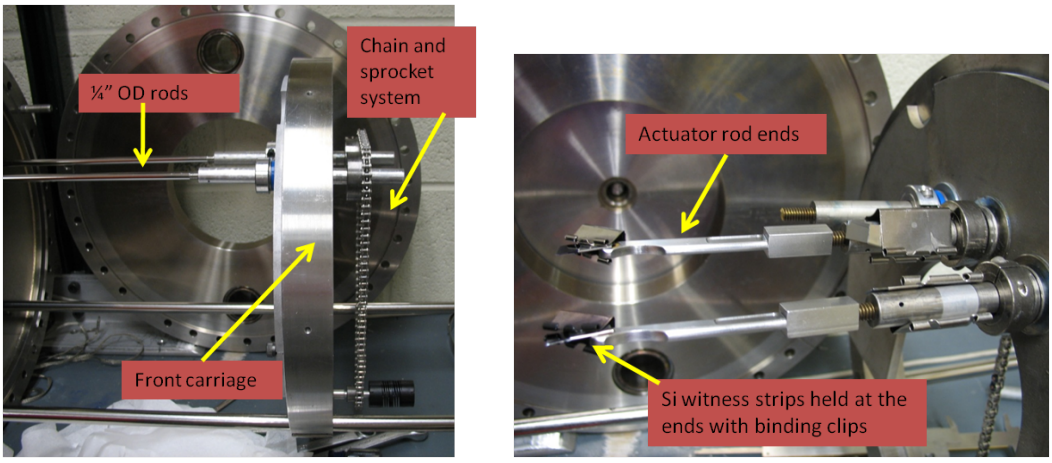

(a) Mounting setup for coating the 1/4" rods

(b) Mounting setup for coating the actuator rods

Figure 6.13: Photographs of the chain driven rotation system for coating the OD of the 2007 Source Insert Actuator Rods.

During the initial operation of the source it was realized that using two actuator arms over-constrained the system resulting in binding and it quickly became standard practice run the flapper with only one actuator rod. The source was quite successful and was operated from late 2007, through all of 2008, and into the early part of the 2009 proton accelerator cycle.

6.6 2009 Source Insert

The 2009 flapper incorporated the core ideas of the 2007 source insert, but used a machined 8 inch diameter tube to take the place of the source bottle and flapper cylinder. This

removed the cracks associated with these couplings as well those at the seam of the tack-welded rolled sheet source bottle tube. The flapper components were designed such that the mounting screws bolted from the outside through the source-insert bottle and into the flapper components, thereby removing the screw heads out of the UCN volume. The flapper mechanism focused greatly on simplifying the UCN surfaces, which reduced the number of required coatings for certain components. In addition the flapper system was designed to be actuated with a single tube.

All the small components were coated with the following process: sonic clean in 2% Citranox® in water solution, Acetone, Methanol, Ethanol, blow dried with N_2, vacuum baked with a quartz lamp for ∼4 hours, coated with ∼200 nm of ^{58}Ni, and lightly annealed for ∼3 hours all at ∼125° C in the physics department's ebeam. The mounting scheme was similar to that used for the 2007 source insert components. The large diameter source bottle tube was cleaned in a similar manner as previous source bottle tubes and mounted in the tube coating chamber. The ID of the tube was vacuum baked at ∼150° C for ∼3 hours before coating with ^{58}Ni via the custom ebeam at ∼4 Å/sec. By this time an in-vacuum chain-driven rotation mechanism and air-side stepper motor drive/rotation system had been installed. Unfortunately, the temperature was allowed spike to ∼190° C during the deposition and even at these temperatures, the differeintial heating was so much that rotation failures requiring vacuum breaks occured. When temperatures were kept near ∼100° C, the deposition process ran very smoothly. The tube was allowed to anneal at ∼100 ° C for ∼3hours after the deposition. The same system for coating the 2007 1/4" diameter rods was used to coat the 1/2" diameter tube, with some modifications, because the length of the tube was ∼44 inches. In the end, about 38 inches of the rod was coated, again with similar cleaning and baking out procedures as the source bottle.

Unfortunately, the 2009 source insert didn't really increase the UCN flux to the UCNA

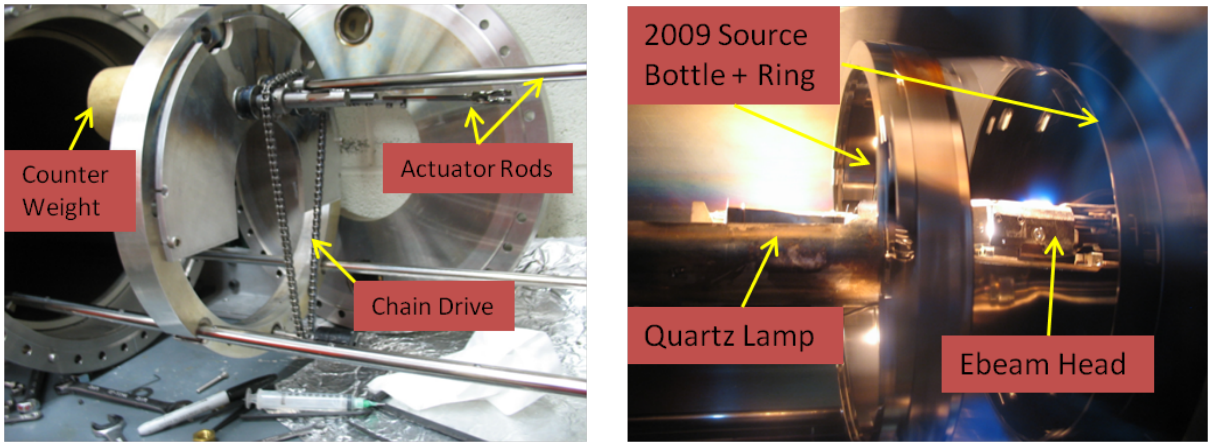

(a) Mounting setup for coating the 2009 Actuator Rods.

(b) Coating the 2009 Source Insert Bottle and Flapper Ring

Figure 6.14: Photographs taken during the 2009 Source Insert ^{58}Ni coating run showcasing the various mounting schemes used inside the tube coating chamber.

experiment. Beam tune studies indicated that only about half of the protons where hitting the tungsten target. It appears that the floor, under the weight of the shield-wall had sunk by several millimeters. Indeed beam on tungsten target tune appears to have degraded over the past few years, despite numerous alignment efforts. In addition shortly after the installation of the new insert a massive LHe leak developed inside the shield-wall, which caused the experiment to be shut down for the rest of the 2009 proton beam run cycle. In lieu of this, a new larger tungsten target was designed and installed in the spring of 2010. Current UCN rates, as as measured by the gate valve just outside the sheild wall, now exceed previous years by about a factor of two.

6.7 Atomic Force Microscopy of the ^{58}Ni Films

Several AFM scans were performed to investigate the surface roughness of the ^{58}Ni films applied to the various source inserts. Figure 6.15 presents the results associated with the

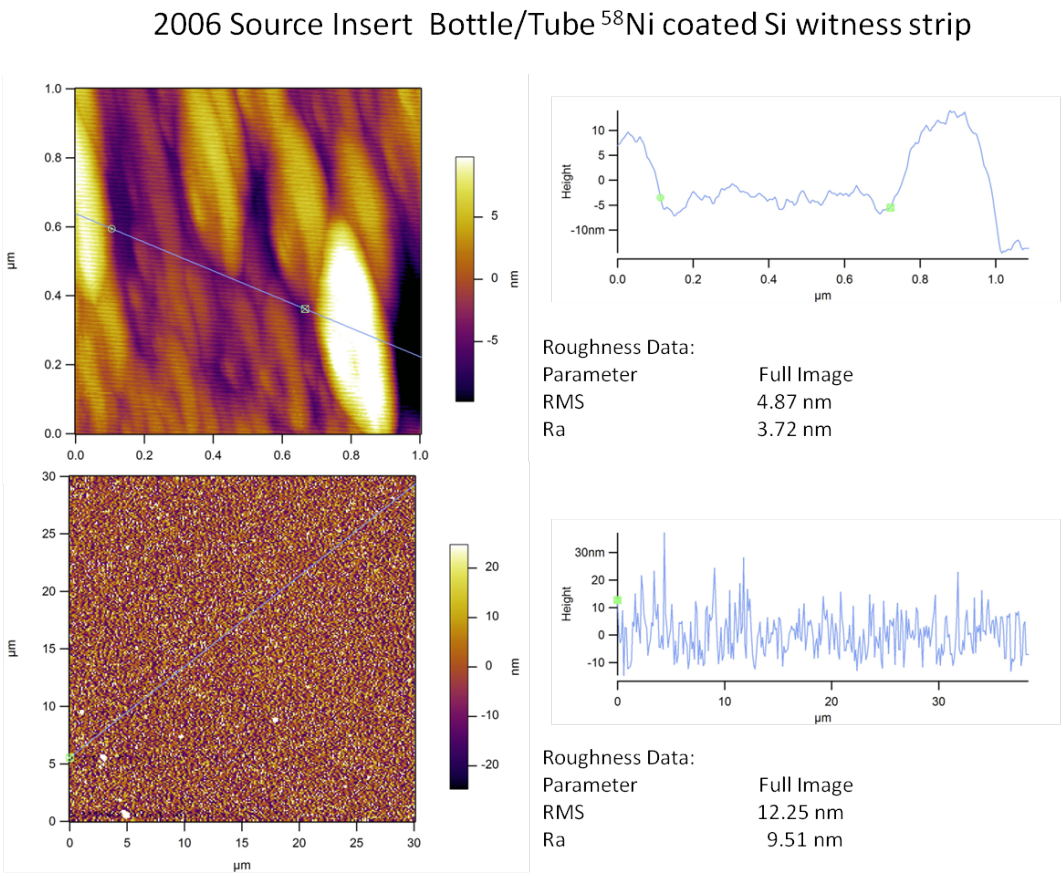

Figure 6.15: Surface roughness scans of a ^{58}Ni coated Si witness strip associated with the 2006 Source Insert bottle/tube ebeam coating session. The quartz heat lamp was not employed and the deposition was carried out in our tube-coating ebeam system. All measurements were made using an Asylum Research Cypher AFM in Tapping Mode.

2006 Source Insert bottle/tube coated with our tube-coating ebeam. Recall this coating session required multiple vacuum breaks, did not employ a quartz lamp during any part of the deposition, and produced a final film thickness near 400 nm. Figure 6.16 shows the results associated with the 2009 Source Insert bottle/tube coated with our tube-coating ebeam. This coating session employed a quartz lamp before, during, and after the deposition and produced a final thickness near 250 nm. In addition, the surface roughness results associated with the 2009 Source Insert Flapper coated in the Physics Department's VE-100 ebeam system are presented in figure 6.17. Again this coating session employed a quartz lamp before, during,

and after the deposition and produced a final thickness near 180 nm. First we note that these values are all roughly consistent with those found for thermal evaporation of ^{58}Ni films by Mark Makela [110]. Secondly, the RMS roughnesses associated with the 2009 Source Insert components are both consistent with each other and slightly lower than the values found from the scan of the 2006 Source Insert witness strip. The increased surface roughness is most likely the result of the multiple vacuum breaks, although the use of the quartz lamp may also play a role.

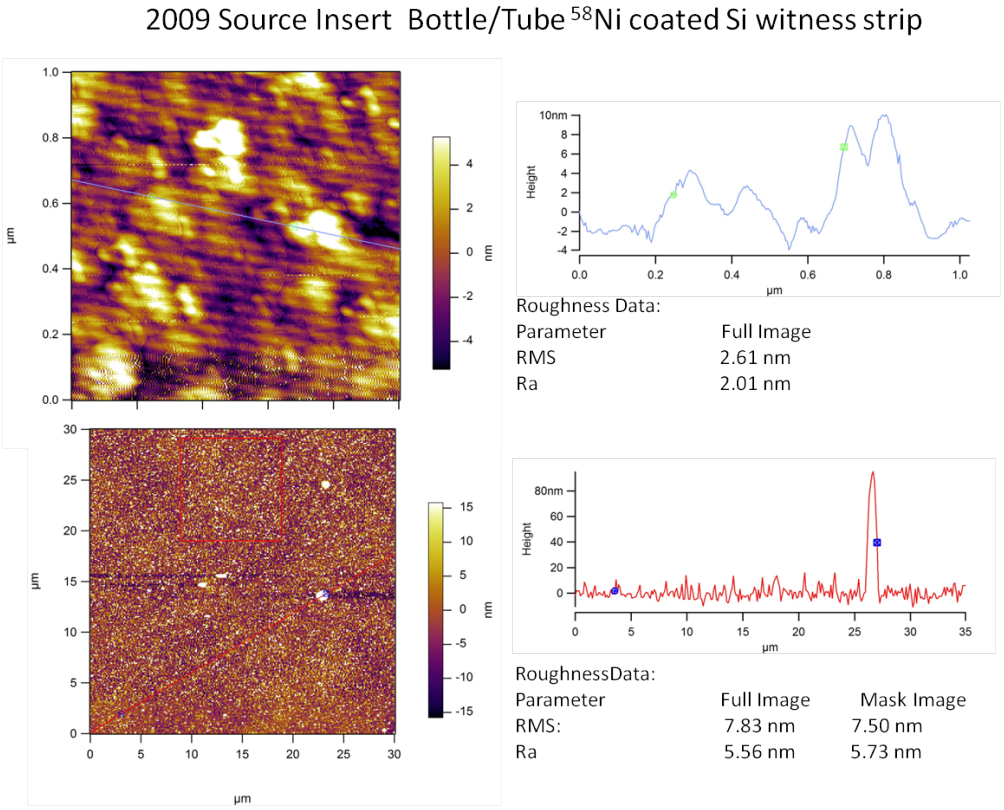

Figure 6.16: Surface roughness scans of a ^{58}Ni coated Si witness strip associated with the 2009 Source Insert bottle/tube ebeam coating session. The quartz heat lamp was employed before, during, and after the deposition, whereas the deposition was carried out in our tube-coating ebeam system. All measurements were made using an Asylum Research Cypher AFM in Tapping Mode.

In addition, the grain sizes of the 2009 ^{58}Ni samples appear to be smaller than the grain

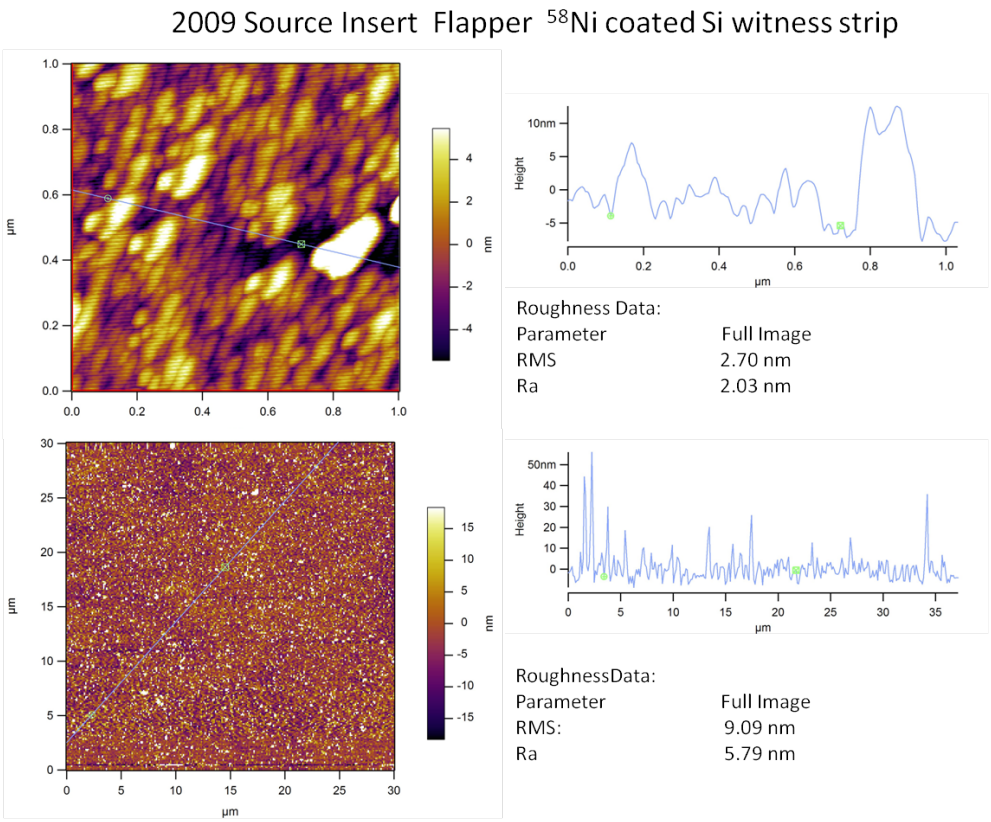

Figure 6.17: Surface roughness scans of a ^{58}Ni coated Si witness strip associated with the 2009 Source Insert Flapper ebeam coating session. The quartz heat lamp was employed before, during, and after the deposition, whereas the deposition was carried out in the Physics Department's VE-100 ebeam system. All measurements were made using an Asylum Research Cypher AFM in Tapping Mode.

size of the 2006 sample. The grain size is important because it affects the ultimate surface roughness of the film as well as its magnetic domain structure; both of which affect how UCN interact with material surfaces. The grain size for our ebeam coated ^{58}Ni films are on the order of the UCN wavelength (50-200nm) and so the magnetic domains may play a role in the overall performance of these films in the SD_2 UCN source at LANSCE. Magnetic Force Microscopy (MFM) may shed light on this issue, especially if the sample can be cooled below LN_2 temperatures. However, this effect can be neglected by making the magnetic domain sizes smaller than the UCN wavelength. For this purpose, Serebrov produces

sputtered ^{58}Ni/Mo(10%) films for UCN applications. Thermal or ebeam evaporation of a bulk ^{58}Ni/Mo(10%) alloy cannot be used to make such a film, as it is not allowed by the Ni/Mo phase diagram. Thus a non-thermal process such as sputtering must be employed. PLD may be used to produce alloy films and a preliminary investigation into using PLD to make smooth nickel films has been performed by David Richardson (an undergraduate working in our group). Figure 6.18 shows the surface roughness of a 40 nm thick PLD Ni film as measured by an AFM, where the RMS surface roughness is 0.8 nm. This result is encouraging and motivates the continuation of this work in hopes of producing extremely smooth ^{58}Ni and ^{58}Ni/Mo(10%) coated guides for UCN experiments.

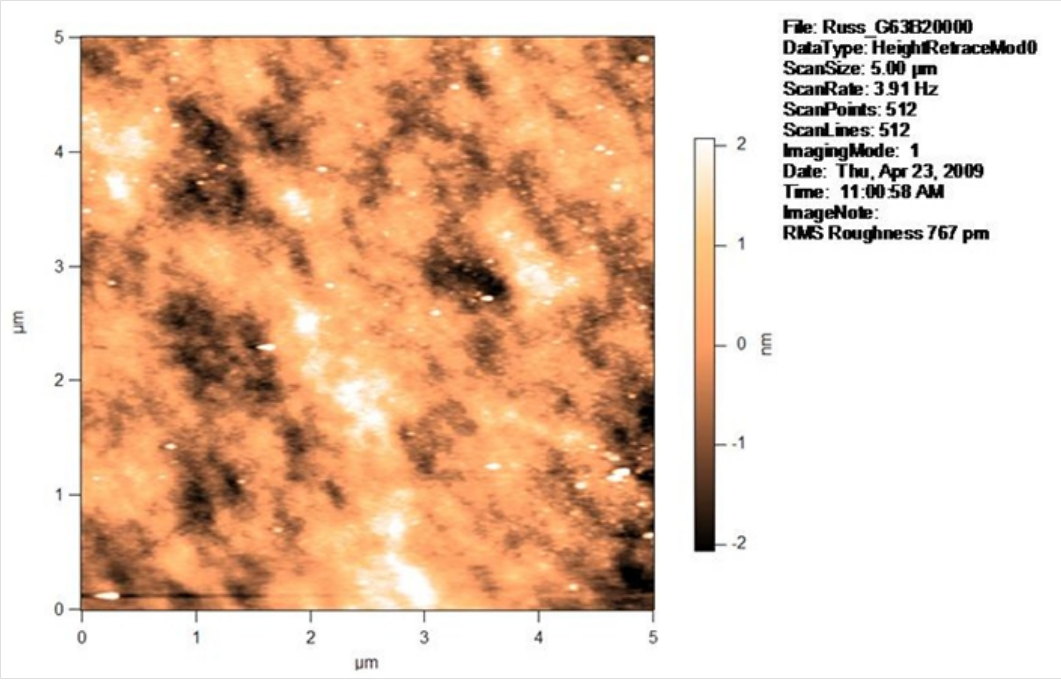

Figure 6.18: Surface roughness scan of a 40 nm thick, PLD coated Ni film on Si witness strip. Note the uniformity of the image and the very low RMS roughness of 0.8 nm. All measurements were made using an Asylum Research Cypher AFM in Tapping Mode.

6.8 Summary

The LANSCE SD_2 source is a testament to the difficulty one encounters when attempting to build and operate such a facility. There are many other parameters involved in operating the source such as: the temperature of the various moderators and SD_2 itself, flapper speed and timing with proton beam pulse, the proton beam pulse time structure and physical position, etc., which have not been discussed, to which the reader is referred to the following references [170] [178]. It is difficult to deconvolve the UCN rate/density effects of these parameters from that of the ^{58}Ni coating and it is not practical to install and run two source inserts, one coated and one uncoated to see how the rates change. However, it is universally agreed that the coatings are a requirement for each and every UCN source. To this end, in the past five years four different source inserts have been installed by the UCNA collaboration and all of the UCN surfaces of these inserts have been coated at Virginia Tech. The size and complexity of the components requiring coating presented its own challenges not normally seen in a university environment, used to coating silicon wafers and glass slides. Thus there was a learning curve associated with getting the production steps right for making a well adhered ^{58}Ni coating on these surfaces. The main points from these lessons are summarized as follows:

1. Some sort of internal diagnostic, in our case a crystal monitor, measuring the deposition rate needs to be in place for every ebeam deposition

2. The target deposition rate should be $\sim$3 Å/sec and definitely less than 10 Å/sec

3. Employing a quartz lamp before, during, and after the deposition is the most critical step in obtaining a well adhered/robust coating.

It is debatable whether the Ar glow-discharge cleaning had any effect on coating adhesion, at least with these settings. In hind sight, a DC discharge or higher voltage transformer should have probably been used, but with the current cleaning/coating procedure, which includes solvent sonic cleaning, implementation of a quartz lamp to clean the surfaces, and depositing at relatively low rates of $\sim$3 Å/sec, the resulting coatings are quite robust for their intended purpose.

Chapter 7

Development of DLC Coated Beam Line Components for the UCNA Experiment

7.1 Introduction

Research into the preparation and characterization of Diamond-like carbon (DLC) films has been quite active over the past two to three decades. Due to its high hardness and low friction coefficient, it has primarily been pursued as a wear resistant coating to increase the life of components such as computer hard disk read heads, IR scanners used in grocery stores, or on the edges of razor blades. Interest in using DLC films for UCN applications began in the late 1990's because of its theoretically high Fermi Potential, low neutron absorption, and expected low depolarization per bounce. The hope was that DLC films could replace the historically used toxic beryllium coatings in depolarization UCN experiments [12]. In this context DLC

films need to have a high density, high purity, and be thick enough to prevent the tunneling of UCN through the film. As the density increases, the Fermi Potential increases and is directly related to the sp^3 bond fraction in the film, which will be discussed in section 7.2. The films need to have extremely low levels of foreign elements, especially ones that have a propensity to absorb and/or upscatter UCN, such as ^{10}B and ^{1}H. Finally the film must be able to be grown to a thickness of about 150 nm and still adhere to the desired substrate, which are often the inside of large beamline components.

To accomplish this task Virginia Tech employs pulsed laser deposition, as described in section 3.6. Here two DLC coating methods have been developed which we call the DLC Quartz and DLC Copper processes. The DLC Quartz process is an extension of that developed by Mark Makela, where the focus has been to increase the sp^3 fraction and reproducibility of our DLC coatings on the inside of quartz tubes through the use of the target raster and TOF ion probe systems, previously discussed in section 3.7.3. When the UCNA collaboration decided to move away from quartz tubes for beamline guides, except in the spin flipper region, and replaced them with stainless steel and copper guides, we were asked to provide DLC-coated copper components for the polarized section of the UCNA beamline. This task ended up being extremely difficult as DLC and copper do not form a good chemical bond, i.e. they don't form a strong carbide. We were able to produce adhered 50-70 nm thick DLC coatings on copper, but the coating began to delaminate for thicknesses above 100 nm. Many modifications to the DLC quartz process were attempted to produce 150 nm thick DLC coatings on copper, but in the end a completely new and very exciting process was developed to accomplish this task. Here a magnet was glued to the back of the graphite target and then the target was negatively biased. These additions produced a very different ablation plasma plume that produced an adhered film on the copper substrate. Several samples, and then full-length beam line components, were coated with this process and tested

with UCN. Online data analysis of these tests indicate that the DLC copper tubes would fit the requirements for the Polarization Region of the UCNA beamline and so the rest of these guide components were coated with our DLC Copper process. These guides were in place for the 2009 UCNA data taking run and will be used in the UCNA data run planned for 2010, with which the experiment hopes to produce a 0.3% measurement of A. An important component in improving the quality and reproducibility of our DLC coatings was the use of surface characterization tools to probe various properties of the coating on witness strips associated with every deposition. Here profilometry, ellipsometry, SIMS, and XPS analysis were used to determine the thickness, thickness and relative diamond properties via the optical constants, hydrogen content, and purity plus Fermi Potential of the coating respectively. This chapter will disucss the pertinent features of these developments and coating analysis.

7.2 Diamond-like Carbon

Carbon has six electrons, to which the electrons in the 2s and 2p orbitals may interact to form hybridized orbitals. Here one of the electrons in the 2s orbital is promoted into the p orbital and the left over 2s electron "merges" with all three p orbital electrons to form sp^3 orbitals. These four sp^3 electrons can now form very strong covalent bonds, sometimes referred to σ bonds, and are arranged in a tetrahedral shape, see figure 7.1a. This is the bonding configuration of diamond. When the 2s electron only hybridizes with two of the three electrons in the p orbital, the hybridization is said to be sp^2. Here three sigma bonds form, leaving a 2p electron available to form π bonds which are much weaker than the σ bonds. This is the bonding configuration of graphite, where the sp^2 bonds form a trigonal planar arrangement where the π bond forms perpendicular to this plane, as shown in figure 7.1b. (Carbon can also exist in the sp^1 state where only one 2p orbital electron has hybridized with

the 2s electron. Here two σ bonds and two π bonds are available.) As a UCN surface, the main difference between the two states of carbon is the density. Recall the Fermi Potential, equation 1.24, is a function of the bound coherent scattering length and the density of the material. The scattering length is a nuclear property that is the same for graphite and diamond. However, diamond is much more dense than graphite, 3.52 g/cm^3 as compared to < 2.25 g/cm^3 and it is this density that gives diamond and DLC films their relatively high Fermi Potential.

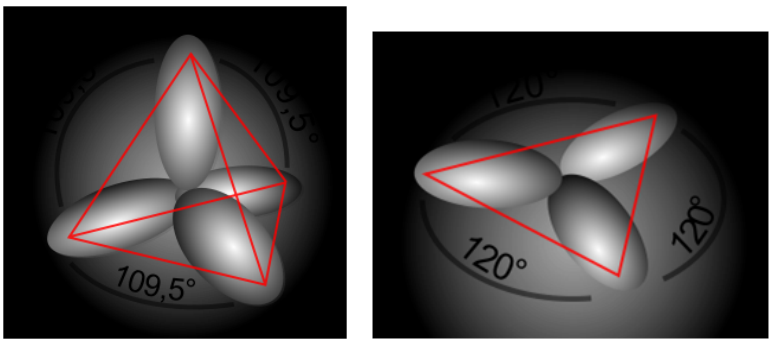

(a) sp^3 Tetrahedral Bonding Structure

(b) sp^2 Trigonal Planar Bonding Structure

Figure 7.1: Hybridized orbital structure of sp^3 and sp^2 bonds for diamond and graphite. DLC is a mixture of these bonds, where the sp^3 fraction determines the density of the film.

DLC is an amorphous mixture of these graphite and diamond bonds and is usually denoted by a-C, which stands for amphorphous carbon with mostly graphite bonds, a-C:H, amorphous carbon with mostly graphite and hydrogen bonds, ta-C, amorphous carbon with mostly diamond bonds, and ta-C:H, amorphous carbon with mostly diamond and hydrogen bonds. They are made by creating a plasma of carbon (and hydrogen in the case of hydrogenated DLC) which then can condense on a substrate. For UCN applications ta-C is usually preferred as it has the highest density and is hydrogen free; recall hydrogen has a negative bound coherent scattering length which reduces the Fermi Potential of coatings and has a very large UCN upscatter cross section. Hydrogenated DLC is usually made with a CVD

process, where hydrogenated carbon precursors are used to form the DLC film. As previously mentioned, deuterated precursors have been used to produce a-C:D films with a measured ∼220 neV Fermi Potential [85]. However, much higher densities can be attained by using PVD processes such as PLD and Cathodic Arc Deposition (CAD). PLD uses a laser, usually in the UV wavelength range, to initiate the plasma. Cathodic-arc systems use a low-voltage high-current power supply with one end connected to a graphite cathode and the other to a smaller carbon striker. The striker touches the cathode causing an arc between the two carbon elements. A highly ionized carbon plasma is formed between the two which can be furthered filtered and accelerated using magnetic and electric fields. The main drawbacks to this method is the complex and large filter and accelerating systems, which would force the UCN guide diameter to be much larger than desired. PLD DLC on the other hand has been studied frequently in the literature and does allow a more reasonable deposition system for UCN guides than filtered cathodic arc techniques.

7.3 DLC Formation Theory

There are a variety of DLC formation models, but the subplantation model seems to be the prevailing theory for the formation of ta-C DLC films. Here the sp^3 bonds are produced from the penetration of a carbon ion/neutral atom that is either from the carbon plasma plume or a carbon atom on the surface that was given enough energy from collisions with the plume to drive into the film, the so called "knock on" process of ion-assisted depositions. At the start of the deposition, an initial amorphous sp^2 carbon layer forms on the substrate. As this layer builds up, carbon atoms with enough energy can penetrate this layer and become lodged somewhere in the film. During this process about 30% of the penetrating atom's energy is lost to displacing atoms before giving up the rest of its energy as heat in a local thermal

spike. Here the new atom locally densifies the film, promoting sp^3 bonds. This same heat energy allows some sp^3-bonded carbon atoms to relax back toward the sufrace via thermally activated diffusion. Thus the film is built up from a combination of carbon atoms sticking to the surface of the film and those atoms subplanting into the film causing densification and outward relaxation. Experimentally the highest sp^3 faction films occur when the impinging a carbon ion energy is around 100 eV [134] [148]. Below 100 eV the measured sp^3 fraction decreases, as fewer and fewer atoms/ions have enough energy for subplantation, while above 100 eV the sp^3 fraction decreases as the relaxtion process dominates as more heat energy is injected into the film.

The substrate temperature also influences the balance between densification and relaxation in the subplantation model. Above a deposition temperature of about 150° C the density of the films starts to drop significantly, as shown in figure 7.2, which also follows the experimental trends. It is believed that as the substrate temperature increases the sp^2 -bonded carbon atoms become more and more mobile and tend to cluster together. When combined with the local thermal spike temperatures, sp^2 formation dominates over sp^3 formation during the relaxation phase of the growth. For this reason heating the substrate with the quartz lamp in an effort to clean the surface of the substrate, as is done with our ^{58}Ni films, is generally not performed as it runs the risk of producing a graphitic film instead of a diamond like one.

7.4 DLC Quartz Process

The observation that a C^+ ion energy near 100 eV produces the most dense DLC films motivated the development of the target raster system and use of the TOF ion probe, described in sections 3.7.3 and 3.7.5, to monitor the DLC deposition. Before these systems were im-

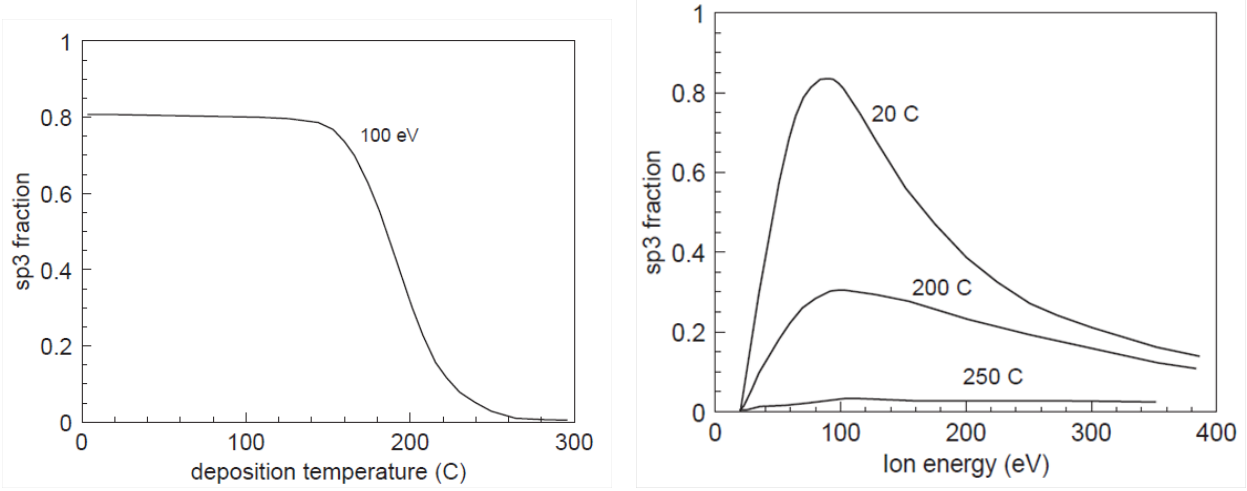

(a) sp^3 fraction vs. substrate temperature.

(b) sp^3 faction vs. ion energy for several substrate temperatures.

Figure 7.2: Prediction from the subplantation DLC formation model of J. Robertson. As discussed, C^+ ions near 100 eV at a substrate temperature close to room temperature form the highest sp^3 fraction films. Figure used with permission from Elsevier Limited (2010) [149].

plemented we suffered from two effects: allowing a large fraction of low-energy carbon ions through the collimator mask (inherent in the laser raster process) and a decrease in the deposited C^+ energy due to a decrease in laser energy on target from absorption/scattering off the DLC film growing on the laser window. These effects were compounded when we discovered that the coating thickness really should be ∼150 nm thick, instead of the nominal 80-100 nm, used in the early 2000's. Without an internal diagnostic providing information as to when and how to change the laser energy settings, we quite often either increased the energy too much promoting sp^2 bonds, or too little, also promoting sp^2 bonds, which led to lower Fermi Potential guides and poor guide to guide reproducibility.

Before the development of the target raster system a series of TOF ion probe measurements were made as a function of angle with respect to the graphite target surface. Here the probe was positioned on a rod protruding through a Conflat to Quick Connect flange that

was mounted on an aluminum plate, as shown in figure 7.3, which was attached to the horizontal viewport of the tube coating chamber. TOF measurements were taken for two laser energy and lens settings. Knowing the distance between the target and the probe allowed the calculation of the kinetic energy of the ions hitting the probe, which were assumed to be C^+ ions. This data is presented in figure 7.4. Two scans were performed to see if there are any differences in the measured signals as the laser spot on target increases. Here lens positions of 12.7 cm and 18 cm correspond to spot sizes of $\sim$0.009 cm^2 and $\sim$0.02 cm^2 as measured with a caliper. We chose laser energies that provided C^+ energies near 100 eV when measured perpendicular to the target for the two different laser spots sizes as this is the optimum energy for making dense DLC films and where we would be running when producing a DLC coated UCN guide. This corresponded to about the same energy density for the two scans: 14.9 J/cm^2 (5.9×10^8 W/cm^2) for the 12.7 cm lens position and 14.8 J/cm^2 (6.0×10^8 W/cm^2) for the 18 cm lens position. We note that there is a slight departure from 90° for the location of the highest energy part of the plume for the larger spot size. This was also seen in the signal strength vs. angle plot, see figure 7.4a. One should also notice the the signal strength of the broader spot size is larger than that from the smaller spot size, especially around the target normal. This indicates ablation plume forward peaking as the laser spot size increases as described by [57]. Based upon this data we chose to make three different collimators that would allow the plume from roughly $\sim$85-95° , $\sim$80-100° , and $\sim$70-110° , named A, B and C, respectively, to pass through and deposit on the substrate. Figure 7.5 shows a photograph of the short quartz coated samples with these different collimators. The coating time for collimator A was double that of collimator B which was double that of collimator C. In this way we expected to have all three samples with about the same thickness of DLC film to analyze with ellipsometry to estimate the relative diamond likeness between the samples. Ellipsometry analysis, using the two Lorentz Oscillator (LO) model developed by Mark Makela [110], showed that the optical constants were very similar

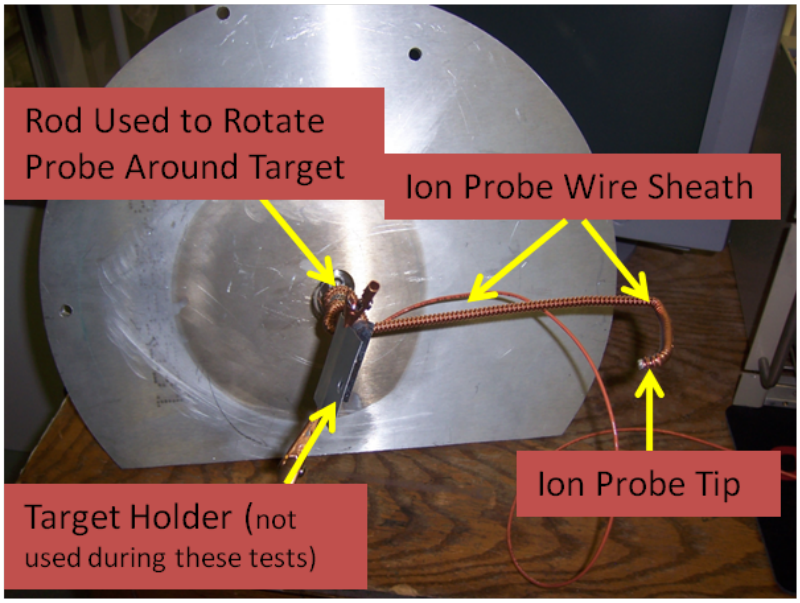

Figure 7.3: Photograph of the ion probe setup used to measure the KE of the C^+ as a function of angle wrt. to target. Here a copper sheathed RF cable was cut on one end to expose the tip to act as our probe. The sheath was grounded and the tip biased to -3 V using the circuit described in section 3.7.5. At the end of the rod is a target holder that was only used for test purposes. For the scans shown in figure 7.2, the target was mounted 30° wrt. the laser beam using a large target holder and the probe rotated about the laser spot.

for all three films and the thickness approximately doubled as the opening angle doubled as expected. As there appeared to be no major benefit from employing a highly collimated plume, we decided to use the 70-110° opening angle collimator for all future depositions.

7.4.1 ID Thickness Test

After selecting the plume collimator we decided to perform a coating uniformity test on a realistic size quartz tube. For this test we fastened Si witness pieces at various locations along a thin piece of aluminum with aluminum foil and inserted the strip down the end of a 65.6 mm ID quartz tube. This strip was held against the ID of the tube with two hose clamp sections that provided tension against the ID of the quartz tube, as shown in figure

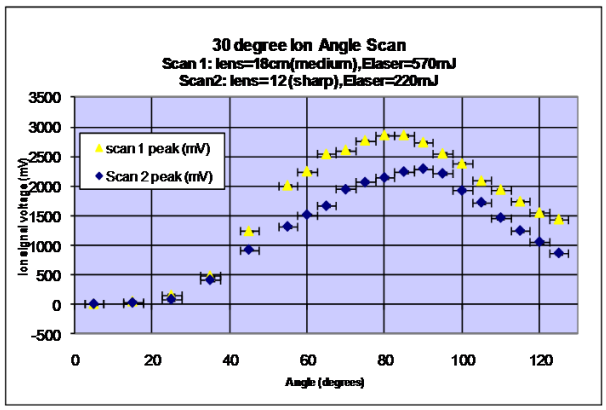

(a) signal strength vs. angle

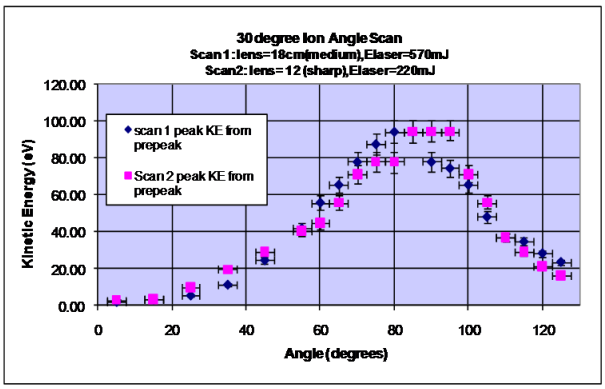

(b) C^+ kinetic energy vs. angle

Figure 7.4: TOF ion probe signal strength and calculated C^+ kinetic energies as a function of angle wrt. the target plane. The target was oriented at 30° with respect to the laser beam and the probe was rotated around the laser spot. The vertical error bars were assigned to the estimated error associated with the resolution of the voltage scale used to view the signal, while the error in angle determination was found to be ±2.5° . Both scans employed a laser energy density of ∼14.9 J/cm^2 as described in the text.

7.6a. The strips were analyzed via ellipsometry again using the two LO model to extract thickness and optical constants as a function of length inside the quartz tube. Figure 7.6c shows the thickness results from these samples. Here we see that the thickness along the length of the tube is uniform, ± 3 nm, and that the witness piece hanging off the edge of the tube under-predicts the thickness of the coating on the ID of the tube by about 15 nm. The thickness discrepancy is caused by carbon atoms inside the tube having multiple chances of sticking to a surface along the ID of the tubes. Here if a carbon atom does not stick on the initial interaction with the surface or is knocked off the surface by another carbon atom, that carbon atom is contained inside the tube and so has another chance of sticking to another part of the tube. On the other hand, the probability of this happening for the witness strip is very small as the carbon atoms near the witness strip are only contained by the vacuum chamber itself and not the ID of the guide. Thus if the thickness of a witness strip hanging off the edge of a guide is measured to be about 120 nm we can safely assume the thickness

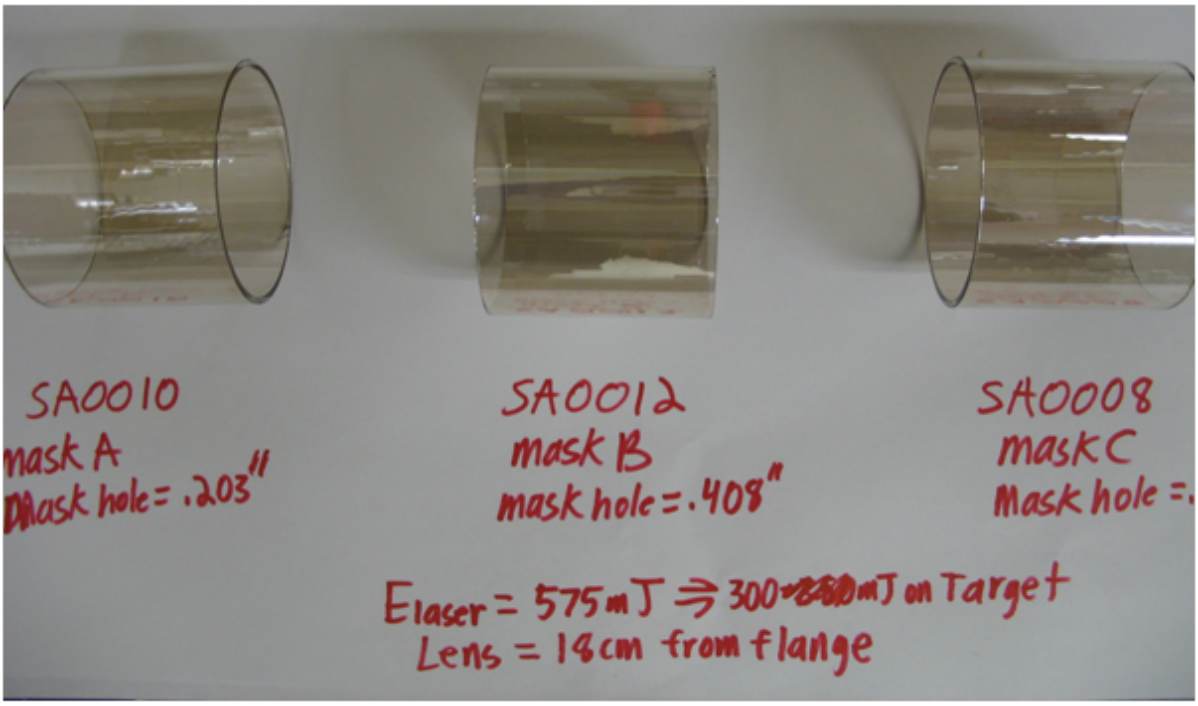

Figure 7.5: Summary photograph of the coated sample quartz tubes from the three different plume collimators. Mask C's diameter is ∼0.81 inches. Samples were prepared for coating with the standard cleaning method for quartz described in 5.2.

along the ID is greater than 140 nm for ∼ 65 mm ID tubes.

Based upon these and other tests we were ready to coat quartz guides for the UCNA experiment. The typical guide coating followed the following steps: load the guide and witness strips into the carriage system, then install and align the graphite target. These steps usually took a day to perform and so we would pump down overnight before starting the coating session. After a pressure of about 3×10^{-6} Torr was reached, the target was first laser cleaned with a laser energy such that the ion probe measured a C^+ energy of about 100 eV. Here the target made at least two up and down raster scans, so that each ablation site had been hit twice with a focused laser spot, ablating any contaminates off the surface. The tube was of course kept as far away as possible from the target during this step. Then the coating process began. The laser energy was set to achieve a C^+ energy of

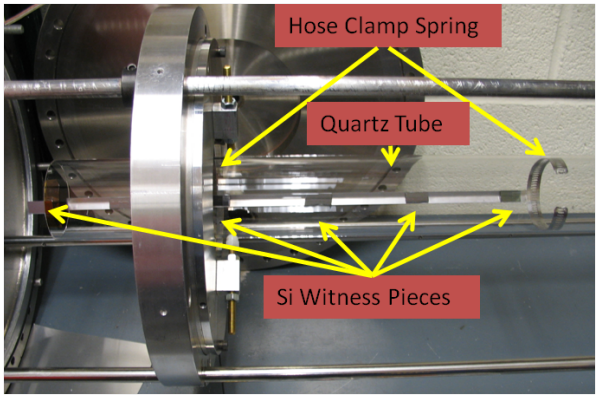

(a) Witness piece setup before coating.

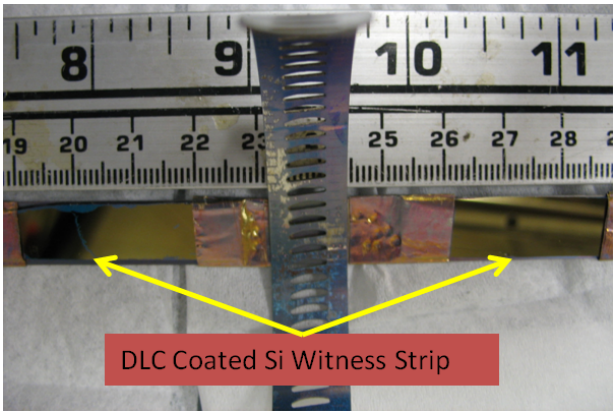

(b) Zoom in on the witness pieces after coating.

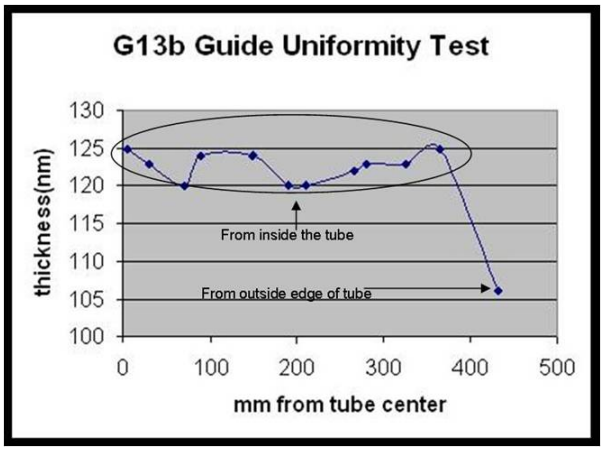

(c) Thickness along the length tube.

Figure 7.6: Photographs of the ID Thickness Test setup both before and after the DLC coating. As usual the copper disc TOF ion probe was used to keep the C^+ energy around 100 eV with a lens position of 14 cm as measured by the ruler shown in figure 3.24b. The gold color on the witness strips is characteristic of our DLC films being ∼125 nm thick. Each sample was analyzed with ellipsometry to extract the thickness, which is plotted in figure 7.6c. Here we see the thickness along the length of the tube is quite uniform (± 3nm) and ∼15 nm thicker than that measured on the witness strip hanging off the end of the tube. Thus when coating this size of guide one should aim for ∼135 nm of coating as measured by witness strips hanging off the ends of the guide so that the coating on the inside of the tube meets the 150 nm goal thickness.

about 100 eV and then the laser energy was measured just after the copper collimator and recorded. Sometimes the drop in the laser energy through each of the atmospheric optic elements was also measured at this time. The tube motion was started with a drive rate

of 2.6 cm/min and a guide rotation of about 12 rpm. A meter long guide took about 45 minutes to completely go over the entire plume. During this time the C^+ scope trace was saved and several drive and rotation checks were performed. If either drive or rotational rate had dropped, the change was noted and then corrected at the start of the next pass. About 30 passes were needed to make a 150 nm thick DLC coating on a 65.6 mm ID quartz tube. This translated into about 23 hours of actual coating which was spread over three to four days. Thus it took about one week to make a guide if everything went well. Often the guides were cleaned on Friday, allowed to bake over the weekend, installed on Monday, and then coated Tuesday, Wednesday, and Thursday. The tube was taken out on Friday, and the whole process repeated for a new guide. Unfortunately, this time-line assumes everything works all the time, which rarely happened. We should note that the number of coating passes increased by a factor of four when the target raster system was implemented. A factor of two is easily explained by the fact that we had to double our nominally achieved thickness of 75 nm to about 150 nm. The other factor of two is attributed to the production of higher sp^3 fraction DLC films and the change in the plume collimator. A total of eight quartz

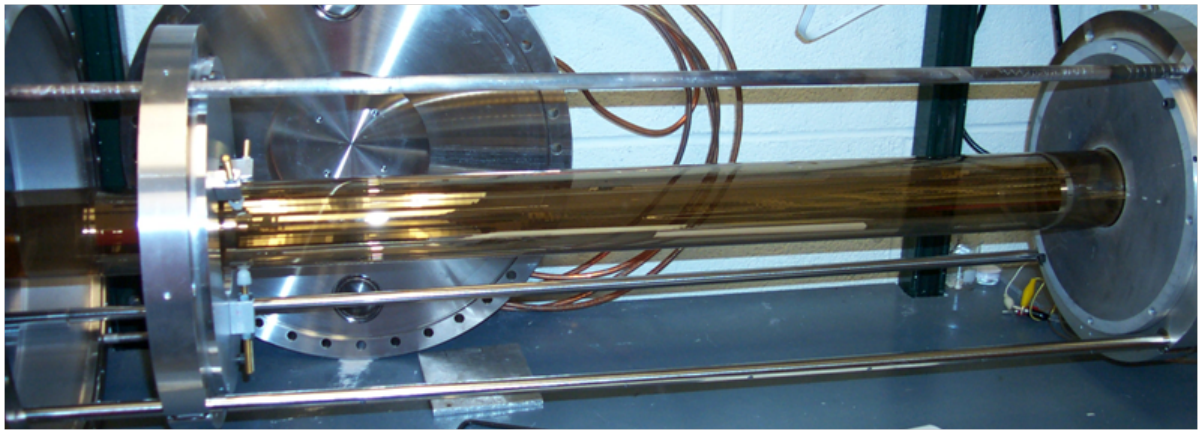

Figure 7.7: Photograph of freshly coated guide g15 just before being taken out of the carriage system. The rich gold color is characteristic of our 150 nm high sp^3 fraction films on quartz.

guides were coated with this method in 2006. Unfortunately, we ran into a multitude of problems during 6 of the coating sessions. These problems ranged from difficulties with the

drive and rotation system stopping during a pass, which if not caught fast enough (within seconds) ruined the whole coating session and tube preparation. In addition we had a hard time keeping the C^+ energy near 100 eV during the whole coating session for a certain batch of pyrolytic graphite targets. Thus only two of the eight guides were coated with about 150 nm of high sp^3 fraction DLC. These tubes were labeled g15 and g31, where we should thank Albert Young for sending Grant Palmquist (and for Grant agreeing to come out to Virginia Tech) to help coat g31. Guide g15's witness strips have been measured to have a high surface sp^3 fraction, about 80%, low optical absorption coefficient, high thickness, $\sim$150 nm, and be very smooth as measured with an AFM. A photograph of guide g15 just after coating is shown in figure 7.7. Unforutnately, during installation at LANL, g15 was accidentally dropped and shattered. Guide g31 on the other has been handled very carefully and is the guide that has been installed in the RF region of the AFP spin flipper since 2007. This guide also tested well in terms of sp^3 fraction, thickness, optical constants, and smoothness. We will use witness strips from these two guides as our baseline when comparing the DLC quartz guide production process to the DLC copper guide production process.

7.5 DLC Copper Guides

Between 2007 and 2008 the use of stainless steel and copper guides became the standard beamline material for the UCNA experiment instead of quartz, except for the RF flipper region which still employed the DLC coated quartz guide g31. This is due to the difficulty in producing and installing a large number of high quality DLC coated quartz guides in the experiment where as the metal guide material was readily available, and there was pressure to start taking physics data. The task given to Virginia Tech was to produce a new set of DLC-coated copper guides to replace the bare copper section of the beamline. Here the copper

substrate ensures a Fermi Potential of 170 neV, instead of the 90 neV provided by quartz. Unfortunately, producing 150 nm thick DLC coatings on copper was very challenging. In the past we routinely produced 50 - 70 nm thick DLC coatings on copper, but after doubling the thickness and following the same cleaning, sans the acid etching, and coating procedure used with quartz guides, each and every DLC coating delaminated from the copper substrate during or right after the deposition concluded.

During these initial tests no effort was made to remove the copper oxide on the electropolished copper test samples and in fact the use of DI water as the final solvent cleaning stage just increased the oxide layer. It is believed that during the deposition on these samples, the carbon was mixing with the copper oxide to form copper carbonate as an interlayer between the copper and DLC film. Copper carbonate has a very low decomposition point, 290° C, which could have been reached, locally, from the thermal spike and relaxation stages of the DLC formation. Thus the oxide was stripped from the copper surface using a citric acid based soap solution, Citranox® by Alcanox® and only 200 proof Ethanol was used to clean the copper after this solution in order to prevent/hinder a new oxide layer from forming. With this procedure, the DLC copper samples only began to show signs of delamination several hours to a couple of days after the coating process was finished, instead of during or right after the coating process.

As noted in the literature, DLC does not easily form a strong chemical bond with the copper substrate, i.e. it does not form a carbide with copper, [20] [5]. Usually people add an intermediate layer in between the copper and DLC that forms a stronger bond between both the copper and the DLC that just the copper to DLC. This technique is commonly employed in other deposition methods, such as ebeam depositions where Cr or Ti are used as an adhesion layer. Sometimes people produce a graded film of DLC and another metal, where there is a high concentration of the metal at the copper surface, which decreases as the

film thickness increases. Here the metal forms a strong bond to the copper and provides a scaffolding for the DLC to bind with and grow. This method has also been shown to reduce the internal stress of the film [127].

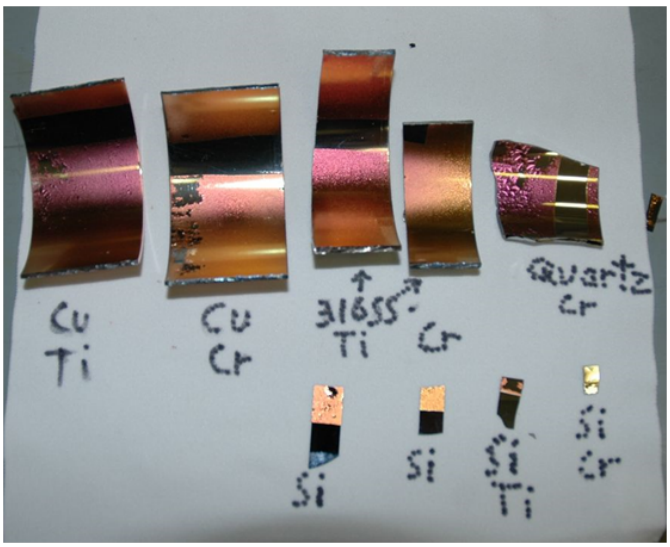

Figure 7.8: DLC coating on stainless steel, copper, quartz, and SiO_2 substrates with either an Ti or Cr interlayer. The Ti and Cr layers were applied in an ebeam chamber and then transfered into the tube coating chamber where they were coated with Quartz DLC process. The DLC delaminated from every sample, while the Cr and Ti coating stayed adhered to the substrates.

Employing an interlayer was attempted but with exposure to air in-between the Ti/Cr and DLC layers. The samples were coated with about 10 nm Cr or Ti in the VE-100 ebeam coater and then transfered to the tube coating chamber for coating with DLC. As shown in figure 7.8, the DLC on all the samples including the witness strips delaminated. Tape tests indicated the Ti and Cr were well adhered to the substrates and that it was the DLC/Cr and DLC/Ti bond that was very weak. Obviously the Ti and Cr became oxidized and probably contaminated during the transfer process and so the both the interlayer coating and DLC really need to be applied in the same chamber without breaking vacuum. Unfortunately, this required engineering changes to our current procedure and so was put on the 'back burner' as we investigated other modifications. We attempted heating the copper substrate from

both the outside and inside the tube at different times and lengths during the deposition, employing higher and lower C^+ kinetic energies, and positively biasing the target. Originally suggested by Bruce Vogelaar, positively biasing the target produced an adhered coating except there were "arc spots", as shown in figure 7.9, that were questionable as to what would happen to the UCN in these locations. To address this issue a 33 inch long copper tube was coated with just biasing the target to 250 V and shipped to LANL for guide testing with UCN. However, the coating began to show signs of delamination during the deposition process and once the tube was pulled out from the coating chamber, most of the DLC had delaminated, making the tube unusable. The delamination seemed stem from the arc spots, where the coating of the actual arced location appeared to be well adhered while the area around them often delaminated. Thus we needed to control the arcing to either arc the entire surface of the tube, reminiscent of a CAD process, or reduce/eliminate the arcing altogether. In the end, we were able eliminate almost all the arcing by the introduction of a strong magnet behind the graphite target. This development is discussed in the next section.

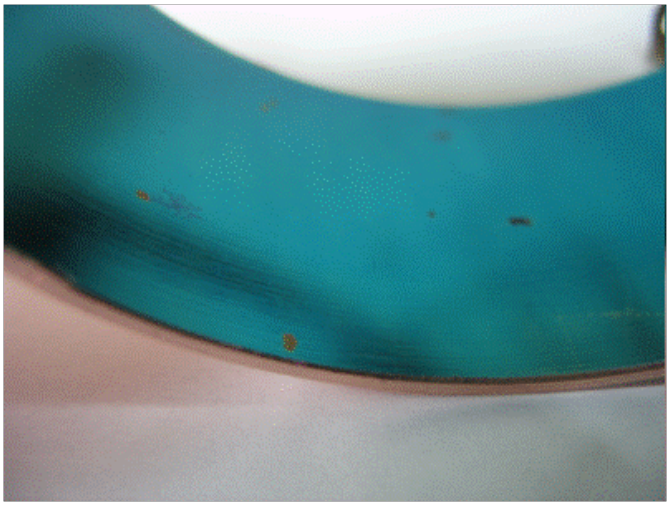

Figure 7.9: Arc spots resulting from coating a copper tube sample with the graphite target biased to 250 V.

7.6 Biasing the Graphite Target

Using a bias voltage to enhance a deposition procedure is not uncommon and can be tailored to make a variety of thin film structures. In most DLC filtered CAD systems, the substrate is negatively biased from 0 - 300 V so that the induced electric field guides the carbon ions toward the substrate. A maximum sp^3 fraction was observed with a bias around 200V [52]. Biasing the UCN guide in our tube coating deposition chamber is not trivial, as the tube would have to be isolated and a bias cable management system would have to be developed that would not impede the rotation and translation of the tube over the target. On the other hand, biasing the target is relatively easy. Here a current limited, 500 V DC power supply was connected on the atmosphere side of the target rod with an electrical break separating the rod to the wiggler system. The bias on the target was checked via a multimeter before each pump down. As with our DLC Quartz process the plume collimator was installed.

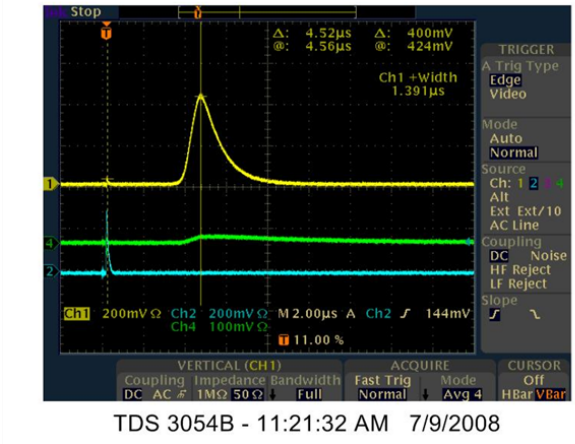

(a) TOF ion probe signal with 0 V bias

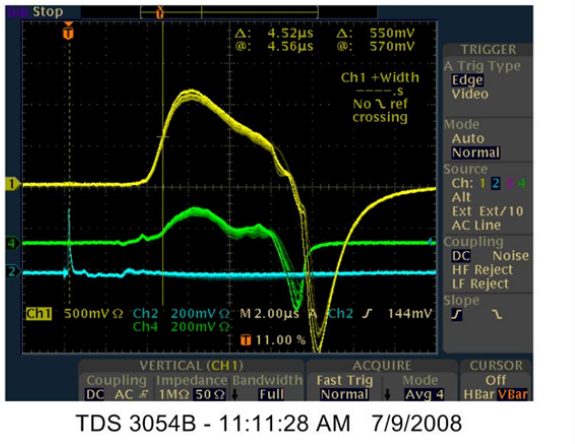

(b) TOF ion probe signal with 250 V bias

Figure 7.10: Oscilloscope screen capture of the TOF ion probe signal for target bias voltages of 0 V and 250 V. The yellow and blue curves are the standard ion probe and UV photodiode signals, respectively, discussed in section 3.7.5. The green curve is a test (wire tip style) probe located along the chamber wall, but located to measure the edge of the unbiased collimated plume.

As shown in figure 7.10, the ion probe signal looked very different with and without a bias. It appears that the bias is causing a charge separation in the plume, where the electrons arrive much later than the positively charged ions. This positive signal grows with increasing bias voltage, as does the negative electron signal (gets more negative). However the C^+ signal does not arrive sooner as one would expect if the bias voltage was pushing the carbon ions out from the target. We also acknowledge that biasing the target to ∼200 V seems at odds with our assertion that the highest sp^3 fraction DLC films occurs with a C^+ KE ∼100 eV. Very complex physics is at work and unfortunately a detailed study of this phenomenon was not performed. We postulate that the incorporation of other plasma probes, such as an optical emission spectrometer or a triple Langmuir probe, will be required to elucidate this phenomenon.

Nevertheless when we attempted to coat copper samples and the aforementioned 33 inch long copper tube, we observed a large amount of arcing between the target and the nearby grounded components throughout the entire deposition, i.e. target support tube, the carriage system, and the copper guide itself. We also noticed that the amount of arcing increased as the bias voltage was increased. Although the arc itself is most likely a 100% ionized, very energetic stream of carbon ions, which in prinicple could produce a great DLC coating if properly controlled, the arcing to the other grounded components surrounding the target pose a concern. Here arcs on these components tend to produce showers of brightly colored debris, mostly likely constituents of stainless steel and aluminum, that not only hit and stick onto the surface of a guide, but also fall onto the graphite target which then is ablated onto the guide. This arcing was almost elminated by imposing a strong magnetic field in the ablation plume plasma formation region.

The introduction of a strong magnet behind the graphite target in PLD DLC films was proposed in Mark Makela's thesis [110] and has been studied elsewhere [58]. Here

the electrons, having a much smaller mass, spiral around the field lines with a radius and frequency given by

$$r_e = \frac{mv_\perp}{qB} \qquad and \qquad f = \frac{qB}{2\pi m} \tag{7.1}$$

were m is the electrons mass, $v_\perp$ is the the velocity of the electron perpendicular to the magnetic field, q is the electron charge, and B is the magnetic field. For 100 eV electrons with 50% of their KE moving perpendicular to the magnetic field their radius of curvature around the field lines is 0.16 mm with a frequency of 4.2 GHz. This radius is smaller than the size of the laser spot on the target and so it is clear that the electrons would circle inside the plamsa plume many times before leaving the magnetic field. This increases the probability of colliding with the carbon atoms/clusters, possibly ionizing them and breaking them up. The ionization fraction of the plume may increase, which always helps make a higher density DLC film with better adhesion. This effect is futher enhanced by positively biasing the target. Now the electrons are attracted back toward the target slowing them down and increasing their time within the plume. We first used a 3/4 inch diameter 3/8 inch thick grade N52 Neodymium permanent magnet, magnetized through its thickness, glued behind the target with some conductive vacuum compatible epoxy. This later evolved to the target/magnet shown in figure 7.11, where the magnet is glued to the target using Hysol 1C® , which is much cheaper than the conductive vacuum compatible epoxy previously used. Here the field lines emerge perpendicular to the face of the target. During this initial test the plume collimator was not used so that one could better see what the full plasma plume looked like to the eye. Without any target bias, the plume did not appear to change as measured by the ion probe or the eye, see figure 7.12b. However when the target was positively biased, the arcing previously observed disappeared. Even with a bias up to about 400 V (the measured maximum of the supply) no arcing was observed to the target support tube or chamber walls. This was repeated without the magnet behind the target, and the arcing returned

as before. In addition, the plume from the biased target/magnet appears brighter to the

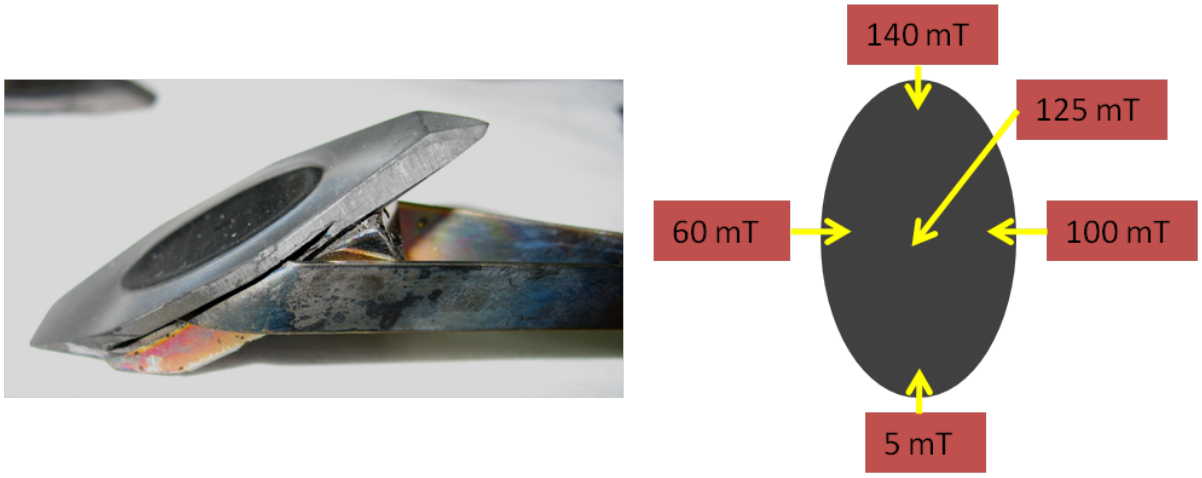

Figure 7.11: Photograph of pyrolytic graphite target magnet 3/4 inch by 1.5 inch by 1/4 inch thick rectangular N52 Neodymium magnet glued to the back. Also included are typical magnetic fields measured at various locations along the ablation raster spot of the target with a hall probe. Often the magnetic field decreases by 25-50% after a coating, due to heating the magnet to about 50° C as measured by a thermocouple near the target during the deposition.

eye than without the bias. With the bias, the optically active part of the plume extends out father from the target and very bright "plasma shoots" appear to be ejected parallel to the target, see figure 7.12. We speculate the ionization fraction of the plume is increased when the target is biased. This increased ionization leads to more recombination in the plasma, which would cause the plume to appear brighter. To truly answer this question a high resolution optical CCD spectrometer with an wavelength range of 200 - 858 nm with a FWHM around 0.15 nm was purchased to view the laser induced plasma. Here the dominant C^+ emissions lines are at 296 nm and 424 nm [138]. Lines at 247.8 nm, 393 nm, and 733 nm have are also used to identify the C^+ [175] [30]. This technique is known as laser induced breakdown spectroscopy (LIBS) where it is commonly used to identify elements of samples ranging from bomb residues and bioaerosols to metals, and even the composition of paints for use in the art history industry [98]. Here an increase in the emission spectrum

would verify that indeed the ionization fraction of the plume does increase as the target is biased. From this, plasma properties beyond the ionization fractions - such as the electron temperature - can be calculated [175], which may provide insights into producing higher sp^3 fraction DLC and other diamond like coatings, such as diamond nitride, which should have a higher Fermi Potential than DLC because of nitrogen's larger scattering length. In addition, the system can be used to identify the elemental composition of the plasma which would be helpful in monitoring the concentration of unwanted elements such as Fe, as well as aid in understanding of the hydrogen concentration in our DLC films, see section 7.11. Unfortunately, there was not enough time to properly setup the system before this document was written. Once the system is in place it will provide valuable data for understanding our current and future depositions.

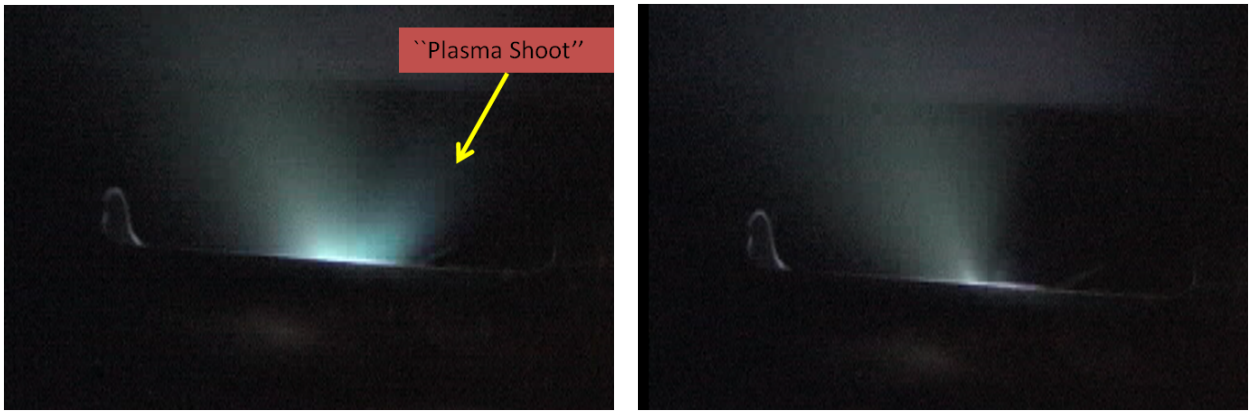

(a) Photograph of the carbon ablation plume with 150 V bias

(b) Photograph of the carbon ablation plume with 0 V bias

Figure 7.12: Photographs of the carbon ablation plume with and without biasing the target/magnet. The plasma plume is brighter and extends out further from the target than the unbiased plume. Also notice the bright column of material that runs parallel to the target on the 150 V bias photograph. For reference we call this column the "plasma shoot".

After the discovery that a bias target/magnet configuration showed hardly any arcing to ground, a first round of copper tube samples was coated without the plume collimator as this was the configuration that had no arcing. A 100 eV C^+ kinetic energy was first dialed

in with a lens position of 14 cm, as is standard for our DLC quartz process. Then the bias was turned up to 280V and several arcs were observed when a copper tube was translated across the target. A bias of about 100 V produced very little arcing and so several passes were done on these tube samples. A total of nine passes were performed where during the 8th pass, significant arcing to the tube was observed and the coating appeared to be very black and delaminated. A picture of these samples is shown in figure 7.13. Although much of the witness strip was peeling, we were able to take profilometer step height measurements, which showed the thickness was close to 300 nm. Thus another set of copper samples were installed and coated in a similar way, but this time with a target bias of 125 V and only 5 passes over the target. These samples are shown in figure 7.14. Here very few arc spots to the ID of the tube were observed and the coating was not delaminating. Another set of copper samples were coated, but this time with a target bias at 150 V and the addition of a 3 inch OD RATH True 10 stainless steel tube sample. These samples are shown in figure 7.15. The thickness of the samples was measured to be about 160 nm and 140 nm for samples 11-16-08 and 11-18-08 respectively. Described in section 7.10, XPS analysis of the two successful samples gave an sp^3 fraction near 53% and 57%. This corresponds to about a 230 neV Fermi Potential, which is adequate for the polarization section of the UCNA beamline. We should note that along with these samples, short quartz-tube samples were coated along side the copper samples. Every quartz tube showed some signs of delamination a few days after the deposition, which propagated to cover the entire sample within a week, and so we concluded that using this target biasing process cannot be used to coat our quartz tubes. The explanation is that the quartz, being an insulator, is charging up and altering the DLC deposition process.

With the success of samples 11-16-08 and 11-18-08 we were ready to attempt a real UCNA beamline guide. We started with the $\sim$34 inch long 2.75 inch OD copper guide that

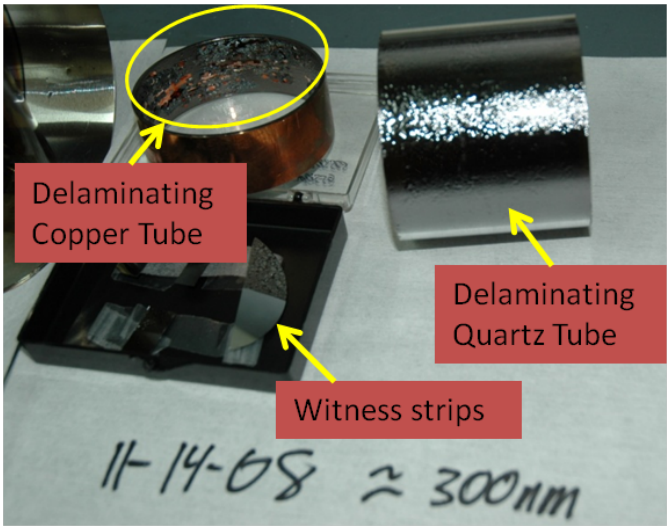

Figure 7.13: Quartz and copper tube samples coated with about 300 nm of DLC using an uncollimated target/magnet bias of 100 V.

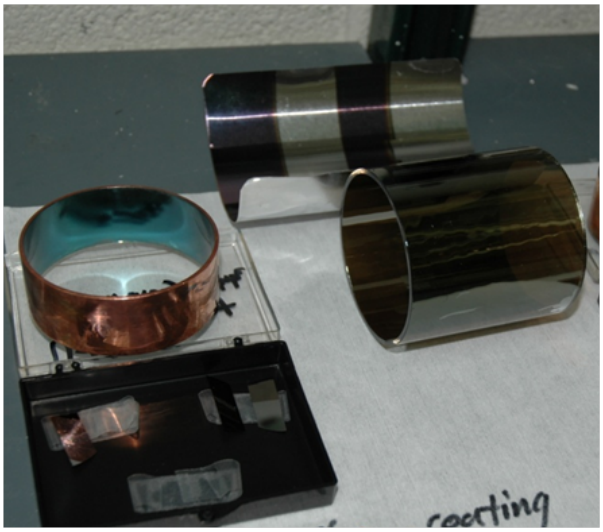

(a) The 11-16-08 successfully coated copper tube sample using an uncollimated target/magnet and 125 V bias.

(b) Close up of the DLC coating on the copper tube

Figure 7.14: Copper and Quartz tubes samples successfully coated without collimating the plume and using a target/magnet biased to 125 V. Only small amounts of delamination can be seen on the quartz tube a few hours after the deposition. Within a few days the entire coating on the quartz tube had delaminated.

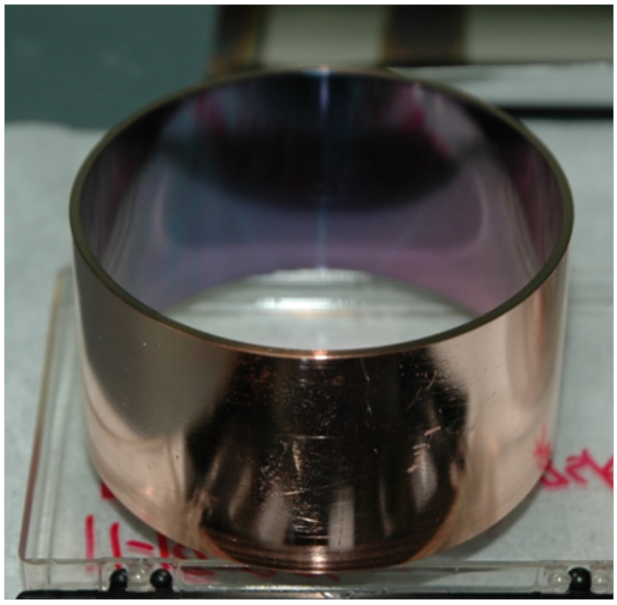

(a) Close up of the DLC coating on the 11-18-08 copper tube sample.

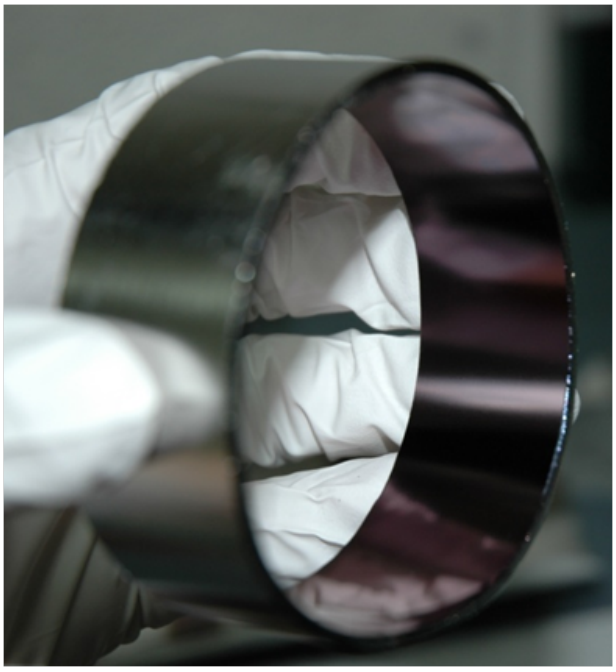

(b) Close up of the DLC coating on the 11-18-08 stainless steel tube sample

Figure 7.15: The 11-18-08 successfully coated copper and stainless steel tube samples using an uncollimated target/magnet bias of 150 V.

fits between the AFP Fe foil guide and the rectangular guide. We have named this guide the 34 in. AFP-SCS guide. It was cleaned and baked in the standard way and coated with the standard quartz tube parameters, i.e. lens position of 14 cm, unbiased C^+ energy of about 100 eV, but with a target bias of 125 V and a magnet behind the target providing a magnetic field profile as shown in figure 7.11. The coating of this tube was quite successful, where very little arcing was observed and the film looked turquoise indicating a thickness around 150 nm. A total of 4.5 passes were performed over the target, where after each pass the bias was turned off and the C^+ energy measured and then adjusted to be about 100 eV by increasing the laser energy/pulse. A half pass is made by doubling the linear speed of the tube over the target. After the success of this tube, the meter long version that is placed upstream of the AFP was coated in the same manner but with a target bias of 185 V. Five

passes were performed over the target. The rational was to the increase the bias as close to 200 V as possible, but still minimize the observed arcing.

7.7 Guide Tests with UCN

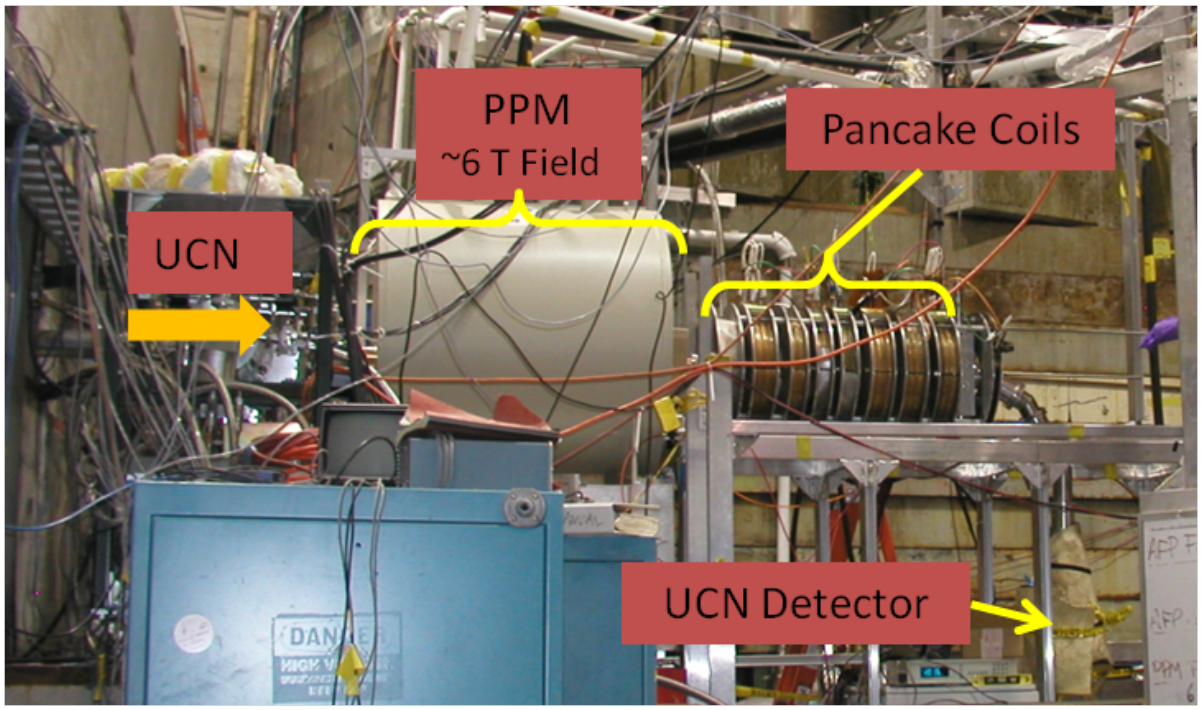

Figure 7.16: The 2008 depolarization experiment at LANSCE. UCN from the LANSCE SD_2 UCN source come in from the left, where only one spin state can pass through the 6 T magnetic field produced by the PPM. The test guide is threaded through the pancake coils. A shutter mechanism is attached to the end of the test guide which can be opened and closed to feed the UCN detector. Figure modified with permission from UCNA collaboration 2010[181].

These two tubes were included in a UCN depolarization experiment that utilized the LANSCE SD_2 source and part of the UCNA beamline. The goal of the experiment was to measure the depolarization probability per bounce as a function of applied magnetic field on stainless steel, electropolished copper, and the newly produced DLC coated copper guides. A diagram of the experimental setup is shown in figure 7.16, where a series of pancake

resistive coils were operated to provide a relatively uniform magnetic field throughout the length of the guide. The depolarization per bounce is ultimately extracted by fitting the data with a Monte Carlo simulation. To define the parameters of the simulation, bottling measurements were made for each test guide at two different beam heights (giving different velocity distributions) as well as transmission measurements. While the full analysis of the experiment will be the subject of Raymond Rios's Ph.D. thesis, the raw data can provide insight into the relative performance of the DLC copper guides. The raw data between the two different beam height measurements tell one about the relative Fermi Potentials and loss probabilities per bounce between the guides. The drain time for these experiments is shown in table 7.1. Here the drain time is the exponential decay constant used to fit the fall-off of UCN measured in the main detector. Figure 7.17 shows a photograph of the two bottling experimental setups, while figure 7.18 shows data from one of the stainless steel guide bottling runs. The drain times for the DLC copper tube were the same, within statistical errors, for the two different beam heights indicating that the Fermi Potential of the DLC coated copper tube is higher than that of stainless steel and bare copper. How much higher requires a Monte Carlo simulation, as the spectrum of UCN entering the tests guides from the 67 cm drop is somewhere between that with a stainless steel cut off, $\sim$180 neV, and 67 neV higher, 247 neV. Nevertheless, these results are promising.

Transmission results were also performed on the test guides and are presented in table 7.1. Unfortunately there was some question as to whether the EP copper and DLC copper tubes were installed properly for the transmission measurements and so they were tested again which is why there are two transmission values for these tubes. We see that the stainless steel tube transmits more UCN than either the EP copper or DLC copper tubes, and that the EP copper tube seems to transmit more than the DLC copper tube, when the second transmission run is considered. Factors such as the Fermi Potential and roughness

are convoluted in transmission measurements so a simulation is required to provide clarity. Our AFM tube measurements do seem to indicate that the copper guides are rougher than the stainless (see section 5.4), however it is unclear whether or not roughness can account for these transmission values. Measured depolarization counts for DLC copper were very similar to those of EP copper and so we felt confident that the DLC copper guides would not reduce the amount of beta-decay rate in the UCNA decay trap. There were many indications, such as our XPS analysis and bottling measurements, that the DLC coating would increase the decay rate in the trap. Assuming a 230 neV Fermi Potential for DLC copper tubes, simulations predicted a beta decay rate increase of ∼2 in the decay trap [122].

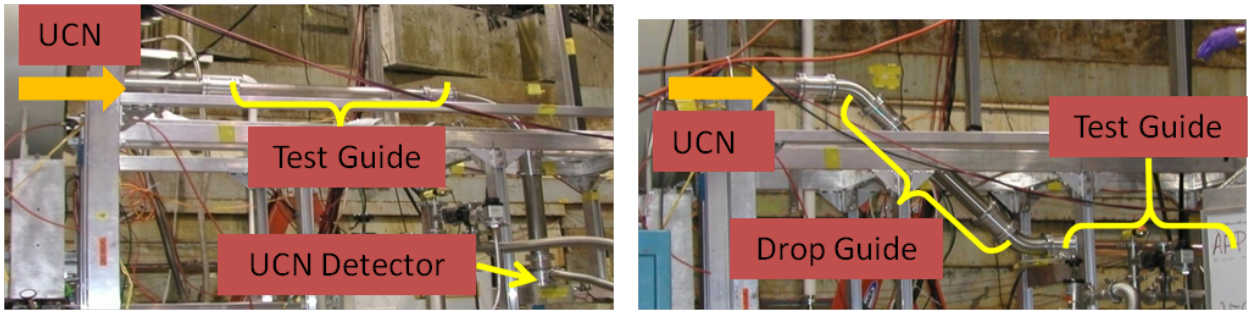

(a) Bottling tests at beam height

(b) Bottling tests 67 cm below beam height

Figure 7.17: UCN guide bottling setup used in the 2008 depolarization experiment at LANSCE. A foil with a hole in it is placed after the test guide to restrict the flow of UCN to the UCN detector. The UCN in the test guide will build up to an equilibrium value as measured by the UCN detector. After one is sure the equilibrium value has been reached, the flow of UCN is shut off and the number of UCN detected will exponentially fall to background levels. How fast this decay, or drain time, takes is used in Monte Carlo simulations to model the Fermi Potential and loss probability per bounce of the test guide. Dropping the UCN increases the velocity of the UCN sampling the test guide surface which is very useful in extracting the Fermi Potential of the test guide. Figure modified with permission from UCNA collaboration 2010[181].

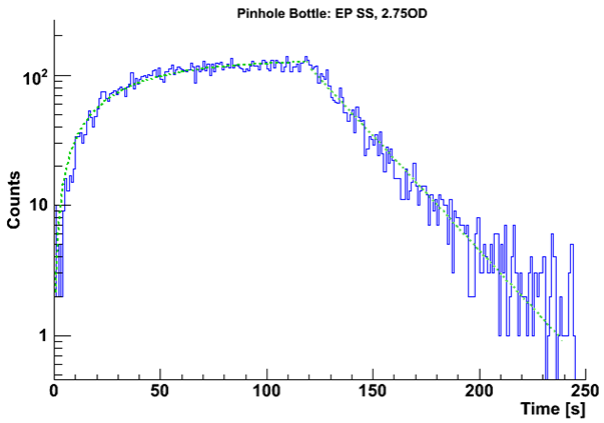

Figure 7.18: The number of UCN detected vs. time for the 2.75 inch OD stainless steel test guide beam height bottling measurement. Exponentials are used to fit the filling and draining parts of the curve. Figure taken from the UCNA online log book courtesy of Adam Holley 2010 [67].

7.8 Production of the Beamline

We finally switched to production mode and coated the rest of the guides inside the AFP to the decay trap inside the SCS. Unfortunately, the end decay trap guides each developed a small area of delamination, $\sim$5 cm^2 at each end. Here the ends of the protective bag material had been sucked into the recently coated guide and when the bag was "vented" the coating came off where the bag had been touching. This had never happened before, but the decay trap guides barely fit the bagging material and so the only place for the bagging material to go was inside the guide when the atmospheric pressure increased. Larger bagging material has since been employed in an effort to prevent this from happening again. The effect of the delamination was simulated and the new predicted increase in beta decay rate from the introduction of the DLC copper guides dropped to about 1.8.

Another set back was encountered when we attempted to coat the 2009 rectangular guide. It was decided that this guide should only be mechanically polished, as the finish after elec-

Table 7.1: UCN transmission and bottling drain times at beam height (BH) and 67 cm below BH for the three, meter long guides used in the 2008 UCN Depolarization Experiment conducted at LANSCE. The fact that the two bottling drain times for the DLC copper tube were measured to be the same indicates that the Fermi Potential is higher than that of stainless steel. Two transmission measurements were done for both the EP copper and DLC copper tubes because each had some uncertainty in the correctness of the installation of the tubes for the first measurement. The first value listed corresponds to the first, questionable measurement, while the 2nd value corresponds to the 2nd transmission measurement.

Test Guide	BH Transmission %	BH Drain (s)	67 cm Below BH Drain (s)
EP 304 Stainless Steel	99	24.7	22.4
EP Copper	89,92	28.2	23.5
DLC Copper	89,88	32.2	32.5

tropolishing was hazy and rougher as measured by an industrial profilometer. In fact it was this guide that motivated the copper polishing practice plate described in section 5.4. A mirror finish was mechanically put onto the plates which were loaded into the rectangular guide holder shown in 3.6. The first coating started to delaminate right away near where the plate was bolted into the holder, indicating contamination during the installation process. Most of the coating was sonic cleaned off in acetone and the rest removed by further mechanical polishing courtesy of Irving Polishing Inc. Meanwhile the 2008 electropolished (EP) copper rectangular guide plates were successfully coated with about 110 nm of DLC. Special attention, including face masks, was given to the installation of the EP plates in an effort to not contaminate them. Next we coated the decay trap plug and the round-to-rectangular transition plate. These were coated with the setup shown in figure 3.29. Due to time constraints, the plate and plug were mechanically polished in-house, using a medium density cotton buff on a drill press rotating near 1600 rpm, first with a white cut/color, i.e. aluminum oxide, compound and then a water based 1 micron diamond paste with a new buffing wheel. The plate and plug were positioned such that they would be coated by the main part of the ablation plume. Unfortunately, the coating delaminated from both components. On a

hunch we repolished/recleaned/rebaked the components and positioned them in the chamber such that the "plasma shoots" depicted in figure 7.12a would be used to provide most of the coating and not the central ablation plume. We postulated that this is a very active part of the plasma, as it is so bright, and seems to have a higher ionization fraction, which has been shown to aid in DLC adhesion. Both sides of the plate were successfully coated where profilometer scans of witness strips located at the center of the rectangular hole showed about 70 nm of DLC for one side and 115 nm of DLC for the other. Here the 70 nm side was a dark gray while the 115 nm side looked red to eye. A thicker coating was attempted on the plug, where we ended up applying $>$ 262 nm of DLC, as measured by ellipsometry. As shown in figure 7.19, this coating looks glossy black to the eye. Clearly we have work to do on estimating the thickness of DLC when coating components with this setup, but the fact that a $\sim$260 nm DLC coating adhered to the copper substrate is very exciting. In fact the plug was dropped several times while at LANL and the coating still does not show any delamination. Another attempt at coating the mechanically polished 2009 rectangular guide plates was made after these coatings, where the same procedure for coating the 2008 rectangular guide was used. Unfortunately, 24 hours after the deposition, the plates showed signs of delamination, which after a week propagated to cover most of the coated area. Thus it appears that electropolishing is a necessary step in producing a DLC coated copper guide without collimating the plume. However the plug and plate coating seem to indicate that if one collimates away the main part of the ablation plume so that only the so called "plasma shoots" are used to coat the components an extremely well adhered DLC coating may be obtained.

Figure 7.19: Photograph of the 7-30-09 DLC coated Plug. The plug was placed such that the "plasma shoots" provided most of the coating. The thickness ended up being > 262 nm.

7.9 Witness Strip Analysis

Every coating session includes witness strips that are used to characterize the coating of that particular guide component. Usually Si wafer strips are used, but sometimes strips made from electropolished copper or stainless steel plates are also included. It is through the analysis of these strips that we are able extract properties such as the sp^3 fraction, thickness, roughness, and elemental composition. In the following we discuss the process and results from these analyses where we have focused on the strips associated with the DLC copper and quartz guides currently being used in the UCNA beamline.

7.9.1 Ellipsometry

Ellipsometry is a useful tool for determining the optical constants and thickness of thin DLC films, where the optical constants provide a qualitative estimate on the diamond-likeness. For this work all the samples were DLC on Si wafer strips, without striping their native

oxide, and so we have at least three layers: DLC on top of SiO_2 on top of Si. Often a dedicated ellipsometry scan of the uncoated part of the witness strip was performed to determine the thickness of the oxide layer (usually $\sim$3 nm). Here three angles are used, 72, 75, and 78°, with a wavelength range of 250-1100 nm and 15 rotations of the analyzer per wavelength/angle combination. Standard tabulated optical constants for Si and SiO_2, provided with the ellipsometer software (VASE32, from Palik [133] and J. A. Woollam [23]) are used to fit the oxide thickness. This thickness is then used as a fixed thickness for the oxide layer in the modeling of the DLC/SiO_2/Si system.

The DLC scans employed 4 angles, 67, 71, 75, 79°, a wavelength range from 250-1100 nm and > 30 analyzer rotations per wavelength/angle combination. These angles were chosen because the ellipsometric parameter Δ crosses 90° several times. Recall that the VASE ellipsometer is most sensitive when Δ is around 90°. The analyzer rotations were increased to > 30 to reduce the statistical error associated with the data which improves the reliability and uniqueness of the model once it has been found, especially in the UV side of the data where the output of the Xe lamp is weaker than the VIS-NIR regions.

Many oscillators have been used to model DLC films: Lorentz Oscillators (LO) the Tauc-Lorentz (T-L) model, Forouhi-Bloomer (F-B) model, a variety Effective Media Approximation (EMA) models, Gaussian Oscillators (GO), and the Cauchy model with Urbach Absorption (CUA) with varied success [18] [84] [148]. We used the two-LO model developed by Mark Makela and a simple graded T-L model with surface roughness to describe our DLC films. The two-LO model describes our DLC films reasonably well from 400 - 1000 nm wavelengths where the MSE values are usually 10 and lower. However when the UV part of the spectrum is included, the two-LO model does not fit the data. To help model the entire spectral range, a T-L model with simple grading and surface roughness was developed with the help of James Hilfiker from J. A. Woollam [60]. Here the modeling layers follow those

shown in figure 7.20.

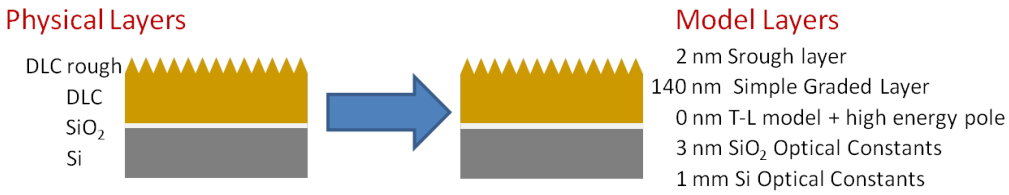

Figure 7.20: Cartoon showing our Simple Graded T-L with surface roughness model used to fit our PLD-DLC ellipsometry data with typical thickness values.

The Si and SiO_2 layers are modeled with tabulated optical constants and the thickness of the oxide determined as previously described. The T-L models the imaginary part of the dielectric function, ϵ_2 as the product of the Tauc edge and the Lorentz factor for an ensemble of non-interacting atoms [82] [81] which is given by

$$\epsilon_{2TL}(E) = 2nk = \frac{(E-E_g)^2}{E} \cdot \frac{A_L E_o C}{(E^2-E_o^2)^2 + C^2E^2} \qquad E > E_g \qquad (7.2)$$

$$\epsilon_{2TL}(E) = 0 \qquad E < E_g \qquad (7.3)$$

where the first part is the Tauc Edge, where E is the wavelength of the light in eV and E_g is the band gap. The second part is the Lorentz oscillator portion where E_o is the energy position of the peak in the joint density of states, A_L is the amplitude of the oscillator, and C is a broadening term. The real part of the dielectric function ϵ_{1TL} is found by performing the Kramers-Kronig integration of equation 7.3. Recall that all models must be K-K consistent to be physical over the entire spectrum. In addition to the T-L oscillator, a zero-width "pole" oscillator is placed at much higher photon energies, around 9-12 eV (value is a fit parameter), in order to include the subtle effects on ϵ_1 from absorption at these high energies. This oscillator does a similar job as the ϵ_{inf} term used in the two LO model.

The T-L layer is linked to a simple graded layer which incorporates the film thickness

and allows the index of refraction, n, to vary linearly in 5 steps, as a function of thickness. This layer is used to account for the variation in the density (i.e. sp^3 fraction) of DLC as a function of thickness, which was observed from low-angle neutron scattering data [110]. This layer is then capped by a roughness layer (called srough in the VASE32 software) which is an EMA of 50% voids and 50% of the layer directly underneath with a variable thickness. The fitted thickness of the srough layer only provides an estimate, usually an overestimate, of the surface roughness over a large area of the sample and does not replace actual AFM roughness measurements. Also included in this model is some nonuniformity in the thickness, usually at the few percent level, of the scanned area to which a small amount is expected due to the nature of the flat strip being coated while taped to the outside of a circular tube. This nonuniformity damps some of the sharp features that are present in model calculated Ψ and Δ data, which better fits our real world data. Thus the parameters fitted by our T-L model

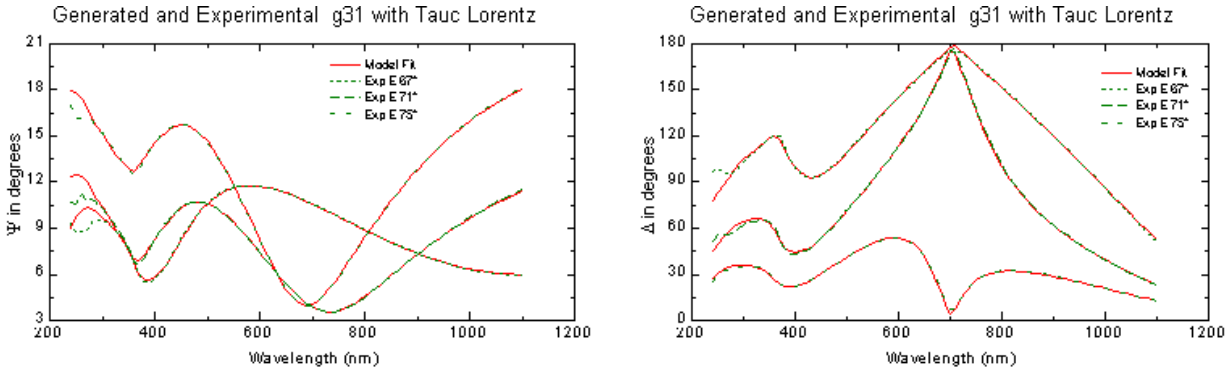

(a) Fitted Ψ data.

(b) Fitted Δ data.

Figure 7.21: Ψ and Δ Ellipsometry data from a DLC coated witness strip from guide g31. The T-L model described has been used to fit the data.

are: A_L, E_o, C, E_g, higher energy pole oscillator position and amplitude, film thickness, index of refraction variation as a function of thickness, and srough thickness. Figure 7.21 shows the Ψ and Δ with the T-L model fit for a witness strip from guide g31 (the DLC coated quartz guide located in the RF region of the AFP spin flipper). From looking at all

these fit parameter one may wonder what can't we fit with so many variables. To address this, we note that the bulk of the model is the T-L layer. The added features, all justified, help bring the MSE values down into the 5 region, where without them they are routinely in the 20 region. Table 7.2 summarizes the fit parameters for the witness strips from almost all of our successful DLC on Copper coatings as well a that from guide g31. A plot of the optical constants of these films is provided in figure 7.22. The higher the density of the DLC, the closer the optical constants look to those of diamond. As one can see from looking at the optical constants, all our films are truly diamond-like in that they don't necessarily follow the (n,k) of either graphite or diamond, however all the ks follow that of diamond more closely than graphite. We also see that g31 has the lowest k value of the films plotted and so is the most diamond like of the samples shown. This also matches well with XPS derived sp^3 fractions, discussed in the next section. This is to be expected as g31 had a plume collimator, while all other films did not employ any collimation. Another interesting aspect is that the k of sample 7-30-09 Plug is in the middle of the other samples, despite the thickness being over 100 nm thicker than the others.

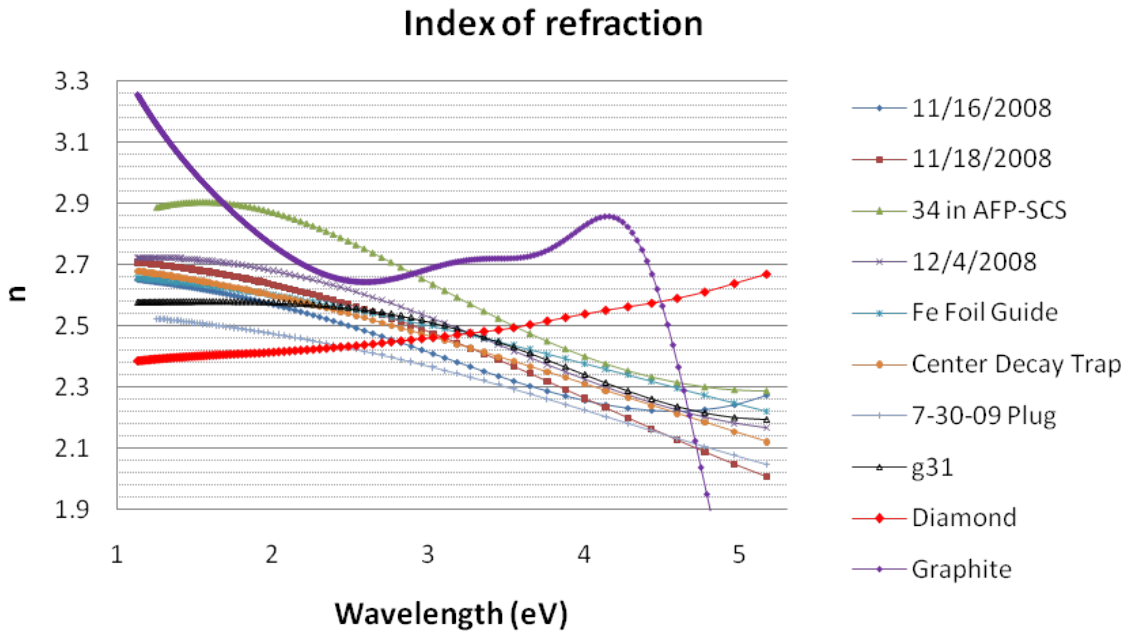

(a) Index of Refraction.

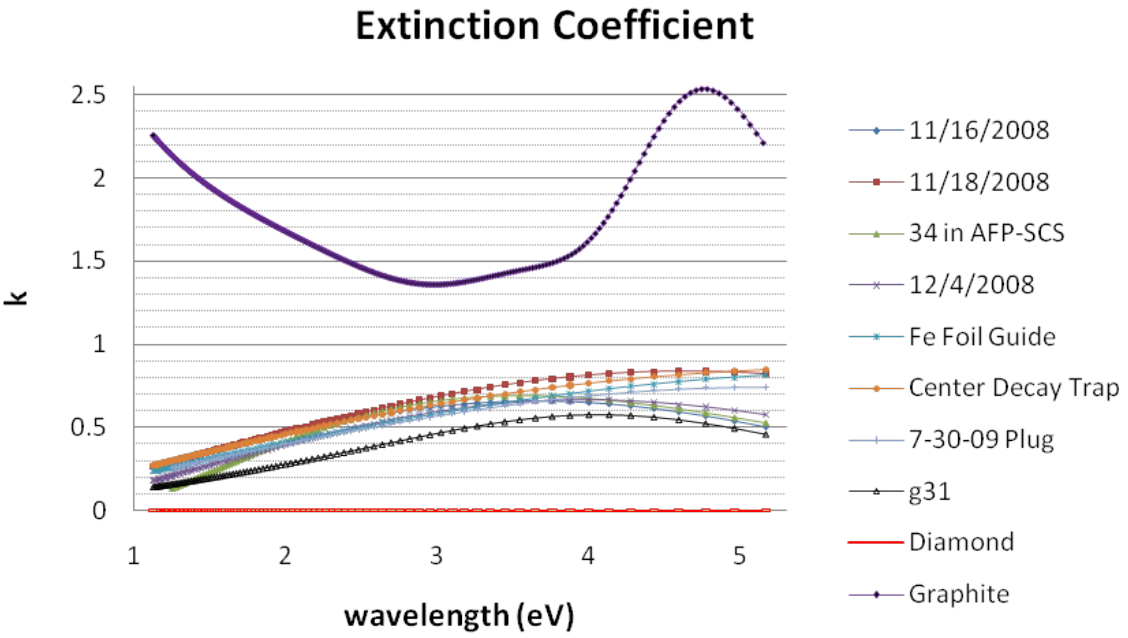

(b) Extinction Coefficient.

Figure 7.22: T-L Model Optical Constants for the DLC coated witness strips listed in table 7.2. The optical constants for Graphite and Diamond, both taken from Palik [133], are also presented for comparison.

Table 7.2: Fit parameters found for the Simple Graded T-L with Surface Roughness model of a series of sample and actual UCNA beamline guide witness strips.

Guide	T-L A_L	T-L E_o	T-L C	T-L E_g	DLC (nm)	DLC Var %	Rough (nm)	MSE
11-16-08	32.6	5.84	11.35	0.227	155	-1.83	0.3	13.7
11-18-08	25.2	5.35	8.09	0.045	138	1.54	0.0	3.52
34 in AFP-SCS	30.8	3.59	5.79	0.721	151	-8.70	2.8	5.6
12-4-08	21.4	4.58	6.71	0.262	123	4.22	2.8	5.3
Fe Foil Guide	42.8	8.17	14.6	0	160	4.25	3.5	14.75
g60 Decay Trap End	29.3	5.01	9.56	0.427	159	-2.67	2.6	13.0
Center Decay Trap	43.8	8.00	15.5	0	153	2.62	0	6.22
7-30-09 Plug	24.8	6.01	9.27	0	262	20	10	4
2008 Rect. Guide	26.5	4.82	7.90	0.386	101	-7.91	1.3	7.4
g31 Quartz	11.7	4.45	4.65	0.001	135	8.82	2.6	6.34
g15 Quartz	43.5	7.47	9.40	0.884	145	-0.42	1.8	4.7

As noted by Robertson, using optical methods to probe the sp^3 content of DLC films has met with mixed success, where the sp^3 fractions are routinely overestimated. This is also the case found by the UCN-PSI group [59]. For this reason we only use ellipsometry to provide a qualitative or relative estimate on the diamond likeness of the film. However, one hope with using the T-L model is that the E_g has the possibility of being correlated with sp^3 fraction of the film. In the paper by Lee [95], sp^3 fractions were measured using electron energy loss spectroscopy (EELS) and then correlated with the the T-L E_g. Here E_g values ranged from 0.65 eV to 2.3 eV, where a 76 % sp^3 fraction corresponded to an E_g of 2.3 eV in a 25 nm thick film. Our measured E_g values are much lower than those reported, however our films are thicker and were deposited with PLD while Lee's work employed CAD. It appears the values of E_g are process dependent and so although a universal equation relating E_g to sp^3 fraction may not exist, we may be able to develop a correlation of sp^3 fraction with the our measured T-L E_gs in the future. We mention here that XPS derived sp^3 fraction values should probably not be used to make this correlation as ellispometry samples the entire film while XPS only samples the surface. Lee also employeed an EMA of bulk Diamond and

bulk glassy carbon optical constants and used these fractions to determine the sp^3 content, which matched EELS sp^3 fractions quite well. When we first attempted this, we did not have much success, but it maybe worthwhile to revisit this method again, possibly using optical constants from known sp^3 fraction DLC samples to make up the model.

7.10 XPS Analysis of our DLC films

As described earlier, XPS is a very useful technique for determining the chemical state and composition of a sample's surface, by measuring the binding energy (BE) of surface atom electrons. When looking for carbon, one looks for the BE of the C 1s electron which is generally around 285 eV. However slight changes in the position and width of the C 1s BE peak occur depending on the bonding nature of the atom. For sp^3 (diamond) bonds the BE is 285.5 eV [21] to 285.2 eV [11], while for sp^2 (graphite) bonds the BE is 284.15 eV [21] to 284.4 eV [11]. So the BE separation between the two bonds is about 1 eV, which was also found in [31]. The *full width at half max* (FWHM) for the measured BE also varies depending on bond state and resolution of X-rays used. When Mg K_a x-rays are used, pyrolytic graphite has a FWHM of about 1.1 eV [31], but when monochromated Al K_a x-rays are used the measured FWHM is 0.6 eV, while for diamond the FWHM is 1.0 eV [124] with monochromated AlK_a x-rays. Thus the XPS spectra of DLC films is a convolution of at least these two peaks. Often a third peak is seen around 286.5 eV which has been identified as C-O bonds at the surface. These bonds have been associated to sp^2 bonds [11]. With XPS the ionization cross sections depend upon atomic factors of the sample when the energy of the x-rays is well above the absorption of the core level, and not the chemical state of a particular atom. Since both the Mg K_a and Al K_a x-ray energies are much greater than the absorption of the C 1s level, the relative intensities of sp^3 and sp^2 peaks is directly proportional to the density of

the film [31]. This relationship is given by [42]

$$\rho(g/cm^3) = 1.92 + 1.37 \cdot \kappa \tag{7.4}$$

where κ is the sp^3 fraction. This equation assumes that all the bonds in the film are either sp^3 or sp^2 and that $\rho = (1-\kappa)\rho_2 + \kappa\rho_3 = \rho_2 + (\rho_3 - \rho_2)\kappa$ so that $\rho_2 = 1.92$ g/cm^3 is the density of a solely sp^2 bonded carbon film and $\rho_3 = 3.29$ g/cm^3 is the density of a solely sp^3 bonded film. The slightly lower densities of ρ_2 and ρ_3 than that of pyrolytic graphite and diamond are due to the the disordered amorphous structure of the PVD DLC film. Thus the maximum Fermi Potential of DLC given by this equation is 285 neV, while the lowest is 166 neV.

The sp^3 fraction is extracted by

$$sp^3 fraction = \frac{\int I_{sp^3}(E)dE}{\int I_{sp^3}(E) + I_{sp^2}(E)dE} \tag{7.5}$$

where $I_j(E)$ is the oscillator associated with the the two different bond states, ie. $j = sp^2$ or sp^3, or more plainly by taking area under the sp^3 peak over the sum of the areas under the sp^3 and sp^2 peaks.

For this work the Perkin-Elmer 5400 XPS/ESCA tool housed in the Hahn Hall of the Chemistry Department at Virginia Tech was used employing Mg k_a X-rays. The base pressure was always below 10^{-8} Torr. The samples were mounted on a copper or aluminum puck with double-sided tape. The puck was placed in the chamber via a load-lock system where the X-rays would bombard the surface and the ejected electrons are detected by a hemispherical energy analyzer. A survey scan was always done on the samples to measure the elemental composition of surface. An example survey scan is shown in figure 7.23a. For

all of our DLC samples, the surface was almost entirely composed of carbon and oxygen, with a small amount of fluorine, usually less than 3%. The fluorine is due to the use of Fomblin® grease to lubricate the carriage drive rod during the coating process. Fluorine is relatively friendly to UCN, having a very low neutron absorption cross section and has been used to coat bottles for use in neutron lifetime experiments [114]. In addition, fluorine has been found to increase the flexiblity of DLC coatings [126] and is now being applied to O-rings for use in waterproof cameras [96].

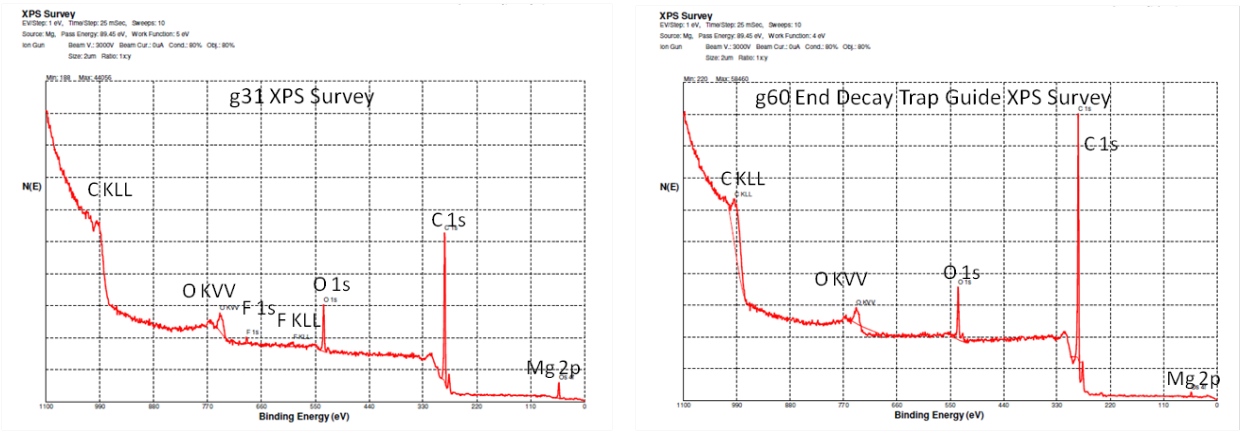

(a) (b)

Figure 7.23: Example XPS survey scans of our DLC coatings. Shown in figure a. is the scan from witness strip of the DLC Quartz guide g31. Figure 7.23b is the scan from a witness strip of the DLC Copper guide g60, which is one of the decay-trap end guides. All our our DLC coating survey scans only showed signals from carbon, oxygen, and sometimes fluorine. The fluorine is due to the Fomblin® grease used to lubricate the carriage drive rod during the deposition. The Mg peak is due to the Mg X-ray source and is a sign that it is nearing the end of its life.

After the survey scan, a multiscan process is performed on particular energy ranges of the survey. In our case, the multiscan usually looked at the binding energies for the C 1s electron from 280-290 eV, fluorine 1s electron from 680-700 eV, and oxygen 1s electron from 525-545 eV. The relative atomic concentrations are derived by using the normalized area

under the respective 1s electron peaks. The multiscan emphasized the C 1s electron where the parameters of the scan are: 0.05 eV/sweep, 25 msec/sweep, and an analyzer pass energy of 4.45 eV. These settings provided the highest resolution of the tool, but with the expense of a low number of detected electrons per sweep. Thus usually more than 200 sweeps of this energy range are performed to provide adequate statistics. In contrast usually only 40 sweeps are performed over the oxygen and fluorine 1s electron BE ranges.

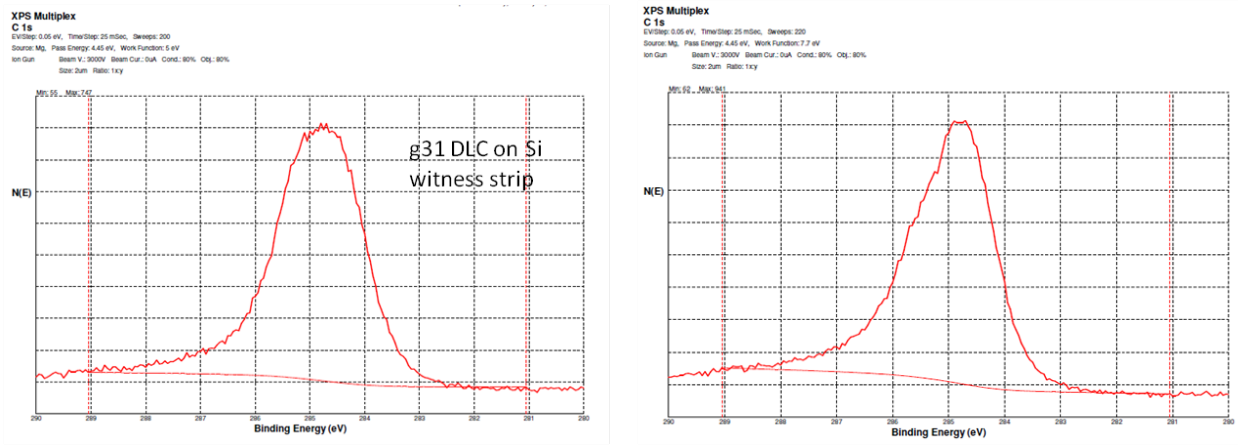

(a) g31 Raw Data

(b) 12-04-08 Raw Data

Figure 7.24: Raw C 1s data for witness strips from guides g31 (DLC Quartz process) and 12-04-08 (DLC Copper process). The red line underneath each peak is the Shirely background that will be subtracted during the data analysis.

Figure 7.24 shows the raw C 1s scan of witness strips from guide g31 and 12-4-08. The data was then analyzed with the AugerScan Software by RBD Enterprises, Inc. provided with the Perkin-Elmer 5400 XPS/ESCA tool. Here the data is first smoothed using a built in smoothing function, and then the background under the peak is subtracted using the Shirley Method [161]. Three Gaussian-Lorentz (G-L) peaks were used to fit the broad C 1s peak: one associated to the sp^3 bonds, one for the sp^2 graphite bonds, and one for the C-O bonds (assumed to be sp^2 bonds) as done in [124] [14][53]. Here the Gaussian peak accounts

for instrumental broadening, sample phonon interactions, and chemical disorder, while the Lorentz peak accounts for the finite lifetime in the core-hole photoionization process [54].

Because the scans were done at different times, the location of the C 1s peak moved around depending on detector conditions and what was chosen as the work function of the analyzer (not the sample). However the FWHM stayed constant, which it should, despite these shifts. To obtain reference FWHM we used our pyrolytic graphite target material (sp^2) and a piece of industrial diamond (sp^3). These values were then held fixed in subsequent fits or our samples. Surface scans were performed on these standards and then sputter cleaned with Ar^+ for 5 minutes. The resulting C 1s peaks are shown in 7.25, where two Gaussian-Lorentz peak functions are used: one for the sp^3 or sp^2 peak and then one for the C-O bonds on the surface.

The FWHM and Gaussian percentage attributed to the C-O bonds in the two standards were close in value and so an average between the two was implemented. Table 7.3 lists the FWHM and Gaussian percentage used as constants in fitting the rest of the DLC samples. One will notice these FWHM values are larger than those often listed in the literature. This is due to the variation in the Mg Kα X-ray energy, whereas most published DLC C 1s analysis used monochromated Al Kα X-ray sources.

Table 7.3: Table listing the FWHM and Gaussian percentages for our graphite and diamond standards as measured in the Perkin-Elmer 5400 XPS/ESCA tool.

Bond	FWHM (ev)	Gaussian %
sp^3	1.59	87
sp^2	1.06	57
C-O	1.60	92

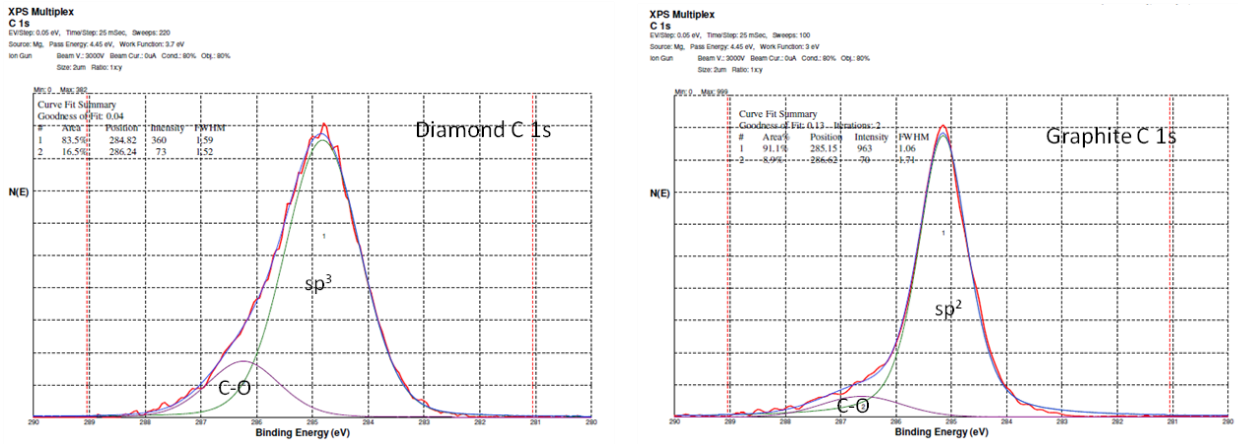

(a) Diamond (b) Graphite

Figure 7.25: C 1s curves of Diamond and Graphite used to determine the FWHM and Gaussian percentage for the G-L peaks associated with sp^3, sp^2, and C-O bonds. These values are listed in table 7.3.

With these constants in hand, the three peaks were used to fit the C 1s peak of the DLC coated witness strips. Figure 7.26 shows the fitted curves for witness strips from guides g31 and 12-5-08. The sp^3 fraction extracted from this analysis is used with equation 7.5 to determine the density at the surface of the film which is then used to calculate the Fermi Potential at the surface. This data is provided in table 7.4. From looking at this table, the DLC films made with the DLC quartz process are much more diamond-like than those processed with the DLC copper method. This also correlates well with the optical ellipsometry results, where the optical constant k of g31 was slightly lower than the rest of

the samples. This is primarily attributed to the use of a plume collimator that is used in the DLC quartz process, but not in the DLC copper process. In principle, the DLC copper process could employ a plume collimator, and is worth investigating. Here the plume could be collimated to different degrees, as was done for the DLC Quartz process. One could also collimate the plume to only allow the "plasma shoots" that were used to coat the decay-trap source plug, 7-30-09 Plug. Nevertheless we see that most of the DLC copper samples have a Fermi Potential near 230 neV which is at the level needed between the AFP and SCS sections and so further studies were deferred.

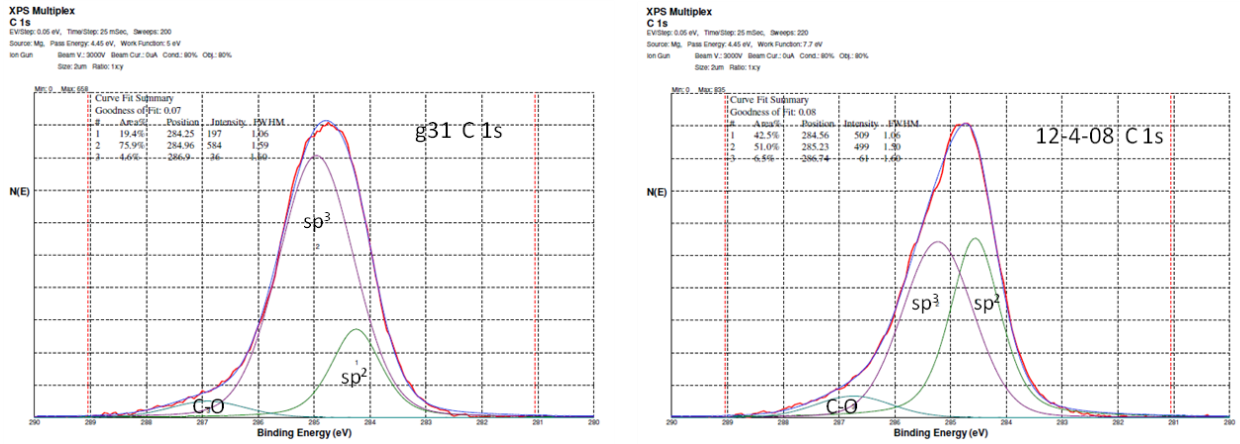

(a) g31 Fitted C 1s Peak

(b) 12-04-08 Fitted C 1s Peak

Figure 7.26: Fitted C 1s curves of the samples shown in figure 7.24.

7.11 Secondary Ion Mass Spectroscopy

As previously discussed, hydrogen is particularly bad for UCN, having a negative scattering length, which lowers the effective Fermi Potential, and a high probability of causing inelastic upscattering. These are the negative aspects for using hydrogenated DLC films for UCN applications. We anticipated that our PLD DLC films would, intrinsically, have very low

Table 7.4: sp^3 fraction, density, Fermi Potential , and critical velocity, V_c, of the UCNA beamline guide witness strips determined from XPS

Guide	sp^3 %	Density (g/cm^3)	Fermi Potential (neV)	V_c (m/s)
11-16-08	53	2.65	229	6.60
11-18-08	57	2.70	234	6.67
34 in AFP-SCS	58	2.71	235	6.69
12-4-08	51	2.62	227	6.57
g60 End Decay Trap	63	2.78	241	6.77
g63 End Decay Trap	54	2.66	230	6.62
7-30-09 Plug	55	2.67	231	6.64
g31 Quartz	76	2.96	256	6.98
g15 Quartz	80	3.02	261	7.05

hydrogen content, and decided to confirm this assumption. There are a number of techniques used to measure the hydrogen content in thin films, with Rutherford Backscattering (RB) and Secondary Ion Mass Spectroscopy (SIMS) the most common. The UCN-PSI group working on DLC used Hydrogen Forward Scattering, a RB technique, where ions, such as He, C, O, Au, etc., impinge the sample at a glancing angle and knock off hydrogen atoms which are then detected. The down side with this technique is that the maximum depth probed is about 30-50 nm for high depth resolution scans. SIMS on the other hand can be used to interrogate the entire thickness of the film at $\sim$1 nm depth resolution. However SIMS is notoriously difficult to calibrate which is necessary to obtain absolute concentrations. Without this calibration, the measured concentration for our tool could be off by a factor of 100 [73]. Thus a calibration standard is usually used to determine the relative sensitivity factor for the particular element in the particular sample, in our case hydrogen in DLC. To make a hydrogen standard, we decided to implant protons into a piece of pyrolytic graphite. This was chosen over a DLC sample because the relative uncertainty in the density profile of the DLC samples makes it difficult to determine the correct implantation parameters. Core Systems was commissioned to implant the protons [71]. Figure 7.27a shows the calculated

implantation profile and measured profile in our SIMS tool, where a clear implantation peak is observed. The relative sensitivity factor was determined by integrating from about 150 nm (the minimum between surface and implanted hydrogen) to about ∼300 nm, and setting this total equal to the total number of implanted hydrogen atoms. The standard was measured during the same pump down session as the other four DLC samples, which are shown in figure 7.28. Here Cs^+ ions were used to sputter the DLC surface while the analyzer was set to look for only H^- anions. The standard allowed the error on the concentration to be brought to ±50%.

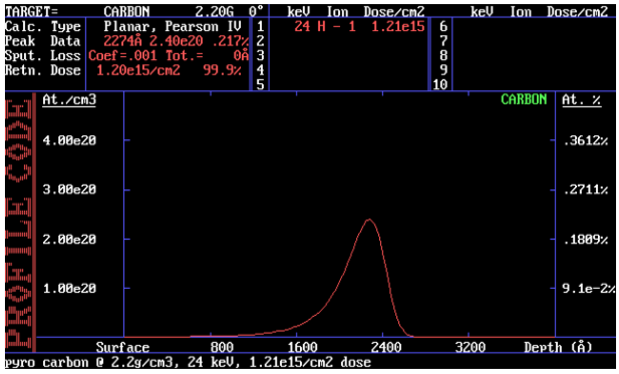

(a) Calculated proton implantation curve in graphite

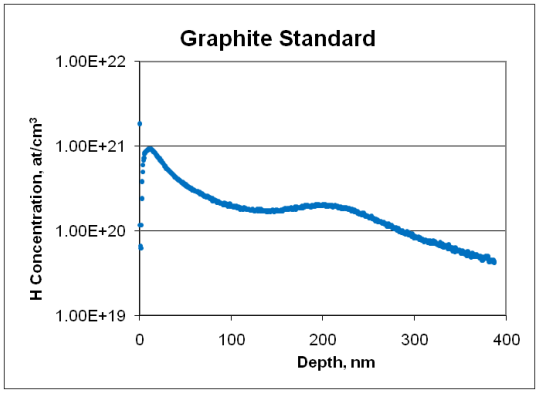

(b) Measured hydrogen concentration in the standard.

Figure 7.27: A hydrogen in graphite SIMS standard was made by implanting protons in a puck of pyrolytic graphite. Figure a) shows the calculated curve of the implantation of 24 keV protons, flux equal to 1.21×10^{15} protons/cm^2, normal to the 2.2 g/cm^3 graphite puck. The peak concentration is calculated to be about 2.4×10^{20} at/cm^3 at 227 nm. This is roughly observed in the SIMS measurement where a hydrogen peak appears near the predicted depth with the expected concentration. This standard reduces the error on the absolute concentration of the hydrogen in our DLC samples to 50%, down from a factor of 100.

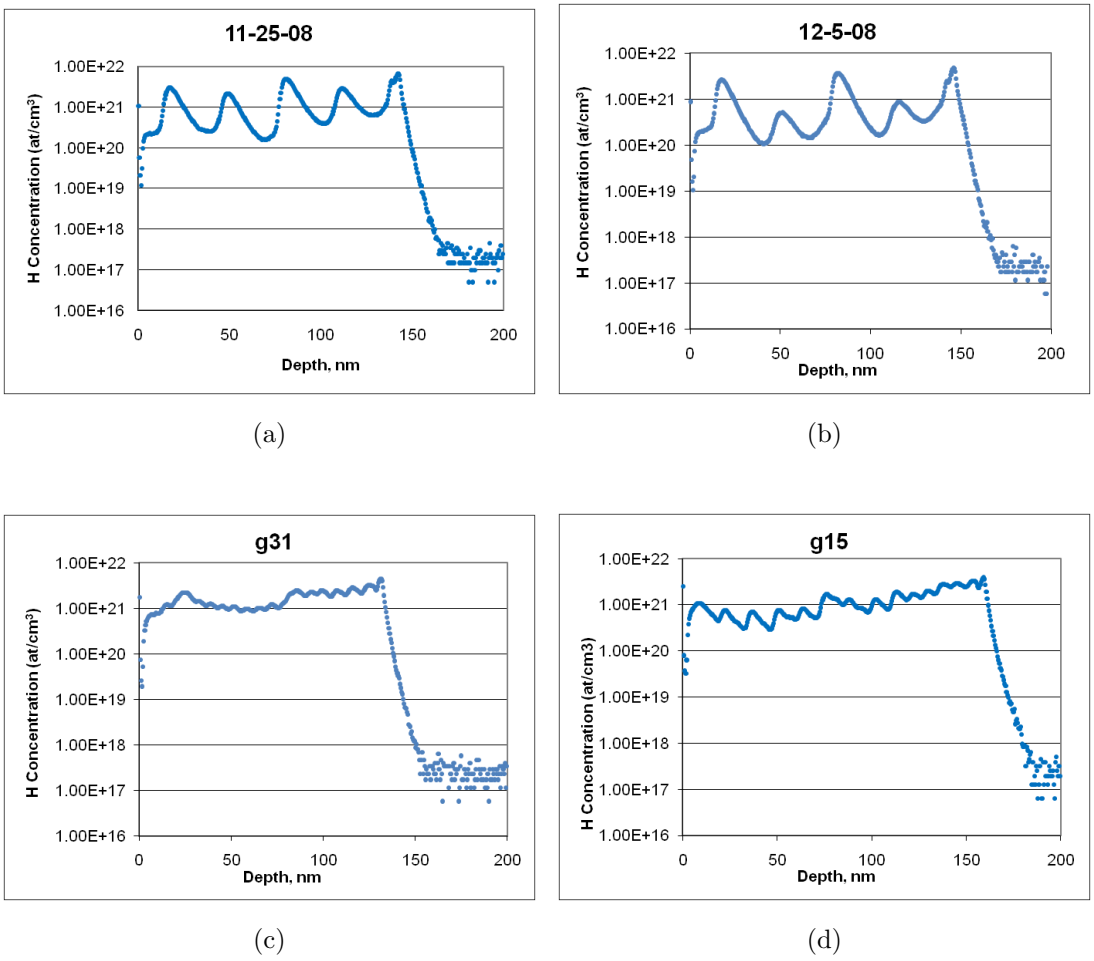

Figure 7.28: Hydrogen concentration as a function of depth in our DLC samples as measured by SIMS. The surface of the film is at 0 nm, while the DLC-SiO_2/Si interface is when the hydrogen concentration falls to 10^{18} at/cm^3.

The first thing that jumps out is the peak structure of all the scans, where g31 and g15 have many more peaks than the 11-25-08 and 12-5-08 witness strips. Guides g31 and g15 were coated with the DLC quartz process, where greater than 30 passes over the pyolytic graphite target are required to obtain a 150 nm coating, while guides 11-25-08 and 12-5-08 were coated with the DLC copper process requiring 5 to 6 passes. The number of peaks do not exactly correlate with the number of linear passes over the PLD target and so further

Table 7.5: Average hydrogen concentration throughout the four DLC samples measured along with the hydrogen/carbon ratio assuming a density of carbon obtained through our XPS analysis.

Guide	Max ^{1}H $\times 10^{21}$ at/cm^3	AVG. ^{1}H $\times 10^{21}$ at/cm^3	AVG. ^{1}H/C ratio %
34 in AFP-SCS	6.75	1.24	0.9
12-04-08	4.76	0.76	0.6
g31	4.44	1.61	1.1
g15	3.93	1.21	0.8

SIMS studies like this need to be performed while varying the pass number and speed of the pass to confirm this correlation. Nevertheless, the point of the study was to measure the hydrogen concentration and here we see that this hovers around 1×10^{21} atm/cm^3. Table 7.5 lists the average hydrogen concentration of each sample along with the ratio of hydrogen to carbon, where the carbon density throughout the whole film is assumed to be that determined for the surface using XPS. One also can see that the DLC thickness, as measured where the hydrogen concentration drops off sharply as the sputtering breaks into the Si substrate, roughly agrees with that measured by our other techniques. We should also mention that the dip in the hydrogen concentration very near the surface seems to be a property of the tool, not the sample, as this also appears that in the graphite standard scan. It would be incorrect to think that this is evidence of the deuterium gas which is used in the venting procedure of all our DLC coated guides.

7.12 Atomic Force Microscopy of the DLC Films

Earlier in section 1.5 we discussed how the surface roughness affects the transportation of UCN through a guide. Here a guide surface should have lower than 5 nm RMS roughness over a 50-200 nm $\times$ 50-200 nm area (about the wavelengths of most of our UCN). The smaller

the roughness the more specular the reflection and thus more efficient the transport system which translates into more neutrons into the UCNA decay trap where their beta decay can be observed. Any coating applied to the inside of the guide material should add very little extra surface roughness. Mark Makela showed that our PLD-DLC films were very smooth with Ra roughnesses $\ll 1$ nm [110]. However it was not clear that our DLC-copper process would produce similar roughness as this process does not collimate the ablation carbon plume, which could allow larger particulates that tend to be at the fringes of the plume, the so called splashing phenomenon of PLD [174]. So AFM measurements were performed on several samples and the RMS roughness of these films were below 1 nm as shown in figure 7.29. Scan 7.29a is DLC on an electropolished copper witness strip, from guide 34 in AFP-SCS. The majority of the 3.5 nm RMS roughness is due to the copper substrate itself. Scan 7.29b is a witness strip from an end guide of the UCNA decay trap section. Here the DLC coating is on a Si witness strip and we see an RMS roughness of 0.8 nm. There appears to be slightly more particulates in our DLC copper films than with the DLC quartz process, but a larger study of all our witness strips is required to determine if this is generally true or just particular to these scans. It would be interesting to collimate the plume in our DLC copper process and see if the roughness and number of large particulates changes.

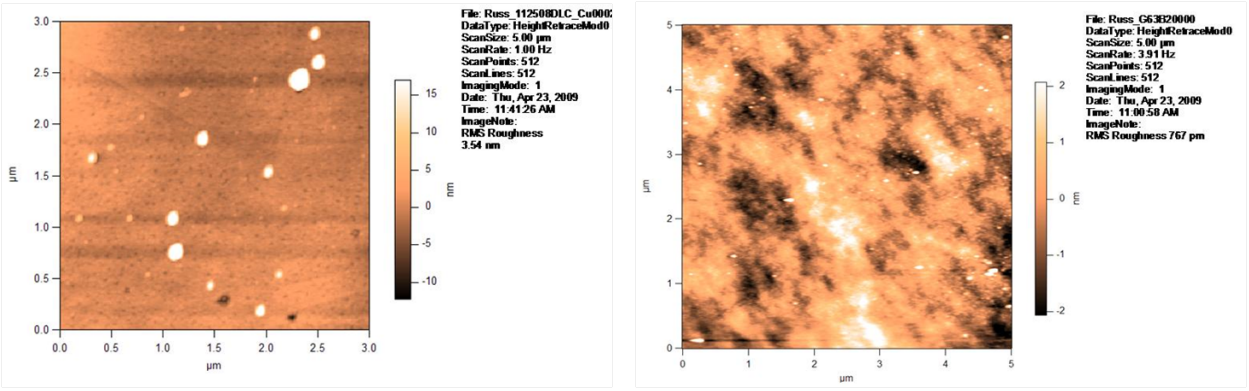

(a) (b)

Figure 7.29: AFM height images of the DLC coating resulting from our DLC Copper process. Figure 7.29a is a DLC coated EP copper witness strip from the AFP-SCS guide coating session. The 3.5 nm RMS roughness is primarily due to the EP copper plate itself. Figure 7.29b is a DLC coated Si wafer from the g63 guide (end decay-trap piece) coating session. Here we see the RMS roughness is less than 1 nm.

7.13 Conclusion

Diamond-like carbon has quickly become an attractive coating for UCN applications because of its relatively high Fermi Potential, low loss, and low depolarization probability. Indeed the SD_2 source at PSI is being completely coated in DLC because of these properties. In the context of the UCNA experiment, DLC fits all the requirements of the beamline, especially in the region the RF spin flipper. Unfortunately, applying a well adhered high sp^3 fraction $\sim$150 nm thick DLC coating on the inside of a meter-long tube is quite challenging. Reproducing the feat many times in an effort to build a UCN beam line can be a daunting task. This has been our charge in the past six years, to which several new devices and procedures have been implemented. The development of the target raster system along with the use of the internal TOF ion probe to monitor the plasma plume has been extremely valuable in the

production of our DLC coatings. These developments are incorporated in our DLC Quartz process, and the DLC quartz guide located in the RF spin flipper region was coated back in 2006 and is still being used with no signs of of degradation.

In 2007/2008 the UCNA collaboration moved to using copper and stainless steel UCN guides, leaving the use of quartz tubes to only where they were absolutely required, such as the RF spin flipper region. We were asked to provide 150 nm thick DLC coated copper guides to replace the uncoated copper versions in the Polarization Region of the UCNA beamline. Unfortunately, this task was much more difficult than anticipated and as a result led us to develop a very different coating process, our DLC Copper process. Here a strong magnet is placed behind the pyrolytic graphite target and then negatively biased from 100 V to 250 V. The ablation plasma plume is visibly altered which is indicative of a higher ionization fraction. With this process, DLC coated copper guides have been produced to replace the bare copper beam line from the AFP magnet to the decay trap inside the SCS magnet.

In addition to our coating processes, our coating characterization processes have also improved. Every DLC coating includes several witness strips that hang off the ends of the guides and are used to characterize the coating for that particular guide. Here the thickness is measured with a profilometer and ellipsometer. The ellipsometer is also used to obtain the optical constants of the films used to provide a qualitative measurement of the diamond likeness of the film, via the Tauc-Lorentz model. XPS analysis of the carbon 1s peak has been critical in quantifying the sp^3 fraction of the films, and SIMS has been employed to show that the hydrogen content in our films is very small. These techniques allow us to quickly evaluate the quality and content of our thin films. One should note that the reason we use so many thin film analysis techniques is that the ultimate test, using UCN themselves, is not possible prior to actual running of the experiment.

While a lot has been done over the past six years in developing our DLC coating and characterization processes, there is still more to do. The implementation of the OES system in combination with a TOF ion probe bias study should provide valuable information on how the plasma is changing between the DLC Quartz and DLC Copper deposition methods. Exploration into using the so called "plasma shoots" to coat the inside of copper tubes seems warranted with the success of the decay trap plug coating. Also, many other characterization techniques can be developed, such as Raman spectroscopy, both visible and UV, as well as electron energy loss spectroscopy (EELS), and X-ray reflectivity to name a few. In addition other films promising even higher Fermi Potential's, such as carbon nitride [110] or carbon boron nitride [164] could be developed with suitable modification to these processes.

Chapter 8

Closing Remarks

The use of UCN to make precision measurements of fundamental parameters of the standard model is both exciting and challenging at the same time. UCN are currently being used to provide every more precise measurements of the neutron's lifetime and are pushing the frontier on searches for the neutron's electric dipole moment. In addition, UCN can and are being used to measure several letters of the neutron decay correlation "alphabet". Indeed, the UCNA experiment is measuring the angular correlation A, pronounced "Big A", which is the correlation between the neutron's spin and the emitted electron's momentum, in polarized neutron beta decay, which is directly related to g_A, the axial-vector weak coupling constant, which has important nuclear and astrophysical implications, see section 1.7.

However, unlike typical charged particle beams used in nuclear physics experiments, UCN can not be easily guided through the use of electric and magnetic fields. UCN act more like a classical gas, rather than a quantum mechanical particle, although it is the quantum mechanical nature of the strong interaction that allows the UCN to reflect from surfaces. At an elementary level, the UCN will expand into the vacuum of a bottle or

beamline and either pass through, be absorbed, or be reflected by the container, quickly sampling the entire surface area of the container in the process. How well a surface reflects UCN is partly described by the Fermi Potential, V_F, which sets the maximum energy a UCN can have and still reflect, and partly determined by the neutron's probability to be lost, via absorption or inelastic upscattering. Materials with high Fermi Potentials and low loss probabilities make the best UCN reflectors. Table 1.1 lists the V_F and loss probabilities for a number of common UCN materials, where ^{58}Ni , nickel, beryllium, and diamond, and diamond-like carbon (DLC) top the list of materials with high Fermi Potentials. In addition, experiments such as UCNA require the UCN to be polarized when the beta decay occurs. Often the UCN will make many reflections as they transverse the beamline from where they are polarized and where their decay is actually observed. Thus guide and bottle materials need to preserve this polarization, and beryllium, diamond, and DLC satisfy this requirement. Generally one desires the highest Fermi Potential and lowest loss material where the UCN are created, and then makes a compromise between V_F and the loss/depolarization probabilities when choosing materials for the polarization region of the experiment. Materials like nickel, especially ^{58}Ni , are used in the source regions of a UCN beamline, while beryllium and DLC are used in the polarization regions.

Often, it is too expensive and/or difficult to construct the entire guide and bottle components from the desired UCN reflection material and so more common materials, such as stainless steel, aluminum, copper, etc., are machined and then coated with the desired UCN reflection material. This has been my role in the UCNA experiment where I have provided the ^{58}Ni coatings on all of LANSCE SD_2 UCN source components and DLC coatings on the UCN guides in the Polarization Region of the experiment. In addition I have provided a number of uncoated beamline components, such as the electropolished copper guides between the PPM and AFP magnets of the 2010 UCNA beamline. To accomplish these tasks

I have assisted in the development of a UCN guide coating facility at Virginia Tech. Here we have a custom tube coating deposition chamber that can be fitted with either a custom length single pocket e-beam or a pulsed laser deposition (PLD) target system to apply the thin films on the inside of meter long tubes ranging in ID from about 1 to 9 inches in diameter, depending on what film needs to be applied. The tube/guide is situated into a carriage system that rotates and translates the tube over the deposition source, be it the ebeam head or PLD target. Recently this system has been improved by the addition of a set of rollers that allow one end of the tube to rotate freely while the other end is connected to a chain-driven sprocket rotation system. In addition, this system is now operated with a home-made stepper motor rotation and drive apparatus. As a result of these systems, the tube coating process has greatly improved our throughput of guide components. In fact the system has never failed when the temperature inside the chamber is kept below 100° C. Furthermore, we also employ a bell-jar style ebeam evaporator which has been mostly used to apply ^{58}Ni films onto the variety of SD_2 source insert components. In addition several cleaning stations are utilized, such as the ultrasonic tube cleaning station, the quartz guide etch station, and the homemade guide vacuum oven to prepare the components for deposition.

Moreover several new coating procedures have been developed to ensure a well adhered coating on the guide/component substrates. With many of our coatings the film would often delaminate or peel away from the substrate, delaying the UCNA experiment. Thus a large effort has been focused on increasing the adhesion of our films to their particular substrates. With respect to our ^{58}Ni films, a successful coating process was developed while working through delamination issues encountered with the 2007 source insert. This process was used to successfully coat the 2009 source insert, which passed LN_2 cold tests. Here all components were machined, then mechanically polished, electropolished, sonic cleaned in organic solvents, rinsed with Ethanol or DI water, blown dry with UHP N_2, and loaded

into the vacuum chamber. Once under vacuum, the components are baked with a quartz lamp near 100° C for 1-2 hours. The lamp is also left on during the deposition process. The deposition rate is kept near 3 Å/sec and the film is allowed to grow up to 180 nm as measured by a crystal monitor. The components are baked for another 1-2 hours after the deposition and then allowed to cool to room temperature before venting with UHP N_2. Employing the quartz lamp before, during, and after the deposition along with a crystal monitor (providing deposition information) were essential in providing a well adhered ^{58}Ni coating on the source insert components.

It is difficult to quantify the improvement or effectiveness of the ^{58}Ni coatings, as it is not practical to test a coated vs. uncoated source insert, due to the activation of the source components as well as the large amount of effort that goes into installing and testing the source insert with real UCN. Nevertheless the collaboration uniformly agrees that the source inserts need to be coated with a film that provides a higher Fermi Potential than that of stainless steel. Thus the ^{58}Ni coating provided by Virginia Tech has been an essential component to the improvements in UCN rate increases attributed to the installation of each new source insert. Figure 8.1 shows the UCN gatevalve (GV) monitor rate history (UCN detector just outside the source shield wall) for the 2008 and 2009 UCNA data sets. Here we see that the average GV monitor rate actually dropped after the installation of the 2009 source insert. This is primarily attributed to a poor proton beam tune, where only about half of the protons were hitting the tungsten target. The floor supporting the source and shield wall sunk many millimeters, causing the tungsten target to partially drop out of the range of the proton beam. The fact that the GV monitor rates were close to the 2008 rates despite this problem provides evidence to expect the rates should be much higher with the installation of a larger tungsten spallation target in 2010.

My other responsibility to the UCNA experiment was to provide the diamond-like carbon

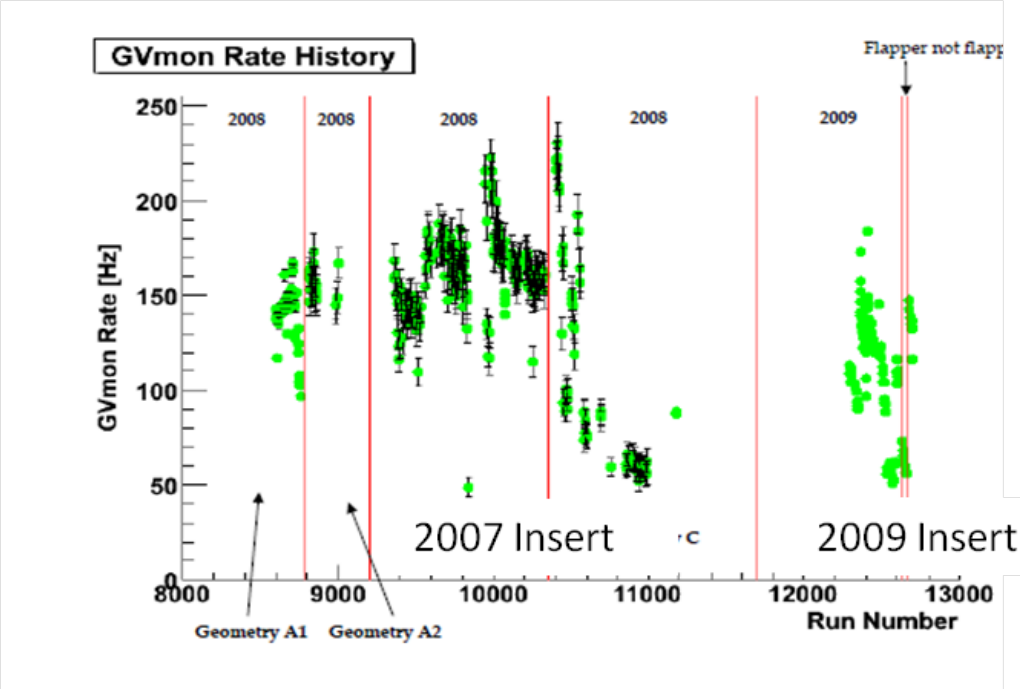

Figure 8.1: 2008-2009 GV monitor rate history vs. run number. The run numbers are further grouped according to spectrometer geometry (different decay-trap and MWPC foils thicknesses). The average GV monitor rate for the 2009 source insert is ∼125 Hz, as compared to ∼150 Hz measured for the 2007 source insert. Figure used with permission from Adam Holley (2010) [68].

(DLC) coatings for the rest of the UCNA beamline, but most importantly the Polarization Region of the experiment, where it is critical to preserve the UCN polarization. DLC, if properly prepared, fits all the requirements for this region of the beamline, as it has a high Fermi Potential, is smooth, and has very low UCN loss and depolarization probabilities per bounce. There are a variety of ways to make DLC, but pulsed laser deposition of DLC (PLD-DLC) has been shown to produce a film with the desired properties and lends itself more easily to coating the inside of tubes that could be used to build up a UCN beamline. To this end, the VT and NCSU UCNA groups, led by Mark Makela, developed a procedure for applying DLC on the inside of quartz tubes, which were used to make DLC coated quartz guides for a DLC depolarization probability per bounce measurement conducted at the Institut Laue-Langevin [110].

Continuing this work, much of my time at Virginia Tech has been spent developing systems and procedures that improve the quality and reliability of these coatings. One of the first procedures implemented was the religious incorporation of several witness strips, usually pieces of a Si wafer, so every coating could be analyzed after the deposition to shed light on the properties, such as the thickness and diamond likeness, of the coating. The next major evolution of our DLC coatings was to standardized the use of the TOF ion probe initiated by Mark Makela, to monitor the carbon ablation plasma plume during the course of a deposition. Measurements from this probe combined with the importance of the plasma plume kinetic energy in making high sp^3 fraction DLC (recall sp^3 fraction is $\propto$ Fermi Potential) led to the construction of the target-raster system, which allows the laser spot on the graphite target to be fixed with the respect the vacuum chamber. When combined with a plume collimator, the same portion of the plasma plume is allowed to deposit onto the tube with every laser shot. The TOF ion probe, which measures the energy of the C^+ in the center of the plume, is then used to dial in the required laser energy to provide a C^+ energy of 100 eV. With our standard plume collimator only carbon ions with energies around 60-100 eV are allowed to deposit on the guide tube. Thus the DLC Quartz process was born, where around 30 passes of the tube over the ablation plume are required to make a 150 nm thick coating. Witness strip analysis from guides made with this process show that the film's optical constants are very diamond like. The average hydrogen concentration of the film is about 1%, and the sp^3 fraction at the surface, as measured by XPS, is near 80%, which translates into a $\sim$260 neV Fermi Potential. The DLC coated quartz guide located in the RF region of the AFP spin flipper, guide g31, was coated with this process in 2006 and is still being used to this day. We remind the reader that it is this region of the beamline that requires a guide techonology that allows the RF signal to transmit into the guide unimpeded, a requirement which DLC coated quartz guides uniquely satisfies.

Given the time to produce enough DLC coated quartz guides, about 2-3 weeks per meter long tube, to make up the UCNA beamline and the ever pressing need to collect beta decay data, the UCNA collaboration decided to move away from DLC coated quartz guides and replaced most of the beamline with electropolished stainless and copper tubes, where copper was reserved for the polarization portion of the beamline since it has a much lower UCN depolarization probability per bounce than stainless steel. The metal tubes proved to be a more robust beamline material and allowed for the development a very small gap beamline, where the tubes are butted up against each other. Unfortunately, this procedure does not lend itself easily to using quartz tubes, as the quartz will often chip and shatter as they are butted up against each other several times. Also at the time our chain drive/stepper motor systems had not yet been invented and we still had many drive/rotation failures ruining the production of a number of DLC coated quartz guides. Thus using DLC coated copper guides were seen as a solution because the same small gap beamline construction techniques could be used and the Fermi Potential of the guide would be at least 170 neV, that of copper, and not the 90 neV of quartz if the DLC coating was thin in some areas. However, producing an adhered 150 nm thick DLC coating on the copper substrate turned out to be quite difficult, as carbon does not form a strong chemical bond with the copper substrate. This led to the development of our DLC Copper process in which a strong magnet is attached to the back of the graphite target and a 100-250 V bias is applied to the target/magnet during the deposition. The ablation plume is brighter and less directional as compared with the unbiased the plume, which is indicative of a higher plume ionization fraction (which always makes a better DLC film). It is my hope that this is indeed verified with the the recently received optical emission spectrometer in the future. The Polarization Region of the UCNA beamline has been coated with this process where witness strips show that the surface of the film has a sp^3 fraction near 55% which implies a Fermi Potential around 230 neV, a RMS rougness less than 1 nm, an average hydrogen content of less than 1%, and more

diamond-like than graphite-like optical constants. The reason for the lower sp^3 fraction and higher extintiction coefficient when compared to the DLC Quartz process is mostly likely due the fact that a plume collimator is not used with the DLC Copper process. Due to time constraints the incorportation of the plume collimator hasn't been fully explored, although it should be in future work.

In addition an investigation into the surface roughness of our copper guides was presented, where roughness measurements from various mechanical polishing steps were measured with an industrial profilometer and an AFM both before and after electropolishing. Here the mechanical polishing process prepares the surface for the electropolishing process, which cleans and smooths the surface on the sub-micron scale. The industrial profilometer measures roughness on a length scale ranging from tens of microns to millimeters, while the AFM measures the roughness on the nanometer to micron length scale. Both scales are important for UCN guide transmission. These measurements do indicate that mechanically polishing the copper surface to as close a mirror finish as possible, i.e. finish with a color compound loaded cotton buff, and then electropolishing produces an overall smoother finish on both these scales, but still not at the level of our previously used quartz tubes. Nevertheless these measurements provide a benchmark for future guide roughness studies, where other techniques, such as slurry polishing and/or chemical etching may be employed.

During these developments at Virginia Tech, the UCNA experiment at LANSCE was churning along and polarized neutron beta decay taken was taken in 2007, 2008, and 2009, where the beta decay rates slowly increased each year as improvements to the SD_2 UCN source, i.e. the source inserts, and beamline, i.e. DLC copper guides, were installed. Table 8.1 details these rate increases. Here the modest increase from 2008 to 2009 is mainly due to the fact that we had a very poor proton beam tune. In addition we had difficulty cooling the SD_2 to optimum levels, which also hindered the UCN production. The difficulty eventually

Table 8.1: Approximate Observed UCNA Beta Decay Rate vs. Year.

Year	Rate Hz	Comments
2006	< 2	Poor Source + Lossy Guides
2007	6.5	Stainless + Copper Guides
2008	20	2007 source insert
2009	25	DLC copper guides + 2009 source insert + poor beam tune

manifested itself in the massive cryogenic helium leak which shut the experiment down at the end of 2009. The fact that the decay rate actually increased is a testament to the improvement provided by the new 2009 source insert and DLC copper guides. Currently a new, larger target has been installed, the helium leaks fixed, and now the UCN monitor located just outside the shield wall guides, the GV UCN monitor, is measuring a rate of 350 Hz, which is the largest rate seen at this location in the beamline by more than 100 Hz.

Furthermore, one can look at the beta decay rate divided by the GV UCN monitor rate for each beta decay run to gain a better idea as to how much improvement can be attributed to the DLC coated copper guides themselves. Adam Holley performed this analysis which is shown in figure 8.2, where the run numbers are grouped by year and further by what thickness of Mylar end cap and wire chamber windows were used denoted by geometry A1, A2, B, and C. The DLC copper guides were installed in 2009, where we see this ratio increased by about a factor of 1.4 over the 2008 ratios. We acknowledge that this is lower than the expected factor of 1.8, noted in section 7.8 and currently believe the disparity is due to increased loss of UCN via tunneling through the rectangular guide and the rectangular transition plate coatings, where the DLC coating is a little thin, $\sim$110 nm in the case of the rectangular guide and either 70 nm or 115 nm for the transition plate depending on what side is exposed to the UCN. In addition, the disagreement may be also be attributed to a slightly lower DLC Fermi Potential area in one of the guides and/or a larger gap(s) between guides than was simulated. Nevertheless the DLC coated copper beamline guides have increased

the amount of observed beta decays in the UCNA experiment, all while preserving the UCN polarization.

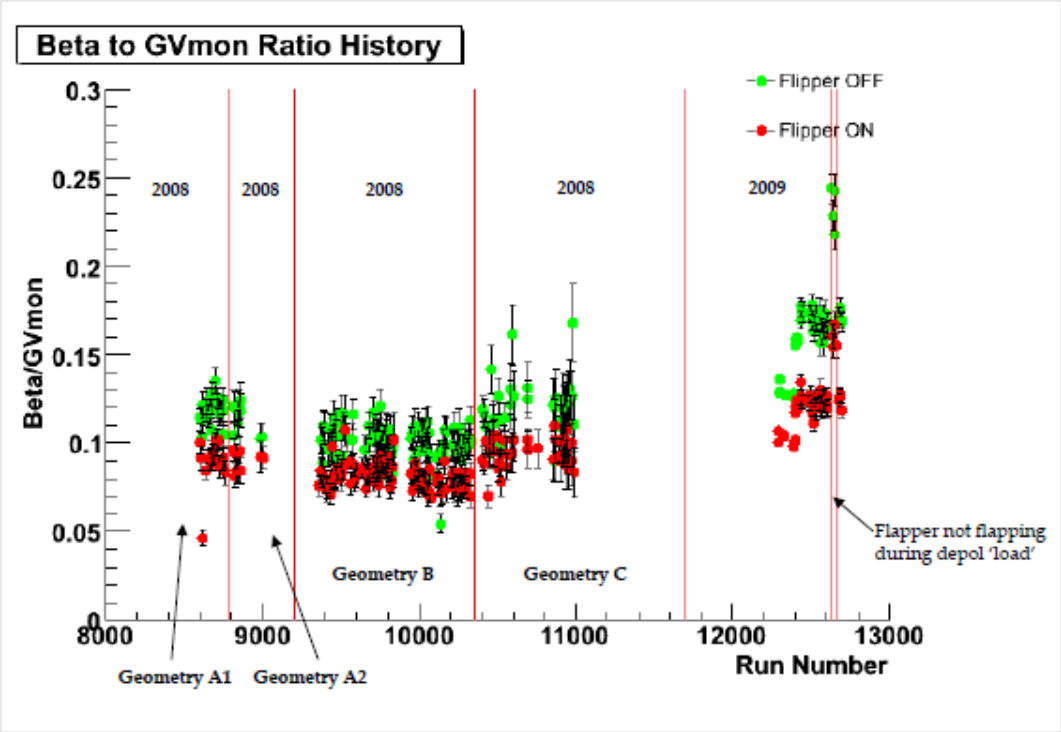

Figure 8.2: Beta decay rate divided by GV UCN monitor rate vs run number (year/MWPC foil configuration). The DLC coated copper guides were installed in 2009 and are the primary cause for the increase in this ratio. The difference between in beta decay rate for the two different spin states arises from the 60 neV potential hill/well caused by the SCS 1 T magnetic field. When the flipper is on, some UCN are reflected by this potential and so fewer UCN are able to make it into the decay trap and decay. When the flipper is off, the UCN are accelerated into the decay trap. Figure used with permission from Adam Holley (2010) [68].

We close with a summary of the measurements of A made by the UCNA collaboration. The 2007 data produced a 5% proof of principle measurement where the error bar was highly statistics limited [136]. A very large data set was taken in 2008, where again uncoated electropolished stainless steel and copper guides made up most of the beamline. Here 0.7 and 13.2 micron thick Mylar foils, both coated with 200 nm of berylium, were attached to the end of the decay trap in order to trap more UCN in the decay region of the experiment.

In addition two different wire chamber window foils, 25 and 6 microns thick, were installed. The different foils allow one to study the energy loss and backscattering effects from the beta decay electron traversing the various materials. In 2009 the Polarization Region of the experiment was fitted with DLC coated copper guides, but due to the previously mentioned cryogen leak inside the SD_2 UCN source, the experiment had to be shut down before a self sustaing data set was obtained, and so this data has been included in the 2008 data set. This 2008-2009 data set was analyzed this spring and has resulted in a 1.3% measurement of $A = -0.11966 \pm 0.00089^{+0.00123}_{-0.00140}$, where the measurement is now systematics limited, although the statistics error bar still makes up about 40% of the total error. Thus increasing the observed beta decay rate is still useful. Figure 8.3 shows this result in relation to the previous measurements of A mentioned in section 1.9.1 (recall all these other measurements employed cold neutrons, not UCN). Here we see we are consistent with the most precice measurement of A which is from Perkeo II/Abele 2002. It is also interesting to note that our value of A produces the value of $\lambda = -1.27590^{+0.00409}_{-0.00445}$, which is in better agreement with Serebrov's neutron lifetime measurement, $\tau_n = 878.5 \pm 0.7stat \pm 0.3sys$, as is Perkeo II, than the PDG 2009 value as shown in figure 8.4. Time will tell if this neutron lifetime is correct. Meanwhile, the LANSCE SD_2 source is runing better than ever and the UCNA experiment is poised to make a 0.3-0.5% measurement of A this year, to which the UCNA group at Virginia Tech has played a important role in making this a reality.

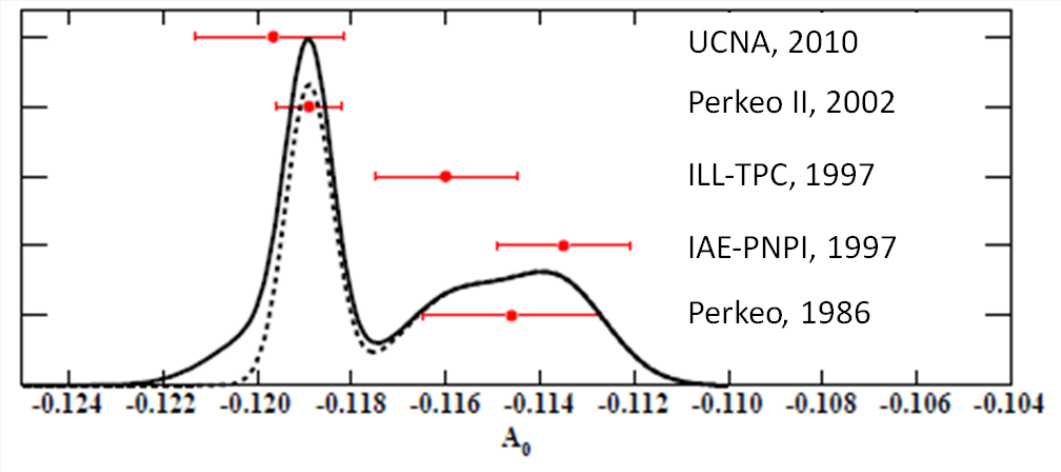

Figure 8.3: Ideogram comparing the previous measurements of A discussed in section 1.9.1 with the 2010 UCNA result. The dashed line is the ideogram with the previous four data points, and the solid line shows the result of including the 2010 UCNA result. Figure modified with permission from UCNA collaboration (2010) [181].

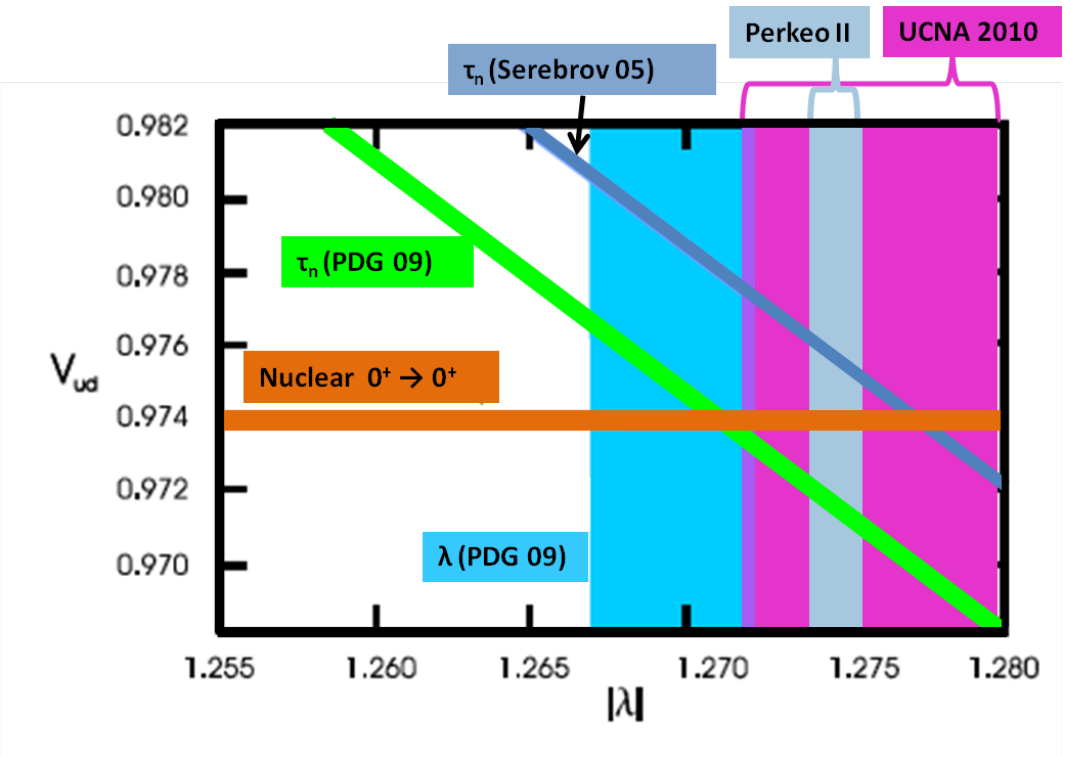

Figure 8.4: Plot of CKM matrix element V_{ud} vs. λ. Notice how the 2010 UCNA result agrees well with the 2008 Perkeo II result and the new 2005 τ_n measurement. Here the Perkeo II band employs the preliminary 2008 values [3]. Figure modified with permission from Brad Plaster (2010) [140].

Bibliography

[1] H. Abele et al. Is the unitarity of the quark-mixing ckm matrix violated in neutron beta decay? *Physical Review Letters*, **88**(21):211801, 2002. Copyright (C) 2010 The American Physical Society Please report any problems to prola@aps.org PRL.

[2] Hartmut Abele. The standard model and the neutron [beta]-decay. *Nuclear Instruments and Methods in Physics Research Section A: Accelerators, Spectrometers, Detectors and Associated Equipment*, **440**(3):499–510, 2000.

[3] Hartmut Abele. The neutron. its properties and basic interactions. *Progress in Particle and Nuclear Physics*, **60**(1):1–81, 2008.

[4] Eric G. Adelberger et al. Solar fusion cross sections. *Reviews of Modern Physics*, **70**(4):1265, 1998. Copyright (C) 2010 The American Physical Society Please report any problems to prola@aps.org RMP.

[5] Nasar Ali, Qi Hua Fan, J. Grcio, E. Pereira, and Waqar Ahmed. A comparison study of diamond adhesion on ductile metals. *Thin Solid Films*, **377-378**:193–197, 2000.

[6] C. Amsler et al. Review of particle physics. *Physics Letters B*, **667**(1-5):1–6, 2008.

[7] Bogdan Povh .and Klaus Rith .and Christoph Scholz .and Frank Zetsche Martin Lavelle. *Particles and Nuclei: An Introduction to the Physical Concepts*. Springer, 4 edition, 2004.

[8] S. I. Anisimov, D. Bauerle, and B. S. Lukyanchuk. Gas dynamics and film profiles in pulsed-laser deposition of materials. *Physical Review B*, **48**(16):12076, 1993. Copyright (C) 2010 The American Physical Society Please report any problems to prola@aps.org PRB.

[9] Wolfram Weise Anthony W. Thomas. *The Structure of the Nucleon*. Wiley-VCH, 2001.

[10] Mike Ashfold. Laser ablation, 2007.

[11] F. Atchison et al. Surface characterization of diamond-like carbon for ultracold neutron storage. *Nuclear Instruments and Methods in Physics Research Section A: Accelerators, Spectrometers, Detectors and Associated Equipment*, **587**(1):82–88.

[12] F. Atchison et al. Diamondlike carbon can replace beryllium in physics with ultracold neutrons. *Physics Letters B*, **642**(1-2):24–27, 2006.

[13] F. Atchison et al. Loss and spinflip probabilities for ultracold neutrons interacting with diamondlike carbon and beryllium surfaces. *Physical Review C*, **76**(4):044001, 2007. Copyright (C) 2010 The American Physical Society Please report any problems to prola@aps.org PRC.

[14] F. Atchison et al. Structural characterization of diamond-like carbon films for ultracold neutron applications. *Diamond and Related Materials*, **16**(2):334–341, 2007.

[15] P. Bopp, D. Dubbers, L. Hornig, E. Klemt, J. Last, H. Schtze, S. J. Freedman, and O. Schärpf. Beta-decay asymmetry of the neutron and g_A/g_V. *Physical Review Letters*,

56(9):919, 1986. Copyright (C) 2010 The American Physical Society Please report any problems to prola@aps.org PRL.

[16] Thomas J. Bowles. Ultra cold neutrons at a spallation source. *Journal of Neutron Research*, **4**(1-4):191–196, 1996.

[17] J. D. Bowman, S. I. Penttil, and W. B. Tippens. A spin reversal system for polarized epithermal neutrons. *Nuclear Instruments and Methods in Physics Research Section A: Accelerators, Spectrometers, Detectors and Associated Equipment*, **369**(1):195–204, 1996.

[18] J. Budai and Z. Toth. Optical phase diagram of amorphous carbon films determined by spectroscopic ellipsometry. *physica status solidi (c)*, **5**(5):1223–1226, 2008.

[19] Ning Cao, Zhen-yi Fei, Yong-xin Qi, Wen-wen Chen, Lu-lu Su, Qi Wang, and Mu-sen Li. Characterization and tribological application of diamond-like carbon (dlc) films prepared by radio-frequency plasma-enhanced chemical vapor deposition (rf-pecvd) technique. *Frontiers of Materials Science in China*, **3**(4):409–414, 2009.

[20] Chun-Chin Chen and Franklin Chau-Nan Hong. Structure and properties of diamond-like carbon nanocomposite films containing copper nanoparticles. *Applied Surface Science*, **242**(3-4):261–269, 2005.

[21] Paul K. Chu and Liuhe Li. Characterization of amorphous and nanocrystalline carbon films. *Materials Chemistry and Physics*, **96**(2-3):253–277, 2006.

[22] F. E. Close and R. G. Roberts. Spin content of the proton. *Physical Review Letters*, **60**(15):1471, 1988. Copyright (C) 2010 The American Physical Society Please report any problems to prola@aps.org PRL.

[23] J.A. Woollam Co. Wvase32, 2007.

[24] Inc. Coherent, 2010.

[25] Rbc Ukqcd Collaborations, T. Yamazaki, et al. Nucleon axial charge in (2+1)-flavor dynamical-lattice qcd with domain-wall fermions. *Physical Review Letters*, **100**(17):171602, 2008. Copyright (C) 2010 The American Physical Society Please report any problems to prola@aps.org PRL.

[26] D*égagé* Corp. Clean room bags, films & tubing, 2010.

[27] Andrzej Czarnecki, William J. Marciano, and Alberto Sirlin. Precision measurements and ckm unitarity. *Physical Review D*, **70**(9):093006, 2004. Copyright (C) 2010 The American Physical Society Please report any problems to prola@aps.org PRD.

[28] Micheal K. Zuraw Daniel M. Dobkin. *Principles of Chemical Vapor Deposition: What's Going on Inside the Reactor*. Springer Netherlands, 1st edition, 2009.

[29] Phil Danielson. Conditioning vacuum chambers. 2005.

[30] Leon J. Radziemski David A. Cremer. *Handbook of Laser-Induced Breakdown Spectroscopy*. Wiley, 2006.

[31] Javier Daz, Guido Paolicelli, Salvador Ferrer, and Fabio Comin. Separation of the sp3 and sp2 components in the c1s photoemission spectra of amorphous carbon films. *Physical Review B*, **54**(11):8064, 1996. Copyright (C) 2010 The American Physical Society Please report any problems to prola@aps.org PRB.

[32] J. Deutsch. Status and future prospects in searches for new interactions in neutron and nuclear beta decay, muon decay and pion decay. *nucl-th/9901098*, 1998.

[33] T. W. Dombeck et al. Production of ultra-cold neutrons using doppler-shifted bragg scattering and an intense pulsed neutron spallation source. *Nuclear Instruments and Methods*, **165**(2):139–155, 1979.

[34] D. Dubbers, H. Abele, S. Baeßler, B. Märkisch, M. Schumann, T. Soldner, and O. Zimmer. A clean, bright, and versatile source of neutron decay products. *Nuclear Instruments and Methods in Physics Research Section A: Accelerators, Spectrometers, Detectors and Associated Equipment*, **596**(2):238–247, 2008.

[35] A.I. Egorov, V.M. Lobashev, V.A. Nazarenko, G.D. Porsev, and A.P. Serebrov. Production, storage, and polarization of ultracold neutrons. *Journal Name: Yadern. Fiz., v. 19, no. 2, pp. 300-310; Other Information: Orig. Receipt Date: 30-JUN-74*, page Medium: X, 1974.

[36] Yair Ein-Eli and David Starosvetsky. Review on copper chemical-mechanical polishing (cmp) and post-cmp cleaning in ultra large system integrated (ulsi)–an electrochemical perspective. *Electrochimica Acta*, **52**(5):1825–1838, 2007.

[37] Aicha Elshabini-Riad and Fred D. Barlow III. *Thin Film Technology Handbook*. McGraw-Hill, 1 edition, 1998.

[38] B. G. Erozolimskii, I. A. Kuznetsov, I. V. Stepanenko, I. A. Kuida, and Yu A. Mostovoi. New measurements of the electron-neutron spin asymmetry in neutron beta-decay. *Physics Letters B*, **263**(1):33–38, 1991.

[39] S. Esposito, G. Mangano, G. Miele, and O. Pisanti. Precision rates for nucleon weak interactions in primordial nucleosynthesis and 4he abundance. *Nuclear Physics B*, **540**(1-2):3–36, 1999.

[40] Philip H. Bucksbaum Eugene D. Commins. *Weak Interactions of Leptons and Quarks*. Cambridge University Press, 1983.

[41] Extorr, 2010.

[42] A. C. Ferrari et al. Density, sp3 fraction, and cross-sectional structure of amorphous carbon films determined by x-ray reflectivity and electron energy-loss spectroscopy. *Physical Review B*, **62**(Copyright (C) 2010 The American Physical Society):11089, 2000. PRB.

[43] P. Fierlinger, A. Pichlmaier, and H. Rauch. A time-of-flight chopper for ultracold neutrons. *Nuclear Instruments and Methods in Physics Research Section A: Accelerators, Spectrometers, Detectors and Associated Equipment*, **557**(2):572–575, 2006.

[44] Rodger L. Gamblin and Thomas R. Carver. Polarization and relaxation processes in he3 gas. *Physical Review*, **138**(Copyright (C) 2010 The American Physical Society):A946, 1965. PR.

[45] S. Gardner and C. Zhang. Sharpening low-energy, standard-model tests via correlation coefficients in neutron beta decay. *Physical Review Letters*, **86**(25):5666, 2001. Copyright (C) 2010 The American Physical Society Please report any problems to prola@aps.org PRL.

[46] Rath Gibson. http://www.rathgibson.com/downloads/public/pdfs/ 122009RathGibson_True10_SellSheet_sfs.pdf, 2010.

[47] F. Glück and K. Tóth. Order- alpha radiative corrections for semileptonic decays of polarized baryons. *Physical Review D*, **46**(5):2090, 1992. Copyright (C) 2010 The American Physical Society Please report any problems to prola@aps.org PRD.

[48] M. L. Goldberger and S. B. Treiman. Decay of the pi meson. *Physical Review*, **110**(5):1178, 1958. Copyright (C) 2010 The American Physical Society Please report any problems to prola@aps.org PR.

[49] G. Green, V. Cianciolo, P. Koehler, R. Allen, W. M. Snow, P. Huffman, C. Gould, D. Bowman, M. Cooper, and J. Doyle. The fundamental neutron physics beamline at the spallation neutron source. *Journal of Research of the National Institute of Standards and Technology*, **110**(3):149–152, 2005.

[50] A. Grigonis, V. Sablinskas, M. Silinskas, and D. Tribandis. The role of hydrogen in a-c:h films deposited from hexane or acetylene using direct ion beam deposition method. *Vacuum*, **75**(3):261–267, 2004.

[51] CVI Melles Griot. Clcx-uv - clcx-uv fused silica round cylindrical plano-convex singlet lenses, 2008.

[52] W. S. Guo, S. P. Wong, and Y. H. Yu. Spectroscopic ellipsometry characterization of diamond-like carbon films formed by filtered arc deposition. *Nuclear Instruments and Methods in Physics Research Section B: Beam Interactions with Materials and Atoms*, **169**(1-4):54–58, 2000.

[53] Rainer Haerle, Elisa Riedo, Alfredo Pasquarello, and Alfonso Baldereschi. sp2/sp3 hybridization ratio in amorphous carbon from c 1s core-level shifts: X-ray photoelectron spectroscopy and first-principles calculation. *Physical Review B*, **65**(4):045101, 2001. Copyright (C) 2010 The American Physical Society Please report any problems to prola@aps.org PRB.

[54] Rainer Haerle, Elisa Riedo, Alfredo Pasquarello, and Alfonso Baldereschi. sp2/sp3 hybridization ratio in amorphous carbon from c 1s core-level shifts: X-ray photoelectron spectroscopy and first-principles calculation. *Physical Review B*, **65**(4):045101, 2001. Copyright (C) 2010 The American Physical Society Please report any problems to prola@aps.org PRB.

[55] C. Haosheng, L. Jiang, C. Darong, and W. Jiadao. Nano particles behavior in non-newtonian slurry in mechanical process of cmp. *Tribology Letters*, **24**(3):179–186, 2006.

[56] J. C. Hardy and I. S. Towner. Superallowed $0^+ \to 0^+$ nuclear beta decays: A new survey with precision tests of the conserved vector current hypothesis and the standard model. *Physical Review C*, **79**(5):055502, 2009. Copyright (C) 2010 The American Physical Society Please report any problems to prola@aps.org PRC.

[57] J. Haverkamp et al. Plasma plume characteristics and properties of pulsed laser deposited diamond-like carbon films. *Journal of Applied Physics*, **93**(6):3627–3634, 2003.

[58] Jason Dirk Haverkamp. *Plasma Physics in Pulsed Laser Depoition of Hydrogen-free Diamond-like Carbon Films and Nanocomposites*. PhD thesis, 2004.

[59] Stefan Heule. *Production, Characterization and Reflectivity Measurements of Diamond-like Carbon and other Ultracold Neutron Guide Materials*. PhD thesis, Universität Zürich, 2008.

[60] James Hilfiker. Dlc tauclor model, 2007.

[61] R. Hill. Improved source scenarios septebmer 9, 2004. collabration email, 2004.

[62] R. E. Hill et al. Performance of the prototype lanl solid deuterium ultra-cold neutron source. *Nuclear Instruments and Methods in Physics Research Section A: Accelerators, Spectrometers, Detectors and Associated Equipment*, **440**(3):674–681, 2000.

[63] S. Hoedl. personal communication, 2006.

[64] A. T. Holley. personal communication, 2010.

[65] A. T. Holley et al. Studies of the production and transport of highly polarized ultracold neutrons for the ucna experiment. In *2007 American Physical Society Division of Nuclear Physics Meeting*, Newport News,VA, 2007.

[66] A. T. Holley et al. Progress towards a <1% measurement of the neutron beta asymmetry using ultracold neutrons. In *Workshop for Ultra Cold and Cold Neutrons Physics and Sources*, St. Petersburg, 2009.

[67] Adam Holley. UCNA elog entry: 18876, 2008.

[68] Adam Holley. 2008-2009 ratios comparison, 2009.

[69] Adam Tarte Holley. Technical report, North Carolina State Univeristy, 2005.

[70] Hubbard-Hall. Chemical polishing products, 2009.

[71] Chuck Hudak. Hydrogen implantation of samples, 2009.

[72] Paul Huffman. Neutron lifetime measurements, 2009.

[73] Jerry Hunter. Sims hydrogen search. 2009.

[74] V. K. Ignatovich. *The Physics of Ultracold Neutrons*. Oxford University Press, 1990.

[75] Able Electropolishing Inc. Able electropolishing advanced metal improvement technologies, 2010.

[76] Deep-Coat Metallizing Inc., 2010.

[77] Princeton Instruments. Acton optics and coatings, 2008.

[78] Steve Irving. Slurry polishing, 2010.

[79] T. M. Ito et al. A multiwire proportional chamber for precision studies of neutron [beta] decay angular correlations. *Nuclear Instruments and Methods in Physics Research Section A: Accelerators, Spectrometers, Detectors and Associated Equipment*, **571**(3):676–686, 2007.

[80] J. D. Jackson, S. B. Treiman, and H. W. Wyld. Possible tests of time reversal invariance in beta decay. *Physical Review*, **106**(3):517, 1957. Copyright (C) 2010 The American Physical Society Please report any problems to prola@aps.org PR.

[81] Jr G. E. Jellison and F. A. Modine. Erratum: "parameterization of the optical functions of amorphous materials in the interband region" [appl. phys. lett. [bold 69], 371 (1996)]. *Applied Physics Letters*, **69**(14):2137–2137, 1996.

[82] Jr G. E. Jellison and F. A. Modine. Parameterization of the optical functions of amorphous materials in the interband region. *Applied Physics Letters*, **69**(3):371–373, 1996.

[83] Barry R. Holstein John F. Donoghue, Eugene Golowich. *Dynamics of the Standard Model (Cambridge Monographs on Particle Physics, Nuclear Physics and Cosmology)*. Cambridge University Press, 1994.

[84] G. E. JELLISON JR., D. B. GEOHEGAN, D. H. LOWNDES, A. A. PURETZKY, V. I., and MERKULOV. Characterization of pulsed-laser deposited amorphous diamond films by spectroscopic ellipsometry. *Mat. Res. Soc. Symp. Proc.*, **526**:349–354, 1998.

[85] Y. Kawabata et al. Characteristics of deuterated diamond-like carbon as neutron mirror. *Nuclear Instruments and Methods in Physics Research Section A: Accelerators, Spectrometers, Detectors and Associated Equipment*, **529**(1-3):84–86, 2004.

[86] Werner Kern. *Handbook of Semiconductor Wafer Cleaning Technology - Science, Technology, and Applications*. William Andrew Publishing/Noyes, 1993.

[87] K. Kirch et al. Status of the new los alamos ucn source. volume **576**, pages 289–292, Denton, Texas (USA), 2001. AIP.

[88] K. Kirch, B. Lauss, P. Schmidt-Wellenburg, and G. Zsigmond. Ultracold neutronsphysics and production. *Nuclear Physics News*, **20**(1), 2010.

[89] Glenn R. Knoll. *Radiation Detection and Measurement*. Wiley, 3 edition, 2000.

[90] M. Kreuz, V. Nesvizhevsky, A. Petoukhov, and T. Soldner. The crossed geometry of two super mirror polarisers–a new method for neutron beam polarisation and polarisation analysis. *Nuclear Instruments and Methods in Physics Research Section A: Accelerators, Spectrometers, Detectors and Associated Equipment*, **547**(2-3):583–591, 2005.

[91] A. Kurylov and M. J. Ramsey-Musolf. Charged current universality in the minimal supersymmetric standard model. *Physical Review Letters*, **88**(7):071804, 2002. Copyright (C) 2010 The American Physical Society Please report any problems to prola@aps.org PRL.

[92] D. Landolt. Fundamental aspects of electropolishing. *Electrochimica Acta*, **32**(1):1–11, 1987.

[93] S. D. A. Lawes et al. Evaluation of the tribological properties of dlc for engine applications. *Journal of Physics D: Applied Physics*, **40**(18):5427, 2007.

[94] D. H. Lee, S. Fayeulle, K. C. Walter, and M. Nastasi. Internal stress reduction in diamond like carbon thin films by ion irradiation. *Nuclear Instruments and Methods*

in Physics Research Section B: Beam Interactions with Materials and Atoms, **148**(1-4):216–220, 1999.

[95] Joungchel Lee, R. W. Collins, V. S. Veerasamy, and J. Robertson. Analysis of the ellipsometric spectra of amorphous carbon thin films for evaluation of the sp3-bonded carbon content. *Diamond and Related Materials*, **7**(7):999–1009, 1998.

[96] K-R Lee, K. Bewilogua, and H. Saitoh. 1st workshop for the international standardization of diamond-like-carbon coatings, 2008.

[97] Shuo-Jen Lee and Jian-Jang Lai. The effects of electropolishing (ep) process parameters on corrosion resistance of 316l stainless steel. *Journal of Materials Processing Technology*, **140**(1-3):206–210, 2003.

[98] Won-Bae Lee, Jianyong Wu, Yong-Ill Lee, and Joseph Sneddon. Recent applications of laser-induced breakdown spectrometry: A review of material approaches. *Applied Spectroscopy Reviews*, **39**(1):27 – 97, 2004.

[99] Michael A. Lieberman and Alan J. Lichtenberg. *Principles of Plasma Discharges and Materials Processing , 2nd Edition*. Wiley-Interscience, 2 edition, 2005.

[100] Chi-Cheng Lin and Chi-Chang Hu. Electropolishing of 304 stainless steel: Surface roughness control using experimental design strategies and a summarized electropolishing model. *Electrochimica Acta*, **53**(8):3356–3363, 2008.

[101] Chi-Cheng Lin, Chi-Chang Hu, and Tai-Chou Lee. Electropolishing of 304 stainless steel: Interactive effects of glycerol content, bath temperature, and current density on surface roughness and morphology. *Surface and Coatings Technology*, **204**(4):448–454, 2009.

[102] C. Y. Liu et al. An apparatus to control and monitor the para-d2 concentration in a solid deuterium, superthermal source of ultra-cold neutrons. *Nuclear Instruments and Methods in Physics Research Section A: Accelerators, Spectrometers, Detectors and Associated Equipment*, **508**(3):257–267, 2003.

[103] C. Y. Liu and A.R. Young. An application of the "bird cage resonator" as the adiabatic fast passage spin flipper for ucn. http://www.physics.ncsu.edu/weakint/, 2003.

[104] Dongping Liu et al. Surface roughness of various diamond-like carbon films. *Plasma Science and Technology*, **8**(6):701, 2006.

[105] J. Liu et al. Determination of the axial-vector weak coupling constant with polarized ultracold neutrons. *arXiv:1007.3790v1 [nucl-ex]*, 2010.

[106] Anstrom Technology Ltd. Cleanroom supplies, 2009.

[107] Chih-Shun Lu and Owen Lewis. Investigation of film-thickness determination by oscillating quartz resonators with large mass load. *Journal of Applied Physics*, **43**(11):4385–4390, 1972.

[108] B. Major, W. Mrz, T. Wierzchon, W. Waldhauser, J. Lackner, and R. Ebner. Pulsed laser deposition of advanced titanium nitride thin layers. *Surface and Coatings Technology*, **180-181**:580–584, 2004.

[109] M. Makela. 2008 UCNA Collobration Meeting, 2008.

[110] Mark Makela. *Polarized Ultracold Neutrons: their transport in diamond guides and potential to search for physics beyond the standard model*. PhD thesis, Virginia Polytechnic Institute and State University, 2005.

[111] Mark Makela. Effect of guide fermi potential on ucn transmission, 2006.

[112] Mark Makela. personal communication, 2007.

[113] W. Mampe, P. Ageron, C. Bates, J. M. Pendlebury, and A. Steyerl. Neutron lifetime measured with stored ultracold neutrons. *Physical Review Letters*, **63**(6):593, 1989. Copyright (C) 2010 The American Physical Society Please report any problems to prola@aps.org PRL.

[114] W. Mampe, L. N. Bondarenko, V. I. Morozov, Yu. N. Panin, and A. I. Fomin. Measuring neutron lifetime by storing ultracold neutrons and detecting inelastically scattered neutrons. *JETP Letters*, **57**(2):82, 1993.

[115] William J. Marciano and Alberto Sirlin. Improved calculation of electroweak radiative corrections and the value of vud. *Physical Review Letters*, **96**(3):032002, 2006. Copyright (C) 2010 The American Physical Society Please report any problems to prola@aps.org PRL.

[116] D. Margarone et al. Langmuir probe diagnostics of plasma produced by laser ablation. In *35th EPS Conference on Plasma Physics*, 2008.

[117] B. Märkisch et al. The new neutron decay spectrometer perkeo iii. *Nuclear Instruments and Methods in Physics Research Section A: Accelerators, Spectrometers, Detectors and Associated Equipment*, **611**(2-3):216–218, 2009.

[118] Jeff Martin. Ultracold neutrons at triumf. 2009.

[119] Donald M. Mattox. *Handbook of Physical Vapor Deposition (PVD) Processing. Film Formation, Adhesion, Surface Preparation and Contamination Control*. Noyes Publications, 1998.

[120] C. L. Morris et al. Measurements of ultracold-neutron lifetimes in solid deuterium. *Physical Review Letters*, **89**(Copyright (C) 2010 The American Physical Society):272501, 2002. PRL.

[121] C. L. Morris et al. Multi-wire proportional chamber for ultra-cold neutron detection. *Nuclear Instruments and Methods in Physics Research Section A: Accelerators, Spectrometers, Detectors and Associated Equipment*, **599**(2-3):248–250, 2009.

[122] Chris Morris. Baseline and predictions from the 2007 ucna run, April 2008.

[123] Christopher Morris. Fixing the ucn source. Technical report, LANSCE, 2005.

[124] P. Mrel, M. Tabbal, M. Chaker, S. Moisa, and J. Margot. Direct evaluation of the sp3 content in diamond-like-carbon films by xps. *Applied Surface Science*, **136**(1-2):105–110, 1998.

[125] Alan Munter. Neutron scattering lengths and cross sections, 2010.

[126] Takahiro Nakahigashi, Yoshikazu Tanaka, Koji Miyake, and Hisanori Oohara. Properties of flexible dlc film deposited by amplitude-modulated rf p-cvd. *Tribology International*, **37**(11-12):907–912.

[127] Roger Jagdish Narayan. Pulsed laser deposition of functionally gradient diamond-like carbon-metal nanocomposites. *Diamond and Related Materials*, **14**(8):1319–1330, 2005.

[128] O. Naviliat-Cuncic and N. Severijns. Test of the conserved vector current hypothesis in t=1/2 mirror transitions and new determination of —vud. *Physical Review Letters*, **102**(14):142302, 2009. Copyright (C) 2010 The American Physical Society Please report any problems to prola@aps.org PRL.

[129] J. S. Nico, Arif M., M. S. Dewey, T. R. Gentile, D. M. Gilliam, P. R. Huffman, D. L. Jacobson, A. K., and Thompson. The fundamental neutron physics facilities at nist. *Journal of Research of the National Institute of Standards and Technology*, **110**(3):137–144, 2005.

[130] Peter Norberg. Bistep2a 2 amp stepper motor controller, 2010.

[131] Milton Ohring. *The Materials Science of Thin Films*. Academic Press, San Diego, 1992.

[132] Oriel-Instruments. Information on oriel spectral irradiance data, 2010.

[133] Edward D. Palik. *Handbook of Optical Constants of Solids*. Academic Press, 1997.

[134] David L. Pappas et al. Characterization of laser vaporization plasmas generated for the deposition of diamond-like carbon. *Journal of Applied Physics*, **72**(9):3966–3970, 1992.

[135] Jong-Hee Park. *Chemical Vapor Deposition*. ASM International, 1st edition, 2001.

[136] R. W. Pattie et al. First measurement of the neutron beta asymmetry with ultracold neutrons. *Physical Review Letters*, **102**(Copyright (C) 2010 The American Physical Society):012301, 2009. PRL.

[137] R. Paul et al. Synthesis of dlc films with different sp 2 /sp 3 ratios and their hydrophobic behaviour. *Journal of Physics D: Applied Physics*, **41**(5):055309, 2008.

[138] Richard Payling and Peter Larkins. *Optical Emission Lines of the Elements*. Wiley, 2000.

[139] Hugh O. Pierson. *Handbook of Chemical Vapor Deposition, 2nd Edition, Second Edition: Principles, Technology and Applications (Materials Science and Process Technology)*. William Andrew, 2nd edition, 2000.

[140] B. Plaster. personal communication, 2010.

[141] B. Plaster et al. A solenoidal electron spectrometer for a precision measurement of the neutron [beta]-asymmetry with ultracold neutrons. *Nuclear Instruments and Methods in Physics Research Section A: Accelerators, Spectrometers, Detectors and Associated Equipment*, **595**(3):587–598, 2008.

[142] C. Plonka, P. Geltenbort, T. Soldner, and H. Hse. Replika mirrors–nearly loss-free guides for ultracold neutrons–measurement technique and first preliminary results. *Nuclear Instruments and Methods in Physics Research Section A: Accelerators, Spectrometers, Detectors and Associated Equipment*, **578**(2):450–452, 2007.

[143] Irving Polishing and Manurfacturing Co. Inc. http://www.irvinginc.com/, 2010.

[144] A. A. Puretzky, D. B. Geohegan, G. E. Jellison, and M. M. McGibbon. Comparative diagnostics of arf- and krf-laser generated carbon plumes used for amorphous diamond-like carbon film deposition. *Applied Surface Science*, **96-98**:859–865, 1996.

[145] R. Rios et al. Sealed drift tube cosmic ray veto counters. personal communication, 2009.

[146] R. Rios et al. Suppression of ultrcold nuetron depolarization on material surfaces with magnetic holding fields. In *2009 April Meeting of the American Physical Society*, Denver, CO, 2009.

[147] Steve K. Lamoreaux Robert Golub, David J. Richardson. *Ultra Cold Neutrons*. Adam Hilger imprint by IOP Publishing, 1991.

[148] J. Robertson. Diamond-like amorphous carbon. *Materials Science and Engineering: R: Reports*, **37**(4-6):129–281, 2002.

[149] John Robertson. Mechanism of sp3 bond formation in the growth of diamond-like carbon. *Diamond and Related Materials*, **14**(3-7):942–948, 2005.

[150] Anne Sallaska. Ppm/gravity/3he analaysis-in-progress. Technical report, University of Washington, 2005.

[151] Gnter Sauerbrey. Verwendung von schwingquarzen zur wgung dnner schichten und zur mikrowgung. *Zeitschrift fr Physik A Hadrons and Nuclei*, **155**(2):206–222, 1959.

[152] A. Saunders et al. Demonstration of a solid deuterium source of ultra-cold neutrons. *Physics Letters B*, **593**(1-4):55–60, 2004.

[153] K. Schreckenbach et al. A new measurement of the beta emission asymmetry in the free decay of polarized neutrons. *Physics Letters B*, **349**(4):427–432, 1995.

[154] A. Serebrov et al. Depolarization of ucn stored in material traps. *Nuclear Instruments and Methods in Physics Research Section A: Accelerators, Spectrometers, Detectors and Associated Equipment*, **440**(3):717–721, 2000.

[155] A. Serebrov, V. Varlamov, A. Kharitonov, A. Fomin, Yu Pokotilovski, P. Geltenbort, J. Butterworth, I. Krasnoschekova, M. Lasakov, R. Tal'daev, A. Vassiljev, and O. Zherebtsov. Measurement of the neutron lifetime using a gravitational trap and a low-temperature fomblin coating. *Physics Letters B*, **605**(1-2):72–78, 2005.

[156] A. P. Serebrov et al. Depolarization of ultracold neutrons during their storage in material bottles. *Physics Letters A*, **313**(5-6):373–379, 2003.

[157] A. P. Serebrov et al. Ultracold-neutron infrastructure for the pnpi/ill neutron edm experiment. *Nuclear Instruments and Methods in Physics Research Section A: Accelerators, Spectrometers, Detectors and Associated Equipment*, **611**(2-3):263–266, 2009.

[158] A. P. Serebrov and A. K. Fomin. A new world average value for the neutron lifetime. 2010.

[159] N. Severijns, M. Tandecki, T. Phalet, and I. S. Towner. Ft values of the t=1/2 mirror beta transitions. *Physical Review C*, **78**(5):055501, 2008. Copyright (C) 2010 The American Physical Society Please report any problems to prola@aps.org PRC.

[160] R. T. Shann. *Nuovo Cimento*, **5A**:591, 1971.

[161] D. A. Shirley. High-resolution x-ray photoemission spectrum of the valence bands of gold. *Physical Review B*, **5**(12):4709, 1972. Copyright (C) 2010 The American Physical Society Please report any problems to prola@aps.org PRB.

[162] Rajiv K. Singh and J. Narayan. Pulsed-laser evaporation technique for deposition of thin films: Physics and theoretical model. *Physical Review B*, **41**(13):8843, 1990. Copyright (C) 2010 The American Physical Society Please report any problems to prola@aps.org PRB.

[163] M. Singleton and P. Nash. The c-ni (carbon-nickel) system. *Journal of Phase Equilibria*, **10**(2):121–126, 1989.

[164] Yu Sobolev et al. Cubic boron nitride: A new prospective material for ultracold neutron application. *Nuclear Instruments and Methods in Physics Research Section A: Accelerators, Spectrometers, Detectors and Associated Equipment*, **614**(3):461–467, 2010.

[165] Jefferson Lab Hall C staff. Experiment safety assessment document (esad) for the hall c base equipment, 2008.

[166] A. Steyerl. Effect of surface roughness on the total reflexion and transmission of slow neutrons. *Zeitschrift fr Physik A Hadrons and Nuclei*, **254**(2):169–188, 1972.

[167] B. Tipton. Cosmic ray background in the ucna experiment. personal communication, 2002.

[168] I. S. Towner and J. C. Hardy. Improved calculation of the isospin-symmetry-breaking corrections to superallowed fermi beta decay. *Physical Review C*, **77**(2):025501, 2008. Copyright (C) 2010 The American Physical Society Please report any problems to prola@aps.org PRC.

[169] Plymouth Trent. http://www.plymouth.com/_tmp/Sanitary%20Brochure%201007.pdf, 2010.

[170] UCNACollobration. Technical review report for an accurate measurement of the neutron spin – electron angular correlation in polarized neutron beta decay with ultra–cold neutrons, 2000.

[171] M. G. D. van der Grinten et al. Characterization and development of diamond-like carbon coatings for storing ultracold neutrons. *Nuclear Instruments and Methods in Physics Research Section A: Accelerators, Spectrometers, Detectors and Associated Equipment*, **423**(2-3):421–427, 1999.

[172] D. H. Wilkinson. Analysis of neutron [beta]-decay. *Nuclear Physics A*, **377**(2-3):474–504, 1982.

[173] K. R. Williams, K. Gupta, and M. Wasilik. Etch rates for micromachining processing-part ii. *Microelectromechanical Systems, Journal of*, **12**(6):761–778, 2003.

[174] P. R. Willmott and J. R. Huber. Pulsed laser vaporization and deposition. *Reviews of Modern Physics*, **72**(1):315, 2000. Copyright (C) 2010 The American Physical Society Please report any problems to prola@aps.org RMP.

[175] T. Witke, T. Schuelke, J. Berthold, C. F. Meyer, and B. Schultrich. Deposition of hard amorphous carbon coatings by laser and arc methods. *Surface and Coatings Technology*, **116-119**:609–613, 1999.

[176] J. A. Woollam. A short course in ellipsometry, 2001.

[177] J. A. Woollam, B. D. Johs, C. M. Herzinger, J. N. Hilfiker, R. A. Synowicki, and C. L. Bungay. Overview of variable-angle spectroscopic ellipsometry (VASE): I. Basic theory and typical applications. In G. A. Al-Jumaily, editor, *Society of Photo-Optical Instrumentation Engineers (SPIE) Conference Series*, pages 3–28, July 1999.

[178] Yanping Xu. *Characterization of Solid Deuterium Ultracold Neutron Source Production and UCN Transport*. PhD thesis, 2006.

[179] Y. Lawrence Yao, Hongqiang Chen, and Wenwu Zhang. Time scale effects in laser material removal: a review. *The International Journal of Advanced Manufacturing Technology*, **26**(5):598–608, 2005.

[180] B. Yerozolimsky, I. Kuznetsov, Yu Mostovoy, and I. Stepanenko. Corrigendum: Corrected value of the beta-emission asymmetry in the decay of polarized neutrons measured in 1990. *Physics Letters B*, **412**(3-4):240–241, 1997.

[181] Albert Young and UCNA Collaboration.

[182] Zhaoyan Zhang and George Gogos. Effects of laser intensity and ambient conditions on the laser-induced plume. *Applied Surface Science*, **252**(4):1057–1064, 2005.